Polarization Observables in Strangeness Photoproduction with CLAS at Jefferson Lab

Craig Alexander Paterson

Presented as a Thesis for the Degree of Doctor of Philosophy

Nuclear Physics Group
Department of Physics and Astronomy
University of Glasgow

Abstract

This work presents measurements of several polarization observables for the reactions $\overrightarrow{\gamma}$p$\rightarrow K^+\Lambda^0$ and $\overrightarrow{\gamma}p \rightarrow K^+\Sigma^0$. The data were collected in the summer of 2005 at the Thomas Jefferson National Accelerator Facility, using a linearly polarized photon beam in the energy range 1.66 GeV $< \sqrt{s} <$ 2.24 GeV. In addition to measuring the photon asymmetry, target asymmetry and hyperon recoil polarization, first ever measurements are made for the double polarization observables O_x and O_z. The measurements of the photon and target asymmetries vastly increase the precision of the current world dataset, as well as extending the angular coverage.

The aim of the experiment was to investigate the process of strangeness production on the proton and the role played by different resonances in the reaction dynamics. In particular the role played by missing resonances - the excited baryon states predicted by $SU(6) \otimes O(3)$ symmetric quark models but so far undetected in experiment - will be studied.

The photon asymmetry is found to be positive for almost the full kinematic range for both channels with some structure evident at centre of mass energies above 1.92 GeV, while the recoil polarization results reproduce the large polarizations seen in previous measurements with a much higher precision. For the Λ channel, the double polarization observables indicate that the photon polarization is preferentially transferred to the hyperon along the $\hat{x}$-axis, with the O_x observable displaying a strong signal at forward angles. There is also evidence that the Λ is fully polarized at mid to forward angles, although the behaviour is not reproduced by the Σ^0, where there is also a failure to define a preferred polarization axis. The target asymmetry results for the Λ channel display a negative polarization at backward angles with a very large positive polarization at forward production angles.

The $K^+\Lambda$ results are compared to calculations from an isobaric model and a Regge-plus-resonance approach. Both models include the established $^{****}S_{11}(1650)$. $^{***}P_{11}(1710)$ and $^{****}P_{13}(1720)$ resonances in their calculations, with the isobaric prescription using various Born terms to describe the background, and the Regge-plus-resonance calculation utilizing Regge trajectories. Both approaches give good agreement with the data, with some evidence for an important role to be played by the missing $D_{13}(1900)$ resonance and some weaker evidence for the inclusion of a missing $P_{11}(1900)$ state. For the $K^+\Sigma^0$ results the same model

schemes were used for comparison, this time with the inclusion of the $^{**}S_{31}(1900)$ and $^{****}P_{31}(1910)$ resonances. No missing states were considered for these calculations and the agreement with the data was not as good as the agreement for the Λ channel. Both channels indicate that the models should be re-optimized in light of the extra constraints provided by the new data. Overall, some evidence is presented for the existence of missing resonant states but further theoretical input is required before this can be confirmed.

Declaration

The data presented in this thesis were obtained as part of the g8b collaboration at the Thomas Jefferson National Accelerator Facility, Virginia, USA, and the Nuclear Physics Experiment Group, The University of Glasgow. I participated fully in the preparation and execution of the experiment. The analysis of the experimental data is my own work. This thesis was composed by myself.

Craig A. Paterson

June 2008

Acknowledgements

The completion of this thesis would not have been possible without the help of a number of people, not all of whom I will be able to thank in this short section so a special thank you to those not mentioned. Firstly, I would like to thank my supervisors, Prof. Günther Rosner and Dr. David Ireland, for giving me the opportunity to work on this experiment. Dave deserves thanks for the helpful suggestions he has made during my time in the group, and for taking the time to carefully and critically read this thesis. Special thanks has to go to my *de facto* supervisor Ken Livingston, without whom the completion of this thesis would have been a far more painful experience. I am particularly grateful for the patience he has shown in answering my regular computing related questions, and for helping to guide me through this analysis. You've been a top supervisor Ken. Cheers.

At Jefferson Lab some people deserve a special mention for making great efforts with the preparation and running of the experiment. Such on-site expertise was crucial to having a successful experiment, so a big thank you to Joe Santoro, Eugene Pasyuk, Franz Klein and Phil Cole. Your kind help and suggestions have always been appreciated. Particular thanks are given to Joe for making my time at Jlab a far more pleasant experience and being a great friend. No one else does physics quite like you Joe. Best wishes to both you and Julie in New York.

In the Glasgow Nuclear Physics Group, I'd like to thank all the staff and students who contributed to making my time in the group a very enjoyable one. In particular "the Reverend" Russell Johnstone, Neil Hassall, Stuart Fegan, Bryan McKinnon and Neil Thomson for being good company both in Glasgow and in Jlab; Jamie Robinson, Gordon Hill, Richard Codling, David Howdle and Andrew Osborne for all the laughs we had and for distracting me from my physics-related problems. I'd also like to thank both Derek Glazier and David Hamilton for the help and advice they have given me.

A final thank you to Jennifer, both for her support and for proof reading this work. I know you enjoyed it really.

"Science is a wonderful thing if one does not have to earn one's living at it." - Albert Einstein

"In the beginning the universe was created. This made a lot of people very angry and has widely been considered as a bad move" - The Hitchiker's Guide to the Galaxy

Contents

List of Figures

List of Tables

Chapter 1

Introduction

The process of strangeness production from the proton leading to recoiling Λ and Σ^0 hyperons is a powerful tool in the investigation of non-strange baryon resonances. The reactions $\gamma p \rightarrow K^+\Lambda$ and $\gamma p \rightarrow K^+\Sigma^0$ are characteristic of the broader field of pseudoscalar meson photoproduction, and spin observables measured in these channels can aid the unfolding of the baryon resonance spectrum. This represents a major field of interest in hadronic physics as the spectroscopy of excited states gives physicists an opportunity to explore the structure and interactions of hadronic systems within the realm of non-perturbative QCD. This is analogous to the process of nuclear spectroscopy, where the spectrum of excited states reflects the underlying quantum configurations of the mesons and nucleons.

One of the most important topics to be addressed in baryon spectroscopy is the problem of the so-called missing resonances. These are the excited baryon states predicted by $SU(6) \otimes O(3)$ symmetric quark models to have an influence in the few GeV regime, but which are so far undetected by experiment. The majority of the existing data that has been used to search for these missing excited states has come from pion production and focused on πN decay modes. However, recent quark model calculations [1] have suggested that some of these resonances should couple strongly to photoproduction channels that decay into particles containing strange quarks, such as $K^+\Lambda$ and $K^+\Sigma^0$. A historically important method of accessing the resonances that couple to these states is to measure the reaction cross-section, shown for several different photoproduction channels in figure 1.1. This plot displays the photoproduction cross-section on the proton in the energy range $E_\gamma = 0.2 - 2.0$ GeV. For the total cross section four different resonance regions can be observed, with the lowest energy region associated with the $\Delta(1232)$ excitation. As the energy increases and one moves into the higher resonance regions, the threshold for more decay modes is surpassed and it becomes

extremely non-trivial to identify individual excited states. The fact that these resonances are often very short lived and have large overlapping widths also adds to the difficulty. A possible solution is to use the spin orientation of the incoming beam, recoiling baryon and target nuclei to extract further information about the reaction dynamics. Indeed the use of a polarized beam and target, along with a facility to measure the recoil baryon polarization, allows one to measure various polarization observables. These have been shown to be very sensitive to the underlying physics of the reaction [2–4] and should provide important additional information to the cross section on which excited baryon states couple strongly to the decay channel.

This work will focus on providing high quality, high precision measurements of polarization observables with unparalleled sensitivity to the underlying physics. The photoproduction of $K^+\Lambda$ and $K^+\Sigma^0$ will be studied at photon energies from 1.1 to 2.1 GeV with a linearly polarized photon beam. This will give access to a total of five observables: the photon asymmetry Σ, the target asymmetry T, the hyperon recoil polarization P, and the two double polarization observables O_x and O_z. It is then hoped that the interpretation of these measurements will provide some insight into the missing resonance problem, as well as giving a better understanding of the strangeness production process.

It is evident from figure 1.1 that the cross sections for $K^+\Lambda$ and $K^+\Sigma^0$ photoproduction are approximately two orders of magnitude smaller than for single pion production. This makes the study of hyperon final states experimentally difficult as a large number of reaction events have to be created. In turn there must be a facility capable of detecting a sizeable number of the decay products in order to gain a large event sample. The experimental facility available at Jefferson Lab provides the ideal opportunity to pursue the study of hyperon physics as the CEBAF accelerator delivers a high luminosity beam capable of producing a large number of interaction events. Further to this, the CLAS detector has a large acceptance for charged particles resulting in this analysis having a final hyperon event sample unrivalled in size by any other facility.

This chapter will provide a short introduction to the theory of the strong interaction, QCD, and explain the difficulties in applying the theory in the resonance region. The topic of baryon spectroscopy will then be discussed, focusing on the physics issues that one hopes to illuminate in this work, including a short introduction to strangeness photoproduction and the Λ and Σ^0 hyperons. The basic formalism of polarization observables will also be introduced, with a focus on the measurements that will be made in this work.

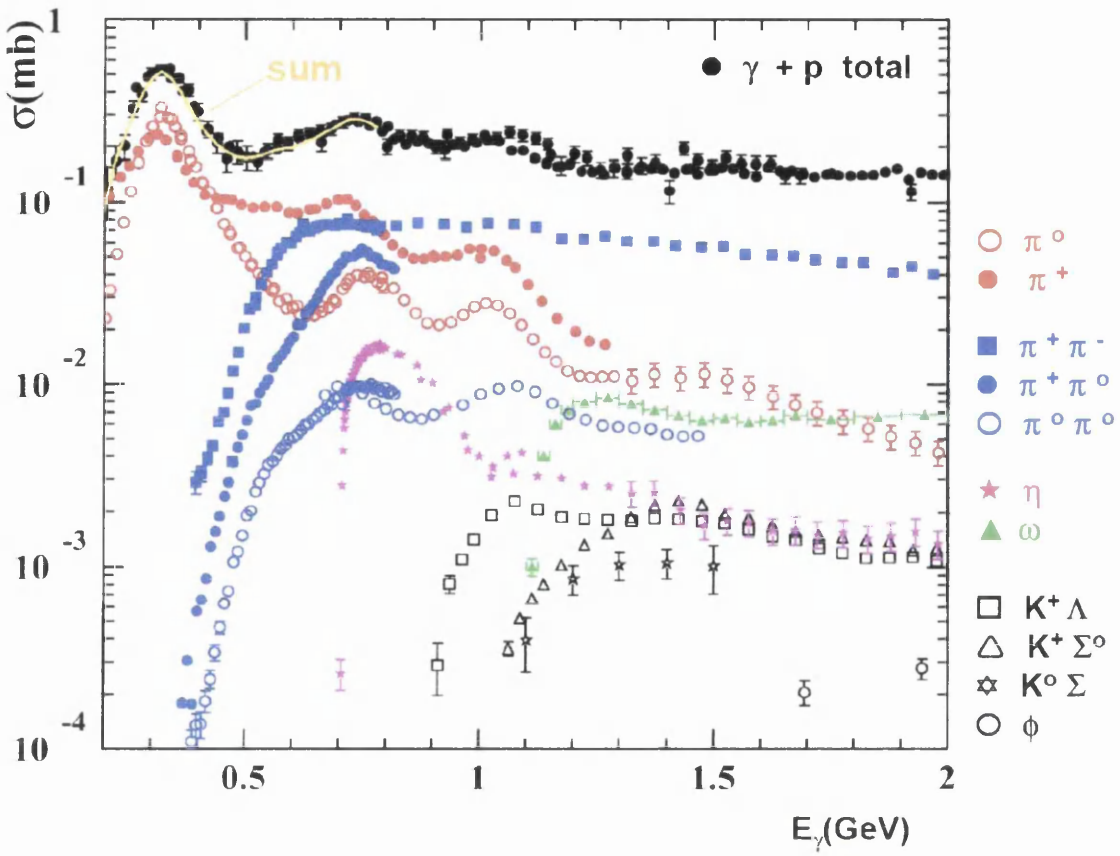

Figure 1.1: Photoproduction cross section on the proton for the energy range $E_\gamma = 0.2 - 2.0$ GeV. Four resonance regions can be observed within the total cross section with the lowest energy region associated with $\Delta(1232)$ excitation. The cross section for both the $K^+\Lambda$ and $K^+\Sigma^0$ channels are also displayed, showing them to be almost two orders of magnitude smaller than for single pion production.

1.1 Quantum Chromo-Dynamics (QCD)

Hadronic physics involves the study of strongly interacting systems under local gauge invariance [5, 6]. The currently accepted theory for this strong interaction is Quantum Chromo-Dynamics (QCD), a non-abelian gauge theory of coloured quarks. QCD, within the standard model, is able to describe a complicated array of composite sub-atomic particles through the arrangement of the underlying quarks, which are currently believed to come in six different flavours - up, down, strange, charm, top and bottom. QCD is able to account for a rich variety of hadronic states through the arrangement of different quantum numbers intro-

duced at various stages during the development of the standard model, such as isospin and flavour [7].

Isospin was introduced by Heisenberg as a quantum number related to the strong interaction to describe various related symmetries for the proton and neutron. This $SU(2)$ symmetry was used to account for the near degeneracy of the proton and neutron masses, as well as the invariance of the strength of the nuclear force under exchange of nucleons. More rigorously the symmetry of isospin arises from the invariance of the strong interaction Hamiltonian under the action of an $SU(2)$ Lie group. To further describe the increasing number of strongly interacting states that were being discovered by experiment, Gell-Mann [8] introduced the "strangeness" quantum number. This allowed for hadrons that displayed similar properties to be grouped according to the so-called "eight-fold way". This arrangement can be interpreted as a consequence of flavour symmetry between the quarks. As theory and experiment advanced three new types of quark flavour were discovered: charm, top and bottom. As QCD is fully independent of quark flavour, any distinction between different quarks comes entirely from the mass differences. The baryon octet of light spin 1/2 baryons, including the Λ and Σ^0, is displayed in figure 1.2.

As well as the increasing number of hadronic states being discovered, another issue to be resolved was the existence of the Δ^{++} state. This particle remained mysterious as it was composed of three up quarks with parallel spins giving it a totally symmetric spin-flavour structure. However, quarks are fermions which satisfy an anti-symmetric wave fuction. In order to resolve this Han, Nambu and Greenberg independently introduced a new quantum label for quarks called colour. This label was required to have three degrees of freedom (called red, green and blue) and was described by an $SU(3)_c$ gauge group with non-abelian internal symmetry. An interesting property of QCD is that the force between two colour charges does not decrease with distance. This leads to the important principle, called confinement, that quarks cannot be liberated from the hadrons.

An interesting feature of the strong interaction is that it becomes weaker and easier to calculate at higher energies, as illustrated in figure 1.3. This phenomena, called asymptotic freedom, results from the QCD coupling constant, α_s, decreasing with increasing energy. Asymptotic freedom occurs when the exchange momentum is very large and the mathematics of the gauge theory become simplified. This results from the quarks becoming effectively free moving, non-interacting particles within the nucleons. The principles that have been well established for photon and electron interactions in QED can then be applied to

quarks and gluons at high energies. QCD also simplifies in the limit of non-relativistic heavy quark states. In this regime the quark can be viewed as a static source of gluon field and corrections can be systematically applied in perturbation theory. In heavy-quark effective theories new symmetries arise that can be used to calculate heavy hadron form factors and simplify sum-rule analyses.

At low energies and momenta, such as those at the quark-hadron interface, the running coupling constant of QCD approaches unity. When this occurs it is no longer possible to carry out expansions in powers of α_s and QCD becomes non-perturbative. Many areas in hadronic physics are described by non-perturbative QCD, for which there are no rigorous solutions. This is a particular problem when regarding investigations of how quarks combine to build nucleons, as well as gaining a fuller understanding of the excited baryon spectrum.

Progress has been made in attempting to solve non-perturbative QCD on a discretized Euclidean space-time lattice. A recent lattice calculation, using bayesian priors and overlap fermions, was able to predict masses of the two lowest state octet and decuplet baryons [9]. The $1/2^+(1440)$ Roper state was also observed for the first time as being the first T=1/2 excited state of the nucleon. Further possibilities for predictions of the nucleon spectrum come from the restoration of chiral symmetry exhibited by some high-lying states [10], along with predictions based on a holographic dual of QCD [11]. However, despite these promising developments lattice QCD and other less phenomenological descriptions are still a long way off from fully describing the excited baryon spectrum.

1.2 Baryon Spectroscopy

A study of meson photoproduction represents an important topic within baryon spectroscopy as it provides an opportunity to accurately determine the parameters of known resonances, as well as aiding the discovery of new baryon states if any exist. The non-perturbative nature of QCD at low momenta and energies, as well as the still developmental status of lattice QCD, has forced hadronic physics to rely upon phenomenological quark models to make predictions about the baryon spectrum. These models can vary in structure, but all essentially employ the same technique of reducing the complicated quark-gluon soup of QCD to a simpler system of constituent quarks interacting in some inter-quark potential. By applying the laws of the standard model these quark models can predict the existence of various excited nucleon states. These states are usually classified by

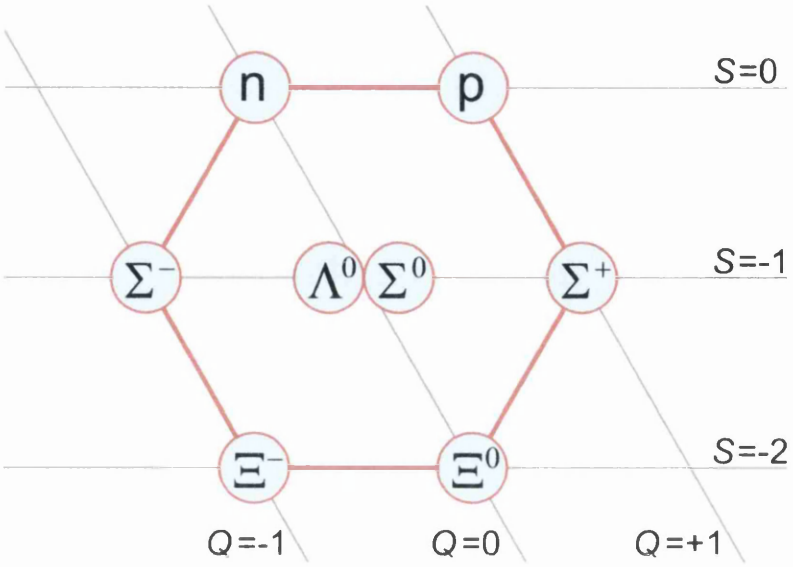

Figure 1.2: Octet of light spin 1/2 baryons arranged in terms of charge Q and strangeness S, displaying the Λ and Σ^0 hyperons.

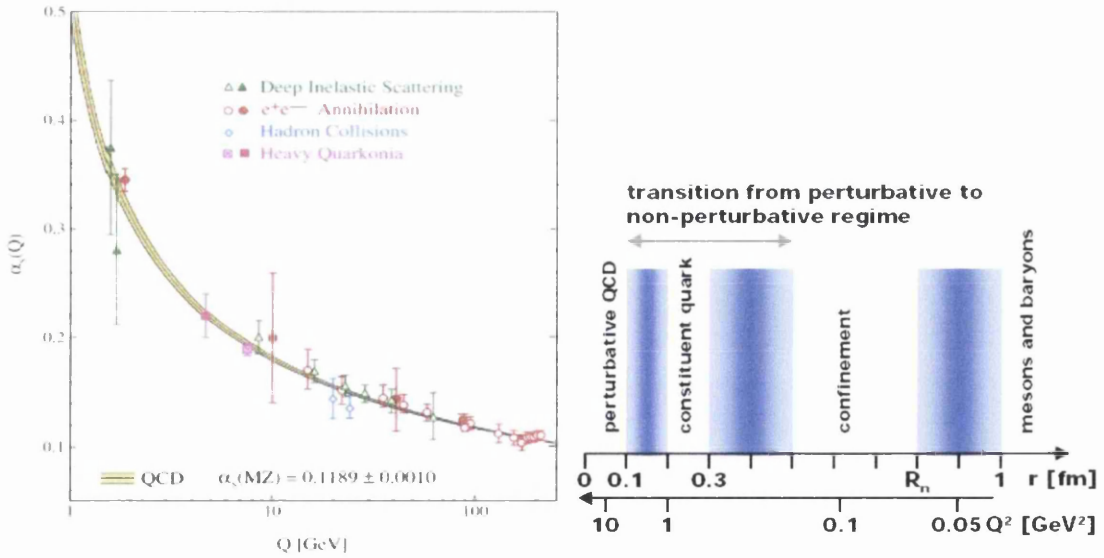

Figure 1.3: On the left is a plot displaying the strength of the QCD running coupling constant as a function of the exchanged gluon momentum, Q. On the right is a scale, as a function of Q^2, showing the transition from perturbative to non-perturbative QCD.

a L_{2I2J} notation, where L is the orbital angular momentum of the resonance given in spectroscopical notation, I is the isospin and J is the total angular momentum.

1.2.1 Symmetric Quark Models

Symmetric quark models, as a regression from pure QCD, allow for a classification of hadrons in terms of the valence quarks. The quantum numbers of these quarks are used to identify the hadrons in terms of the quark flavour and the Poincare symmetry, J^{PC}, where J is the angular momentum, P is the intrinsic parity and C is the charge conjugation. With the introduction of strangeness by Gell-Mann and Zweig [8] the baryon spectrum was unfolded in the $3 \otimes 3 \otimes 3$ symmetry of the $SU(3)$ quark model. A further introduction of quark spins and orbital angular momentum excitations allows one to predict a rich spectrum of nucleon resonances based on $SU(6) \otimes O(3)$ symmetric quark models.

Initial attempts at unfolding the baryon spectrum from a quark model were carried out by Faiman and Hendry [12] who developed a quark-shell model based on harmonic-oscillator forces. The idea was developed from the familiar principles of a particle moving within a three dimensional harmonic-oscillator potential. From this it was possible to predict a spectrum of baryons that was consistent with the data of the time. A QCD improved quark-shell model was developed by Forsyth and Cutkosky [13] to fit masses and elastic widths of the S = 0 baryons. This model was based on a decay operator with the form $S \cdot ((g_1 P_q + g_2 P_{-q})$, where P_q and P_{-q} are the created quark and anti-quark momenta and S is their combined spin. The model included various baryon resonances, many of which were found to be in good agreement with existing data. Further work by Koniuk and Isgur [14] using an elementary-meson emission model allowed for predictions of non-strange baryon decays up to the N=2 band in both $K^+\Lambda$ and $K^+\Sigma^0$ photoproduction. In their reaction scheme a kaon that is treated as point-like couples directly to the quarks in the initial baryon. These models, and other variants, are able to predict a sizeable spectrum of non-strange baryon states that should couple strongly to the strange decay channels. What states are then found by experiment along with how well their extracted properties, such as widths, compare with the calculations will determine how successful the various models are at describing the strangeness production process.

1.2.2 Missing Resonances

A long-standing problem in hadronic physics is the so-called "missing resonances". These are excited baryon states predicted by symmetric quark models but so far undetected in experiment. The missing resonance problem is starkly shown in table 1.1 which displays the states predicted by the $SU(6) \otimes O(3)$ quark model from Forsyth and Cutkosky, along with their PDG ratings [15]. A significant number of the predicted states in this table have either one or zero-star ratings implying that there is very little or no experimental evidence for their existence.

There are two possible explanations as to why these resonant states have not been determined by experiment. One possibility is that the quark models used to date have some intrinsic flaw and require a fundamental modification. Diquark models [16], as illustrated in figure 1.4, are based on the assumption that two of the quarks exist inside the nucleon in a tightly coupled state. This situation can arise when the colours and spins of the two quarks are anti-symmetric, causing the force between them to become attractive. When the two quarks are correlated in this way they form a low-energy configuration that restricts the number of internal degrees of freedom of the nucleon. This lowers the level density of baryon resonances and removes a large number of the missing states from the predictions.

Another possibility is that the measurements made to date are simply not sensitive to these states by virtue of most of the existing data coming from pion production experiments involving πN final states. A recent quark model calculation by Capstick and Roberts [1] predicts that some of these missing resonances should couple strongly to strange baryon final states produced in photoproduction experiments. They describe the baryon decays in a relativized scheme based on a $^3P_0$ creation model. This calculation takes into account the finite spatial extent of the final meson as well as including the excited strange baryons $\Lambda(1405)$, $\Lambda(1520)$, and $\Sigma(1385)$ along with the $K^\star$ exited mesons. The model makes predictions for a series of negative and positive parity states up to the N=3 band. These results are displayed for the $K^+\Sigma^0$ and $K^+\Lambda$ channels in figures 1.5 and 1.6 respectively. It is found that the signs and magnitudes of the predicted amplitudes for both channels are in good agreement with those extracted from the well established states. For the $K^+\Lambda$ channel Capstick and Roberts predicted that there should be several negative parity states in the N=3 band that should be clearly seen by experiment. In particular they predict that the two-star $N(2080)D_{13} = [N\frac{3}{2}^-]_3(1960)$ state be clearly evident in a precision measurement of $\gamma p \rightarrow K^+\Lambda$, dominating its partial wave. They also predict the existence of the weakly established $N(2090)S_{11} = [N\frac{1}{2}^-]_3(1945)$. In the $K^+\Sigma^0$ reaction their calculations suggest an

N*	Status	SU (6) ⊗ O (3)	Parity	Δ*	Status	SU (6) ⊗ O (3)
P_{11} (938)	****	$(56, 0^+)$	+	P_{33} (1232)	****	$(56, 0^+)$
S_{11} (1535)	****	$(70, 1^-)$				
S_{11} (1650)	****	$(70, 1^-)$		S_{31} (1620)	****	$(70, 1^-)$
D_{13} (1520)	****	$(70, 1^-)$	-	D_{33} (1700)	****	$(70, 1^-)$
D_{13} (1700)	***	$(70, 1^-)$				
D_{15} (1675)	****	$(70, 1^-)$				
P_{11} (1520)	****	$(56, 0^+)$		P_{31} (1875)	****	$(56, 2^+)$
P_{11} (1710)	***	$(70, 0^+)$	+	P_{31} (1835)		$(70, 0^+)$
P_{11} (1880)		$(70, 2^+)$				
P_{11} (1975)		$(20, 1^+)$				
P_{13} (1720)	****	$(56, 2^+)$		P_{33} (1600)	***	$(56, 0^+)$
P_{13} (1870)	*	$(70, 0^+)$		P_{33} (1920)	***	$(56, 2^+)$
P_{13} (1910)		$(70, 2^+)$	+	P_{33} (1985)		$(70, 2^+)$
P_{13} (1950)		$(70, 2^+)$				
P_{13} (2030)		$(20, 1^+)$				
F_{15} (1680)	****	$(56, 2^+)$		F_{35} (1905)	****	$(56, 2^+)$
F_{15} (2000)	**	$(70, 2^+)$	+	F_{35} (2000)	**	$(70, 2^+)$
F_{15} (1995)		$(70, 2^+)$				
F_{17} (1990)	**	$(70, 2^+)$	+	F_{37} (1950)	****	$(56, 2^+)$

Table 1.1: The $SU(6)\otimes O(3)$ supermultiplet assignments from the QCD improved model of Forsyth and Cutkosky [13]. The PDG star ratings represent the level of experimental confidence in the existence of the state.

important contribution from the $\Delta(1910)P_{31} = [\Delta\frac{1}{2}^+]_2(1875)$ for which only an upper limit is quoted by the PDG [15]. Although the amplitudes for this channel are considerably less certain than the $K^+\Lambda$ they can also predict the existence of the N=2 missing state $[N\frac{3}{2}^+]_3(1910)$ and the model states $[N\frac{3}{2}^+]_2(1870)$ and $[\Delta\frac{1}{2}^+]_1(1835)$.

One of the major motivations for this thesis is to provide a high-quality data set that can be used to determine the existence of these predicted missing states. In particular the use of a linearly polarized photon beam together with a measurement of the hyperon recoil polarization will give access to the photon beam asymmetry Σ, the beam-recoil double polarization observables O_x and O_z and the target asymmetry T. These measurements have been predicted to be very sensitive to the possible $D_{13}(1960)$ missing resonance [2], and together with previous CLAS results with a circularly polarized beam [17] and a future analysis with a polarized target [18], they should facilitate a model-independent determination of any missing states.

1.3 The Λ and Σ^0 Hyperons

The Λ and Σ^0 particles belong to a larger group called the hyperons (denoted by Y) that contain any baryon composed of one strange quark but no charm or bottom quarks. Both particles have the same uds valence quark structure, but

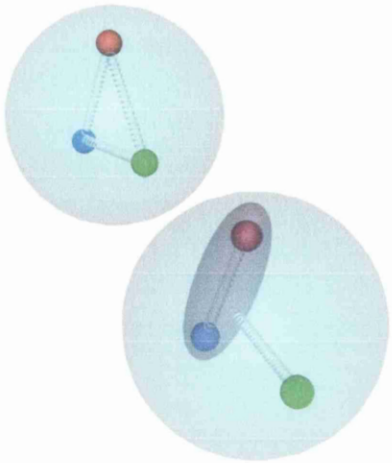

Figure 1.4: Schematic representation of constituent quark (top) and diquark (bottom) models.

in Λ the ud quark are in a spin singlet state, whereas they are in a spin triplet in Σ^0. Each particle has spin 1/2 and comes from the same baryon octet as the proton and neutron, as shown in figure 1.2. Λ has a mass of 1115.68 MeV/c^2 and a mean lifetime of 2.6×10^{-10}s whilst Σ^0 has a mass of 1192.64 MeV/c^2 and a mean lifetime of 7.47×10^{-20}s. A further important difference between the two particles is that Λ has isospin = 0 and Σ^0 has isospin = 1. This is an important property when considering baryon spectroscopy as a $K\Sigma^0$ final state can involve the excitation of both $N^\star$ and Δ states whereas the $K\Lambda$ channel can only involve intermediate isospin 1/2 $N^\star$ states. This isospin selectivity is an important feature of $K\Lambda$ photoproduction as it makes the reaction easier to describe with no Δ states contributing. A list of the main properties of each particle is given in table 1.2.

An obvious consequence of the relatively short lifetimes of both particles is that they will not travel far enough before decaying to be detected by the CLAS spectrometer. Instead they will have to be reconstructed from their decay products. In the case of Λ, it decays 63.9% of the time through the mode

$$\Lambda \rightarrow p\pi^- \tag{1.1}$$

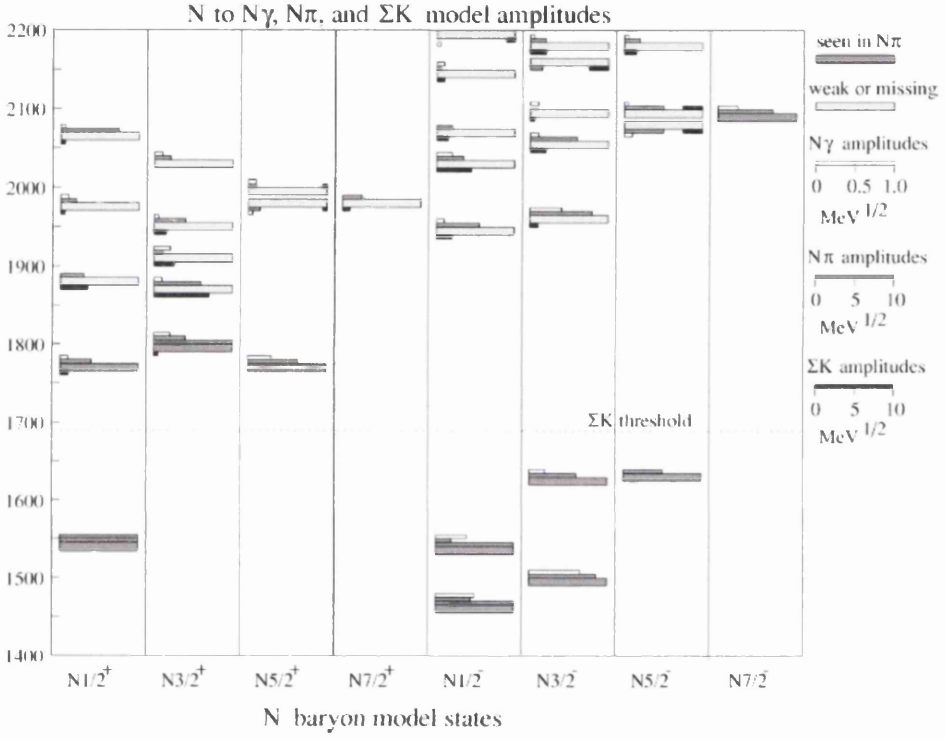

Figure 1.5: Mass predictions for $N\gamma$, $N\pi$ and ΣK final states from the relativized quark model of Capstick and Roberts [1]. Heavy uniform-width bars show states that have been well established in partial wave analyses while the light bars represent states that are weakly established or missing.

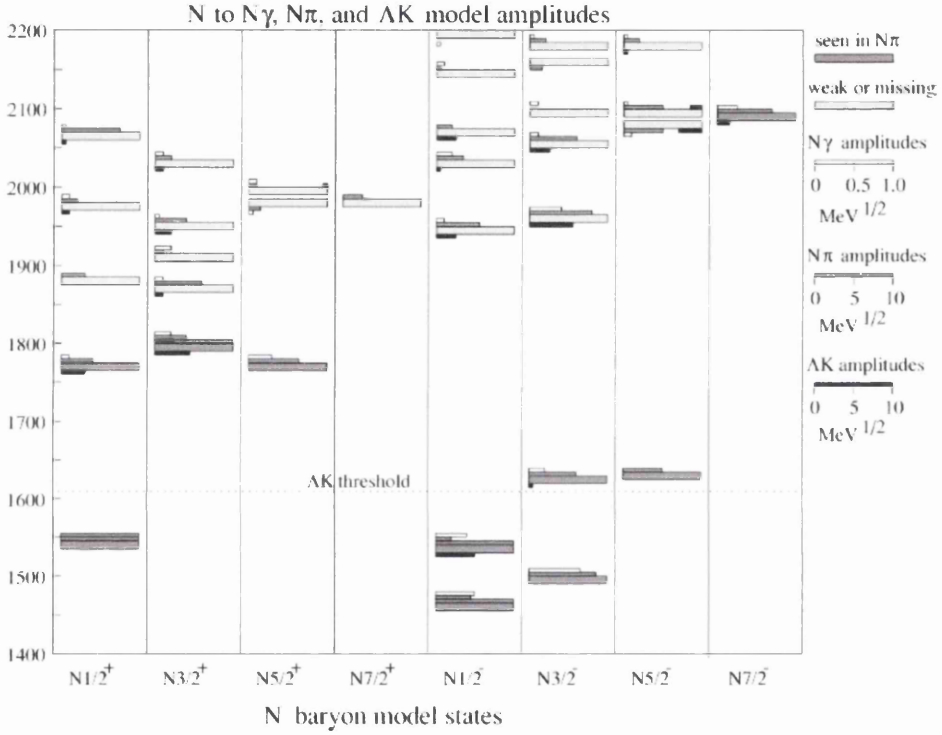

Figure 1.6: Mass predictions for $N\gamma$, $N\pi$ and ΛK final states from the relativized quark model of Capstick and Roberts [1]. Heavy uniform-width bars show states that have been well established in partial wave analyses while the light bars represent states that are weakly established or missing.

as well as having a 35.8% branching ratio into

$$\Lambda \rightarrow n\pi^0. \tag{1.2}$$

Σ^0 decays with a 99.9% branching ratio into

$$\Sigma^0 \rightarrow \gamma\Lambda \tag{1.3}$$

where the decay γ has an energy of 75MeV.

A further property of the Λ hyperon is that it is self-analyzing. That is to say that its parity-violating weak decay allows for a measurement of the hyperon's polarization. This property arises from the interference of the parity violating S and parity conserving P-wave amplitudes. For Λ, one can define a particular polarization component $P_{\Lambda i}$ where $i \in \{x, y, z\}$ is a given axis in space. The proton angular intensity distribution, $I(cos\theta^p_\Lambda)$ as a function of the proton polar angle in the hyperon rest frame θ^p_Λ is given by

$$I(cos\theta^p_\Lambda) = \frac{1}{2}(1 + \alpha P_\Lambda cos\theta^p_\Lambda), \tag{1.4}$$

where α is the self-analyzing power of the hyperon (or weak decay asymmetry parameter) which has been measured experimentally to be 0.642 [15]. The result of this relation is that one can extract the Λ polarization from the proton angular distribution without the requirement of a polarimeter device.

It is also possible to measure the polarization of Σ^0 through the self-analyzing decay of its daughter Λ. A detailed proof of this result is given in reference [17] but the details are outlined here. The main principle is that a produced Σ^0 will have some polarization, P_{Σ^0}, and the Λ arising from its magnetic dipole transition decay will preserve some of the polarization. The authors of [17] show that, when the direction of Λ is not explicitly measured, the polarization of Λ is related to the polarization of the parent Σ^0 by:

$$P_\Lambda = -\frac{1}{3}P_{\Sigma^0}. \tag{1.5}$$

A complication will arise in this work due to the analysis only involving a semi-inclusive detection of the kaon and the decay proton from Λ. This means that it will be impossible to transform into the Λ rest frame, resulting in a requirement to measure the angular distribution of protons from the Λ decay in the rest frame of

	Λ	Σ^0
Rest Mass (GeV)	1.115	1.192
Makeup	uds	uds
Isospin	0	1
Spin	$\frac{1}{2}$	$\frac{1}{2}$
Parity	+	+
Mean Lifetime	2.6×10^{-10}	7.4×10^{-20}

Table 1.2: Main properties of Λ and Σ^0. Data taken from PDG [15].

the parent Σ^0. It is shown in reference [17] by means of both an explicit integration and a Monte Carlo simulation that this situation results in a modification of equation 1.5 to the form

$$P_\Lambda = -\frac{1}{3.90} P_{\Sigma^0}. \tag{1.6}$$

Therefore it will be possible to extract the polarization of both hyperons in this work through the weak decay of Λ, although the statistical uncertainty for the Σ^0 results will be almost four times as large as for the Λ. As will be discussed in the next section, this self-analyzing phenomena greatly increase the number of polarization observables that can be measured in this work.

1.4 Polarization Observables in Hyperon Photoproduction

1.4.1 Formalism

Polarization observables have historically been shown to be amongst the most sensitive probes of hadronic processes. These observables are of particular interest in reactions that involve the photoproduction of pseudoscalar mesons, as it is possible for a suitable combination of the observables to allow for model independent analyses. Polarization observables arise naturally from a study of the transversity amplitudes which can be related to the scattering amplitude of the reaction. It is possible to derive a suitable expression for the scattering amplitude for kaon photoproduction by writing down the S-matrix in the form

$$s_{fi} = \frac{1}{(2\pi)^2}\left[\frac{M_p M_\Lambda}{4E_\Lambda E_K E_p E_\gamma}\right]^{\frac{1}{2}} M_{fi} \times \delta^{(4)}(p_p + p_\gamma - p_K - p_\Lambda) \tag{1.7}$$

where M, E and p are the mass, energy and 4-momenta of the various reaction particles, each represented by the appropriate subscript [19]. M_{fi} represents the Lorentz-invariant matrix element given by

$$M_{fi} = \overline{u}(p_\Lambda, s_\Lambda)\Sigma_{j=1}^{4} A_j M_j u(p_p, s_p) \tag{1.8}$$

The amplitudes A_j contain information on the contributions of each state and channel to the overall amplitude. Examples of these are tabulated in the work of Adelseck and Saghai [19]. It is then possible to express equation 1.7 in terms of the two-component spinors χ, which leads to an alternative representation of the amplitudes. This allows for the matrix element to be written as

$$M_{fi} = \left[\frac{E_\Lambda + M_\Lambda}{2M_\Lambda}\right]^{\frac{1}{2}}\left[\frac{E_p + M_p}{2M_p}\right]^{\frac{1}{2}} \langle \chi(\Lambda) \left| F \right| \chi(p) \rangle \tag{1.9}$$

where F can be expressed as a combination of the four well known Chew, Goldberger, Low and Nambu (CGLN) amplitudes [20]. These amplitudes are subject to analyticity and unitarity requirements, and can be written down as functions of scattering angle and energy [21]. This formalism is advantageous as the CGLN amplitudes can easily be subjected to a multipole analysis [3]. However, in order to facilitate the study of polarization observables it is convenient to change to a representation using transversity amplitudes. These amplitudes, denoted by b_i, can be written in terms of the CGLN amplitudes as

$$b_1 = -\frac{i}{\sqrt{2}}(F_1 - F_2 e^{-i\theta})e^{\frac{i\theta}{2}}, \tag{1.10}$$

$$b_2 = -\frac{i}{\sqrt{2}}(F_1 - F_2 e^{i\theta})e^{\frac{-i\theta}{2}}, \tag{1.11}$$

$$b_3 = -b_1 - \frac{sin\theta}{\sqrt{2}}(F_3 + F_4 e^{-i\theta})e^{\frac{i\theta}{2}} \tag{1.12}$$

$$b_4 = -b_2 - \frac{sin\theta}{\sqrt{2}}(F_3 + F_4 e^{i\theta})e^{\frac{-i\theta}{2}} \tag{1.13}$$

It is also possibe using the formalism of reference [22] to express these transversity amplitudes in terms of s-channel helicity flips N, S_1, S_2 and D. Here N is a no-flip amplitude, S_1 and S_2 are single-flip amplitudes and D is a double-flip amplitude. The transversity amplitudes can now be written as:

$$b_1 = \frac{1}{2}\left[(S_1 + S_2) + i\,(N - D)\right],\ b_3 = \frac{1}{2}\left[(S_1 - S_2) - i\,(N + D)\right],$$

$$b_2 = \frac{1}{2}\left[(S_1 + S_2) - i\,(N - D)\right],\ b_4 = \frac{1}{2}\left[(S_1 - S_2) + i\,(N + D)\right]. \tag{1.14}$$

The four amplitudes are complex, and completely describe the photoproduction process. As such we can derive 16 real numbers by taking bilinear combinations. Thus we can define 16 polarization observables, listed in table 1.3 along with their relations to the transversity amplitudes. Also shown in this table is the type of experiment required to extract each observable. A measurement of all 16 observables will produce redundant information due to various linear relations between them. Several groups [22–24] have investigated how many observables are required to be measured to allow a determination of the amplitudes without any discrete ambiguities. These groups eventually concluded that a measurement of the differential cross section, along with the three single polarization observables and four appropriately chosen double-spin observables are sufficient to resolve all ambiguities. This analysis aims to measure the three single polarization observables P, T and Σ along with the beam-recoil double spin observables O_x and O_z. Although these measurements will not allow for a complete measurement on their own, when taken in conjunction with the results from a previous CLAS analysis with circularly polarized photons [17,25,26], and a current analysis with a polarized target [18], they should allow for a model-independent determination of the reaction amplitude.

The derivation of the polarization observables from the scattering amplitude implies an important relationship to the physics processes at work during the photoproduction of associated strangeness. In particular, there are several model calculations [2–4, 27] which suggest that the observables to be measured in this analysis should be extremely sensitive to the underlying resonance contributions.

Symbol	Transversity representation	Experiment required	Type
$d\sigma/dt$	$\lvert b_1\rvert^2 + \lvert b_2\rvert^2 + \lvert b_3\rvert^2 + \lvert b_4\rvert^2$	$\{-;-;-\}$	S
$\Sigma d\sigma/dt$	$\lvert b_1\rvert^2 + \lvert b_2\rvert^2 - \lvert b_3\rvert^2 - \lvert b_4\rvert^2$	$\{L(\frac{1}{2}\pi,0);-;-\}$	
$Td\sigma/dt$	$\lvert b_1\rvert^2 - \lvert b_2\rvert^2 - \lvert b_3\rvert^2 + \lvert b_4\rvert^2$	$\{-;y;-\}$	
$Pd\sigma/dt$	$\lvert b_1\rvert^2 - \lvert b_2\rvert^2 + \lvert b_3\rvert^2 - \lvert b_4\rvert^2$	$\{-;-;y\}$	
$Gd\sigma/dt$	$2\ \mathrm{Im}(\mathrm{b_1 b_3^* + b_2 b_4^*})$	$\{L(\pm\frac{1}{4}\pi);z;-\}$	BT
$Hd\sigma/dt$	$-2\ \mathrm{Re}(\mathrm{b_1 b_3^* - b_2 b_4^*})$	$\{L(\pm\frac{1}{4}\pi);x;-\}$	
$Ed\sigma/dt$	$-2\ \mathrm{Re}(\mathrm{b_1 b_3^* + b_2 b_4^*})$	$\{C;z;-\}$	
$Fd\sigma/dt$	$2\ \mathrm{Im}(\mathrm{b_1 b_3^* - b_2 b_4^*})$	$\{C;x;-\}$	
$O_x d\sigma/dt$	$-2\ \mathrm{Re}(\mathrm{b_1 b_4^* - b_2 b_3^*})$	$\{L(\pm\frac{1}{4}\pi);-;x'\}$	BR
$O_z d\sigma/dt$	$-2\ \mathrm{Im}(\mathrm{b_1 b_4^* + b_2 b_3^*})$	$\{L(\pm\frac{1}{4}\pi);-;z'\}$	
$C_x d\sigma/dt$	$2\ \mathrm{Im}(\mathrm{b_1 b_4^* - b_2 b_3^*})$	$\{C;-;x'\}$	
$C_z d\sigma/dt$	$-2\ \mathrm{Re}(\mathrm{b_1 b_4^* + b_2 b_3^*})$	$\{C;-;z'\}$	
$T_x d\sigma/dt$	$2\ \mathrm{Re}(\mathrm{b_1 b_2^* - b_3 b_4^*})$	$\{-;x;x'\}$	TR
$T_z d\sigma/dt$	$2\ \mathrm{Im}(\mathrm{b_1 b_2^* - b_3 b_4^*})$	$\{-;x;z'\}$	
$L_x d\sigma/dt$	$2\ \mathrm{Im}(\mathrm{b_1 b_2^* + b_3 b_4^*})$	$\{-;z;x'\}$	
$L_x d\sigma/dt$	$2\ \mathrm{Re}(\mathrm{b_1 b_2^* + b_3 b_4^*})$	$\{-;z;z'\}$	

Table 1.3: Polarization observables listed along with their transversity representations and the type of experiments required to measure them. Table from reference [22].

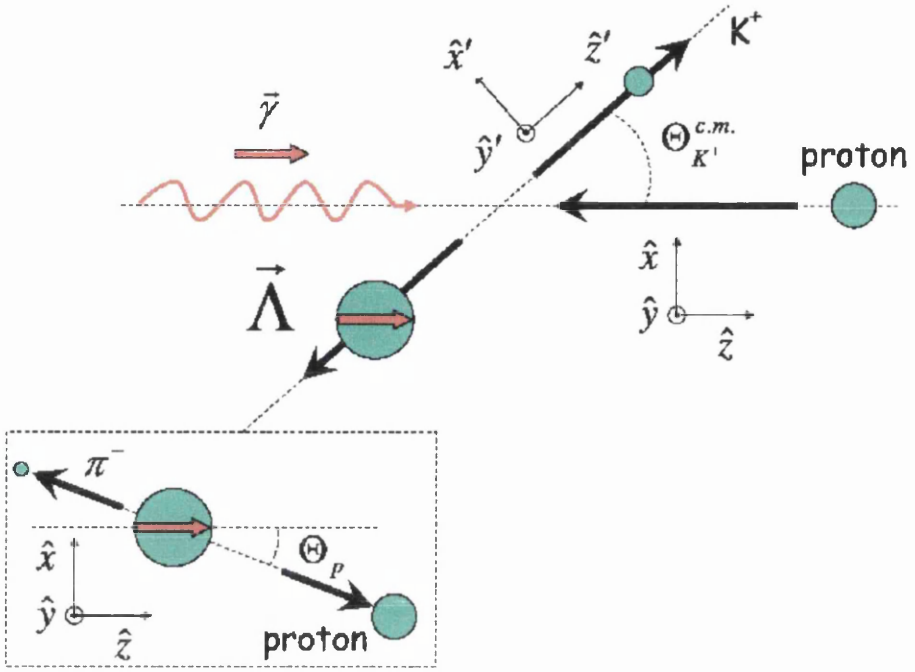

Figure 1.7: Representation of the reaction kinematics for $\vec{\gamma}\mathrm{p} \rightarrow K^+\Lambda$ shown with the two different choices of coordinate system. The primed system is defined with the z-axis along the kaon momentum axis while the unprimed system defines the z-axis along the photon helicity axis. Figure from reference [17].

1.4.2 Extraction of observables

The coordinate system and kinematical variables used in the description of kaon photoproduction are shown for the centre-of-mass reference frame in figure 1.7. Two coordinate systems are commonly used in the literature. In the primed system the z-axis is orientated along the direction of the outgoing K^+ meson. For this analysis the second, or "unprimed" coordinate system was chosen where the z-axis is orientated along the momentum axis of the ingoing photon and the quantization axes are defined as follows:

$$\underline{z} = \frac{\underline{k}}{|\underline{k}|}, \quad \underline{y} = \frac{\underline{k} \times \underline{q}}{|\underline{k} \times \underline{q}|}, \quad \underline{x} = \underline{y} \times \underline{z} \tag{1.15}$$

where $\underline{k}$ is the momentum of the photon beam and $\underline{q}$ is the momentum of the outgoing kaon. This system was chosen as previous measurements with a circularly polarized beam have shown the polarization to be preferentially transferred along the z-axis, as defined in the unprimed system [17].

Having defined an appropriate coordinate system it is possible to extract the various polarization observables by analyzing the angular distributions of the reaction decay products [28]. For the situation where one has a linearly polarized photon beam, and the ability to measure the hyperon recoil polarization, it is possible to relate the observables as follows

$$\begin{aligned}\rho_f \frac{d\sigma}{d\Omega} = \ & \tfrac{1}{2}\tfrac{d\sigma}{d\Omega}_{un} \ \left\{1 - P_\gamma^{lin}\Sigma\cos 2\phi - \sigma_x\left(P_\gamma^{lin}O_x \sin 2\phi\right)\right. \\ & \left. +\sigma_y\left(P - P_\gamma^{lin}T\cos 2\phi\right) - \sigma_z\left(P_\gamma^{lin}O_z \sin 2\phi\right)\right\} \end{aligned} \quad (1.16)$$

where $\frac{d\sigma}{d\Omega}$, Σ, P, T, O_x and O_z are the various photoproduction observables as defined in table 1.3. P_γ^{lin} is the degree of beam linear polarization and the σ_i matrices are the hadron quantization axes of equation 1.15. Adelseck and Saghai [19] show that for an outgoing hyperon with arbitrary axis $\hat{\underline{n}}$ the differential cross section is given by the following trace

$$P_f \cdot \hat{\underline{n}}\frac{d\sigma}{d\Omega} = Tr\left[\sigma \cdot \hat{\underline{n}}\rho_f \frac{d\sigma}{d\Omega}\right]. \quad (1.17)$$

One can then substitute equation 1.16 into equation 1.17 and set the identities $S = 1 - P_\gamma^{lin}\Sigma cos2\Phi$, $\varphi_x = P_\gamma^{lin}O_x sin2\Phi$, $\varphi_y = P - P_\gamma^{lin}T cos2\Phi$ and $\varphi_z = P_\gamma^{lin}O_z sin2\Phi$, to derive the relation:

$$\begin{aligned}\rho_f \cdot \hat{\underline{n}}\frac{d\sigma}{d\Omega} = \ & \tfrac{1}{2}\tfrac{d\sigma}{d\Omega}_{un} \ \left\{S.Tr\left[\begin{pmatrix} 1 & 0 \\ 0 & 1 \end{pmatrix}\right] - \varphi_x.Tr\left[\sigma \cdot \hat{\underline{n}} \cdot \sigma_x\right] + \varphi_y.Tr\left[\sigma \cdot \hat{\underline{n}} \cdot \sigma_y\right]\right. \\ & \left. -\varphi_z.Tr\left[\sigma \cdot \hat{\underline{n}} \cdot \sigma_z\right]\right\} \end{aligned} \quad (1.18)$$

Using standard algebraic manipulation of the Pauli matrices, the following relations for the polarization components can be derived:

$$P_x = -\frac{P_\gamma^{lin}O_x sin2\Phi}{1 - P_\gamma^{lin}\Sigma cos2\Phi}, \quad (1.19)$$

$$P_y = \frac{P - P_\gamma^{lin} T cos2\Phi}{1 - P_\gamma^{lin} \Sigma cos2\Phi}, \tag{1.20}$$

$$P_z = -\frac{P_\gamma^{lin} O_z sin2\Phi}{1 - P_\gamma^{lin} \Sigma cos2\Phi}. \tag{1.21}$$

These relations allow for the extraction of the various polarization observables from the angular distributions of the polarization components. By substituting these relations into equation 1.4, which gives the polarization of the recoiling hyperon, and by utilizing the two different polarization states of the photon beam, one can derive the three asymmetry relations from which the observables can be extracted. This will be discussed in more detail for the photon asymmetry and double polarization observables in chapter 5, and for the recoil polarization and target asymmetry in chapter 6. These procedures can be trivially extended to derive relations for cases where the beam is circularly polarized or when the target is polarized.

1.5 Summary

The non-perturbative nature of QCD at the energies of the nuclear-particle physics interface continues to provide a major barrier to a deeper understanding of nucleon structure and interactions. Baryon spectroscopy provides an opportunity to study the internal physics of a nucleon through its excited states. Traditionally the main theoretical work on the baryon resonance spectrum has come from quark models, with chiral perturbation theory not amenable to $N^\star$ physics, and lattice QCD still in a developmental stage. A major challenge arises from the fact that these quark models predict a much richer resonance spectrum than has been observed in experiment. With most of the world data set coming from $\pi N \rightarrow \pi N$ scattering experiments, a recent quark model calculation has predicted that some of these missing states should couple strongly to $K^+\Sigma^0$ and $K^+\Lambda$ final states [1]. This work utilizes a linearly polarized photon beam to measure various polarization observables in associated strangeness photoproduction, with some of the observables predicted to be very sensitive to the resonance contributions.

The results of this analysis, along with their theoretical interpretation, should provide some insight into the strangeness production process. Further to this, the observables from this analysis, when taken in conjuction with results from a previous [17] and current [18] CLAS analysis, should facilitate a model-independent determination of any missing states without phase ambiguities. This should hope-

fully go someway to settling the missing resonance problem and establish the correct degrees of freedom to be used in the resonance energy region.

Chapter 2

Previous Measurements and Theoretical Models

This chapter will provide the motivation for the analysis and extraction of polarization observables in $K^+\Lambda$ and $K^+\Sigma^0$ photoproduction. In particular there will be a focus on some of the phenomenological models that are used in the energy range of non-perturbative QCD. A selection of tree-level isobar, coupled-channel and Regge models will be studied, and their relative successes and limitations in describing the baryon spectrum will be investigated. Attention will be paid to the different theoretical "recipes" used, along with the predictions for the various polarization observables. The main interest will naturally be for the observables to be measured in this work, and the final results will be compared with some of the model calculations. Attention will then be given as to which resonance states these models predict to couple strongly to the $K^+\Lambda$ and $K^+\Sigma^0$ channels,

The current world database for polarization observables in $K^+\Lambda$ and $K^+\Sigma^0$ photoproduction will also be investigated. This data will be compared to model predictions to give an overview of the current theoretical understanding of hyperon photoproduction. An emphasis will be made on where the current data is lacking and what measurements will be needed to further develop a phenomenological understanding of the reaction processes. There will then be a discussion of how the measurements made in this analysis will help to enhance the world database and constrain the various theoretical models for hyperon photoproduction.

2.1 Previous Measurements

2.1.1 SAPHIR Cross Sections and Recoil Polarizations

Although some scattered data has existed for strangeness photoproduction since the 1960s [29–31], much of the recent interest in the subject was ignited with results from the SAPHIR collaboration in the 1990s. Three sets of results were published by SAPHIR, using ELSA, the 3.5 GeV electron stretcher ring at Bonn. The first data were published in 1994 [32], with follow up results in 1998 [33] and then final results published in 2003 [34]. The 1998 published results for the hyperon recoil polarizations along with cross section measurements for both the $K^+\Lambda$ and $K^+\Sigma^0$ photoproduction channels generated a great deal of theoretical interest. These results were taken with the multiparticle detector SAPHIR at photon energies ranging from 0.9 to 2.0 GeV. The final event sample of the analysis contained 7591 $\gamma p \rightarrow K^+\Lambda$ and 5869 $\gamma p \rightarrow K^+\Sigma^0$ events.

The measurements made for the cross sections for both the $K^+\Lambda$ and $K^+\Sigma^0$ channels were of particular interest. The results for the $K^+\Lambda$ channel are displayed in figure 2.1. These results display a steep rise in the cross section from threshold up to a peak at $E_\gamma \approx 1.1$ GeV, with some structure evident at $E_\gamma \approx 1.5$ GeV. The peak at 1.1 GeV corresponds to an invariant mass coinciding with the three $N^\star$ resonances, $S_{11}(1650)$, $P_{11}(1710)$ and $P_{13}(1720)$ that are known to decay strongly into the $K\Lambda$ channel. The structure at 1.5 GeV would later become the subject of several theoretical studies, with a potential missing resonance being suggested as a possible explanation for the "bump". These theoretical studies will be discussed later in section 2.2. The total cross section measured for $\gamma p \rightarrow K^+\Sigma^0$ shows a smoother rise up to a peak at around 1.45 GeV, as displayed in figure 2.2. This was interpreted to be the result of $S_{31}(1900)$ and $P_{31}(1910)$ states that are predicted to play an important role in $K\Sigma^0$ photoproduction [15].

2.1.2 CLAS Cross Sections

Following on from the SAPHIR measurements, CLAS produced a series of high statistics, high precision measurements of cross sections for both the $K^+\Lambda$ and $K^+\Sigma^0$ channels [25]. These measurements were made for centre-of-mass energies between 1.6 and 2.53 GeV, covering almost the entire angular range. The results were generally more precise than the SAPHIR measurements, with about twice

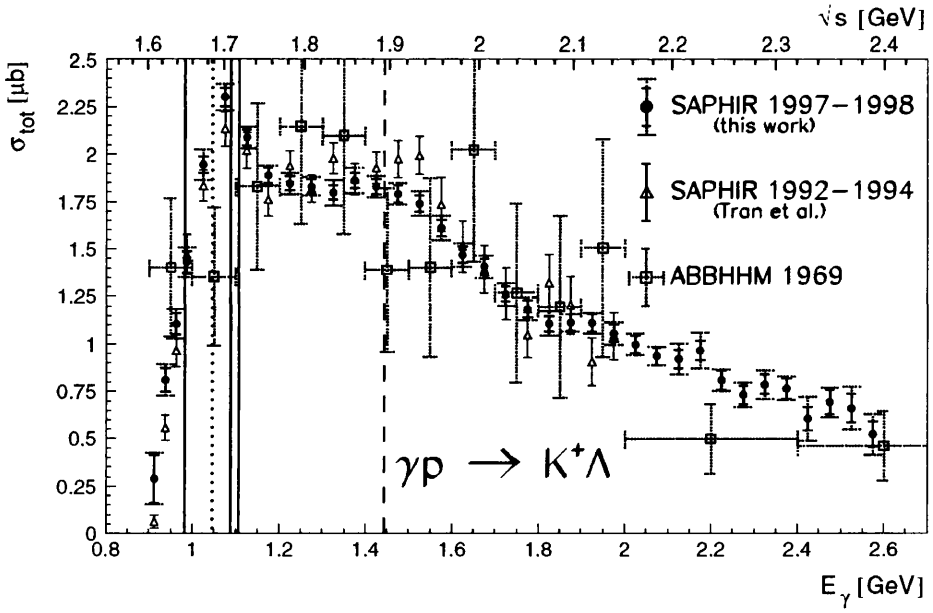

Figure 2.1: Total reaction cross section published from the SAPHIR collaboration [33, 34] for the reaction $\gamma p \to K^+\Lambda$. The vertical lines indicate the mass values of the known resonances $S_{11}(1650)$, $P_{11}(1710)$ and $P_{13}(1720)$ (solid lines) and the position of the hypothetical $D_{13}(1895)$ (dashed line).

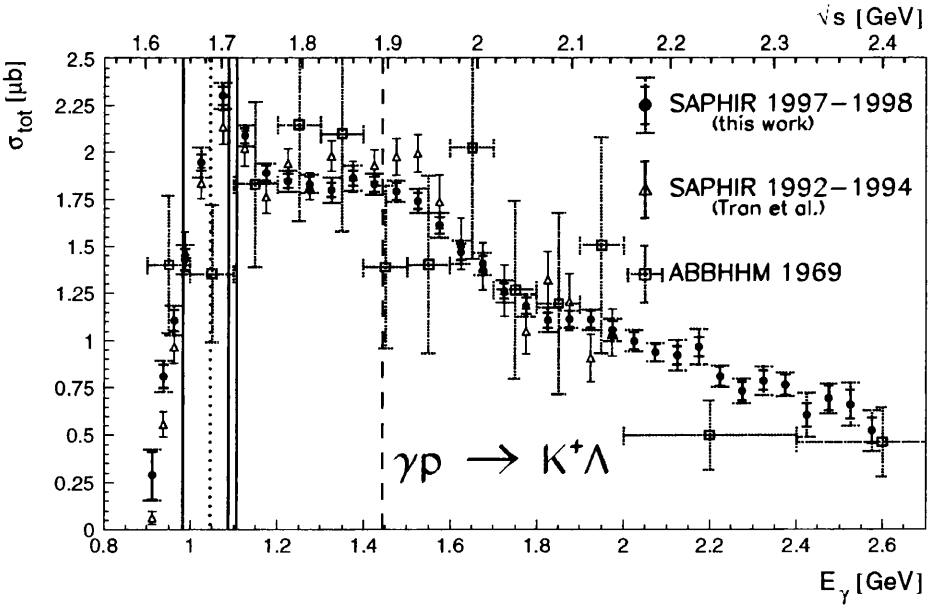

Figure 2.2: Total reaction cross section published from the SAPHIR collaboration [33,34] for the reaction $\gamma p \to K^+\Sigma^0$. The vertical lines indicate the threshold energy of $\gamma p \to K^+\Sigma^0$ (dotted line) and the mass values of the known resonances $S_{11}(1650)$, $P_{11}(1710)$ and $P_{13}(1720)$ (solid lines) and the position of the hypothetical $D_{13}(1895)$ (dashed line).

as many energy bins, and statistical uncertainties which were approximately one-quarter as large. The CLAS measurements found the differential cross sections to be flat as a function of $cos(\theta_{cm}^{K^+})$ near threshold, before developing a significant forward peak as the energy increases to about 2 GeV. With a further increase in energy the cross section develops a slower rise in both the forward and backward angles, before becoming predominantly forward peaked at energies above 2.3 GeV. This behaviour can be explained by s-wave effects near threshold with either t-channel contributions or s-channel interference effects becoming important as the energy increases. For the $K^+\Sigma^0$ channel the cross section was found to have no forward peak below 2 GeV which is consistent with a reaction mechanism which is more s-channel resonance dominated and displays less t-channel influence than the $K^+\Lambda$ reaction.

The total cross sections for both channels are calculated from the integrated angular distributions, and are displayed for the $K^+\Lambda$ and $K^+\Sigma^0$ reactions in figures 2.3 and 2.4 respectively. The results are compared to those from the SAPHIR and ABBHHM [35] collaborations at Bonn. In general the CLAS cross sections are larger than the SAPHIR results by a factor of around 4/3 for the $K^+\Lambda$ channel, but are mostly in good agreement for the $K^+\Sigma^0$ results. The authors can offer no reason for why there is a discrepancy in one channel and, as will be discussed in the next section, this disagreement raises some serious issues for model interpretations of the cross section results.

Qualitatively the CLAS measurements reproduce the two structures found in the SAPHIR cross sections at 1.7 and 1.9GeV. The authors found the 1.7 GeV peak to be consistent with contributions from the $P_{11}(1710)$ and $P_{13}(1720)$ states. For the structure at 1.9GeV, it was inferred that this was reflective of the contributions of several resonances rather than resembling a single Lorentzian feature. For the $K^+\Sigma^0$ channel the results reproduce a previously seen strong peak at 1.88 GeV with a slight shoulder evident at around 2.05GeV. The location of the peak at 1.88 GeV is believed to be consistent with the mass of several Δ resonances which can contribute to the isospin 3/2 final state.

2.1.3 CLAS Recoil Polarizations and C_x/C_z Double Polarization Observables

The same CLAS data set that was used to measure the cross sections for both hyperon channels was also utilized to extract high statistics measurements for the

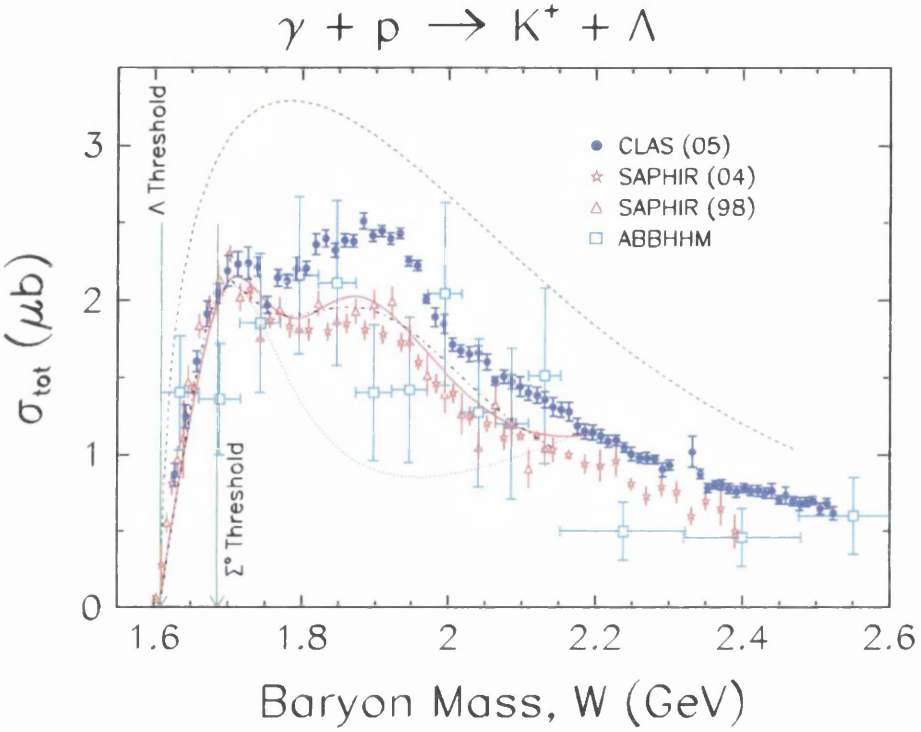

Figure 2.3: Total cross section for $\gamma p \rightarrow K^{+}\Lambda$ showing the latest CLAS data overlayed with several previous measurements from Bonn. In both plots the CLAS data are shown as the blue dots with the SAPHIR 04 (red stars), SAPHIR 98 (red triangles) and ABBHM (blue squares) data included. The plots also display a comparison with several theoretical models: Regge model [36,37] (dashed blue), Kaon-MAID [38] (solid red), Kaon-MAID with the $D_{13}(1895)$ resonance turned off (dotted red) and the model developed by Saghai *et al* [39] (dot-dashed black).

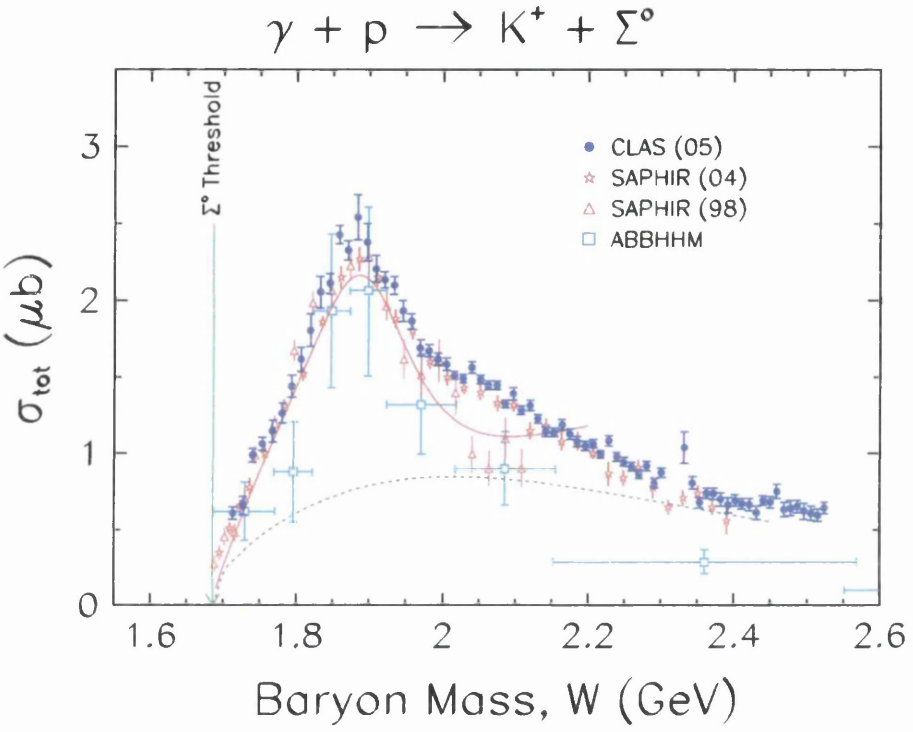

Figure 2.4: Total cross section for $\gamma p \rightarrow K^{+}\Sigma^{0}$ showing the latest CLAS data overlayed with several previous measurements from Bonn. In both plots the CLAS data are shown as the blue dots with the SAPHIR 04 (red stars), SAPHIR 98 (red triangles) and ABBHM (blue squares) data included. The plots also display a comparison with several theoretical models: Regge model [36,37] (dashed blue), Kaon-MAID [38] (solid red), Kaon-MAID with the $D_{13}(1895)$ resonance turned off (dotted red) and the model developed by Saghai *et al* [39] (dot-dashed black).

hyperon recoil polarization P in addition to the first ever measurements of the beam-recoil double polarization observables C_x and C_z. As discussed in Chapter 1 for an unpolarized beam, parity conservation allows an induced polarization of the hyperon along the axis perpendicular to the reaction plane. In the instance where the photons are circularly polarized, the polarization can be transferred to the spin orientation of the produced hyperons. This polarization transfer can be characterized by the transfer coefficients C_x and C_z.

2.1.3.1 Recoil Polarization

Results for the hyperon recoil polarization were published by CLAS for centre-of-mass energies from near threshold up to 2.3 GeV [26]. These measurements were made to a much higher precision than previous results from SAPHIR and are plotted in figure 2.5 for the Λ hyperon. The plots show the polarization as a function of W for the complete angular range. These results were generally found to be consistent with the previous SAPHIR data, but the finer binning allowed for greater structure resolution. For almost the entire energy range it was found that the hyperon had a strong positive polarization at backward angles, with a comparably large negative polarization as the kaons go forward.

The plots also show some model calculations by Janssen *et al* [4] (magenta dashed line), kaon-MAID [38] (dashed green) and a Regge model [36, 37] (solid blue). Only the model by Janssen reproduces the large polarization at backward angles at around 2GeV. At forward angles the Janssen model provides a similar reproduction of the data as the other two calculations. This analysis will aim to measure the hyperon polarizations with higher statistics than the previous CLAS results. It is hoped that these measurements will provide finer binning than has been achieved to date, thus allowing for greater resolution of any features.

2.1.3.2 C_x/C_z Double Polarization Observables

CLAS published first ever measurements of the polarization transfer coefficients C_x and C_z for both $K^+\Lambda$ and $K^+\Sigma^0$ photoproduction in 2006 [17]. These results are plotted in figure 2.6 for the $K^+\Lambda$ channel. It is immediately evident that for almost the full kinematic range, the polarization is preferentially transferred to the Λ hyperon along the photon helicity axis, characterized by C_z. The results demonstrate that at energies from threshold up to around 1.9GeV, C_z=+1 for the Λ, meaning that it has nearly the full polarization transferred to it regardless

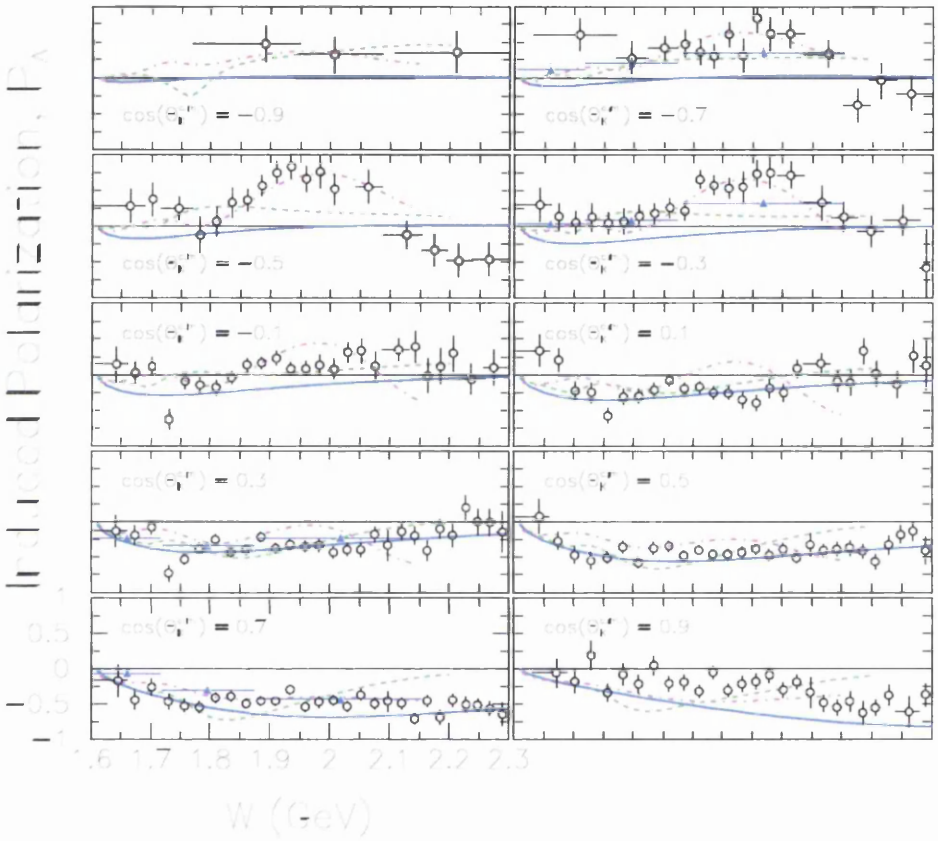

Figure 2.5: Induced hyperon polarization measured by CLAS [26] for the reaction $\gamma p \rightarrow K^+\Lambda$ compared to some previous data from SAPHIR (blue triangles). The model calculations are from a Regge model [36, 37] (blue line), Kaon-MAID [38] (dashed green) and Gent [4] (magenta).

of the kaon production angle. At higher energies this full polarization behaviour appears to fall-off as a function of kaon angle, particularly at backward angles. For C_x the results are generally closer to zero for most of the kinematic range. The only deviation from this comes at backward kaon angles and high energies, and also forward angles at very high energies where the results have large negative values.

For the $K^+\Sigma^0$ channel, the radiative decay of the Σ^0 hyperon results in an almost factor four dilution of its polarization, as discussed in Chapter 1. This results in only six kaon bins being used to present the data, as shown in figure 2.7 for the C_x and C_z observables. It is immediately clear that full polarization transfer along the z-direction, evidenced in the $K^+\Lambda$ results, is not reproduced for the $K^+\Sigma^0$ channel.

2.1.3.3 Fully Polarized Lambda

Further to providing a high quality data set to constrain the various models that describe associated strangeness production, the hyperon polarization results measured at CLAS also raised two exciting phenomenological puzzles. First, when one considers the magnitude of the Λ polarization vector, $|P_\Lambda|$, which is comprised of the three measured orthogonal components of the polarization, one finds that it is unity for all centre-of-mass energies and production angles. This can be interpreted as the Λ hyperon being 100% polarized. These results are plotted in figure 2.8 for the equivalent quantity R, where

$$R^2 = C_x^2 + P^2 + C_z^2. \tag{2.1}$$

The second result of interest is that there appears to be a simple linear relation between the two polarization transfer observables, given by $C_z = C_x + 1$. These results are of interest since there is no *a priori* reason for the hyperon to have full polarization, nor is there any simple relationship between the production amplitudes that should lead to such a result. In an attempt to offer some explanation of these results, a heuristic model was developed by Schumacher [42], which aimed at showing how the hadronization process could preserve the polarization.

Full details of the model are given in the reference but the important feature is that the reaction creates a virtual $s\bar{s}$ quark pair in a $^3S_1$ state, as illustrated in figure 2.9. Using the theory of vector meson dominance this can be thought of

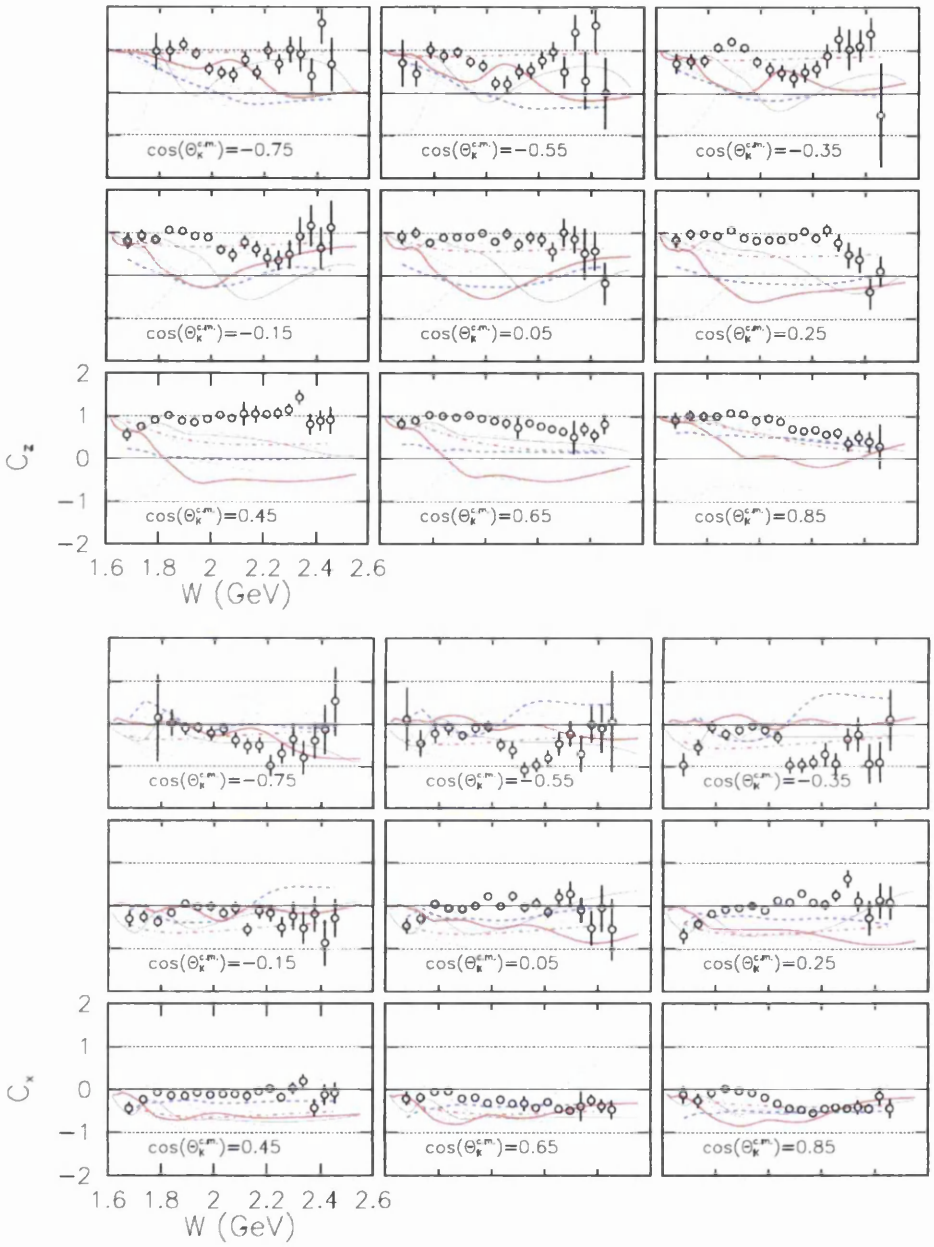

Figure 2.6: C_z (top) and C_x (bottom) double polarization observables measured at CLAS [17] for the reaction $\gamma p \to K^+\Lambda$. The model calculations used for comparison are: Kaon-MAID [38] (dashed green), partial wave analysis [40] (blue), regge-plus-resonance [41] (solid black), Gent model [4] (magenta)

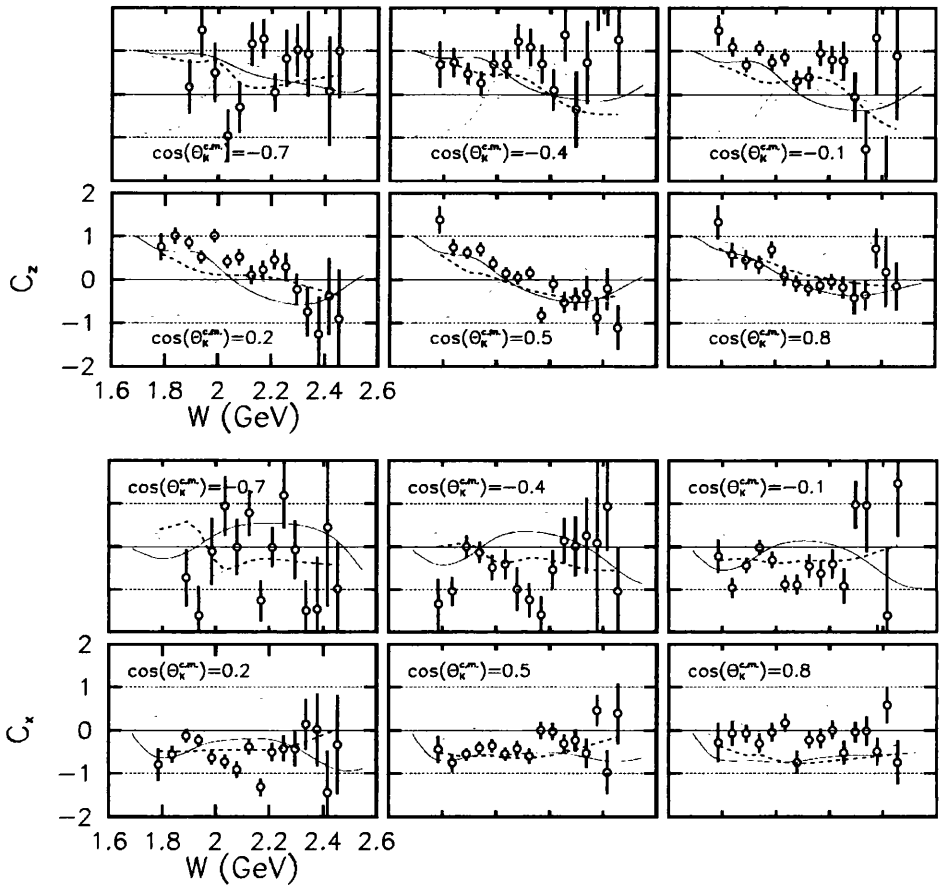

Figure 2.7: C_z (top) and C_x (bottom) double polarization observables measured at CLAS [17] for the reaction $\gamma p \rightarrow K^+\Sigma^0$. The model calculations used for comparison are: Kaon-MAID [38] (dashed green), partial wave analysis [40] (blue), regge-plus-resonance [41] (solid black), Gent model [4] (magenta)

as the creation of a virtual ϕ-meson that carries the polarization of the incoming photon. The next important feature of the model is that the polarized s-quark, produced in a pure spin state, must survive the hadronization process. To achieve this a spin-orbit interaction Hamiltonian is introduced for the spin 1/2 quark in the field of the unpolarized nucleon, which is treated as being spinless. It is shown in the reference that this spin-orbit interaction preserves the magnitude of the polarization, only acting to precess it in some way [43]. The apparent linear relationship between the observables is explained by there being two interfering amplitudes in the reaction - spin-flip and non spin-flip - that are everywhere proportional to each other.

This model is of interest in that it differs from the traditional reaction picture, where a non-strange resonance state is produced that couples to the final $K^+\Lambda$ state. Here the interaction is explained in terms of spin couplings that are treated at the quark rather than hadronic level. The hypothesis is also able to make predictions for other observables which will be of interest to this analysis. In particular it predicts that in the case of a linearly polarized photon, a transversely polarized s-quark is produced in a $^3S_1$ pair, before going through the spin-orbit hadronization process that preserves the polarization. In this instance the three orthogonal components of polarization are the induced polarization P and the double polarization observables O_x and O_z, giving the prediction:

$$O_x^2 + O_z^2 + P^2 = 1. \tag{2.2}$$

All three of these observables will be measured with high precision in this analysis, over a large kinematic range. The test of this prediction should give some further insight into the strange quark production process as well as hinting at the appropriate degrees of freedom, quark or hadronic, that should be used in such a description.

2.1.4 LEPS Photon Asymmetries

The first photon asymmetry data for associated strangeness photoproduction was measured for the reactions $p(\gamma, \vec{K^+})\Lambda$ and $p(\gamma, \vec{K^+})\Sigma^0$ by the LEPS collaboration at SPring8 in Japan [44]. A backward-compton scattering facility was used to produce a beam of photons with a high degree of linear polarization at photon energies ranging from 1.5 to 2.4GeV. The asymmetry measurement was made

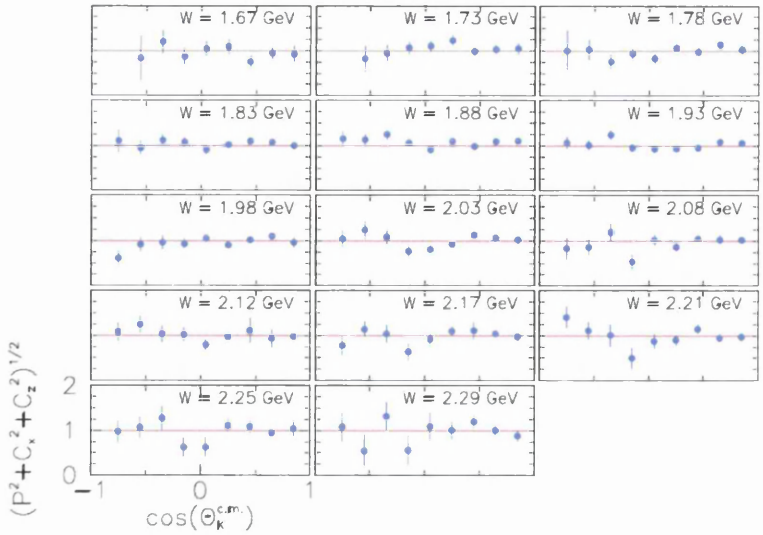

Figure 2.8: Magnitude of the Λ polarization for the full kinematic range of the CLAS analysis. When averaged over all energies the magnitude is consistent with unity everywhere.

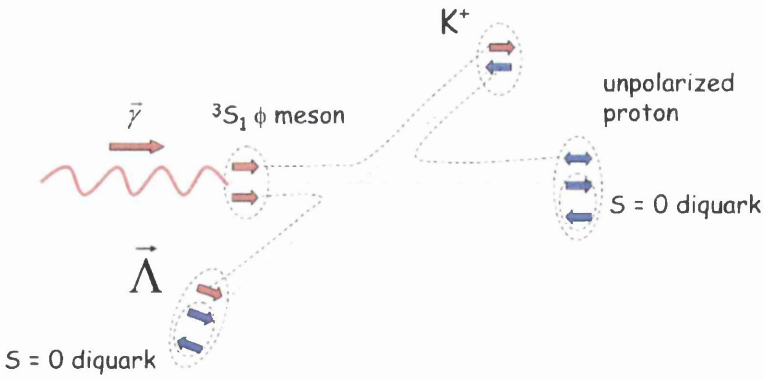

Figure 2.9: Schematic representation of the possible $s\bar{s}$ creation process where the $s\bar{s}$ quark pair are produced as a virtual ϕ-meson. In this scenario the photon hadronizes in such a way that the s-quark in the Λ hyperon retains its polarization after being precessed by a spin orbit interaction.

possible by taking half the data with horizontally polarized photons and the other half with vertically polarized photons. A silicon-strip vertex detector and two drift chambers were used to make precision measurements of the momentum of the K^+ meson to facilitate particle identification. A plastic scintillator trigger counter was placed behind the target cell to provide a reliable start signal, with an additional 40 scintillators placed behind the tracking detectors to provide the stop signal.

For the presentation of the results the datasets were divided into nine 0.1GeV wide photon energy bins, with an additional five angular bins covering the range $cos(\theta^{K^+}_{cm}) = 0.6$ to 1.0. The results for both the $K^+\Lambda$ and $K^+\Sigma^0$ channels are displayed in figure 2.10 along with model calculations from the Kaon-MAID program [38] and Janssen *et al* [4]. These results, all at forward angles, show the observed photon asymmetries to be positive, displaying a gradual increase with photon energy. Both the model calculations employ a tree-level isobar approach, which will be discussed in detail in section 2.2. The same s-channel resonances are taken into account and the missing $D_{13}(1895)$ state is included in both prescriptions. The only difference between the two models lies in how the non-resonant background terms are treated, as well as the choice of hadronic form factor.

In the case of the $K^+\Lambda$ channel, the predictions by Janssen appear to underpredict the asymmetry measurements while the Kaon-MAID results overpredict the asymmetries. For the $K^+\Sigma^0$ channel the two calculations roughly agree for the magnitude of the asymmetry but have the opposite sign. It is the Janssen calculations that give the best agreement here but the magnitude is higher than the actual results. These discrepancies could be a result of the freedoms being too large in the models, coupled with a sparsity of data. The results of the analysis being described in this work will greatly enhance the current database for the photon asymmetry, including providing measurements that cover the entire angular range.

2.1.5 GRAAL Photon Asymmetries and Recoil Polarizations

In 2007 the GRAAL collaboration at Grenoble in France published results for the beam asymmetry and hyperon recoil polarization for both $K\Lambda$ and $K\Sigma^0$ photoproduction, at photon energies from threshold up to 1.5 GeV [45]. This was carried out using the European Synchrotron Radiation Facility (ESRF) to

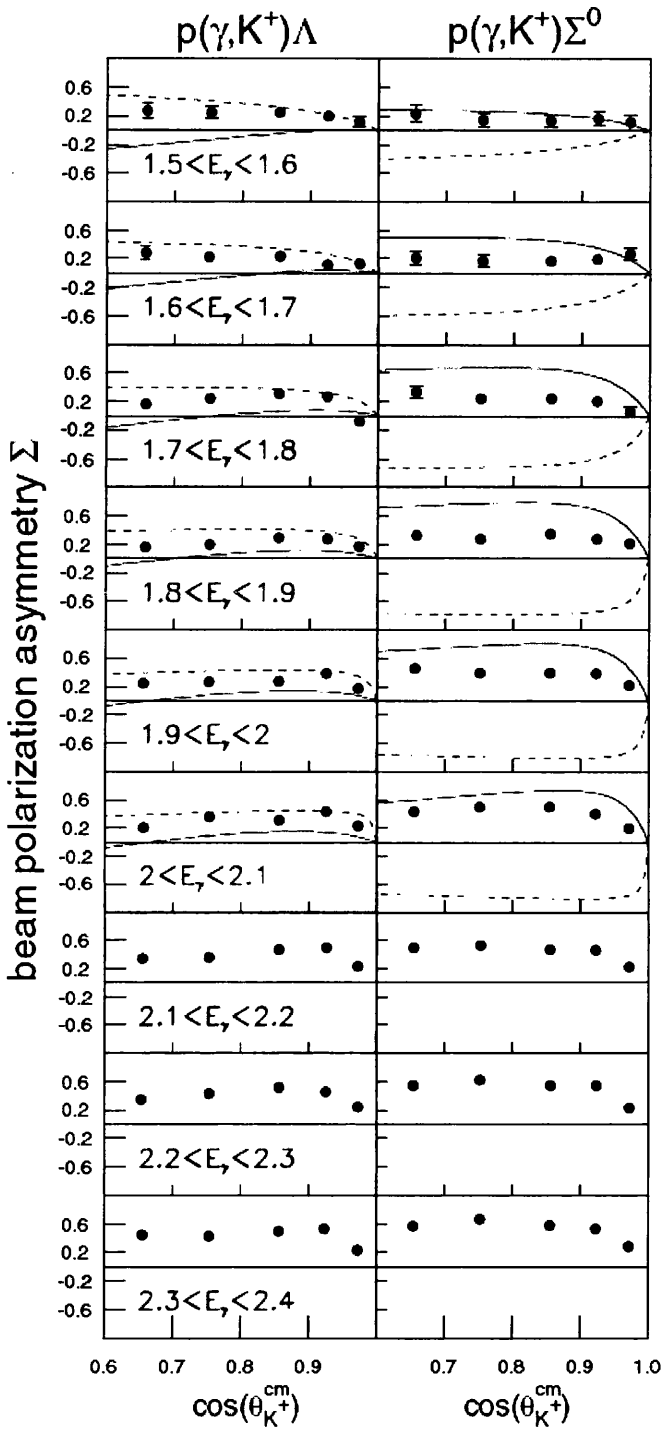

Figure 2.10: Photon asymmetry measurements from the LEPS collaboration for the reactions $p(\gamma, \vec{K^+})\Lambda$ (left) and $p(\gamma, \vec{K^+})\Sigma^0$ (right). The results are displayed over the full kinematic range of the analysis, and are compared to model calculations from the Kaon-MAID program [38] (dashed lines) and by Janssen *et al* [4] (solid lines). The theory calculations only extend to 2.1GeV.

produce tagged, polarized photons by the Compton scattering of laser photons off circulating electrons in the storage ring. For the hyperon experiment a set of UV lines at 333, 351 and 364 nm were produced by an Argon laser, giving photon energies of 1.40, 1.47 and 1.53 GeV respectively. The 4π LAγRANGE detector was used to detect both neutral and charged particles. The system utilized a set of MultiWire Proportional Chambers (MWPCs) to provide tracking information for the charged particles. For particle identification a plastic scintillator barrel was used, supplemented by a double plastic scintillator hodoscope which gives time-of-flight measurements. A detailed description of the experimental set-up is provided in reference [45].

The results for the reaction $\gamma p \rightarrow K^+\Lambda$ are displayed in figures 2.11 and 2.12 for the recoil polarization and photon asymmetry respectively. The results for the photon asymmetry provide the first ever coverage of the energy range from threshold up to 1500MeV. There was found to be good agreement with the previously published LEPS results at the energies where there was an overlap. Further to this the GRAAL measurements showed the photon asymmetry to be positive for almost the full range of kinematics, only changing sign at energies close to threshold. For the recoil polarization there was found to be good agreement between the GRAAL results and previous measurements from both SAPHIR [33] and CLAS [26].There was also good agreement for the $K^+\Sigma^0$ channel despite the larger statistical uncertainties.

2.2 Theoretical Models

2.2.1 Isobar Models

Effective-Lagrangian isobar frameworks at the order of the tree-level have been developed by various groups to try and unfold the nucleon resonance excitation spectrum [27, 49, 50]. Originally pioneered by Thom [51] these models aim to describe the hadronic reaction by evaluating various tree-level Feynman diagrams for both the resonant and non-resonant exchange of mesons and baryons. In this formalism every particle in the reaction can be treated as an effective field with properties such as photocoupling amplitudes, mass and strong decay widths. Although a tree-level approach does not account for the effects of channel coupling and final state interactions, it does reduce the complexity of the interaction and gives a reliable first order understanding of the resonance parameters. For a typ-

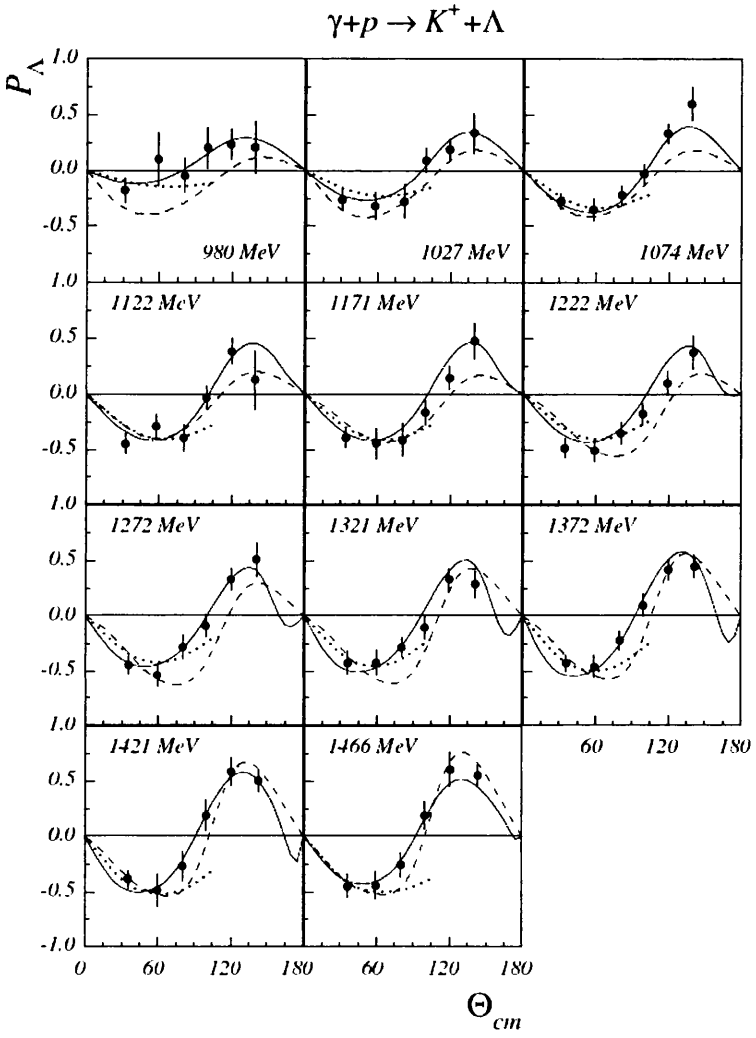

Figure 2.11: Angular distributions of the hyperon recoil polarization measured at GRAAL [45] for the reaction $\gamma p \rightarrow K^+\Lambda$ for the full photon energy range. Data is compared to model calculations for the Bonn-PNPI partial wave analysis [46, 47] (solid line), Saclay-Argonne-Pittsburgh coupled-channel model [48] (dashed line) and the Gent Regge-plus-resonance model [41] (dotted line).

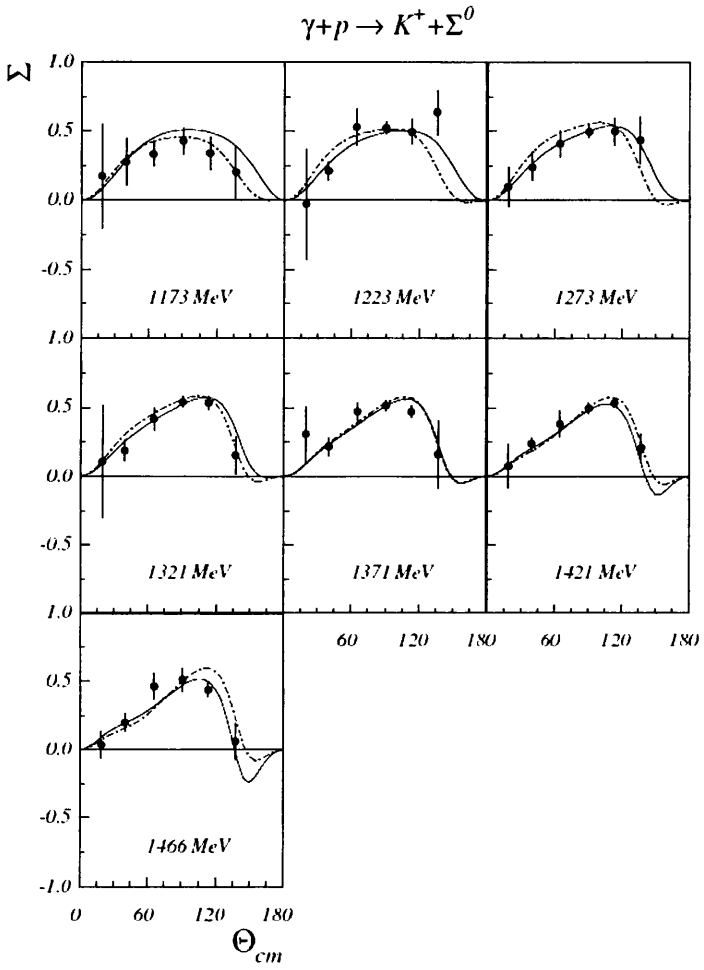

Figure 2.12: Angular distributions of the photon asymmetry measured at GRAAL [45] for the reaction $\gamma p \rightarrow K^+\Lambda$ for the full photon energy range. Data is compared to model calculations for the Bonn-PNPI partial wave analysis [46, 47] (solid line), Saclay-Argonne-Pittsburgh coupled-channel model [48] (dashed line) and the Gent Regge-plus-resonance model [41] (dotted line).

ical tree-level approach, the Feynman diagrams contributing to the $\gamma p \rightarrow K^+\Lambda$ reaction are shown in figure 2.13, diagrams (a) through to (g). Diagrams (a) through (d) represent the background Born terms while (e) through (g) represent the resonant contributions in the t, u and s-channels respectively. When considering the $K^+\Sigma^0$ final state, contributions also have to be included from the Δ states as shown in diagram (h).

One of the first isobar models to provide evidence for a potential missing resonance in strangeness photoproduction was the prescription of Mart and Bennhold [2]. Their model investigated $K^+\Lambda$ photoproduction, as its isospin structure only allows the excitation of $N^\star$ states, whereas the $K^+\Sigma^0$ channel also allows Δ states to contribute making it more difficult to describe. In their analysis they were guided by the coupled-channels approach of Feuster and Mosel [52] which indicated that the three "core" resonant states $S_{11}(1650)$, $P_{11}(1710)$ and $P_{13}(1720)$ should dominate the $K^+\Lambda$ channel. The model used standard Born terms to describe the background along with $K^\star(892)$ and $K_1(1270)$ vector meson poles in the t-channel. The gauge method developed by Habberzettl [53] was used to include hadronic form factors, and separate cut-off masses of 800 and 1890MeV were used to suppress the background and resonance sectors respectively.

This model was developed to attempt to reproduce the cross-section results from the SAPHIR collaboration [33] as shown in figure 2.14. Clearly the model can describe the general trend of the data well but not the structure at around W=1900MeV. In order to describe this feature they were lead by the constituent quark model of Capstick and Roberts [1] which predicts the existence of various new states around 1900MeV. Of these, the $D_{13}(1960)$, was predicted to have a large decay width into the $K^+\Lambda$ channel and also to have a significant photocoupling. This state, which is considered to be a missing resonance, was then included in the model calculations. The results then agreed well with the cross-section measurements, as shown in figure 2.14. This result, when taken with the good agreement between the extracted partial widths for the core resonances with the quark model predictions, gave some confidence that the structure in the SAPHIR cross section does indeed correspond to the $D_{13}(1960)$. Their calculations also predict large differences between the models with and without the $D_{13}(1960)$ resonance for the target asymmetry and photon asymmetry as displayed in figure 2.15. In particular Mart and Bennhold conclude that a measurement of the photon asymmetry will be well suited to examining the role of the $D_{13}(1960)$ missing resonance in kaon photoproduction.

A further investigation of the SAPHIR data in an effective-Lagrangian descrip-

tion by Saghai *et al* [39] showed that the cross-section results could be equally well reproduced without the inclusion of the $D_{13}(1960)$ resonance. This model adjusts the background with the inclusion of two hyperonic resonances, $P_{01}(1810)$ and $P_{03}(1890)$, to reproduce accurately the fitted data. This analysis highlights the danger of using limited observables to draw conclusions about the existence of predicted missing resonances in an isobar approach.

Janssen *et al* [4, 54] also produced an isobar prescription to reproduce the SAPHIR results. They demonstrate, using a model with the same set of core resonances as Mart and Bennhold, that there is a large model dependence in the handling of the background which can influence final calculations. In particular it is shown that the choices made with respect to modelling the background can affect both the magnitude of $N^\star$ contributions, as well as the interference pattern between overlapping resonances. A further result when dealing with hadronic degrees of freedom, is that background Born terms on their own can give rise to cross section results that wildy overshoot the existing data. In order to resolve this, while respecting $SU(3)$ symmetry-breaking, hadron form factors with specific cut-off masses are introduced. Janssen investigated the effect of different prescriptions used to reduce the strength of the Born terms and found that the cut-off masses used in the model of Mart and Bennhold were unrealistically small. Further to this, Janssen was able to use more realistic cut-off masses along with a $P_{13}(1950)$ resonance to well reproduce the measured cross section results without having to add in a $D_{13}(1960)$ missing state. Calculations from this model are compared to the induced hyperon polarization measurements from CLAS in figure 2.5 as well as the CLAS double polarization observables for the $K^+\Lambda$ channel in figure 2.6 , and for the $K^+\Sigma^0$ channel in figure 2.7. The summary of this work was that the data set at that time was not complete enough to allow firm statements to be made about which, if any, missing resonances should contribute to the $K^+\Lambda$ channel. It was concluded that more measurements were required to make further progress on elucidating the physics of strangeness production.

2.2.2 Coupled-Channel Analyses

A major limitation for tree-level isobar models is their failure to account for multi-step, coupled-channel effects from intermediate πN states along with final state interactions. It is believed that the multi-step sequence $\gamma N \rightarrow \pi N \rightarrow KY$ should have a large effect in kaon photoproduction due to the $\gamma N \rightarrow \pi N$ amplitudes

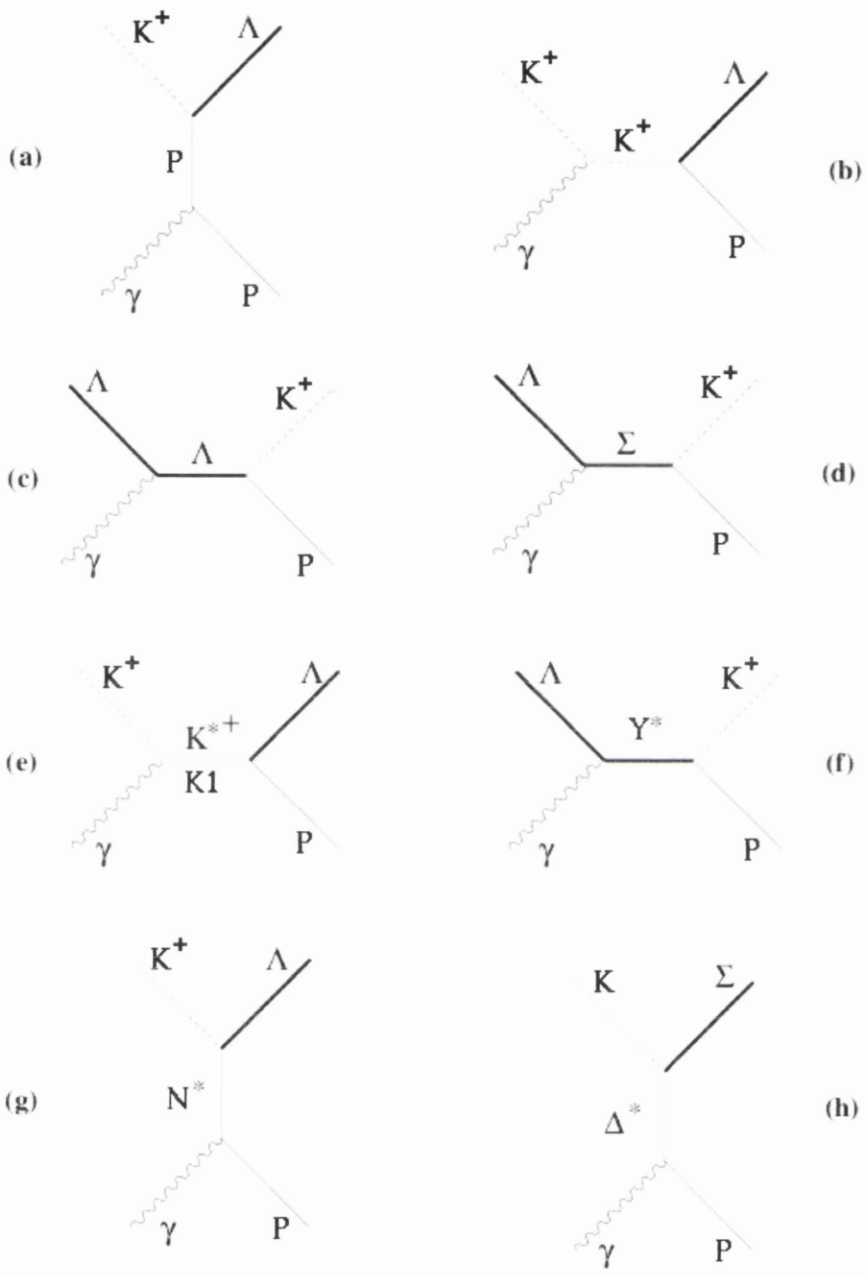

Figure 2.13: Feynman diagrams for the reaction $\gamma p \rightarrow K^+\Lambda$, diagrams (a) through (g) and for the $\gamma p \rightarrow K^+\Sigma^0$ reaction with the additional diagram (h). Diagrams (a) through (d) represent the background Born terms while (e) through (g) represent resonant contributions in the t, u and s-channels respectively. Diagrams from reference [18].

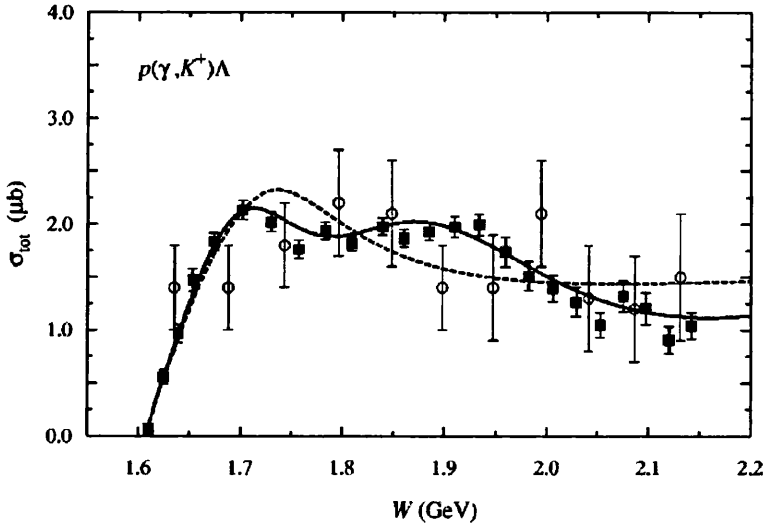

Figure 2.14: Total cross section for $K^+\Lambda$ production on the proton, with calculations included from the Mart and Bennhold model [2]. The dashed line shows the calculation without a $D_{13}(1960)$ resonance included, while the solid displays the calculation with the $D_{13}(1960)$. The data is from reference [33].

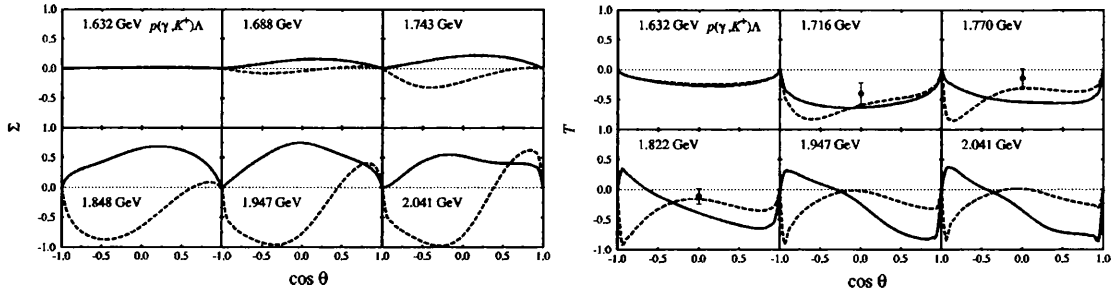

Figure 2.15: Calculations from Mart and Bennhold [2] for the photon asymmetry (left) and the target asymmetry (right). The dashed line represents calculations without the $D_{13}(1960)$ while the solid line represents calculations with a $D_{13}(1960)$ state included. These calculations predict that the photon asymmetry should be very sensitive to the inclusion of the missing $D_{13}(1960)$ resonance.

being significantly larger than the direct production process. Various groups have attempted to account for coupled-channel effects [55–58] including approaches based on $SU(3)$ chiral dynamics [59] and a K-matrix interpretation [55].

A dynamic coupled-channel model developed by Chiang *et al* [60] investigated the $\gamma p \rightarrow K^+\Lambda$ channel, using the isobar model of Williams, Ji and Cotanch [50] to fix the number of leading order tree-diagrams to be considered. Their approach defined the $\gamma N \rightarrow \pi N$ and $\pi N \rightarrow KY$ amplitudes using the results from the VPI partial wave analysis [40]. In order to reduce the number of free parameters in the calculation an approach similar to that used in some isobar models was developed, in which the coupling constants are fixed from either PDG values or $SU(3)$ flavour symmetry. The Chiang model did not attempt to provide an accurate reproduction of known kaon photoproduction data, but rather aimed to demonstrate the importance of coupled-channel effects. To this end, Chiang concluded that πN channels provide $\sim$ 20% contribution through the coupled-channel mechanism demonstrating a clear need for these effects to be included into kaon photoproduction calculations. This was further confirmed by the K-matrix approach of Usov and Scholten [61] which demonstrated that channel coupling effects are large and should not be ignored.

A dynamic coupled-channel formalism was also developed by Julia-Diaz [48] for the processes $\gamma N \rightarrow \pi N \rightarrow KY$ and $\gamma N \rightarrow \pi N$, to provide a comprehensive description on the $\gamma p \rightarrow K^+\Lambda$ reaction. The calculations were based on a chiral constituent quark model that properly incorporates off-shell effects. An effective-Lagrangian approach utilizing unitarity transformations was used to determine the non-resonant interaction within the $KY \oplus \pi N$ subspace. In their model the photoproduction amplitude calculations were simplified by casting the coupled-channels into such a form that the $\gamma N \rightarrow \pi N$ amplitudes are explicitly input. Therefore, only the parameters associated with the KY channels need to be determined, which is achieved by fitting to all the existing data for the coupled-channels. Overall, there was found to be good agreement between the model calculations and the data.

Figure 2.16 shows model calculations compared to the available cross section data from both SAPHIR and CLAS. In these calculations two model prescriptions were used, one using fits to to all SAPHIR and the most recent CLAS data (the M1 model), the other utilizing simultaneous fits to all the available cross section and polarization data. A study of the fit results of both models seemed to indicate that the SAPHIR cross section data show greater compatibility with the polarization measurements than the CLAS results. Calculations from this model

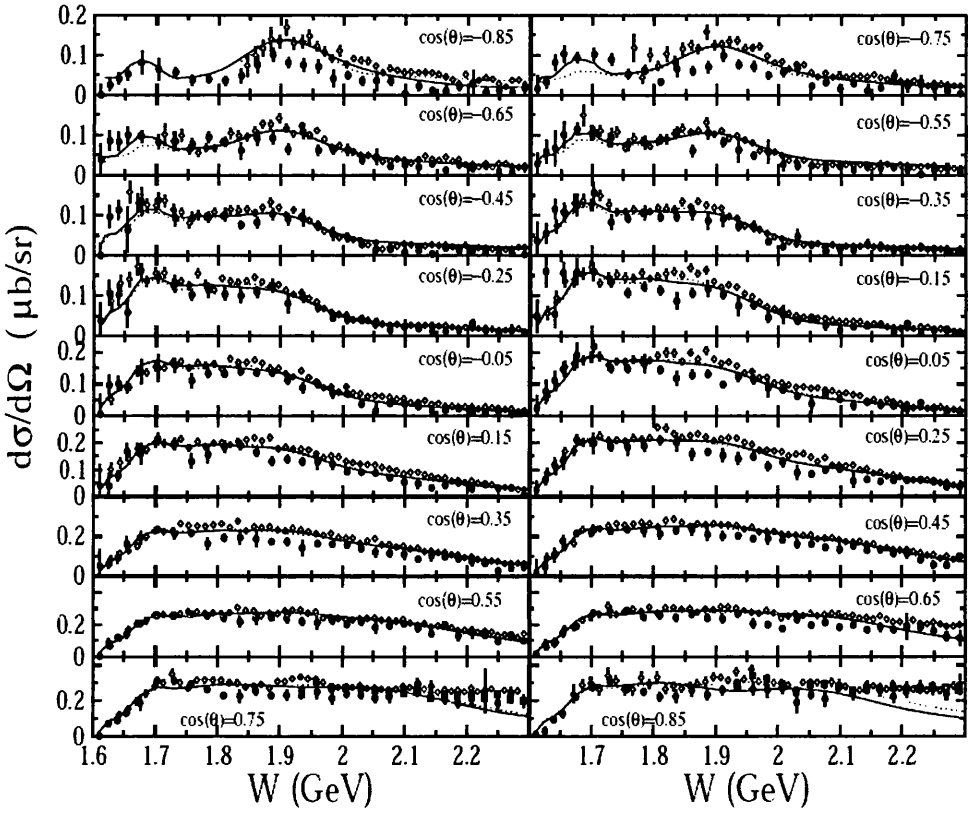

Figure 2.16: M1 (dotted curve) and M2 (solid curve) coupled-channel calculations from Julia-Diaz [48] for the cross section of the reaction $\gamma p \rightarrow K^+\Lambda$. The calculations are compared to the results from CLAS (open diamonds) [25], SAPHIR (full circles) [34] and LEPS (open squares) [44].

are also compared to the polarization results from GRAAL in figures 2.11 and 2.12. Overall, the authors found that the main known resonances that contribute to the $\gamma p \rightarrow K^+\Lambda$ reaction are the $S_{11}(1535)$, $S_{13}(1900)$ and the $D_{13}(1520)$ with smaller contributions from the $F_{15}(1680)$ and the $F_{15}(2000)$. Several previous unknown states were also investigated with strong evidence found for the inclusion of a D_{13} resonance at 1.954 GeV and some weak inference of a possible S_{11} state at 1.804 GeV. Observations were also made for non-negligible effects from a P_{13} state at 1.893 GeV.

2.2.3 Partial Wave and Multipole Analyses

A partial wave analysis of the CLAS and SAPHIR cross-section results, along with the CLAS recoil polarizations and LEPS photon asymmetries was carried out by

Sarantsev *et al* [40]. This analysis combined data for the $K^+\Lambda$ and $K^+\Sigma^0$ channels with previous results on π^0 and η photoproduction [46, 47]. The analysis found that the CLAS and SAPHIR cross-section results were incompatible and required an energy dependent normalization factor as shown in figure 2.17. Results from the calculation compared to the photon asymmetry and recoil polarization data are shown in figure 2.18. These results from the combined analysis highlight the need to introduce a baryon resonance, with a P_{11} state observed in the region of 1840 MeV. Further to this, the analysis points to the possible existence of four D_{13} resonances at energies of 1520, 1700, 1870 and 2170 MeV.

Mart and Sulaksono [3] also studied the SAPHIR, CLAS and LEPS data in a multipole approach looking at the contribution from higher spin states. The prescription developed a gauge-invariant, crossing-symmetric background amplitude from tree-level Feynman diagrams. Their investigation also showed a lack of mutual consistency between the SAPHIR and CLAS data, while the LEPS data was shown to be more consistent with the CLAS results. By fitting their calculations to both the SAPHIR and LEPS data they identified the $S_{11}(1650)$, $P_{13}(1720)$, $D_{13}(1700)$, $D_{13}(2080)$, $F_{15}(1680)$ and $F_{15}(2000)$ as the important resonances. However, the fit to the CLAS and LEPS results points to the $P_{13}(1900)$, $D_{13}(2080)$, $D_{15}(1675)$, $F_{15}(1680)$ and $F_{75}(1990)$ as having the main contribution. This illustrates the difficulties in having two mutually incompatible data sets from CLAS and SAPHIR. In particular figures 2.19 and 2.20 show the results from from three different fits compared to the published data for the photon and target asymmetries respectively. In the first fit the LEPS and SAPHIR data were used, in the second fit LEPS and CLAS, and in the third fit all three data sets were included. These results would appear to suggest that when applying the current world database for kaon photoproduction, any attempt to extract resonance information will be data set dependent. Clearly an improved database for these and other observables should help to remove the ambiguities between the different datasets. The multipole approach also demonstrates the importance of including higher spin states in the calculation, as well as highlighting the need for new high precision measurements of as many different observables as possible to allow stable extraction of resonance information.

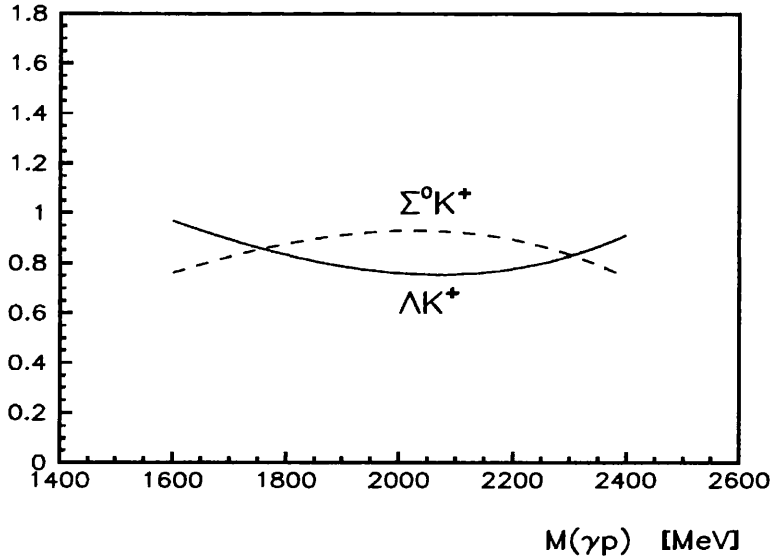

Figure 2.17: Energy dependent normalization factor from reference [40]. This factor had to be introduced to the cross section measurements for both $K^+\Lambda$ and $K^+\Sigma^0$ photoproduction to account for the discrepancies between the CLAS and SAPHIR data.

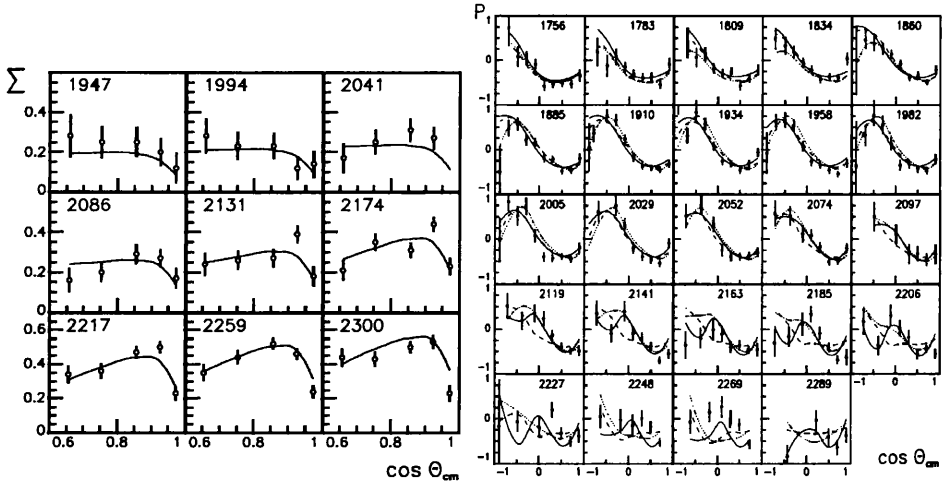

Figure 2.18: Beam polarization aymmetries as a function of W for $\gamma p \rightarrow K^+\Lambda$ from LEPS [44] with the fit results from the partial wave analysis plotted as curves [40] (left). Recoil polarization results from CLAS [26] with the solid line representing the fit results, the dashed line is the fit with $N(2170)D_{13}$ omitted and the dotted line is the fit with the $N(1840)P_{11}$ omitted (right).

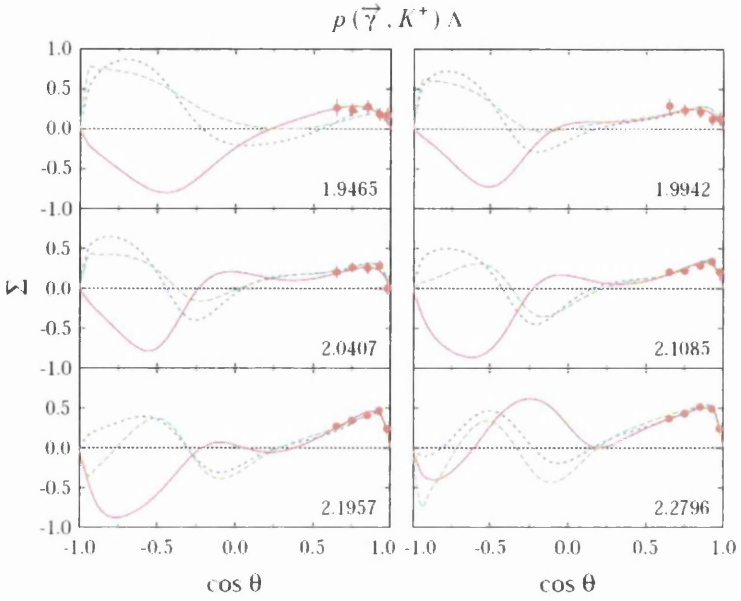

Figure 2.19: Results from the three different fits from Mart and Sulaksono [3] compared to the photon asymmetry data from LEPS [44]. The solid red line is from fit 1, the blue dot-dashed line from fit 2 and the green dashed line from fit 3.

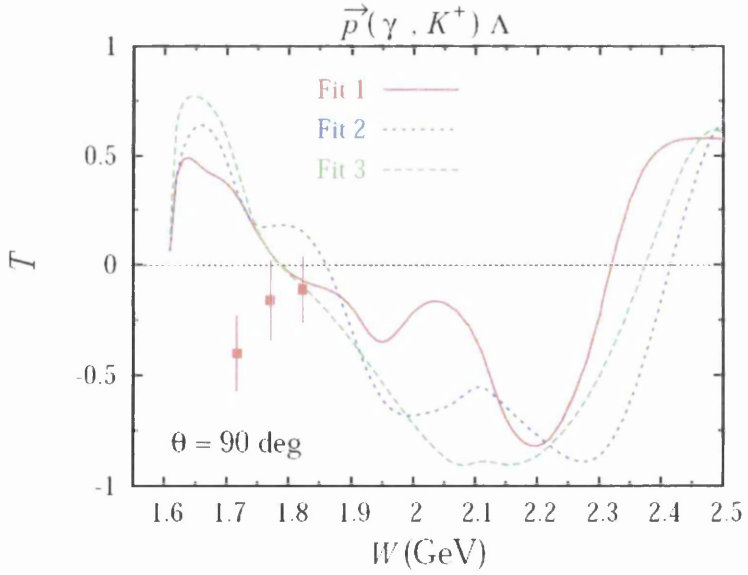

Figure 2.20: Results from the three different fits from Mart and Sulaksono [3] compared to the target asymmetry data from [62]. The solid red line is from fit 1, the blue dot-dashed line from fit 2 and the green dashed line from fit 3.

2.2.4 Regge Models

Regge models have been proven to give extremely good descriptions of high energy particle physics data by extending angular momentum into the complex plane. The theory was developed from a need to account for poles in a partial wave decomposition when crossing symmetry is considered. The formalism groups particles with the same internal quantum numbers but different spin into so called "Regge trajectories". The proposition is then made that at high energies where individual resonances can no longer be distinguished, the photoproduction process is described by the exchange of entire Regge trajectories rather than individual particles. These models are expected to be most valid at high energies and at forward angles, but recent studies have suggested that meson production in the resonance region can be reasonably well described by a Regge approach.

The Guidal-Laget-Vanderhaeghen Regge model [36, 37] describes the exclusive electromagnetic strangeness production reactions $\gamma^{(*)}p \rightarrow K^+\Lambda$ and $\gamma^{(*)}p \rightarrow K^+\Sigma$ through the exchange of only two t-channel trajectories: K and $K^\star$. This model employed no s-channel resonance excitations and the coupling constants at the $[K, (\Lambda, \Sigma), N]$ and $[K^\star, (\Lambda, \Sigma), N]$ vertices were constrained to high energy photoproduction data. One important aspect of the model is that a "Reggeization" of the s-channel nucleon pole is used to restore gauge invariance for the t-channel K exchange.

Figure 2.21 (left) shows the model calculations compared to cross section results from SAPHIR [63] and CLAS [25] for both the $K\Lambda$ and $K\Sigma^0$ channels. Results are shown for two calculations, one with both K^+ and $K^\star$ exchanges and one with only $K^\star$ exchange. The calculations give reasonable agreement to the data, with the forward angle CLAS results in particular lying close to the Regge calculations. The model however, fails to account for the "bumps" seen in the cross sections around W $\approx$ 1.75 GeV and 1.95 GeV in the $K\Lambda$ channel. This is likely due to these structures being the result of s-channel resonances and therefore not reproduced in a pure t-channel exchange model. Figure 2.21 (right) shows photon asymmetry results from the LEPS collaboration at SPring-8 compared to the the calculations. Once again the model can reproduce the general trend of the data, particularly the large rise at forward angles which is indicative of natural parity $K^\star$ exchange dominance. The results of this analysis will extend the current database for the photon asymmetry to more backward angles and lower centre-of-mass energies. This will present an interesting test of the range of applicability of Regge models as they should become less valid in these kinematics.

A recent approach to reproducing cross sections and polarization measurements in hadronic reactions is a "Regge-plus-resonance" (RPR) strategy developed by Corthals, Ryckebusch and Van Cautern [41]. This effective-Lagrangian framework differs from the previously described isobar models by using Regge-trajectory exchange in the t-channel to describe the K^+Y background. The model predictions are then evolved into the resonance region by adding in a number of s-channel resonances to fit the existing data. Since these resonances must, by construction, vanish at higher energies, one can heavily constrain the background to high energy data. This provides an advantage over isobar schemes in that only the resonance couplings are left as free parameters in the resonance region. The use of Regge propagators also reduces the need for strong hadronic form factors for background terms, therefore removing the gauge invariance issues that prove problematic in the pure isobaric approach. A representation of the approach is shown in figure 2.22 where the photoproduction cross section for hyperons is plotted with the different energy regions highlighted for both the resonant and Regge effects.

The Corthals models used K and K^* Regge exchange to describe the background and included the established core resonances to extrapolate into the intermediate energy regime. They investigated the effects of including a 2 star $P_{13}(1900)$ state, along with the contributions from the $D_{13}(1900)$ and $P_{11}(1900)$ missing resonances. Figures 2.23 and 2.24 show the model calculations for different Regge-plus-resonance prescriptions compared to recoil and photon asymmetry data respectively. These results along with comparisons to the previous cross-section measurements provide some evidence for the inclusion of the 2 star $P_{13}(1900)$ state. For the previously unobserved states, the $P_{11}(1900)$ state emerges from the calculations as a more likely candidate for a possible missing resonance than the $D_{13}(1900)$. The authors of reference [41] do, however, qualify these results by stating that they would be reluctant to claim strong evidence for the existence of either of these states. In particular, they demonstrate that a model using only the core set of resonances can provide an equally valid description of the reaction dynamics. From this they conclude that the structure evident in the observables at W $\simeq$ 1900 MeV could be explained by fine tuning the background, rather than being an indication of a missing state.

For the Σ hyperons, a Regge-plus-resonance approach was developed where the reactions $p\,(\gamma, K^+)\,\Sigma^0$ and $p\,(\gamma, K^0)\,\Sigma^+$ could be treated in a common isospin-related description [64, 65]. This was achieved by exploiting the fact that the Σ^+ and Σ^0 hyperons are members of an isotriplet and that the strong coupling

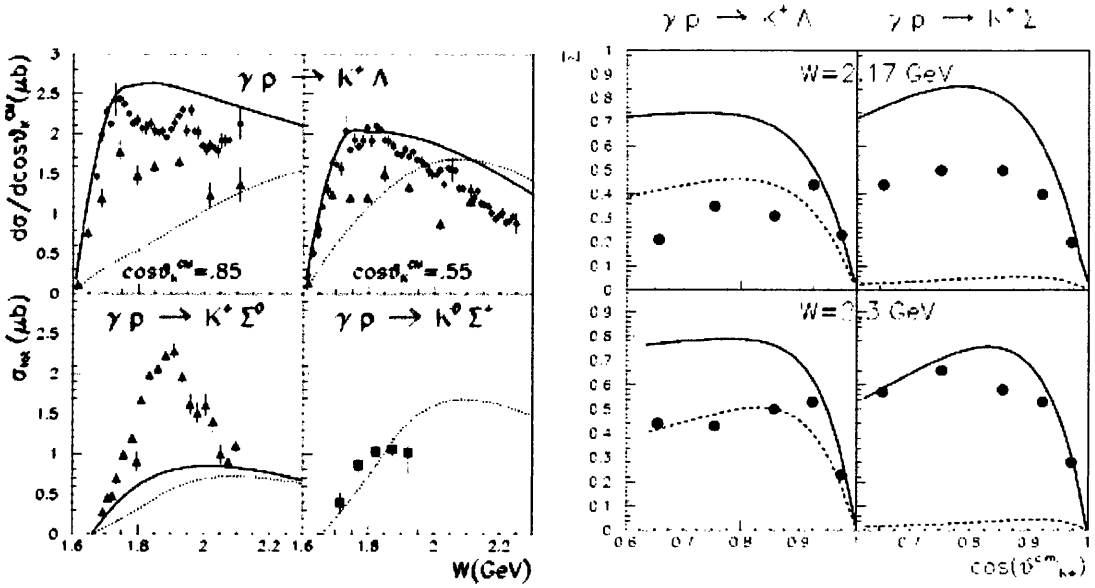

Figure 2.21: Cross section calculations from the Regge model of Guigal, Laget and Vanderhaeghen compared to results from [26] (circles), [63] (triangles) and [66] (squares). On the right the Regge model calculations are compared to the photon asymmetry results from [44].

strengths are related via $SU(2)$ Clebsch-Gordan coefficients. The results of [64] suggest an important role for the two-star $P_{13}(1900)$ along with the standard $N^\star$ core states.

2.3 Summary

The development of high luminosity, high duty-factor accelerators and large acceptance spectrometers has initiated renewed interest in the field of strange meson photoproduction in the last 15 years. This has coincided with a new determination to finally resolve the missing resonance problem, with quark model calculations predicting that some missing states should couple strongly to $K^+\Lambda$ and $K^+\Sigma^0$ final states. An isobar model developed by Mart and Bennhold to reproduce the early cross section results from SAPHIR appeared to find some evidence for one of these missing states. However, recent model calculations were able to equally well reproduce the SAPHIR results by utilizing different approaches to handling the non-resonant background terms, without having to include any missing resonances. These analyses highlighted a major difficulty in attempting to extract resonance information from a limited data set. In particu-

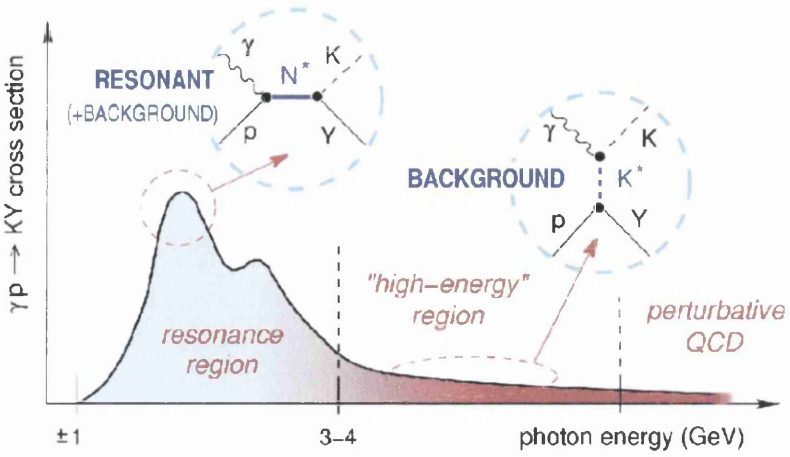

Figure 2.22: Diagrammatic representation of the different energy scales used in the Regge-plus-resonance approach. In the "high-energy" region above 3 GeV the background can be modelled by the exchange of various Regge trajectories, whereas at energies below 3 GeV s-channel resonances become important. Figure from reference [65].

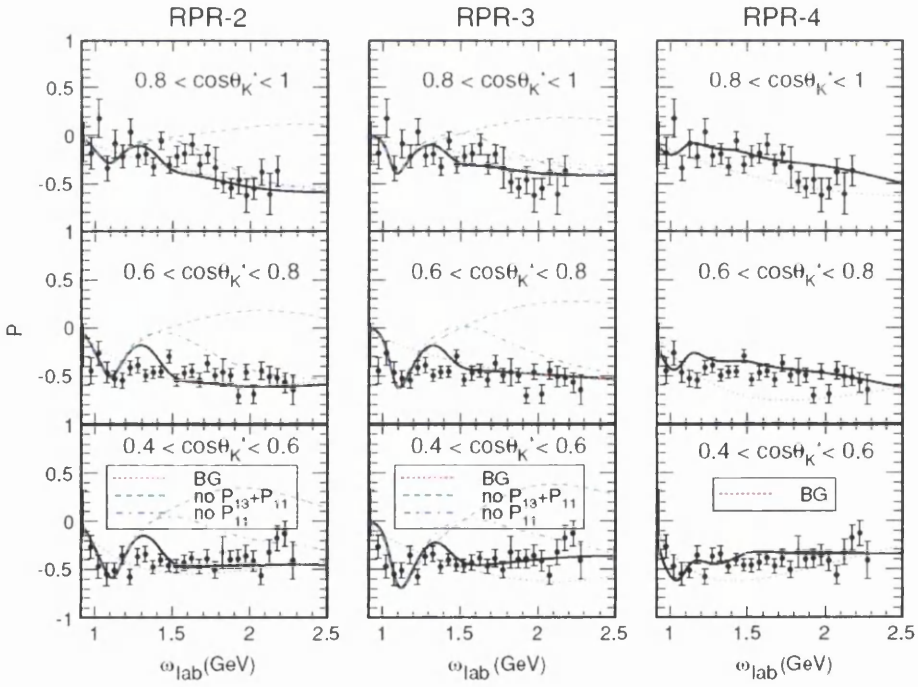

Figure 2.23: Regge-plus-resonance calculations [41] for the Λ recoil polarization compared to the CLAS data [26]. The RPR-2 and RPR-3 models contain the 2-star $P_{13}(1900)$ and the missing $P_{11}(1900)$, wheras the RPR-4 model contains only the "core" resonances.

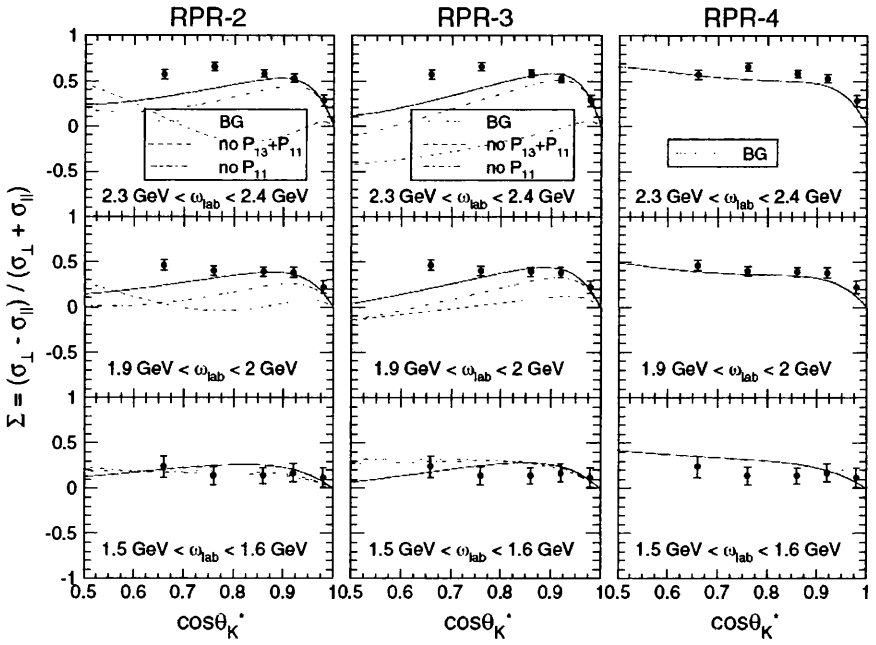

Figure 2.24: Regge-plus-resonance calculations [41] for the photon asymmetry for the $K\Lambda$ channel compared to the LEPS data [44]. The RPR-2 and RPR-3 models contain the 2-star $P_{13}(1900)$ and the missing $P_{11}(1900)$ wheras the RPR-4 model contains only the "core" resonances.

lar these calculations suggest that new data for the photon asymmetry should be extremely sensitive to the contributions from previously missing baryon states. Futher model calculations have also hinted at the possible inclusion of new states, including higher spin contributions, with all the results pointing to the need for significant new data to firmly establish their existence.

Recent analyses have also shown there to be serious lack of consistency between the cross section results measured at CLAS and SAPHIR. The multipole calculations of Mart and Sulaksuno demonstrated a clear dataset dependence in what specific resonances are predicted to couple to the $K^+\Lambda$ channel. This highly undesirable situation requires the addition of new measurements to the the world database to test the consistency of the two sets of cross section data. Further to this, the same CLAS dataset used to make the cross section measurements also provided the first evidence of a fully polarized Λ when a circularly polarized photon is utilized. This result has potentially significant consequences for the current theoretical understanding of the strangeness production process with a model hypothesis involving quark spin currently being developed. The analogous results from this analysis, with a linearly polarized photon beam, should provide an interesting test of the hypothesis and could point to some new physics in the

production of strange quarks from a proton.

The work reported here significantly enhances the current database for both $K^+\Lambda$ and $K^+\Sigma^0$ photoproduction, making an important contribution to the current debate on which resonances should couple to these final states. The measurements of the photon asymmetry will extend the current database above 1.45 GeV to the full angular range and these measurements are predicted to be extremely senstitve to resonance contributions. A significant test of the existing theoretical models will also be provided by measuring the target asymmetry, substantially increasing the current database of only a few data points, along with the first measurements of the double polarization observables O_x and O_z.

Chapter 3

Experimental Detectors and Apparatus

3.1 Introduction

This chapter will describe the various detector components and apparatus used for the study of the reactions $\vec{\gamma}p \rightarrow K^+\Lambda^0$ and $\vec{\gamma}p \rightarrow K^+\Sigma^0$ in the g8b run period. The g8b experiment took data between 20th June and 1st September 2005 at the Thomas Jefferson National Accelerator Facility (Jlab), Newport-News, Virginia, USA. G8b was designed to take data that could be used to study various reactions in hadronic physics, and the analysis presented here involves the experiment "E99-013" - "Photoproduction of Associated Strangeness using a Linearly Polarized Beam of Photons" [67].

Jefferson Lab is primarily designed to study hadronic physics, and in particular the electromagnetic structure of baryons and mesons at the energy scales of the nuclear and particle physics interface, using either electron or photon probes [68]. The laboratory is the world's premier facility for studying physics at the sub-nucleonic level and investigating the transition from quark-gluon to hadronic degrees of freedom. In this experiment the lab's Continuous Electron Beam Accelerator Facility (CEBAF) was used to produce a beam of 4.551 GeV electrons. This beam was delivered to Jlab's experimental Hall B, where the g8b experiment was conducted. Within Hall B a diamond radiator was used to scatter these electrons, in a process called coherent bremsstrahlung, to produce a beam of linearly polarized photons. This photon beam passes through an instrumented collimator, to enhance the relative degree of linear polarization, before being "tagged" by the photon tagging spectrometer. The "tagging" technique was required to determine the energy of the photons that produce a hadronic interaction, as the bremm-

strahlung process is non-monoenergetic. For g8b the photons were produced at 5 different energy settings from 1.3 to 2.1 GeV, with a polarization ranging from 71% to 84%.

The photons then travel into the CEBAF Large Acceptance Spectrometer (CLAS) where they interact with a 40 cm long liquid hydrogen target producing the various decay particles of interest. These particles are detected by the subsystems of CLAS to give accurate measurements of their polar and azimuthal angular distributions and, for charged particles, to allow the reconstruction of their momenta. The CLAS detector is able to provide acceptance covering almost 75% of the 4π solid angle, and has a particularly good acceptance for charged particles. This large acceptance, coupled with the high luminosity of the CEBAF beam make Hall B at Jlab the ideal facility to carry out the g8b experiment.

3.2 Accelerator

The Continuous Electron Beam Accelerator Facility came online in 1996, delivering a high quality electron beam which could be used in the study of hadronic physics at Jefferson Lab. Jlab was one of a number of facilities such as MAMI in Mainz and ELSA in Bonn that had begun to use electromagnetic (EM) probes. For much of the preceeding two decades facilities utilizing accelerators which produced hadronic probes were dominant in intermediate energy physics. These facilities had the advantage that the strong interaction produced events with large cross-sections, copiously producing the particles of interest. Although the cross-sections are relatively small for EM beams they do have the advantage that the interaction is very well understood in QED and the whole volume of the nucleon is probed. Further to this, new technology used in Jlab's CEBAF allows for an extremely high luminosity beam that partially counteracts the problem of low interaction rates.

The CEBAF is designed to deliver a beam of high-luminosity, continous-wave electrons with 100% duty factor to three experimental halls, A, B and C, where each hall provides a different experimental program [69]. The accelerator consists of 2 antiparallel linacs connected by 5 recirculation arcs which are capable of accelerating the electrons up to energies of $\sim$ 6 GeV. Shortly the accelerator will go through an upgrade program designed to push this maximum electron energy up to $\sim$ 12 GeV. A feature of CEBAF is that is capable of delivering a "continuous wave" beam, which means that electrons are delivered in well defined 2.0005 ns "beam buckets" rather than random bursts.

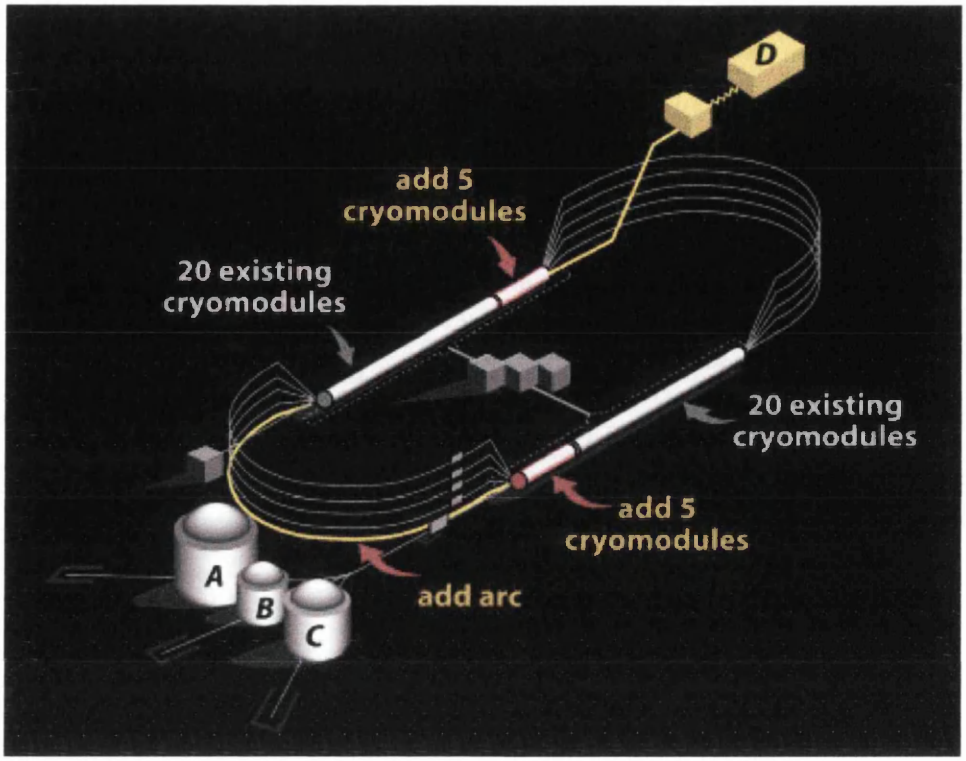

Figure 3.1: Overview of CEBAF showing the linacs, recirculation arcs, three experimental end stations and future plans for an upgrade including a fourth hall(D).

The initial electrons are produced by a photo-emission electron gun before being "injected" into the first linac. Here they are passed through a rotating disk which has three slits, to produce the three different beam "buckets" before being accelerated by the cryomodules through the linac. The electrons are then sent through the recirculation arcs before being accelerated through the second linac, and this "recirculation" can continue up to 5 times. Finally the beam extractor/seperator is used to extract the accelerated electrons and send them to the three different halls. An overview of CEBAF showing the locations of the three experimental halls is shown in figure 3.1.

3.2.1 Injector

The injector at CEBAF is the first stage in the production of high energy electrons and consists of a photo-emission electron gun, an RF accelerating cavity and a chopper. A laser incident upon a strained Gallium Arsenide (GaAs) photocathode is used to produce the electrons, and an anode gives an initial acceleration

of ~100 kV. Two superconducting radio frequency (RF) cavities are then used to accelerate the electrons to 67 MeV before they are "packaged" by an optical chopper and then sent into the CEBAF linacs [70]. The gun actually contains three independent diode lasers, which allows for independent beams to be produced for each of the three experimental halls. This three laser arrangement is crucial to the physics program at Jlab since it allows each hall to independently request and receive beams of different current and polarizations from the other halls. The lasers are each pulsed at 499 MHz, giving the beam a characteristic 2.0005 ns electron beam "bucket" structure [71]. It is possible to circularly polarize the light at this stage using two Pockel cells, where one is used as a quarter wave plate and the other as a half wave plate. This circularly polarized light causes the photo-emission of longitudinally polarized electrons from the GaAs. A Wien filter is then used to compensate for spin precession in the beam transport system and the degree of polarization at the end stations can reach up to $\sim 90\%$. It is possible to cause a flip in the longitudinal direction of the electron spin by altering the voltage of the quarter wave pockel cell. This allows for the production of different beam helicities that can be used to give access to various polarization observables.

3.2.2 Superconducting Linear Accelerators

The electrons are injected into the first superconducting linear accelerator with an initial energy of $\sim$ 67MeV. The central feature of the linear accelerators are 168 RF cavities made out of niobium and supercooled to ~2K using liquid Helium. This superconducting technology has the major advantage that that far less RF power is required than in traditional methods, since no heat is produced by the ohmic processes within the cavities. This allows the machine to operate continuously and a typical RF cavity is shown in figure 3.2. These RF cavities operate at the third sub-harmonic of the overall accelerating frequency to give the electrons a "kick" into the experimental end stations [72]. The niobium at this temperature becomes a superconductor and this allows the electrons to flow through the cavities with no resistance. Each cavity is powered by a Klystron that is capable of generating an electromagnetic wave inside the cavity which causes a charge gradient to form. This is produced by the electromagnetic wave forming a positively charged area in front of the electrons and a negatively charged area behind to induce acceleration, as shown in figure 3.3 . For the electrons to be successfully boosted, the electromagnetic wave must have a frequency of ~1.5 GHz to allow standing waves to form in the cavity and ensure that the electron

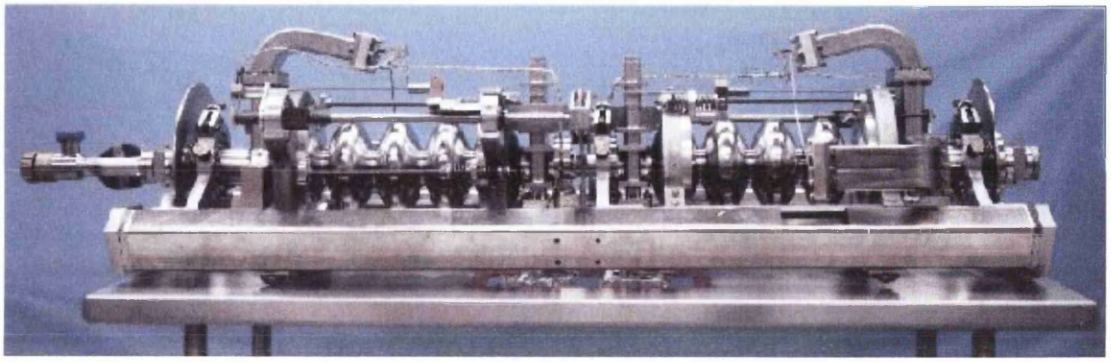

Figure 3.2: Photograph showing two standard CEBAF RF cavities. The system contains elliptical cavities that are orientated perpendicular to the beamline. These cavities are immersed in liquid helium which is cooled to $2K$, where the niobium becomes a superconductor. Each linac contains 168 cavities.

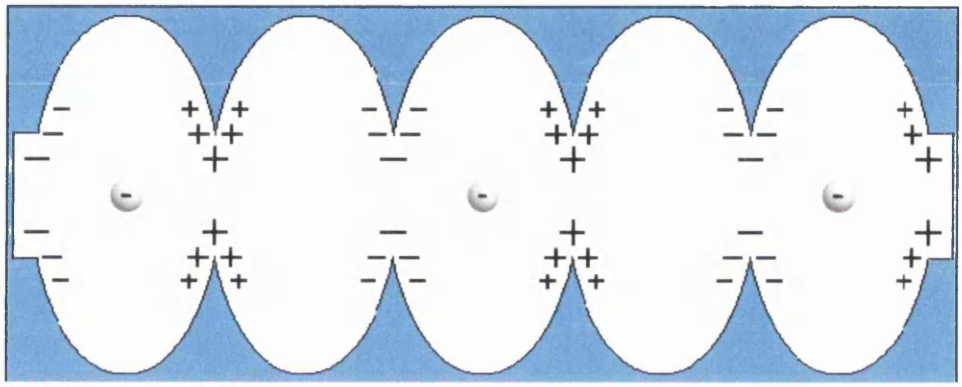

Figure 3.3: Diagrammatic representation of charge distribution within a superconducting RF cavity. The Klystron feeds microwave radiation into the cavity which causes a standing wave to form. This wave can be produced in such a way that there is always a positive electric field in front of the electron and a negative field behind, thus inducing the acceleration.

is always accelerated in the correct direction. This can be achieved through the Klystron which allows one to control the phase of the RF and energy gradient to maximise electron acceleration. At the moment each linear accelerator is capable of accelerating the electrons by ~500 MeV per pass, with a total of 5 passes possible. This allows for a current maximum beam energy of ~5 GeV, although there are ongoing repairs and upgrades to the system that should have the CEBAF back up to its maximum electron energy of 6 GeV [72].

3.2.3 Recirculation Arcs

In order to reach the electron energies required at Jlab while reducing the need for many expensive cavities and cryostats, the accelerator is required to recirculate the beam around the linacs upto 5 times. A series of dipole magnets are located in the recirculation arcs to provide a 180^0 achromatic bend to the electrons [68], which gives CEBAF its characteristic racetrack appearance. The magnets are able to accomplish this bending up to as many as 9 times, while keeping the whole system globally isochronous. One of unique challenges for the recirculation arcs is that electrons of different energy require different magnetic field strengths to achieve the same bending radius. The accelerator can achieve this by splitting the initial electron beam into 5 sub-beams of different energies where each one can pass through different dipole magnets. This results in the electrons of different energy each achieving the same bend-radius, before being recombined into a single beam and then entering the second linac. In total, the combined racetrack course of CEBAF stretches for $\sim$ 8 miles.

3.2.4 Beam Extraction and Experimental Halls

The final stage of the CEBAF accelerator involves the extraction of the beam and subsequent delivery to the three experimental halls. The beam is extracted using RF separator cavities which allow each hall to receive the beam at either maximum energy, or for individual halls to extract beam after a smaller number of passes. An important restriction of the beam extraction process is that the separators can only extract beam for one hall in any given pass. This means that although two different halls can take beam at a lower pass and hence lower energy than the maximum available, they cannot take beam at different energies from each other. The energy of beam delivered to each hall is equal to an energy dependent upon the number of passes through the accelerator plus the initial energy of the accelerator. For g8b a beam energy of 4.551 GeV was delivered to Hall B, home of the Coherent Bremsstrahlung Facility and CLAS detector.

3.3 Experimental Hall B

Hall B is the smallest of the three experimental halls at Jlab. It houses a series of experimental detectors, but the centrepiece device is the CEBAF Large Acceptance Spectrometer (CLAS). The hall also contains the photon tagging spectrometer, which in conjunction with CLAS, allows Hall B to be utilized for

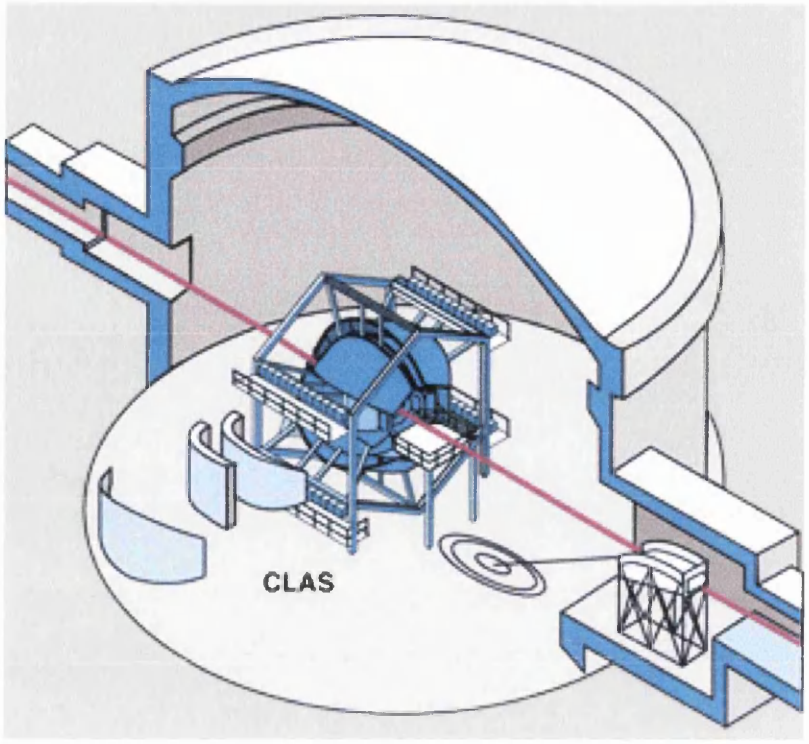

Figure 3.4: Schematic representation of Hall B showing the CLAS detector and tagger as an electron beam enters the hall.

both electron and real photon experiments. Also contained within Hall B are the beamline, pair spectrometer, beam position monitors and devices used for photon normalization. Another important feature of the hall is that it houses the coherent bremsstrahlung facility which allows experiments with linearly polarized photons to be undertaken.

Upon entering Hall B, the electron beam is scattered off a diamond radiator to produce a beam of linearly polarized photons. The photon beam then passes by the photon tagger, while a magnetic field is used to deflect energy degraded electrons onto the hodoscope to allow a determination of the photon energy. The photons continue down the beamline to interact with a hydrogen target within the centre of CLAS. Figure 3.4 shows a schematic layout of the tagger and CLAS when an electron beam enters Hall B.

The following sections in this chapter will describe the various detector systems and apparatus used in the Hall B experimental end station.

3.4 Coherent Bremsstrahlung Facility

The g8b experiment uses a linearly polarized photon beam as this has been shown to greatly enhance the study of photo-induced exclusive reactions [73]. This is because it gives access to more single and double spin observables than is possible with just a circularly polarized beam. It has also been shown that these spin observables are very sensitive to the reaction amplitudes and the contributing nucleon resonances [2–4]. The linearly polarized photon beam was produced through the process of coherent bremsstrahlung (CB), where the electron beam is incident on a suitably orientated diamond radiator [74]. Figure 3.5 shows a schematic layout of the Hall B CB facility, with the relative layout of the main components along the beamline. A brief description of the CB process is given below. A more detailed description can be found in reference [74], with its specific use at Jlab detailed in references [75, 76].

In the bremsstrahlung process an electron incident on a suitable radiator will be decelerated by the electromagnetic field of the radiator's nuclei and will emit an energetic photon. If an amorphous radiator such as carbon is used as the scattering material, then the photons will be produced with an energy spectrum that falls off with increasing photon energy. However if a radiator such as diamond with a regular lattice structure is chosen, then the photons can be produced at discrete fractional energies corresponding to specific momentum transfers of the electrons to the crystal nuclei. This gives an energy spectrum with a characteristic "coherent peak" structure. If one carefully chooses the orientation of the diamond with respect to the direction of the electron beam, then one can select a particular isolated reciprocal lattice vector to scatter off. The photons produced through this process will have a high degree of linear polarization, particularly for those photons within the coherent peak. The orientation of the diamond is controlled by the goniometer which allows sensitive adjustments of position in six degrees of freedom.

3.4.1 Diamond Radiator

The choice of radiator for g8b was crucial as this largely determines the quality and stability of the linearly polarized photon beam produced. Any defects in the radiator can adversely affect the CB process, because the background production of unpolarized photons becomes significant. This can result in a less stable beam with a lower degree of relative polarization.

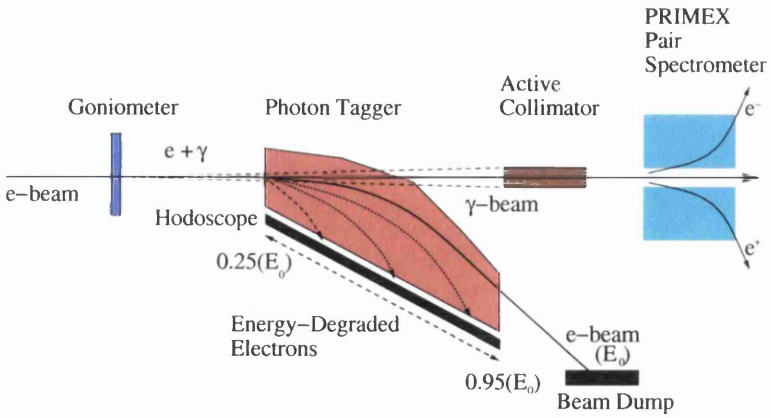

Figure 3.5: Schematic layout of coherent bremsstrahlung facility within Hall B. The incident electron beam scatters off a diamond held by the goniometer to produce linearly polarized photons. The energy degraded electrons are bent on to the tagger hodoscope while the photons pass through the active collimator.

The first requirement of a radiator for CB is that it should have a regular crystal lattice structure. This is because the primary electron has to be scattered in a radiator that allows the recoil momentum to be taken up by the crystal as a whole, rather than by individual atoms [74]. For this to occur the crystal must be positioned with respect to the electron beam in such a way that the recoil momentum is equal to one of the crystal reciprocal lattice vectors. This satisfies the Laue condition $\vec{q} = \vec{g}$ where the $\vec{g}$ is the reciprocal lattice vector of the crystal.

Diamond is usually chosen as the radiator in CB because of its small lattice constant and relatively high Debye temperature. This high Debye temperature means that the amplitude of the thermal motion of the atoms in the lattice is small and the lattice structure is relatively unaffected by thermal effects [77].

It is also important to carefully choose the correct thickness of diamond for CB as this has an effect on the angular divergence of the beam. This results from the fact that when an electron passes through the diamond radiator there is a spread in the direction of the electrons due to multiple scattering effects, crystal defects in the lattice, and divergence of the incident electron beam. To enhance the coherent spectrum this angular variation should be kept smaller than the charcteristic opening angle for CB,

$$\theta_{br} = \frac{mc^2}{E_0} \tag{3.1}$$

where E_0 is the primary electron energy and m is the electron mass. A more detailed explanation of this relation and a description of its importance for CB

is given in reference [74]. This angular variation of the beam is important as any shift in orientation between the primary electron beam and the diamond will cause the coherent edge to move to a different energy. For the incident electron energy used in g8b, the shift in coherent peak produced from the [220] reciprocal lattice with a variation in incident electron direction of order θ_{br}, is estimated to be about $\sim$ 1% [77]. This implies that such an electron angular variation will result in a broadening on the coherent peak structure and thus reduce the maximum degree of polarization [78, 79]. The spatial distribution for electrons from multiple scattering can be approximated by the relation [80]:

$$\theta_{sc} = \frac{19.2}{E_0}\sqrt{t} \times (1 + 0.038ln\,(t)) \tag{3.2}$$

where t is the radiator thickness in radiation lengths. From this one can derive the ratio:

$$\frac{\theta_{sc}}{\theta_{br}} = \frac{19.2}{mc^2}\sqrt{t} \times (1 + 0.038ln\,(t)) \tag{3.3}$$

which is independent of the energy of the primary electron beam. This means that one can select a thickness for the diamond radiator where the effects of multiple scattering are minimized for all beam energies. A sensible upper limit of the radiator thickness, for which the spread of the coherent peak position is minimized and hence the polarization is maximized, is given by:

$$\theta_{sc} = \frac{\theta_{br}}{2}. \tag{3.4}$$

These specifications require a diamond thickness of $\sim 3.6 \times 10^{-4}$ radiation lengths, or 40 μm. For g8b a high quality 50 μm crystal was chosen, being the closest available diamond to the required specifications. Its quality was assessed using several of the techniques decribed in reference [77]. Figure 3.6 shows two of the tests used to probe the quality of the diamond - illumination by polarized light and X-ray rocking curve measurements.

3.4.2 Goniometer

The George Washington University (GWU) goniometer is responsible for controlling the orientation of the diamond [81]. It was designed to be capable of orienting

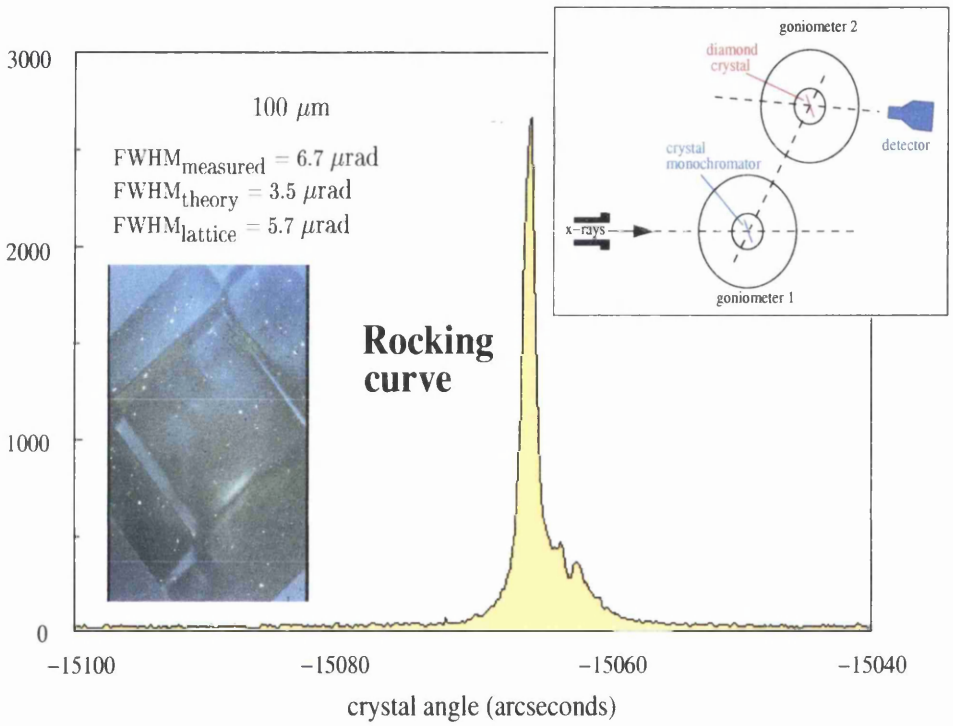

Figure 3.6: Representation of the 2 procedures used to test the quality of a $100\mu m$ diamond before it was cut down to $50\mu m$. The photograph on the left shows the polarized light passing through the crystal. The main picture shows a typical rocking curve measurement. On the top right is the experimental set-up for a rocking curve measurement.

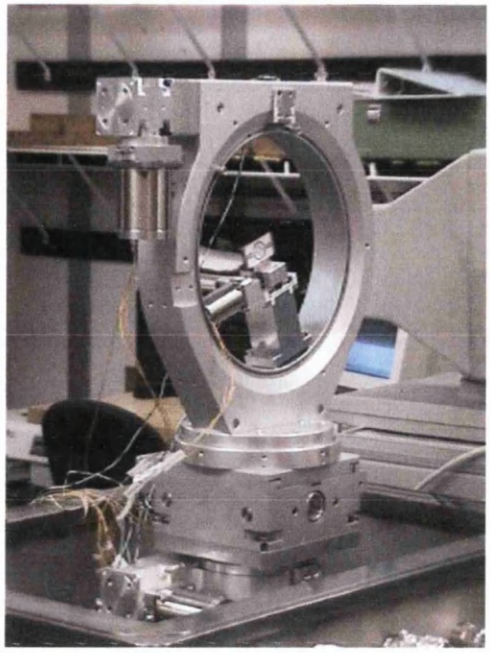

Figure 3.7: GWU Goniometer [81] shown in test condition. The target ladder is visible in the centre of the device.

the diamond crystal to a precision of better than 10 μrad. The device can hold up to six radiators on a target ladder and can move the diamond through three rotational and two translational axes. The system is placed ~10 cm upstream of the photon tagger and maintained in vacuum conditions. The goniometer is controlled by software which allows shift takers to change the type of radiator being used (diamond or carbon) as well as the orientation of the linearly polarized beam (parallel or perpendicular). The goniometer is shown in test condition in figure 3.7 and its degrees of freedom are schematically represented in figure 3.8. The diamond radiators along with a 50 μm thick amorphous carbon radiator are mounted on a target ladder which is placed in the centre of the device. This is shown in figure 3.9 and allows the goniometer to move different radiators in and out of the beamline.

3.4.3 Photon Tagging Spectrometer

The photon tagging spectrometer within Hall B is used for the tagging of bremsstrahlung photons over a range of 20-95% of the incident electron energy [82]. A schematic layout of the tagger is shown in figure 3.10. The system is based on the electron bremsstrahlung process in which the energy transferred to the scattering nucleus is negligibly small, so the reaction can obey the energy conservation relation:

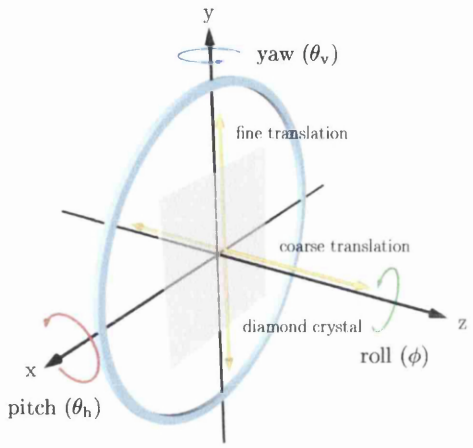

Figure 3.8: Schematic representation of the degrees of freedom for the GWU Goniometer. Shown are the different axes of pitch, yaw and roll as well as the translational axes.

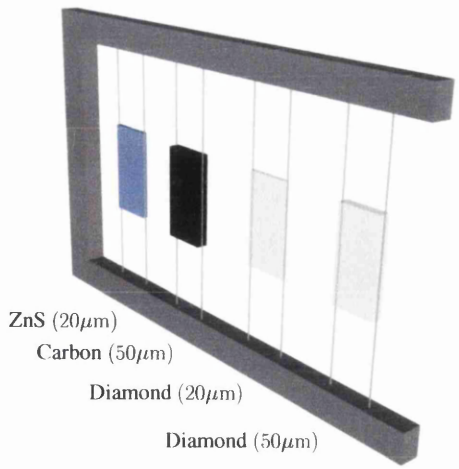

Figure 3.9: Representation of the target ladder showing the different radiators with their respective thicknesses. The target ladder is mounted at the centre of the goniometer.

$$E_\gamma = E_0 - E_e \tag{3.5}$$

where E_γ is the energy of the bremsstrahlung photon, E_0 is the incident energy and E_e is the energy of the scattered electron. As the initial electron energy is uniquely determined by the accelerator, the measurement of the scattered electron energy allows an accurate determination of the photon energy.

Any photons produced in the bremsstrahlung process will pass through the tagger magnetic field and continue undeviated straight on to the CLAS detector. However, when the electrons enter the tagger, the uniform dipole magnetic field acts to bend them towards the tagger hodoscope. The electrons that did not produce a photon retain enough energy so that they are bent into the beam dump, while the energy degraded electrons are focussed onto the tagger hodoscope. The hodoscope, which consists of two scintillator planes known as the energy plane (E-Plane) and the timing plane (T-Plane), can then detect the energy degraded electron and thus determine the energy of the radiated photon. The geometry of the tagging system is sketched in figure 3.10.

The photon tagging system utilized a dipole magnet capable of operating over a photon energy range of 20% - 95% of the inital electron energy [82] to bend the energy degraded electrons onto the hodoscope. The hodoscope itself has three main requirements. It should be capable of providing accurate enough momentum information for the detected electron to allow the photon energy to be determined to the required resolution. It should also provide timing information that is accurate enough for coincidences to be made with any subsequent events triggered by the photon in a downstream detector. In addition it is also important that the hodoscope provides sufficiently good timing resolution to allow the identification of the exact 2 ns beam bucket in which an event occurred. To achieve this the hodoscope E and T-Planes are both highly segmented and have their working surface normal to the beam trajectory.

3.4.3.1 Tagger E-Plane

The tagger E-Plane consists of 384 scintillator paddles for energy measurements, which can be divided into 767 E-bins due to overlaps to give a better resolution. The overlap between the counters is approximately one third of a paddle and each is equipped with one photomultiplier tube and a pipeline TDC. The overall energy resolution for this E-Plane arrangement is $0.001E_0$. The plastic scintillator for each counter is 20 cm long and 4 mm thick with widths from 6 to 18 mm,

chosen such that every paddle subtends approximately equal momentum intervals. Before the g8b run all E-counters had been improved considerably and all 384 counters had received improved shielding, new bases, and individual HV controls [83].

The tagger system was constructed with the E-Plane close to the exit flange of the magnet vacuum box. This minimized the effect of multiple scattering as electrons passed through the exit window and thus optimized the resolution. The paddle array was built to be orthogonal to the electron trajectory as it passed through the focal plane. This arrangement was important in reducing the effect of signals from back-scattered particles [82].

3.4.3.2 Tagger T-Plane

The T-Plane consists of 61 overlapping T-counter scintillators for timing measurements. Similar to the E-paddles, the T-paddles can be divided into 121 T-bins due to the overlaps between adjacent counters. The overlap on this occasion is of the order of 10% and each T-counter scintillator is equipped with two photomultiplier tubes and a pipeline TDC. Also similar to the E-paddles, the T-paddles are aligned orthogonally to the electron trajectory, again reducing the effect of back scattering.

In order to associate a tagged photon with the correct 2 ns beam bucket, the resolution of the T-Plane has to be better than ~300 ps. To achieve this the individual paddles are thicker than the E-paddles, at 2 cm, and are located farther away from the dipole magnet as shown in figure 3.10. The T-paddles were also arranged into two separate groups with the first 19 paddles covering the the photon energy range of 75% to 95% of the incident electron energy being narrower than the remaining 42 paddles that cover the rest of photon energy range [82].

3.4.4 Active Collimator

The UTEP/Orsay active collimator [84] is located directly downstream of the photon tagging spectrometer, and is shown in test condition in figure 3.12. The instrumented collimator has an aperture of 2 mm in diameter and is located 22.9 m downstream of the diamond radiator. The device is composed of 13 nickel diskettes, each with an outer diameter of 50 mm and a thickness of 15 mm. The disks each have a small aperture bored into the centre, and are stacked into a

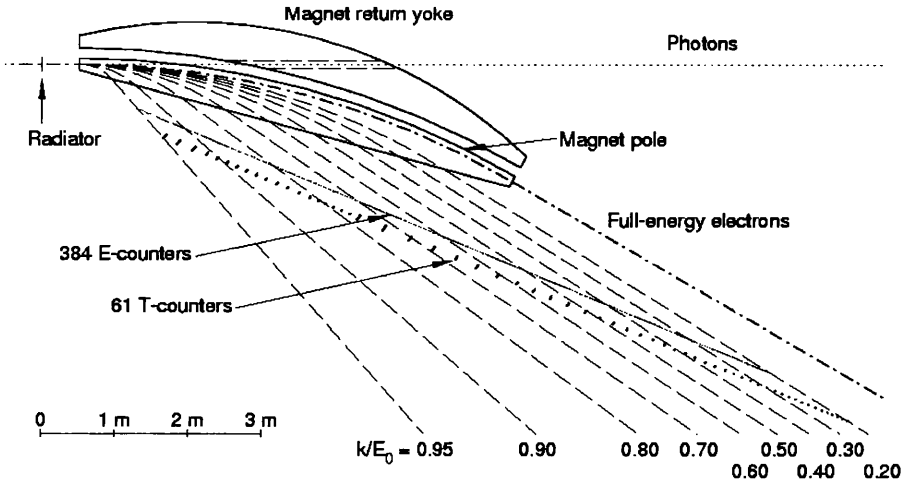

Figure 3.10: Schematic layout of tagger showing the relative positions of the E and T-Counters. Figure from reference [82].

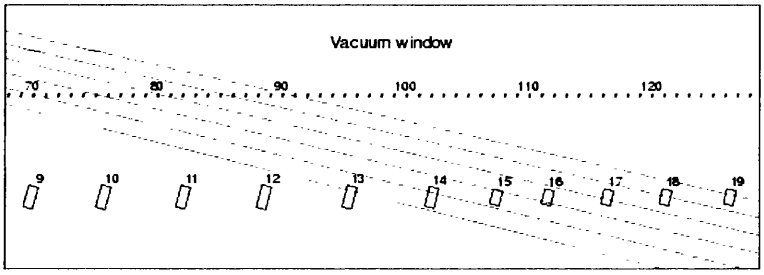

Figure 3.11: Scale drawing of a short hodoscope section. Shown is the orientation of the E and T-Plane scintillators with some typical electron trajectories superimposed. The figure shows the "venetian blind" geometry of the hodoscope. Figure from reference [82].

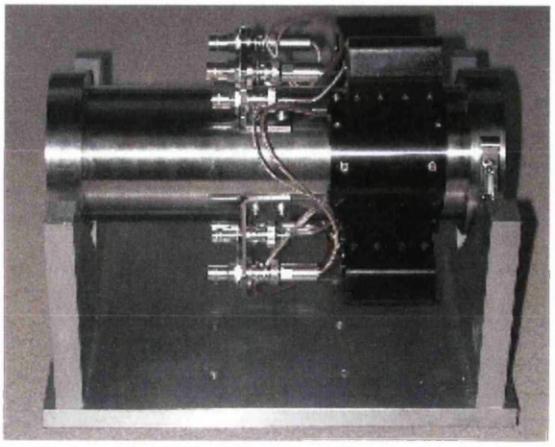

Figure 3.12: The IPN-Orsay/UTEP Instrumented Collimator shown in test condition before installation into the beamline.

cylindrical sheath of stainless steel with a 4mm cubic scintillator sandwiched between them. This is designed to measure the rate of e^+e^- pairs produced by photons outside the 2 mm core incident on the first nickel disk. This allows for online monitoring of the count rates in the scintillator, which can be related to shifts in beam position. These shifts are measured as aymmetries in the measured rates from photomultiplier tubes located at different positions around the scintillator.

The primary objective of the active collimator is to enhance the degree of linear polarization, P_γ, within the coherent peak. As described in [74] the natural emission angle of CB decreases with increasing photon energy according to the relation

$$\theta_{char} = \frac{m_e c^2}{E_0} \tag{3.6}$$

where θ_{char} is the characteristic angle. For incoherent bremsstrahlung the angular distribution is nearly independent of the photon energy. This means that by tightly collimating the photon beam, it is possible to enhance the relative contribution of CB and thus enhance the relative degree of linear polarization.

3.5 CEBAF Large Acceptance Spectrometer (CLAS)

The CEBAF Large Acceptance Spectrometer (CLAS) is a magnetic toroidal multi-gap spectrometer, and is the main detector in Hall B of Jefferson Lab [69, 85]. The system is composed of various multi-layer detector subsystems and six superconducting magnets which geometrically split the detector into six sectors. It is used to track and detect the azimuthal and polar angular distributions of various reaction products. The different sub-systems of CLAS are designed to provide information on the charge, momentum, mass and velocity of any particle of interest. The superconducting magnets generate the toroidal magnetic field which is used to focus the reaction particles. The whole system has near 4π acceptance, although the presence of the magnetic coils act to produce some regions of zero-acceptance.

The centre of CLAS contains a 40 cm long liquid Hydrogen target, surrounded by a highly segmented start counter which is used to determine the hadronic reaction time. There are three layers of drift chambers which provide tracking and momentum information, and an outer scintillator shell for time-of-flight measurements. CLAS also contains a Cerenkov detector for electron experiments, and an electromagnetic calorimeter to detect particle showers. The layout of the drift chambers and time-of-flight systems are shown in figure 3.14 with a top-view of the detector. For g8b, the magnetic field had a positive polarity resulting in positively charged particles being curved outward away from the beamline while the negatively charged particles are curved inward towards the beamline [69, 86–88].

Figure 3.13 shows a photograph of CLAS within Hall B with its clamshell open. The following sections will describe in detail the various sub-systems of CLAS with the exception of the Cerenkov Counters which were not used during the g8b run.

3.5.1 Superconducting Torus Magnet

The magnetic field within CLAS is generated by a system of six superconducting coils arranged into a torroidal geometry around the beamline [69]. This configuration effectively creates six different sectors in CLAS, and the presence of the magnetic coils reduces the acceptance down to $\sim 75\%$ of 4π solid angle. The magnet used to generate the field is approximately 5m in length and 5m in diameter.

Figure 3.13: CLAS detector within the Hall B experimental end-station. The detector has its clamshell open, in which the drift chambers (centre) can be seen with their segmented structure. The time of flight scintillator paddles can be seen to the left of centre.

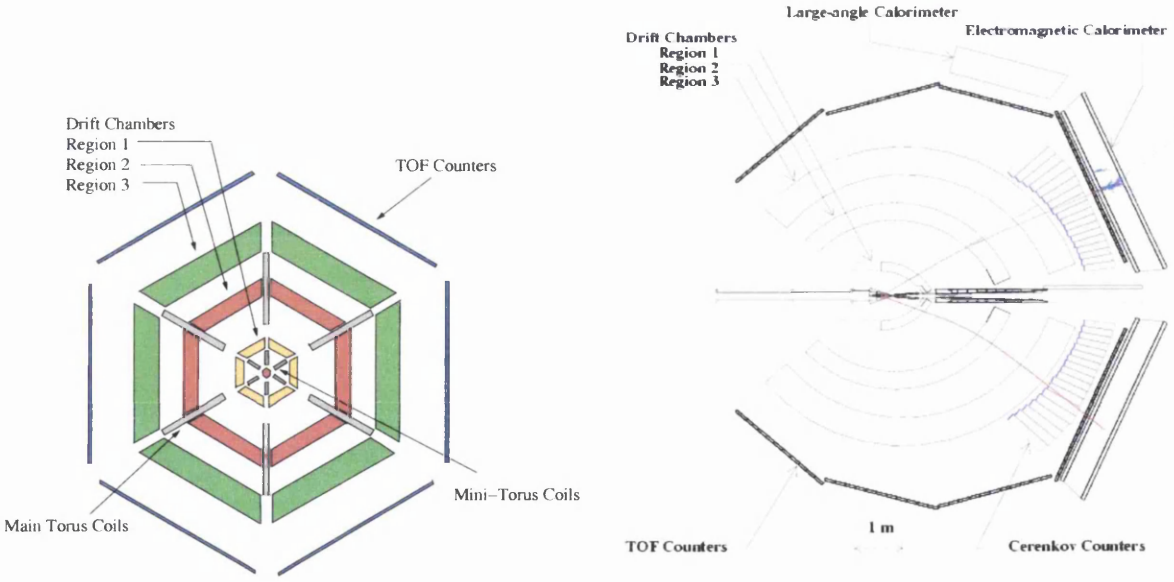

Figure 3.14: Diagram on the left showing a cross-section of CLAS illustrating the relative positions of the magnetic coils, drift chambers and TOF Counters. Within the concentric shape of the detector the main torus magnets can be seen to segment it into six different sectors. For g8b the mini torus was replaced by the start counter. Diagram on right showing a top-view of CLAS cut along the beamline. Typical tracks from a photon, proton and electron are superimposed.

Figure 3.16 shows the contours of the magnetic field in a plane perpenidicular to the torus axis.

The coils are designed with 4 layers and 54 turns of aluminium-stabilized NbTi/Cu conductor and are cooled to temperatures of 4.5 K by forcing supercritical helium through cooling tubes located at the edge of the windings. The maximum intensity of the field is 2 T and the main component is in the azimuthal direction. However, close to the coils there can be some deviation from a pure azimuthal field. The circular inner shape of the coil serves to reduce such deviations and any reaction products tend not to experience any significant azimuthal kick when crossing the inner boundary of the system. The torroidal geometry also has the advantage that it preserves a central field free region that can be utilized for the operation of a polarized target.

During the g8b experiment, data was taken with a positive polarity field and a setting of of 1930 A. This relatively low field setting gives rise to an increased acceptance for negatively charged particles, as less of these will be lost down the beamline hole at forward angles.

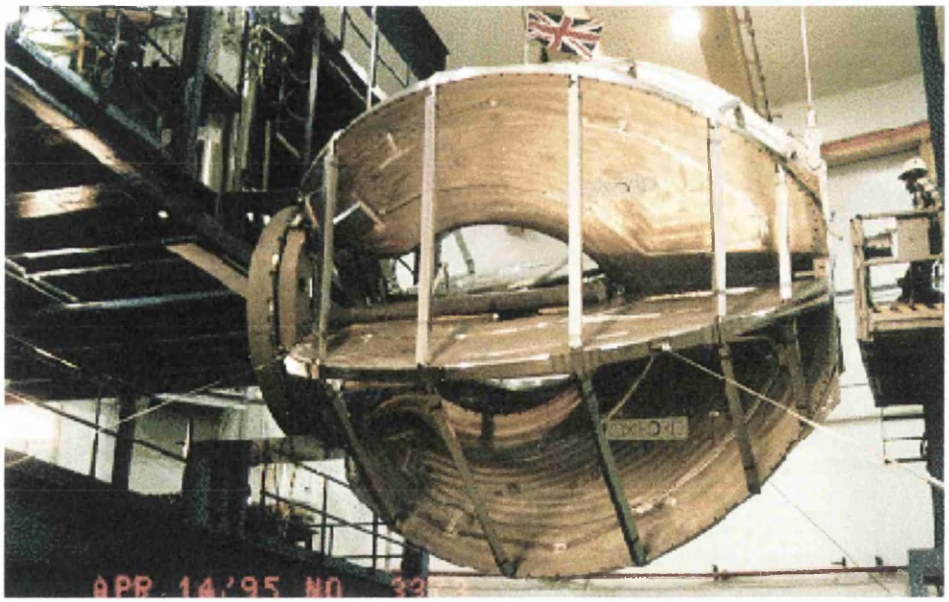

Figure 3.15: Bare coils of the CLAS torroidal magnet during installation

3.5.2 Target

For the g8b run a 40 cm long cylindrical cell containing liquid hydrogen was used as the target. This cell was used to optimize the density of atomic protons to

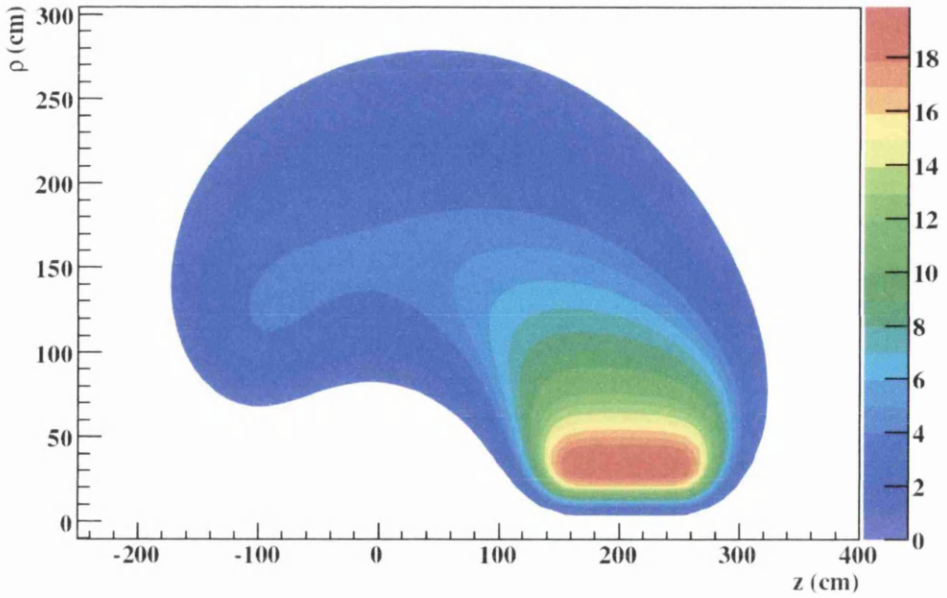

Figure 3.16: Contours of constant absolute magnetic field for the CLAS torroid. For g8b the centre of the 40cm long target was placed at z = -20cm.

enhance the study of the $K^+\Lambda$ and $K^+\Sigma^0$ channels. The cell was made of Kapton and a repesentation of it is shown in figure 3.17.

Figure 3.17: 40cm long g8b Target Cell.

3.5.3 Start Counter

For real photon runs at Jlab the mini-torus within CLAS is replaced by the start counter, a highly segmented ring of plastic scintillators surrounding the

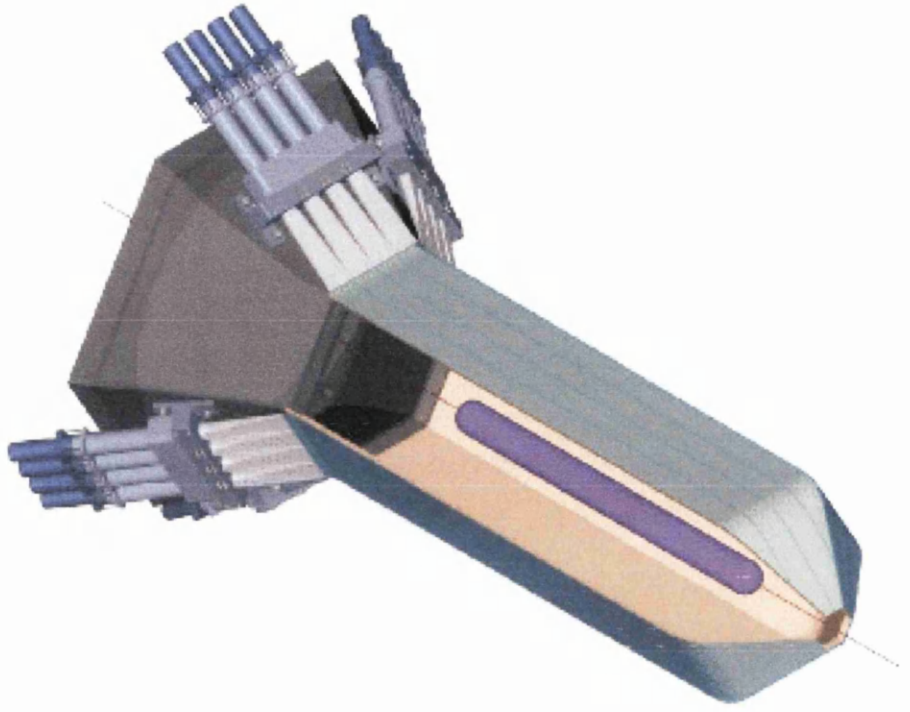

Figure 3.18: Schematic diagram of the new CLAS Start Counter

target. The start counter is used to obtain the correct start time for time-of-flight measurements by determining the interaction time of the incoming photon in the target. It does this by detecting the outgoing charged particles and providing the initial start signal for the experimental trigger. A diagram of the system is shown in figure 3.18.

The start counter was designed to produce full azimuthal and polar acceptance within CLAS and to completely surround the 40 cm long target. The device consists of 24 paddles and maintains the electromagnetic background within acceptable limits by requiring the multiplicity of hit paddles to be equal to or greater than two. The system has six identical sectors surrounding the target cell and each sector consists of four EJ-200 scintillator paddles. Each scintillator is then coupled to an acrylic light guide. The scintillators in each paddle have a 502 mm long straight section, situated between two bends, with a tapered end called the "nose". The paddles, along with their mirror images, make up one sector in the start counter. The timing resolution of the flat "leg" part of the start counter was measured to be $\sim$ 290 ps, while the resolution of the "nose" is $\sim$ 320 ps.

3.5.4 Drift Chambers

The drift chambers in CLAS are designed to provide good tracking resolution and efficiency while maintaining a large acceptance [87]. The system is split azimuthally into six sectors, due to the presence of the six coils of the toroid, and is capable of accurately detecting and measuring the momentum and trajectory of charged particles. Each sector contains three large multi-layer chambers at different radial locations giving a total of 18 drift chamber segments. The system was designed to provide particle tracking over a polar angular range from 8^0 to 142^0 as well as up to 80% coverage in the azimuthal direction.

The three radial locations are referred to as "regions", and each region consists of two superlayers which in turn contain six layers of wire each. The first of the superlayers, referred to as the "axial" superlayer, is positioned axial to the magnetic field. The second superlayer, referred to as "stereo", is tilted at a 6^0 stereo angle around the radius of each layer to provide azimuthal information. In order to allow optimal filling of the wedge-shaped volume between the torus coils, each chamber was designed to be parallel to its neighbouring coil plane, and thus tilted at a 60^0 angle with respect to each other. The advantage of this design is that the directional distribution of the wires is approximately perpendicular to the bend trajectories of the charged particles, thus providing maximum sensitivity to the track momenta. The chamber bodies support the wires running between the two endplates, and the midpoints are arranged into layers of concentric circles, with the wire positions shifted by half the nominal wire spacing in successive layers [69]. This repeating pattern of neighbouring layers with two field wire layers and one sense-wire layer results in a quasi-hexagonal pattern of one field-wire surrounded by six sense-wires. In total the complete drift chamber system consists of 35,148 sense wires. A hexagonal pattern was chosen for the CLAS drift chambers since these cells approximate an ideal circular cell in which drift time to drift distance is independent of entrance angle. This is desirable as typical events in CLAS will traverse the chambers at varying angles. Furthermore, this layout allows for a more straightforward resolution of the side of the sense wire on which the track was located.

The drift chamber sense wires were constructed using 20 μm diameter gold-plated tungsten. This was chosen as the small diameter limits the wire tensions and operating voltages, and the tungsten along with the gold-plate ensures chemical inertness. The field wires were made out of 140 μm gold-plated aluminium alloy. Aluminium was chosen because it has a long radiation length and thus minimizes multiple scattering. A gas mixture containing 90% argon and 10% carbon

dioxide was used to fill the chambers. This mixture is optimal for the chambers as it also minimizes multiple scattering, reduces background effects from Moller electrons and target-generated X-rays, and is relatively inexpensive.

The region 1 drift chambers are the innermost of the three nested packages and lie within a nearly field-free region of the torus. This region consists of two superlayers where the axial layer is at a larger radius than the stereo, in contrast to to the two outer regions. This arrangement was necessary due to spatial constraints within the torus. These constraints also mean that region 1 only has 10 layers of sense wires, as opposed to 12 layers in the other regions. Since this region of the drift chambers is virtually field-free, its primary purpose is to provide the initial trajectory information of the charged particles as they enter the drift chamber assembly. Region 2 is designed to track all charged particles near the point of maximum sagitta in the magnetic field of the torus. As the magnetic field is strongest within this region, the curvature of charged particle trajectories will be maximal allowing excellent momentum resolution. Region 3 has a similar layout to region 2 in that the stereo layers are at a larger radius than the axial layers. This region lies furthest from the target in another region of low magnetic field. Consequently, region 3 provides information on the direction of charged particles as they leave the drift chambers and travel on to the outerlying detector subsystems. The region 2 and 3 drift chambers are shown in figure 3.19 in their installed positions along with a representation of a particle track passing through two of the superlayers.

3.5.5 Time of Flight System

The time-of-flight (TOF) subsystem of CLAS covers the entire active azimuthal angle and a polar angular range of 8^0 to 142^0. The complete system, which is located between the Cerenkov counters and the electromagnetic calorimeter covers a total area of 206 m^2 and consists of 57 scintilator paddles per sector [89]. The TOF system in CLAS was designed to provide good segmentation for flexible triggering and prescaling, and excellent timing resolution for particle identification. One of the principle requirements of the system was that it should be capable of separating kaons and pions up to a momentum of 2 GeV/c.

The scintillator paddles are made of Bicron BC-408 scintillator, which allows for a relatively fast response time and low light attenuation, thus optimizing the timing resolution. The paddles are arranged so that the last 18 in each sector are

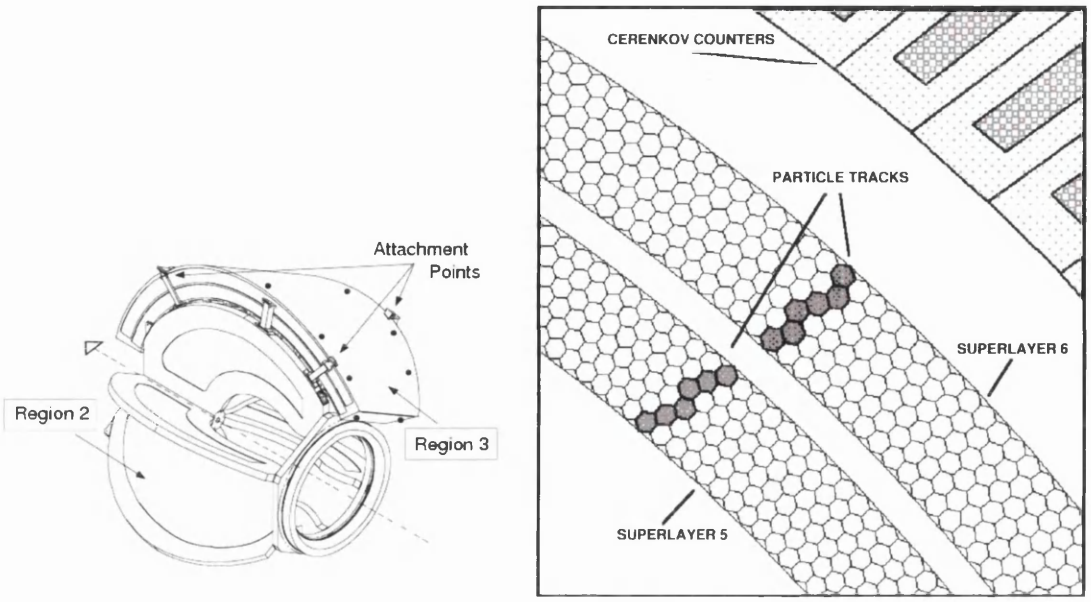

Figure 3.19: Region 2 and region 3 drift chambers (left) shown in their installed positions on the torus cryostat [85]. Particle track shown passing through two of the drift chamber superlayers (right).

coupled into 9 logical pairs, giving a total of 48 logical paddles per sector. Each scintillator has a uniform thickness of 5.08 cm and is positioned perpendicular to the average particle trajectory, such that its width subtends about 1.5^0 of scattering angle. Figure 3.20 gives a schematic representation of a TOF paddle arrangement. The large angle counters (greater than $\sim 70^0$) have a width of 22 cm while the forward counters are 15 cm wide, and the lengths vary from a maximum of 445 cm at large angles down to 32 cm in the forward direction. Each counter is also fitted with a photomultiplier tube (PMT) at either end. [69].

The timing resolution of each counter in the TOF system was measured with cosmic rays and for the shortest scintillators the resolution was found to be ~ 80 ps and ~ 150 ps for the longer counters. Each counter has its signal readout by a QDC and a pipeline TDC, and can be used to generate prompt signals for the CLAS level 1 trigger. This facility was utilized during the g8b run where the rates in the tagger were too high for it to be incorporated into the trigger, so the TOF was used instead. The TOF system was also used during the analysis to calculate the velocity of particles passing through CLAS by measuring the flight time between itself and the start counter. This calculated velocity, along with measured momentum from the drift chamber system, allows the particle's mass to be determined using the relation $p = \gamma mv$. As will be discussed in chapter 4, this TOF mass is used for the initial particle identification.

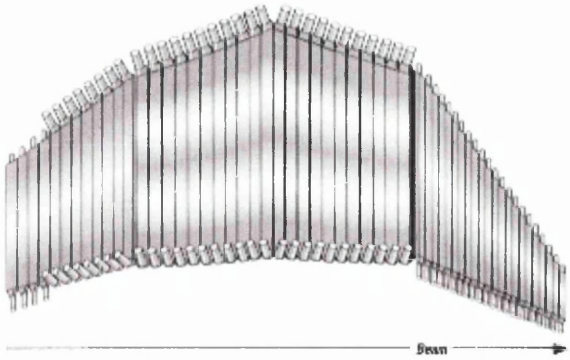

Figure 3.20: Schematic representation of a single sector TOF configuration.

3.5.6 Forward Electromagnetic Calorimeter

The forward electromagnetic ealorimeter (EC) is primarily used for the detection of and triggering on electrons at energies above 0.5 GeV, and the detection of neutral particles such as photons at energies above 0.2 GeV [85]. For g8b the system was also used for the reconstruction of π^0's and η's from the measurement of their 3γ decays. The system covers a polar angular range of $8^0 < \Theta < 45^0$ and consists of alternative layers of scintillator strips and lead sheets with a total thickness of 16 radiation lengths. Each scintillator layer is 10 mm thick and the lead has a thickness of 2.2 mm. A schematic layout of the EC lead-scintillator composition is shown in figure 3.21. There is an EC module for each sector of CLAS, and each one is contained within a volume having the shape of an equilateral triangle, allowing the system to cover the hexagonal geometry of CLAS. Each scintillator consists of 36 strips that are positioned parallel to one side of the triangle, with the orientation of each strip rotated by 120^0. This results in each module having three different rotations, or views (labelled U,V and W), where each view contains 13 layers. This recurring three plane configuration gives rise to stereo information on the position of the deposited energy in the scintillator. The calorimeter also utilizes a "projective geometry" layout, where the area of each successive layer increases linearly with distance from the centre of CLAS.

When a particle enters the EC it can interact with the scintillator-lead layer and lose energy by radiating a bremsstrahlung photon. This photon then induces the production of a e^+e^- pair which leads to more bremsstrahlung, thus producing an energy shower. To reconstruct a valid hit in the EC, the energy deposition is

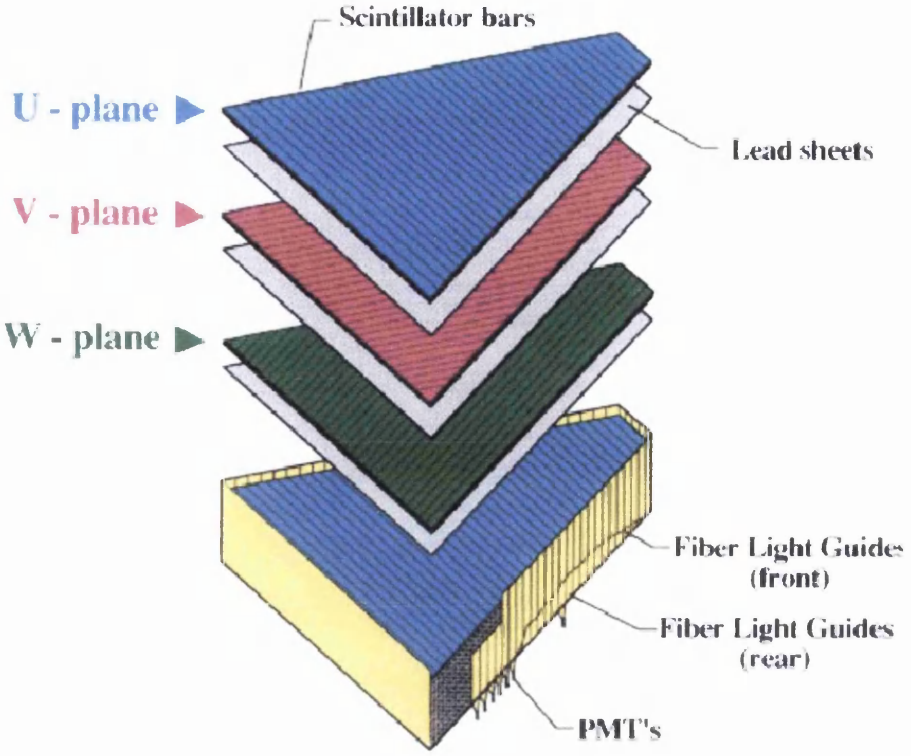

Figure 3.21: Diagram showing the three different views of the electromagnetic calorimeter. Each view contains 13 layers of scintillator.

required in all three views of a module. The energy and time of the hit can then be calculated by measuring the path lengths from the particle hit position to the readout edge.

3.5.7 Large Angle Electromagnetic Calorimeter

The Large Angle Calorimeter (LAC) is primarily used as an extension of the detection capability of the EC to more backward angles in sectors 1 and 2 only. The system tends to be utilized in experiments where there is a desire to study neutral particles at very backward angles. Similar to the EC, the LAC can detect scattered electrons and neutral particles such as photons coming from radiative processes. The LAC covers an azimuthal angle of 120^o, but only covers the polar angle from 45 to 75^o. The principle used for the detection of particles is the same as for the EC. The calorimeters are composed of lead-scintillator sandwiches, with the lead having a thickness of 2 mm and the scintillator a thickness of 15mm.

The complete system contains a total of 33 layers successively orientated at 90^0 to each other.

3.6 Beamline Devices

3.6.1 Beam Position Monitors

The Beam Position Monitors (BPMs) are used to monitor any shift in direction of electrons and/or photons along the beamline. This was important for g8b to ensure that the electrons are correctly incident on the diamond, and that the photons pass through the collimators. The BPMs are located in three different positions along the beamline, 2C21A is just upstream of the goniometer, 2C24A is just upstream of the tagger and 2H01A is downstream of the tagger [69]. The electron beam produces an induced current in wires adjacent to the beamline, and this current is measured by the BPM. The current varies with the position of the electrons and this allows the BPM to determine and record the position of the electron beam. This information is written into the data stream every two seconds.

3.6.2 Total Absorption Shower Counter

The total absorption counter (TASC) is located downsteam of CLAS and is primarily used to provide a method of normalizing the photon beam. The device uses four lead glass blocks to give an accurate determination of the beamline efficiency, thus allowing for a calculation of the number of bremsstrahlung photons that hit the target. Each block has a length of $\sim$ 17 radiation lengths and is coupled to a phototube, providing nearly 100% efficiency. The TASC can only operate effectively at beam currents of $\sim$ 100 pA which means that special TASC data runs have to be taken periodically during the experiment. These "normalization runs" were taken every time there was a change in running configuration for the coherent peak.

3.6.3 Pair Spectrometer

The Hall B Pair Spectrometer (PS) consists of an aluminium pair production converter, eight scintillator paddles and a large aperture dipole magnet. The

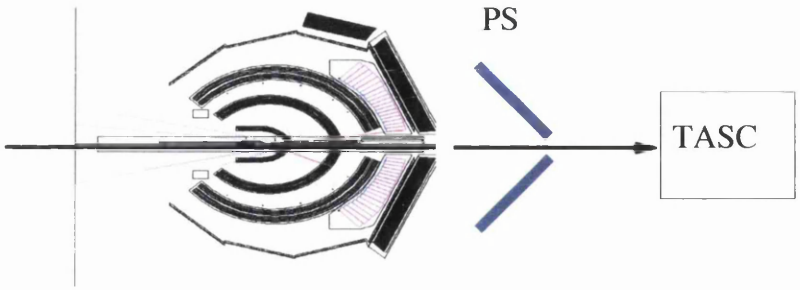

Figure 3.22: Relative positioning of the pair spectrometer and total absorption shower counter downstream of CLAS.

system is located 10 m downstream of the photon tagger radiator. The aluminium foil, which is 10^{-3} radiation lengths thick, is positioned 5.77 cm upstream of the dipole magnet within its magnetic field. The scintillators are positioned symmetrically either side of the beamline, and are arranged so that the PS is able to detect e^+e^- pairs over the full tagger energy range. The PS is also instrumented with 2 pairs of microstrip detectors covering an area of 400 mm^2. These microstrips allow for better determination of e^+e^- position.

The PS operates on the principle that when a photon interacts with the aluminium foil converter, it will produce an e^+e^- pair. The magnetic field then sweeps these pairs out of the beamline and into the spectrometer scintillator and microstrip detectors. The PS can then be used to determine the energy of the e^+e^- pair from their hit positions, and thus can be used to infer the energy of the interacting photon. The system can also be used to measure the photon flux at higher beam intensities than is possible with the TASC. During the g8b run the PS was also utilized for another function. By measuring the rate of e^+e^- pairs detected it was possible to infer if there was any shift in beam position. The PS magnet was tuned to the energy of the coherent peak, which allowed one to monitor that the linearly polarized photons were getting through the collimator. Any shift in the beam, or loss of coherent photons, could be detected from a change in the rates and energies of e^+e^- pairs produced. The relative positions of the pair spectrometer and TASC are shown in figure 3.22.

3.7 Trigger and Data Acquisition Systems

3.7.1 Trigger System

The trigger system for CLAS is essential to deciding when a particular event will be read into the data stream to eventually be analyzed. A variety of processes

such as electronic noise and cosmic rays passing through a detector element could produce a signal in a subsystem that does not correspond to a physics event. The CLAS trigger is therefore required to determine which set of signals correspond to a real physics process.

The CLAS trigger uses logic signals derived from the various detector subsystems to decide on whether to initiate the digitization and readout of QDCs and TDCs or perform a fast clear/reset. Depending on the event rates in the detectors and the system live time the trigger can be configured to be highly specific to a final state configuration of particles, or relatively open ended as was the case for g8b. This is implemented by 3 components: level 1 trigger, level 2 trigger and trigger supervisor. In brief, the level 1 trigger is initiated by the logic from the start counter and is configured to make a decision based on some combination of tagger master OR, TOF and start counter logic. It uses a lookup table to identify true charged particle tracks by checking for a match between hits in the TOF and hits in the start counter which correspond to the same sector. For g8b the requirement was relatively loose, demanding only a single charged particle.

The level 2 trigger uses tracking information from the drift chambers, looking for suitable particle tracks before declaring an event valid. The system is designed to give fast information on a physics event of interest in conjunction with the level 1 trigger, as well as providing a more stringent constraint on which events are read out. For example, a cosmic ray could trigger an event at level 1 but no track would be present in the drift chambers and this would cause level 2 to send a fast clear signal to all TDCs. This event would then not be read into the data stream.

The trigger supervisor takes all level 1 and level 2 trigger inputs and produces all common start and stop signals, busy gates and resets required by the detector electronics. The trigger supervisor can be customized to run in 2 different input configurations, one where only a level 1 input is required and one in which a level 1 input and level 2 confirmation is needed. In the first instance the supervisor generates the gate after receiving any level 1 signal. For the latter configuration a gate is again generated for a level 1 input but this time the supervisor waits a preset time for the level 2 confirmation. For g8b, the latter configuration was selected where a level 1 input and level 2 confirmation were required to validate an event.

3.7.2 Data Acquisition

The CLAS data acquisition system (DAQ) builds events into a format that can be used for analysis using the CODA system [90]. The DAQ receives data from the various detector systems and this is digitized into VME and FASTBUS crates in the hall before being collected by VME readout controllers [69]. These digitized values are then tabulated in such a way that each event is associated with a unique identity number. These data arrays, or event fragments, are then buffered and sent to an online acquisition computer (CLON10). At this point the event builder on CLON10 assembles the fragments and converts them into a BOS format [91, 92]. The event builder then passes the completed events on to the event transporter which transfers them to shared memory where they can be used for data monitoring or online analysis. Finally, the event recorder picks up all the events for permanent storage on the RAID array. From here the data can be transported to the Jlab tape silo where it becomes available for offline analysis.

For g8b the event rate was $\sim$ 4.5 kHz, with a livetime of $\sim$ 87%. The event rate for this run was not actually limited by the DAQ livetime but rather by the tagger, where some of the bases would malfunction if the rates within the coherent peak became too high. This resulted in g8b being run with a relatively low beam current of $\sim$ 10 nA.

3.8 Summary

The CEBAF accelerator utilizes superconducting technology to deliver a high luminosity, high quality electron beam to three different experimental halls at Jefferson Lab. These halls, with complementary detector set-ups, allow for a broad program of physics research to be undertaken at the lab. The coherent bremsstrahlung facility in Hall B enables one to produce a secondary, linearly polarized photon beam by scattering the electrons off a suitably orientated diamond radiator. Beamline devices such as the pair spectrometer and active collimator are then used to monitor and enhance the quality of this beam. This set-up in conjunction with the CLAS detector's high acceptance for charged particles make Hall B the ideal facility to study spin observables in strangeness photoproduction. Once these data have been collected by the data acquisition system, attention then turns to the process of off-line analysis.

Chapter 4

Data Analysis: Event Selection

This chapter describes in detail the event selection process used to identify the reactions

$$\vec{\gamma}p \rightarrow K^+\Lambda^0 \rightarrow K^+p\pi^-$$

$$\vec{\gamma}p \rightarrow K^+\Sigma^0 \rightarrow K^+\gamma\Lambda^0 \rightarrow K^+\gamma p\pi^-$$

in CLAS. In these reactions the Λ^0 decays into a p and a π^- 64% of the time, and into a n and a π^0 with a 36% branching ratio, while the Σ^0 radiatively decays decays into a Λ. Due to the low efficiency of CLAS for the detection of neutral particles, only the $p\pi^-$ mode will be analyzed. The methods used to correctly identify the particles of interest in CLAS will be carefully described, focusing on a semi-inclusive determination of the reactions through the identification of the K^+ and decay p. The Λ and Σ^0 are then reconstructed from the K^+ missing mass before the final yields are extracted. All procedures and cuts used in the particle identification will be discussed in the order in which they were used in the event selection. The complete analysis of the g8b data set was carried out on five different photon energy settings as well as on amorphous data that was taken periodically throughout the run. The following sections will detail the analysis of the 1.5GeV linearly polarized photon data set. The cuts and procedures used for this analysis, however, are the same for all the photon settings.

4.1 Initial Event Filter

The g8b dataset was accumulated to be used for the analysis of various reaction channels, not only $K^+\Lambda$ and $K^+\Sigma^0$. This meant that a fairly loose trigger condi-

tion was used during data acquisition, which accepted a variety of particle events that could be used in multiple proposed analyses. The end result of this was a data set of 11,475 files totalling $\sim$ 25TBytes of disk space, of which $K - \Lambda/\Sigma^0$ events contribute only a small percentage. This data was stored on the Jlab tape silo and simply retrieving it in its original form for analysis would not only use up a large amount of disk space but would also be very time consuming. Instead the dataset was filtered (or skimmed) using the ROOTBEER software package [93], into Data Summary Tapes (DSTs) that were specific to the $K^+\Lambda$ and $K^+\Sigma^0$ reaction channels. These skims reduced the data set down to $\sim$2% of the original size, and at this point the data was transferred over to Glasgow for permanent storage on a local RAID array, where it could be accessed for analysis. The process of reducing the data size and transferring it to Glasgow gave advantages in reduced CPU time required for analysis, as well as making the data easier to handle.

4.1.1 Hit Multiplicity and TOF Mass Cuts

The filtering process initially required a loose determination of the reaction products which identify the $K^+\Lambda$ and $K^+\Sigma^0$ channels. The efficiency of CLAS for detecting photons is low, so although the possibility of a photon being in the data was retained it was not explicitly required for the identification of the Σ^0 from its radiative decay. In addition the field settings used for g8b mean that the acceptance within CLAS for the negatively charged pion is lower than for the positively charged kaon and proton. For this reason a semi-inclusive search for the kaon and proton only was chosen as the best way of selecting the hyperon events, with the pion being determined from the missing mass $MM(pK^+)$.

The first step in the filtering was to only select events where 2, 3 or 4 particles were recorded in CLAS along with a valid tagger hit. Once an event had satisfied these criteria an initial identification of the particles was made using the mass calculated from the drift chambers and time-of-flight system (TOF mass). The following criteria were used to make the initial identification:

- Any particles with mass zero and charge zero were identified as photons
- All particles with non-zero mass and zero charge were removed
- All particles of non-zero charge must have a valid hit in the drift chamber and either TOF or EC
- For positive charge particles the following TOF mass windows were used for identification:

- $0.1 < M^2 < 0.49 GeV^2/c^4$ was a K^+
- $0.49 < M^2 < 1.44 GeV^2/c^4$ was a proton
- For negative charge particles the following TOF mass windows were used for identification:
- $0.0 < M^2 < 0.1 GeV^2/c^4$ was a π^-

Events were then retained which contained a proton and a kaon, and one or no pions as well as one or no photons. This would allow for a semi-inclusive search for the two hyperon channels. The possibility of explicitly detecting a pion was retained at this point in the event of the analysis being changed at a later stage to carry out an exclusive search for the hyperons.

Figure 4.1 shows the TOF mass for positively charged particles, along with the hit multiplicity for events which satisfy the initial selection criteria. As can be seen only events with either 2, 3 or 4 particles were retained, with the number of events decreasing as the number of requested particles increases. From figure 4.1 it is evident that the proton can be reasonably identified at this stage with a simple mass cut. It should be noted that the TOF mass resolution increases at lower momentum as shown in figure 4.2. However, it is clear that the mass window used in the proton selection is large enough so that no good proton events are discarded, even at low momentum.

The identification of the kaon is still preliminary at this stage as there is no clear distinction between positive kaons and pions. This issue of kaon-pion mis-identification provides one of the major difficulties with the analysis of CLAS data and will be addressed in section 4.3.5.

4.1.2 Fiducial Cuts

The next stage in the event filter was to implement fiducial cuts that excluded events from the analysis which occur in regions of the detector that have a non-uniform acceptance and are difficult to model. This allows for a more accurate calculation of the detector acceptance. This is of particular concern when attempting to extract hyperon recoil polarizations that require a correction of the detector acceptance to be made. These regions of non-uniform acceptance tend to occur where the particles interact with the coils of the torus magnet and at the edges of the drift chambers. For this analysis a relatively loose fiducial cut

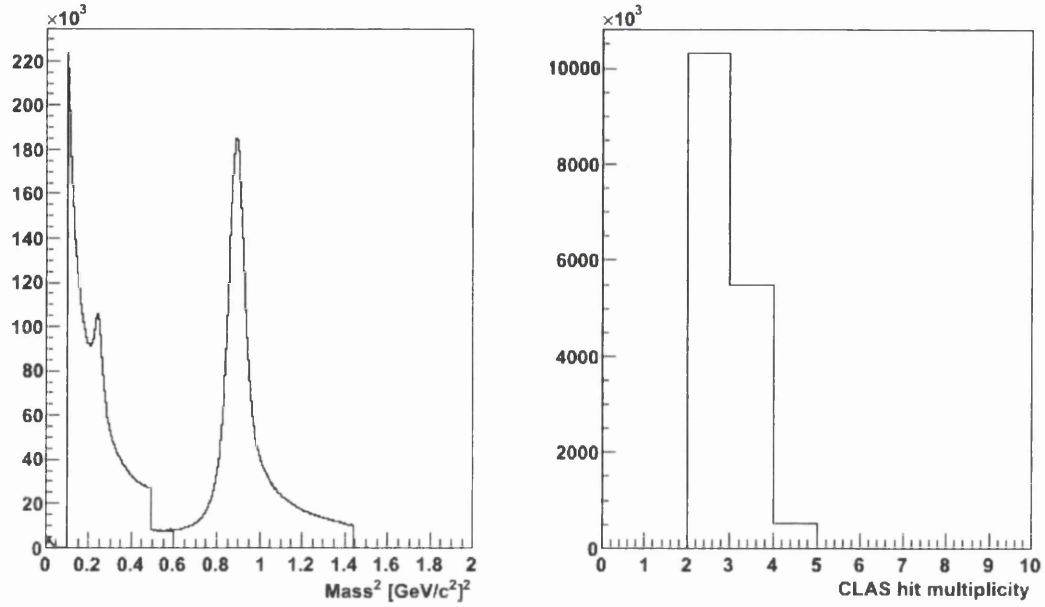

Figure 4.1: TOF mass (left) after simple selection criteria on number of particle events allowed. The multiplicity of hits (right) shows that only 2, 3 or 4 particle events are retained at this stage.

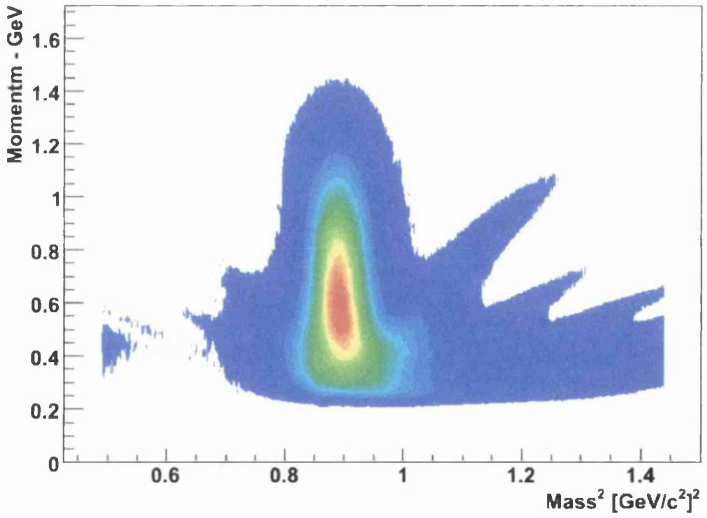

Figure 4.2: Mass vs Momentum in the region of the proton TOF mass. Despite the TOF mass resolution increasing at lower momenta, it is still well within the initial proton mass selection criteria of $0.49 < M(p) < 1.44$.

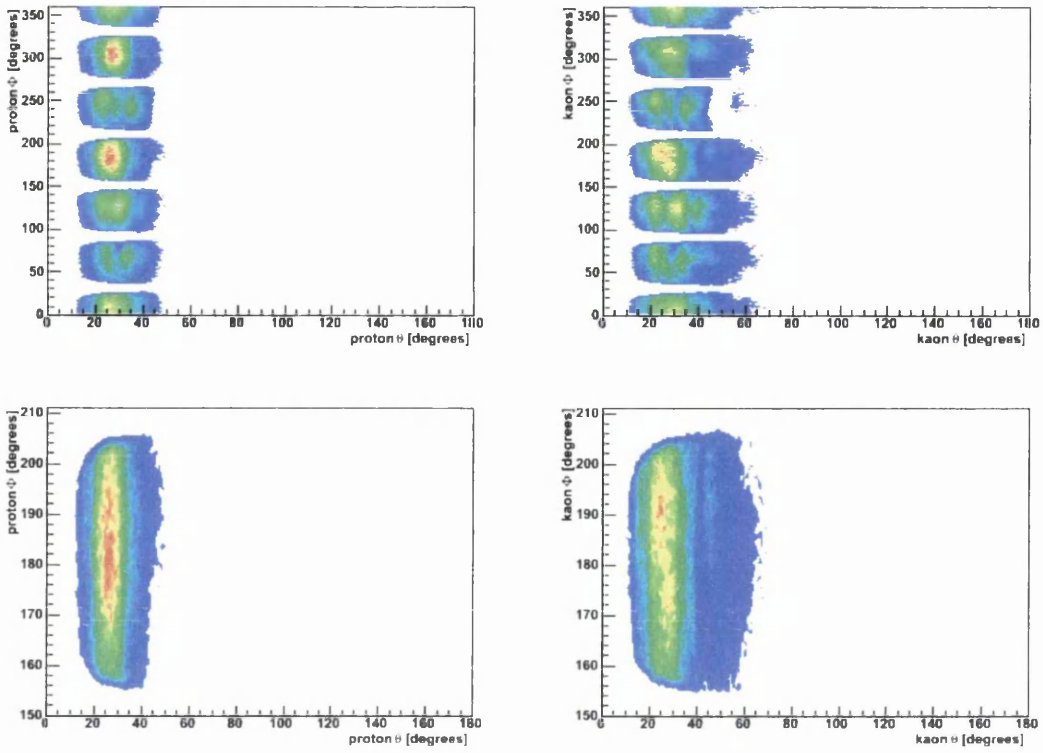

Figure 4.3: Top row shows θ versus Φ in the lab frame for the proton and kaon respectively before the application of any fiducial cuts. Bottom row shows θ versus Φ for one sector for both the proton and kaon after the application of fiducial cuts.

on the azimuthal distributions of $\pm 3^0$ at each sector division in CLAS was used. This cut was chosen to be the same for both protons and kaons, and its effect is shown in figure 4.3.

4.2 Energy Corrections

During the analysis the momentum of any charged particle measured by the drift chambers will be less than its original momentum at the production vertex. This is a result of energy being deposited by the charged particle in the target material (liquid hydrogen), target walls, support structures, beam pipe, start counter, and the air gap between the region 1 drift chambers and the target. These energy losses were corrected by the ELOSS package developed by Eugene Pasyuk [94]. The package operates by taking the 4-vector of the particle of interest, and running it through a series of subroutines to find the pathlength of

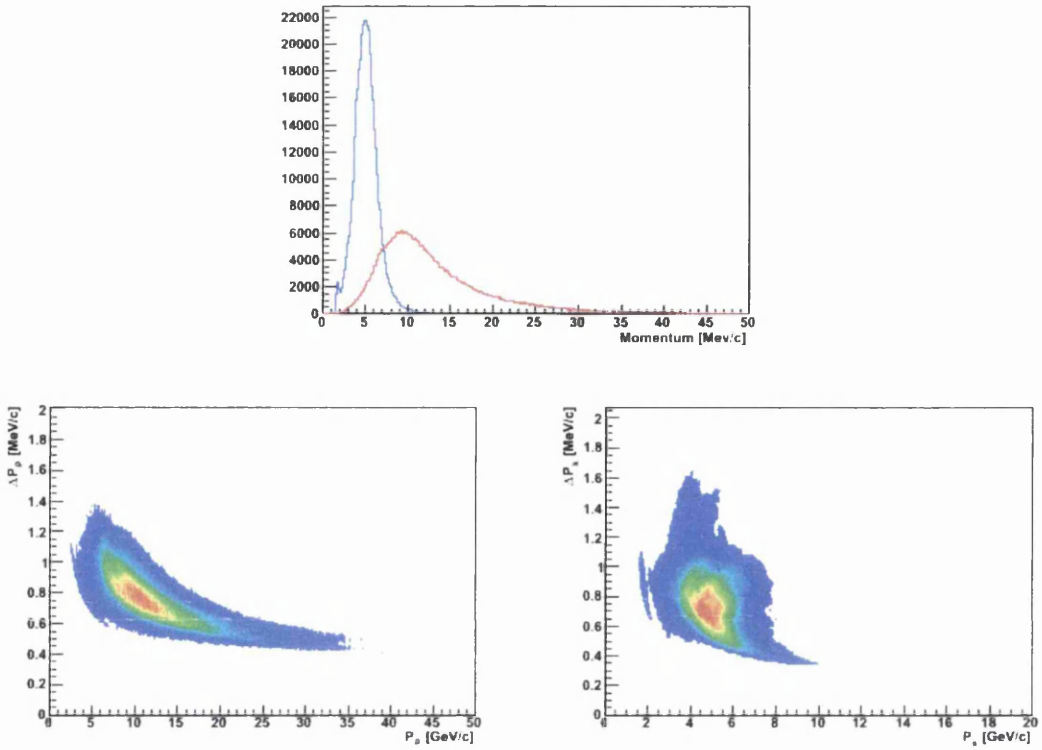

Figure 4.4: Top: Momentum correction distributions for the K^+(blue) and the p (red). Bottom Left: Δp v p for the proton. Bottom right: Δp v p for the kaon.

the particle in each of the materials along the track. The software determines the momentum of the particle at the reaction vertex and can be used for any charged particle heavier than an electron.

The energy losses for the kaon and proton in this analysis are shown in figure 4.4. As can be seen the energy losses are most significant for low momentum particles resulting in the the greatest correction required.

4.3 Particle Identification

4.3.1 Z-Vertex Cut

The first step in the particle identification was to cut on the z-vertex distribution of each particle to be within the target geometry. For g8b this meant a cut of between 0 and -40cm, which represents a relatively tight cut. Figure 4.5 shows the z-vertex distributions for the proton and kaon respectively with lines superimposed to show the cuts.

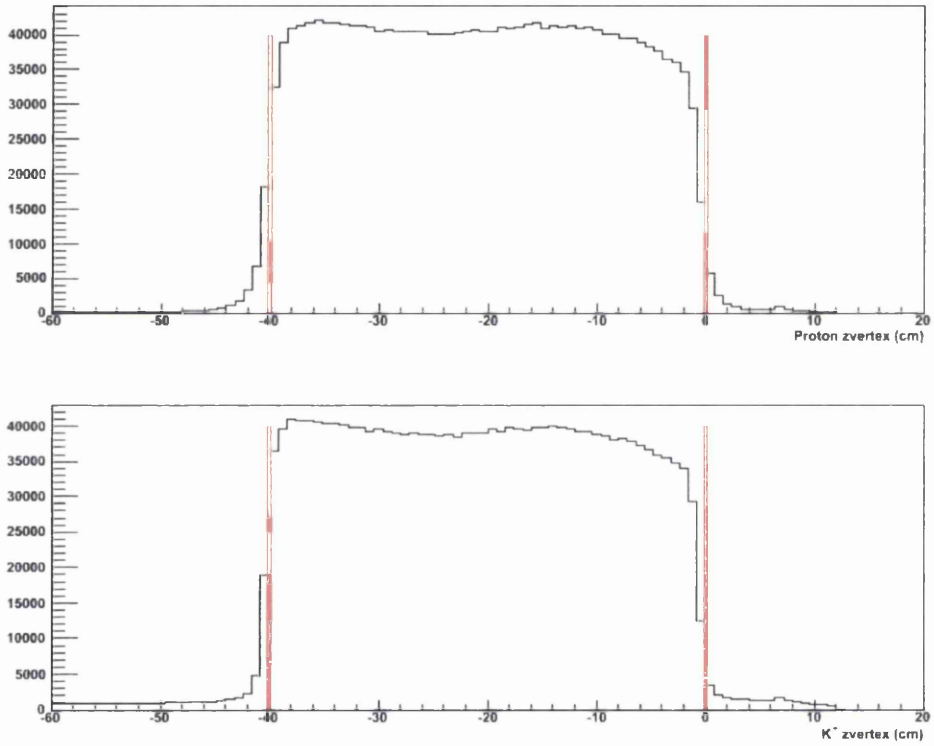

Figure 4.5: Z-vertex distributions of the proton(top) and kaon(bottom) showing the target geometry along with the applied cuts (red lines).

4.3.2 Photon Selection

The next stage in the selection process was to determine the time at which a physics event took place by matching photons to the hadronic tracks within CLAS. To achieve this, information on the hadronic vertex time provided by the TOF was used. The timing information from charged particles detected by the TOF was extrapolated backwards to provide information on when the event occurred. If the TOF and tagger timing calibrations are well defined then the tagger and TOF vertex times are expected to be identical. This is shown to be the case in figure 4.6 (left) where the majority of events have the vertex timing difference between tagger and TOF centered on zero. The 2ns beam bucket structure corresponds to hadrons that have been miscorrelated to random photons. This mismatching of certain hadrons will be addressed in section 4.3.7 where momentum dependent timing cuts will be applied to reject the out-of-time combinations. A major area of ambiguity in the selection of the real interaction photons is that for many physics events there are multiple photons recorded. In order to select the actual photon corresponding to the event, the photon whose time is closest to the hadronic vertex time is chosen. The identification of this "best" photon involves minimizing the difference (Diff) between the proton vertex time and the photon time using the relation:

$$Diff = (TOFtime(p) - (TOFpath(p)/c \times \beta_c(p))) - (\gamma_{time} + (z(p)/c)) \quad (4.1)$$

where:

$$\beta_c(p) = p(p)/\sqrt{p^2(p) + m^2_{pdg}(p)} \quad (4.2)$$

using the PDG mass for the proton and the measured momentum.
Where:

$TOFtime(p)$ = proton TOF time

$TOFpath(p)$ = proton path length to the TOF

γ_{time} = event photon vertex time

$z(p) = z - vertex$ position of the proton

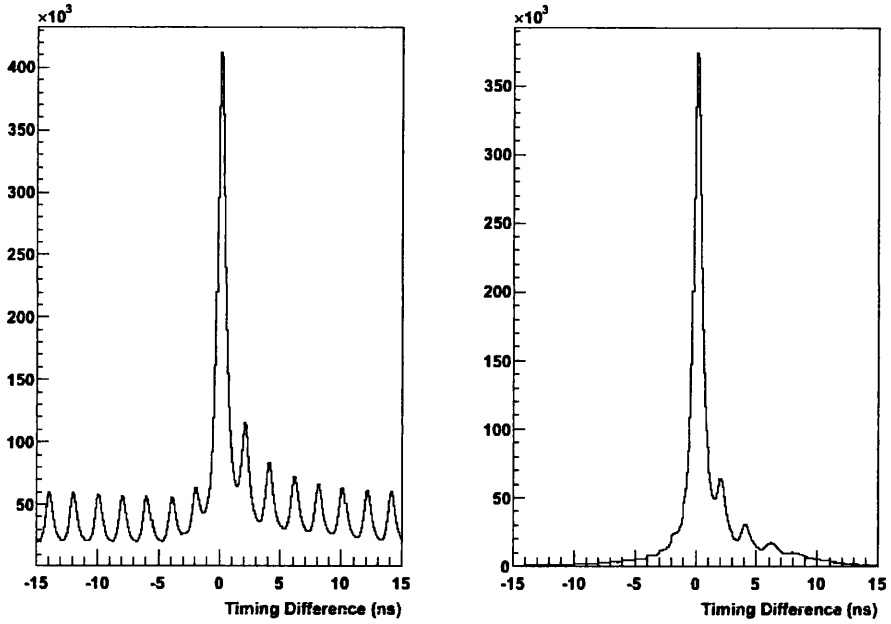

Figure 4.6: Tagger vertex time subtracted from the time-of-flight vertex time. The plot on the left displays events before best photon selection with the 2ns beam bucket structure clearly evident. The plot on the right displays the vertex time after the photon selection. The asymmetric structure on the right side of the vertex timing peak will be dealt with when momentum dependent timing cuts are applied later in the analysis.

$$c = \text{speed of light}$$

Figure 4.6 (right) shows the timing difference after the selection of the best photons using the process outlined above. The plots show a slight asymmetry in the distribution which is due to the proton vertex time having a momentum dependence. This asymmetric distribution will also be resolved when momentum dependent timing cuts are made for the proton and kaon.

4.3.3 $p(\gamma, K^+p)\pi^-$ - Missing Mass Cut

At this point a cut was applied to the $p(\gamma, K^+p)\pi^-$ missing mass to select events that were consistent with a missing pion. As the reactions are exclusive, the missing mass $MM(pK^+)$ calculated from the 4-vectors of the proton and kaon should correspond to the mass of a π^-. This step was carried out before any attempt was made to extract the hyperon yields or to remove mis-identified charged particles and this results in a large background for the $MM(pK^+)$. The actual cut

was carried out on the missing mass squared which is plotted in figure 4.7 (left) with its momentum dependence shown in figure 4.7 (right). A peak can clearly be seen corresponding to the π^- from the $K^+\Lambda$ channel with a mass squared of $0.0185 GeV^2/c^4$. The peak for the π^- from the $K^+\Sigma^0$ channel is shifted to a slightly higher mass squared of $0.045 GeV^2/c^4$ due to there being an undetected photon in this reaction. A third peak can also be seen corresponding to the mass squared of a K^-, which will be removed by the subsequent analysis cuts. At this stage a fairly loose cut was placed on the $MM^2(pK^+)$:

- -0.2 $< MM^2(pK^+) <$ 0.3 GeV^2/c^4.

This cut was originally much tighter but studies demonstrated that a large number of good $K^+\Lambda$ and $K^+\Sigma^0$ events were being rejected. It was therefore decided that the cut should be loosened slightly to allow for a more liberal selection of events. Although this loosening of the cut would allow more background through at this stage it was felt that subsequent cuts in the analysis would compensate for this, allowing for an undiluted final yield.

4.3.4 $p(\gamma, K^+)Y$ - Missing Mass Cut

Another criterion in the selection of good events was that the missing mass recoiling against a potential kaon - $MM(K^+)$ - should be consistent with a hyperon. This missing mass was calculated from the kaon's momentum 4-vector for which the spectrum is plotted in figure 4.8 (left) along with its momentum dependence (right). Any events where the mass lay between 1.07 and 1.22 GeV/c^2 were accepted as potential hyperon events. This represented a relatively tight cut but as can be evidenced from the momentum distributions the hyperon peaks do not broaden much as their momenta increases. In addition, subsequent yield extraction methods will use much tighter 3σ cuts to extract the final hyperons.

4.3.5 Misidentification of Charged Particles

4.3.5.1 Invariant Mass Selection

One of the major sources of dilution of extracted particle yields from CLAS is the misidentification of charged particles - in particular pions that have been

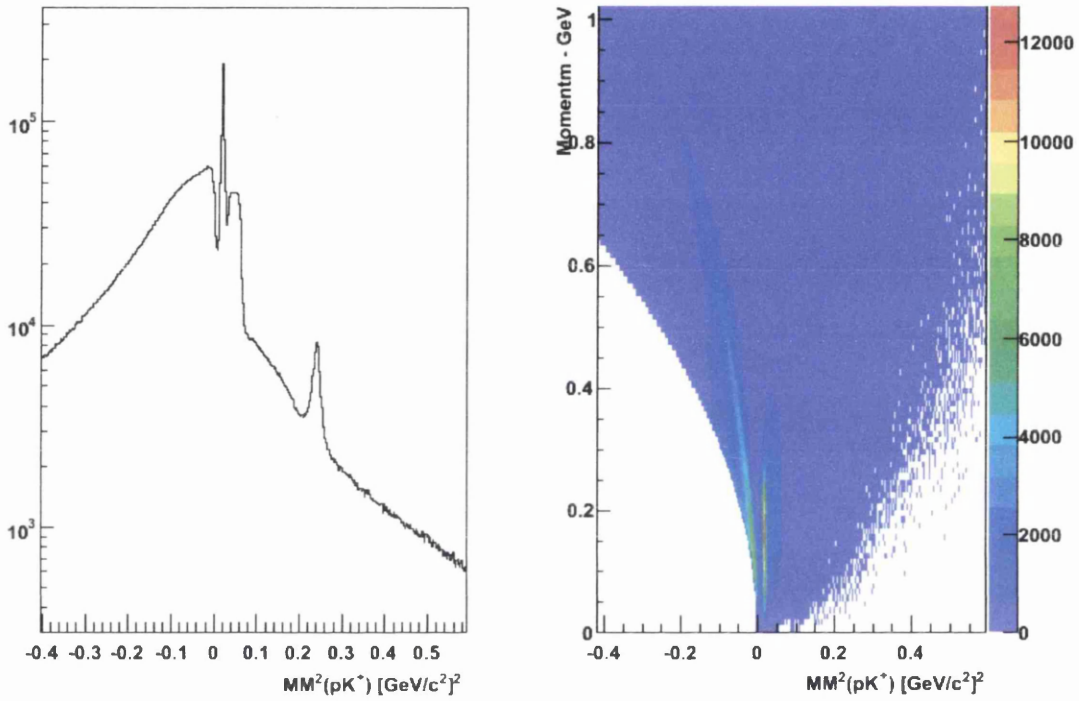

Figure 4.7: $MM^2(pK^+)$ before any selection is made for the recoiling hyperons shown on the left. A peak corresponding to the missing mass squared of the π^- is clearly evident at $0.0185 GeV^2/c^4$ with the π^- from the Σ^0 decay shifted to a slightly higher mass due to the presence of an undetected photon. A peak is also evident for the K^- at a squared mass of $0.240 GeV^2/c^4$ which although not removed by the $MM^2(pK^+)$ cut, will be accounted for in subsequent analysis cuts. The momentum dependence of the missing mass is plotted on the right. A cut is applied to only accept events with a missing mass squared between -0.2 and 0.3 GeV^2.

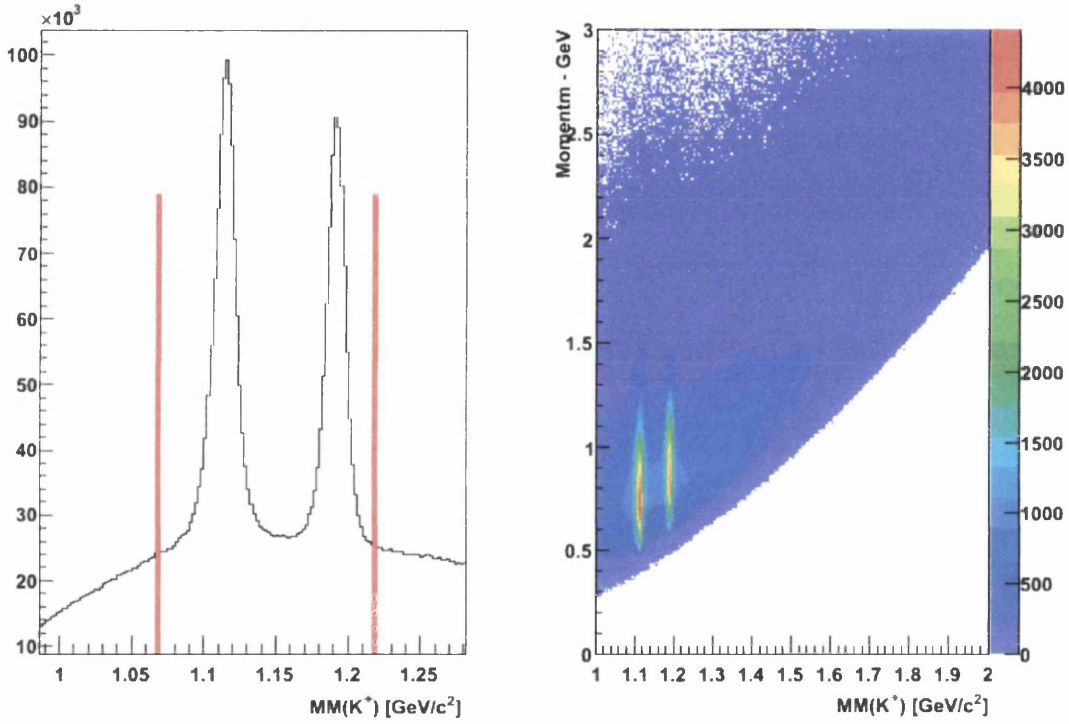

Figure 4.8: $MM(K^+)$ showing clear peaks at the Λ and Σ^0 masses corresponding to potential hyperons recoiling against the K^+ with the analysis cuts superimposed. The momentum dependence of the missing mass spectrum is plotted on the right.

identified as kaons. This problem was illustrated in figure 4.1 where the kaon mass peak sits on a large pion shoulder. One method of separating these mesons involves looking at a two dimensional plot of the $MM(K^+)$ against the invariant mass of the proton and pion from the hyperon decay. Since the pion is not explicitly detected in this analysis we use the 4-vector calculated by subtracting the 4-vectors of the kaon and proton from the target and photon. In the case of a perfect exclusive particle determination this would correspond to the pion 4-vector. We thus assume perfect particle identification and give this 4-vector the π^- PDG mass before plotting it against the $MM(K^+)$ as shown in figure 4.9.

In the two-dimensional plot there is good agreement for the mass of the Λ^0 and Σ^0, with the Σ^0 mass slightly smeared due to the undetected photon from its radiative decay. In the plot the misidentified pions show as a diagonal band as the $MM(K^+)$ increases. This is due to the reaction no longer being exclusive if a π^- is identified as a K^+ , and therefore the reconstructed mass of the Λ^0 must increase to account for the extra mass that has been detected. Hence a cut to only select events with a corresponding invariant mass of between 1.08 and 1.20GeV is imposed to remove the effect of misidentified pions.

4.3.5.2 $p(\gamma, \pi^+ p)X$ - Missing Mass

Another procedure to correct for particle misidentification is to explicitly make the assumption that pions have wrongly been identified as kaons. In order to remove these events for the K^+p final state the 4-vector for each particle is re-calculated using the measured momenta and by allocating the PDG value of the mass. The missing mass of the K^+p is then plotted, assuming correct particle identification, against the missing mass assuming misidentification. For misidentified events the correct particle momenta is retained in the 4-vector but the mass is changed to the PDG mass of the assumed misidentified particle.

Explicitly the $MM(K^+p)$ is assumed to have one possible misidentification permutation where the identified K^+ is in fact a π^+. Therefore what we are in fact reconstructing is the missing mass $MM(\pi^+p)$. The plot on the left of figure 4.10 shows $MM(K^+p)$ versus $MM(\pi^+p)$, with two peaks corresponding to correctly identified $K\Lambda$ and $K\Sigma^0$ events over a large background. In the right hand plot one can see the same distribution but this time after the application of the invariant mass cut from section 4.3.5.1. This illustrates the effectiveness of the invariant mass cut in removing the background of misidentified particles.

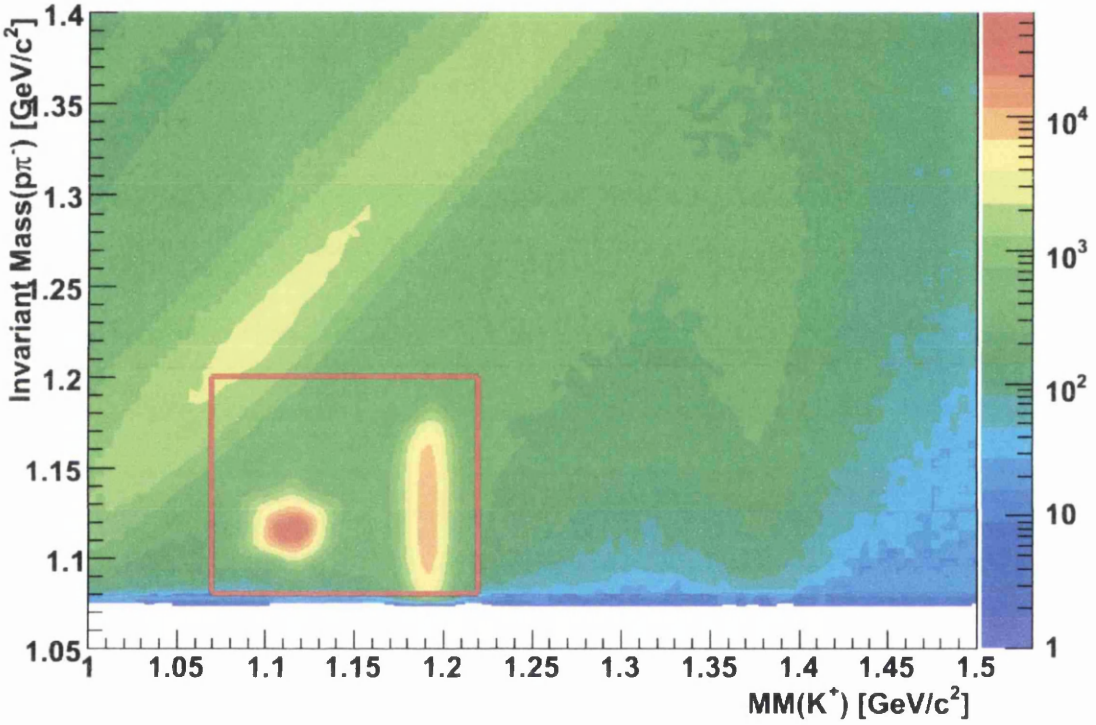

Figure 4.9: $MM(K^+)$ versus Invariant Mass $(p\pi^-)$ showing two clear peaks corresponding to Λ and Σ^0 events. The analysis cuts for the invariant mass and the $MM(K^+)$ are superimposed. The diagonal band corresponds to pions that have been identified as kaons.

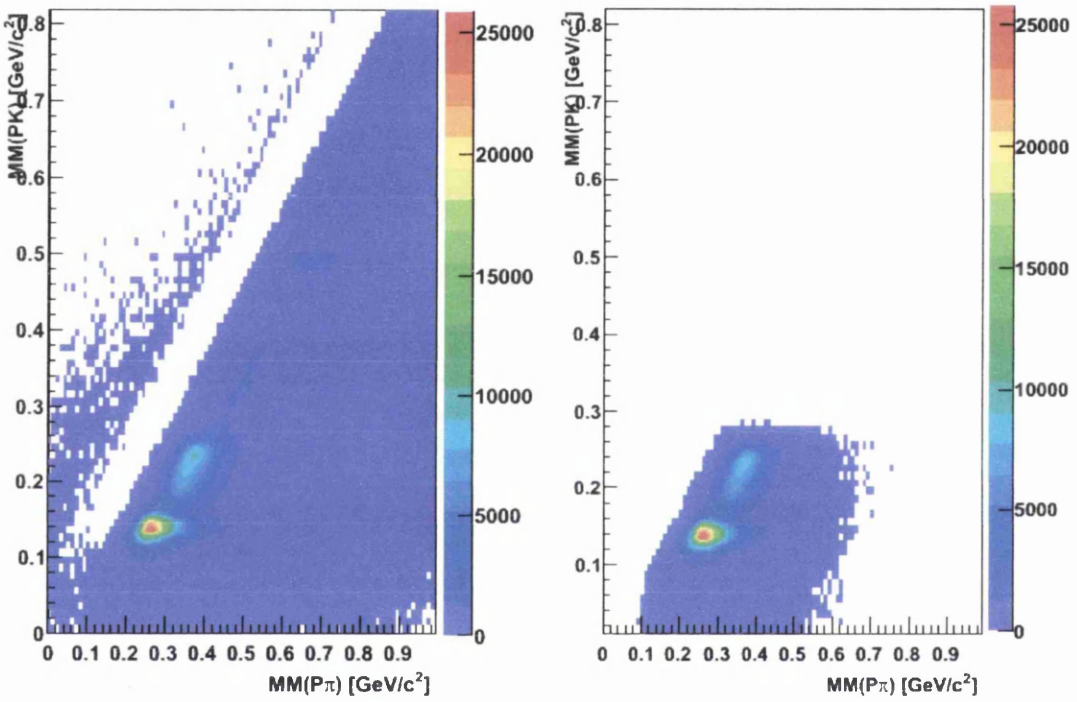

Figure 4.10: $MM(pK^+)$ versus $MM(p\pi^-)$ before (left) and after (right) the cut is made on the invariant mass of the $p\pi^-$. The left plot shows the two peaks corresponding to Λ and Σ^0 events on top of a large background that is mostly removed in the right plot. This illustrates how successful the invariant mass is in removing the effects of background and misidentified particles.

4.3.6 Minimum Momentum Cut

At this stage a cut was made on the minimum momentum of any track that would be considered as an event in the particle selection process. This cut was selected to be the same for all charged particles - 300MeV/c which corresponds to the minimum detection momentum in CLAS.

4.3.7 Hadron - Photon Vertex Timing Cuts

The next stage of the analysis involved imposing timing cuts on the hadron-photon vertex time. As outlined in section 4.3.2, a well defined set of calibrations should provide good agreement between the photon vertex time from the tagger and the hadronic vertex time from the TOF. Figures 4.11 and 4.12 show that the hadron-photon vertex time distribution for the proton and kaon respectively have a substantial momentum dependence. After selecting the best photon, a fairly loose ± 2 ns cut was used to remove events from other beam buckets which could act to dilute the final hyperon yield. Now however, a more rigorous series of momentum dependent $\pm 3\sigma$ cuts are applied to the vertex times when fitted in 100 MeV/c momentum bins.

Figure 4.11 shows the proton-photon vertex and its dependence on the proton momentum. It also shows the vertex time after the momentum dependent cuts have been applied, along with the mean and sigma values from the fits. The fits themselves were simple gaussians on top of a first degree polynomial. The momentum dependence of the kaon vertex time is shown in figure 4.12, with the final vertex after the application of the $\pm 3\sigma$ cuts.

4.3.8 Hyperon Yield Extraction

The final stage in the event selection process involved extracting the yield for the reaction channels $\vec{\gamma}\mathrm{p} \rightarrow K^+\Lambda$ and $\vec{\gamma}p \rightarrow K^+\Sigma^0$. These yields were extracted after the kaon identification and subsequent rejection of misidentified charged particles by performing a minimum chi squared fit of the kaon missing mass. Originally a double Gaussian on top of a flat background was chosen as the fitting function along with a subsequent sideband subtraction routine to remove any background. This fitting algorithm was used while the event selection process was

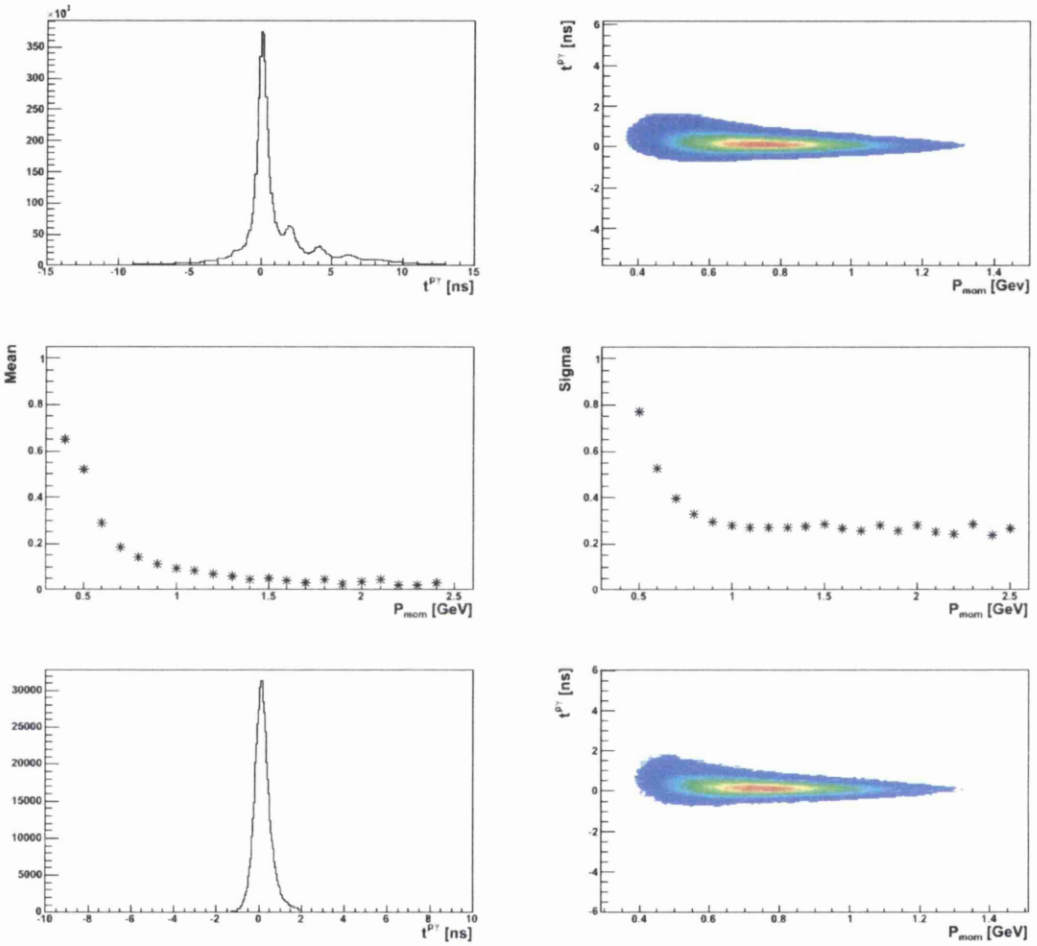

Figure 4.11: $t_v^{p\gamma}$ plotted on the top left showing some asymmetric 2ns structure with its momentum dependence plotted on the top right. $t_v^{p\gamma}$ and its momentum dependence are then plotted on the bottom row after 100MeV/c momentum cuts have been applied. The momentum dependence of the mean (left) and sigma (right) of the vertices are shown quantitatively in the middle row.

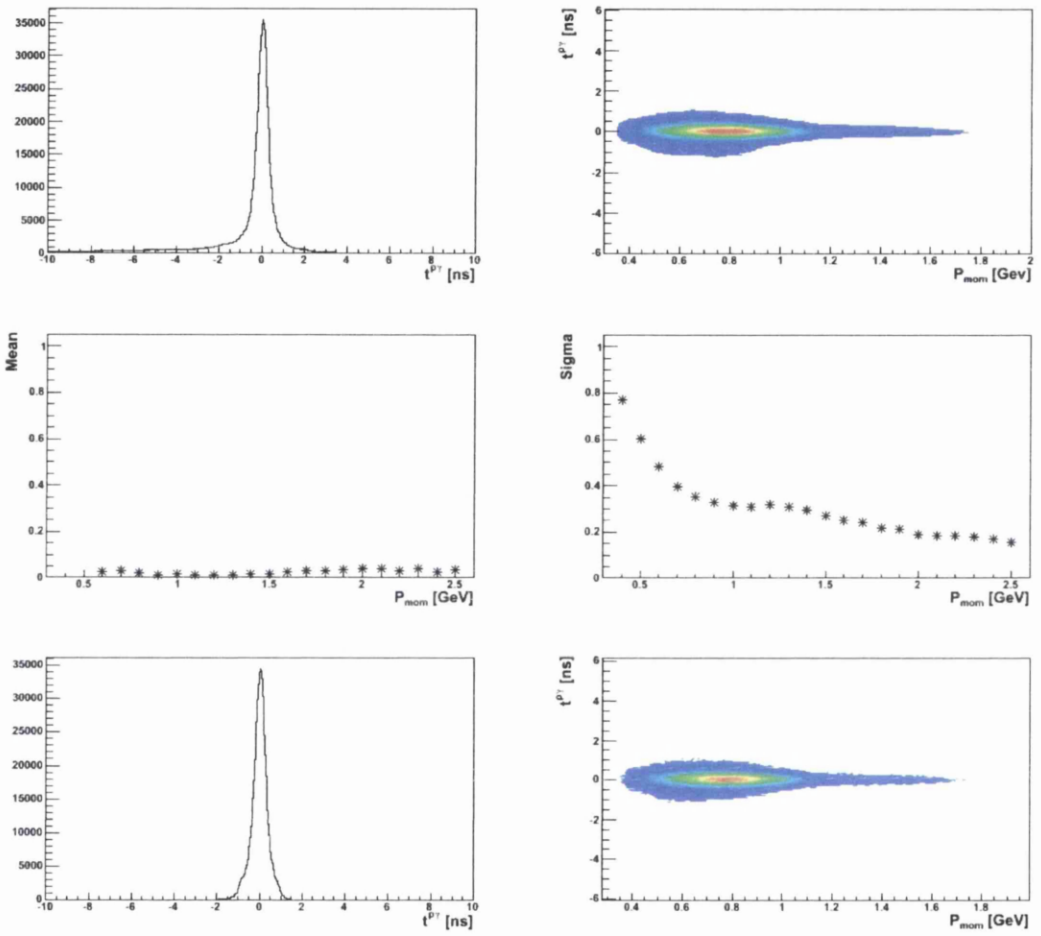

Figure 4.12: $t_v^{K\gamma}$ plotted on the top left with its momentum dependence plotted on the top right. $t_v^{K\gamma}$ and its momentum dependence are then plotted on the bottom row after 100MeV/c momentum cuts have been applied. The momentum dependence of the mean (left) and sigma (right) of the vertices are shown quantitatively in the middle row.

still in its infancy and the kaon missing mass distribution had a relatively large background with significant overlap between the two kaon peaks. Later refinements to the the event selection largely removed this background, and subsequent studies demonstrated that a sideband subtraction was no longer necessary.

It was then decided that a simple single Gaussian fit of each potential hyperon mass should be sufficient to give a reliable, accurate and clean extraction of the final yield. To this end a selection was made on the kaon missing mass such that any mass above 1.15 GeV would be considered a potential Σ^0, and any mass below 1.16 GeV a potential Λ. At this stage a Gaussian was fitted to the missing mass spectra in 100 MeV/c momentum bins. The results are shown for the Λ in figure 4.13 with the respective plots for the Σ^0 shown in figure 4.14. Figure 4.15 shows the Λ mass before the chi-squared fitting (top left) along with its momentum dependence (top right). Also shown are the mean values of the fits with their momentum dependence (bottom left) along with the σ-values from each fit (bottom right). All events within 3σ of the mean value were accepted as final events. The corresponding plots for the Σ^0 are shown in figure 4.16.

The mass of the final extracted hyperon yield integrated over all kinematic bins is shown in figure 4.17. This plot demonstrates that the final hyperons have negligible background and overlap between the Λ and Σ^0 . This was confirmed by studies of preliminary photon asymmetry and recoil polarization results where the cuts and extraction methods were investigated to see what dilution effect they may have on any final results. These tests all confirmed that no significant background was being allowed into the final yield by the cuts outlined above. These studies also provide a good estimate of any systematic uncertainty in the final result from the yield extraction process.

4.4 Summary

A sophisticated and detailed analysis algorithm was developed to allow for the identification of the particles of interest and the extraction of final yields for $\overrightarrow{\gamma}$p$\rightarrow$ $K^+\Lambda^0$ and $\overrightarrow{\gamma}p \rightarrow K^+\Sigma^0$. Initial filters based on simple TOF mass and fiducial cuts were used to skim the dataset down to a manageable size for full analysis. Various cuts were then implemented to reduce the background and correctly identify kaons, without discarding too many good events. The final hyperon mass plots demonstrate the success of these procedures with negligible background and overlap between the two hyperon yields. Any systematic uncertainty from

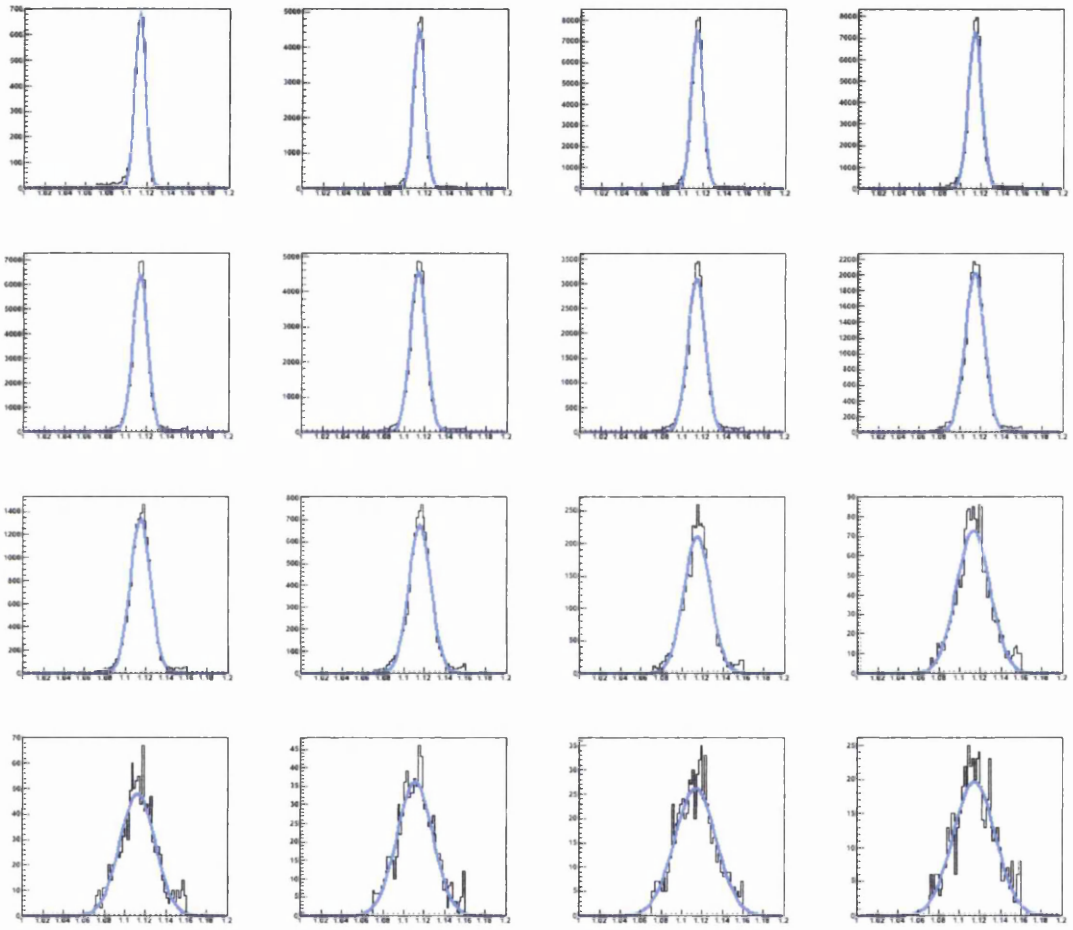

Figure 4.13: Plots showing the Gaussian fits to potential Λ events from the $MM(K^+)$. Each histogram is binned in 100 MeV/c momentum bins ranging from 0.5 GeV/c (top left) to 2 GeV/c (bottom right). All events outside this momentum range were extracted by a single integrated Gaussian fit.

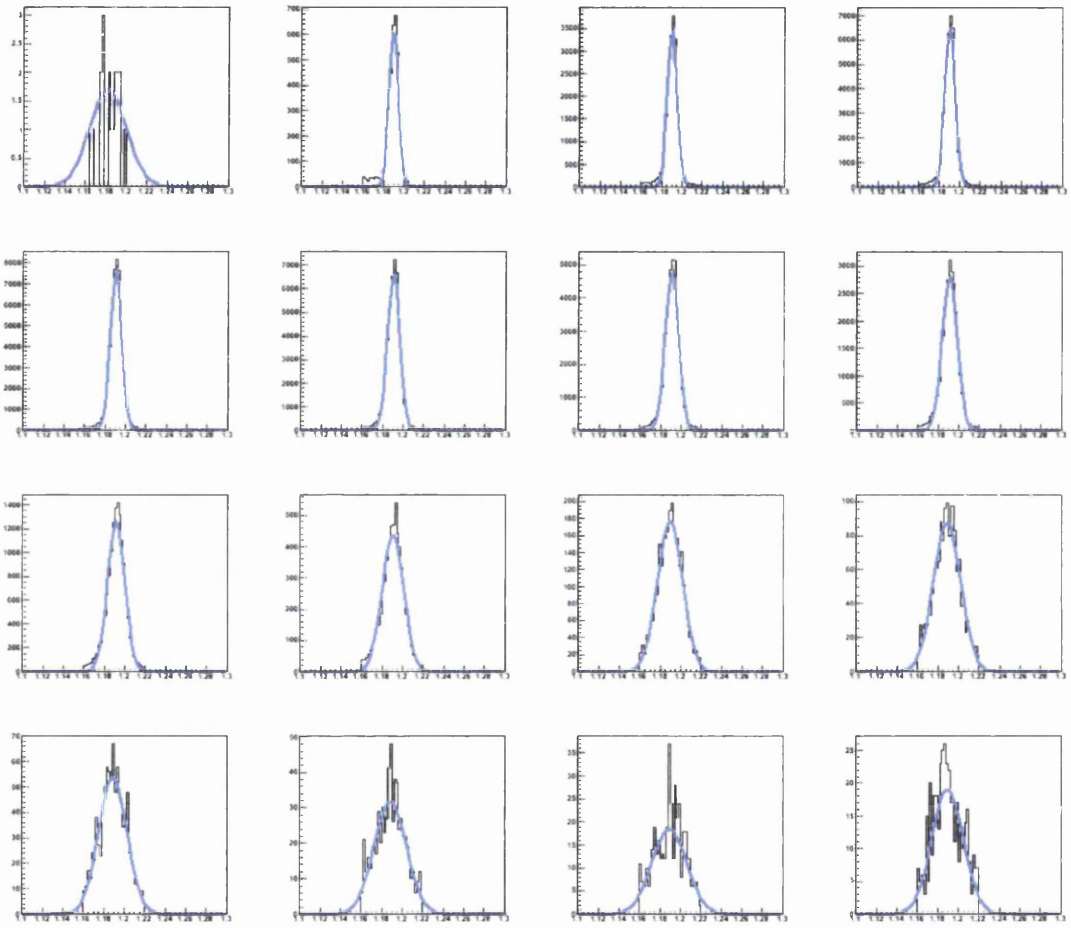

Figure 4.14: Plots showing the Gaussian fits to potential Σ^0 events from the $MM(K^+)$. Each histogram is binned in 100 MeV/c momentum bins ranging from 0.5 GeV/c (top left) to 2 GeV/c (bottom right). All events outside this momentum range were extracted by a single integrated Gaussian fit.

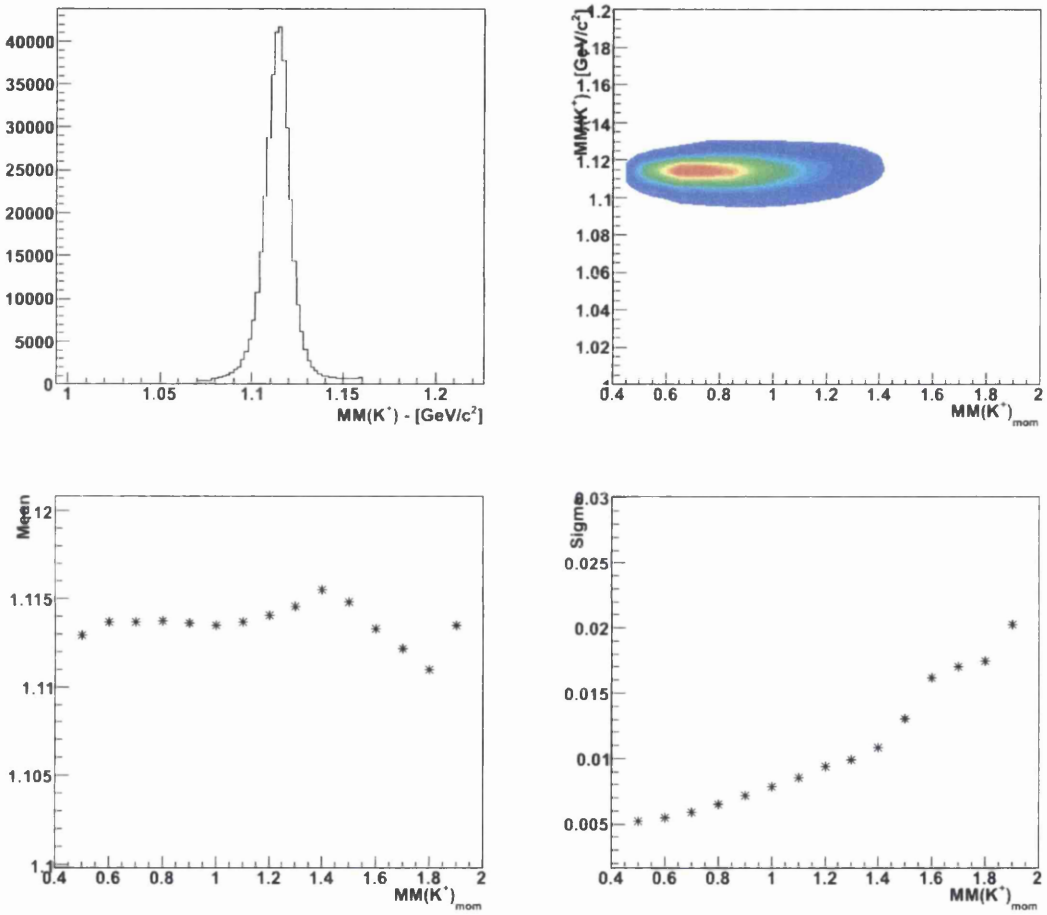

Figure 4.15: Λ mass after the yield extraction process (top left) along with its momentum dependence (top right). Bottom row shows the quantitative momentum dependence of the Λ mean (left) and sigma (right).

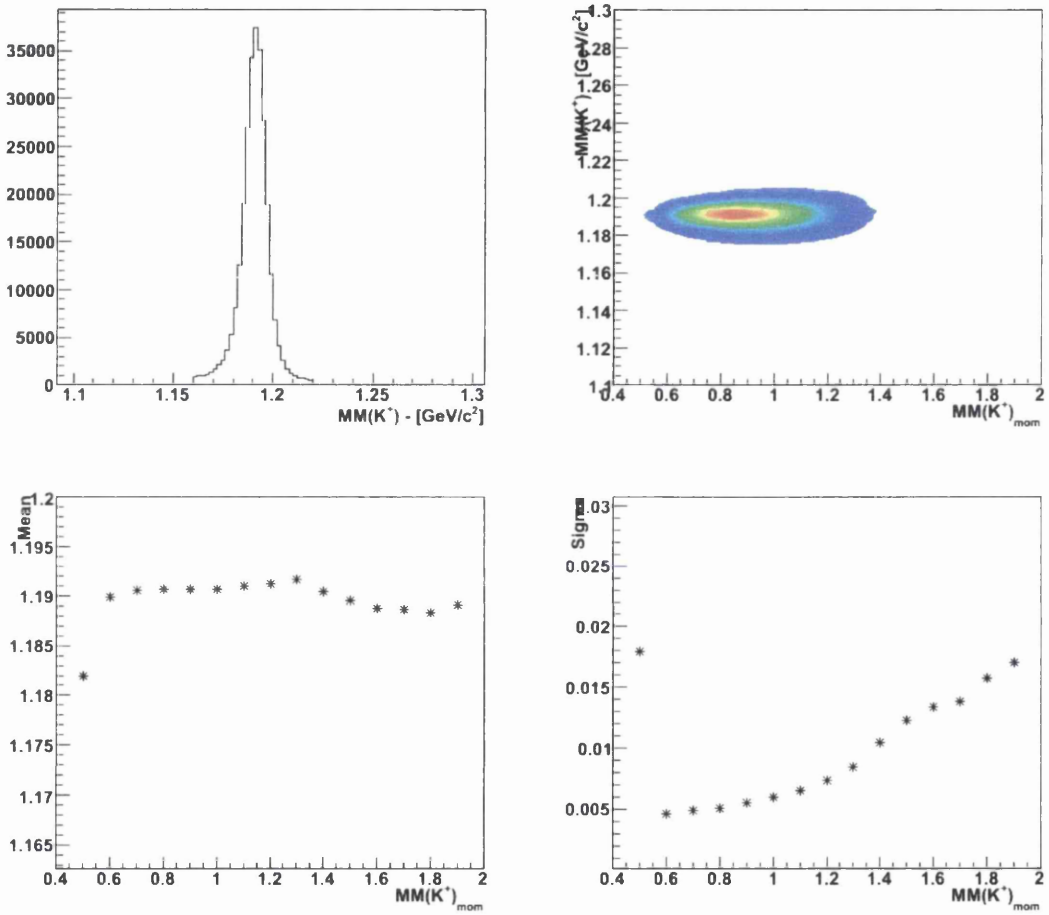

Figure 4.16: Σ^0 mass after the yield extraction process (top left) along with its momentum dependence (top right). Bottom row shows the quantitative momentum dependence of the Σ^0 mean (left) and sigma (right).

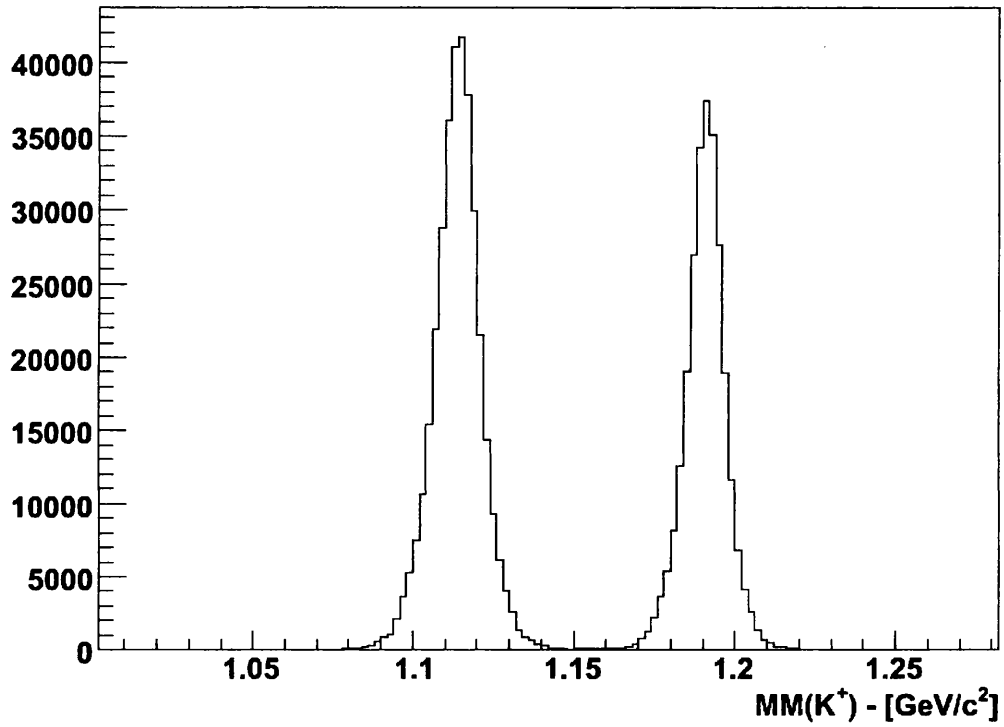

Figure 4.17: Final Hyperon mass after the yield extraction process. Both the Λ and Σ^0 masses agree to within 1 MeV of the PDG value. The plot also shows that there is very little background and overlap between the hyperon events.

the event selection process was studied by varying the implemented cuts and analyzing the effect this had on the final polarization results. In particular, if the photon aymmetry values systematically decreased then this was interpreted as the analysis cuts allowing extra background into the final yields. These studies estimated the systematic uncertainty to be less than 2%. Overall, the event selection routine was very successful in allowing the extraction of a clean final hyperon yield. Attention will now be paid in the following two chapters to the methods used to extract physics results from this dataset.

Chapter 5

Data Analysis: Extraction of Σ, O_x and O_z

Having established the event selection and yield extraction processes required to identify the reactions $\overrightarrow{\gamma}\mathrm{p}\rightarrow K^+\Lambda$ and $\overrightarrow{\gamma}p \rightarrow K^+\Sigma^0$ within CLAS, attention is now turned to the extraction of the various polarization observables. This chapter will outline the methods used to extract the photon asymmetry along with the double polarization observables O_x and O_z from the data set. The kinematics of the $K\Lambda$ reaction along with the selected coordinate system are illustrated in figure 1.7. As explained in Chapter 1, the unprimed coordinate system, where the z-axis is taken to be along the momentum direction of the incident photon beam, was chosen to present the final polarization results. This system was chosen because it will be shown that most of the hyperon polarization is preferentially transferred along $\hat{z}$, as defined in figure 1.7.

The results will be extracted for as wide a range of $\theta_{cm}^{K^+}$ and E_γ bins as possible and the choice of final bin widths used to present the results will be discussed. This Chapter will also outline the methods used to obtain the degree of photon polarization as well as estimating the systematic uncertainty associated with this measurement.

5.1 Measurement Method

The analysis strategy for the extraction of the photon asymmetry, Σ, along with the double polarization observables, O_x and O_z, requires a measurement of the x and z-components of the hadron polarization. These were derived in Chapter 1 and have the following form:

$$P_x = -\frac{P_\gamma^{lin} O_x sin2(\Phi)}{1 - P_\gamma^{lin} \Sigma cos2(\Phi)} \tag{5.1}$$

$$P_z = -\frac{P_\gamma^{lin} O_z sin2(\Phi)}{1 - P_\gamma^{lin} \Sigma cos2(\Phi)} \tag{5.2}$$

where P_γ^{lin} is the degree of linear polarization and Φ is the kaon azimuthal angle. As detailed previously, the recoil polarization of a hyperon in kaon photoproduction can be measured through its weak parity violating decay. The angular distribution, $I_i(cos\theta_i)$, for the decay products in the hyperon rest frame can be related to the polarization components by

$$I_i(cos\theta_i) = \frac{1}{2}(1 + \nu\alpha P_{Yi} cos\theta_i), \tag{5.3}$$

where $i \in \{x, y, z\}$ is one of the three axes in the specified unprimed coordinate system. One can then define θ_i to be the polar angle between the proton and the corresponding axis in the hyperon rest frame and α is the weak decay asymmetry, with a well documented value of 0.642 ± 0.013 [15]. The factor ν represents a dilution of the self analyzing power in the case of the Σ^0, resulting from its decay to a photon and a Λ, and is equal to $-\frac{1}{3}$. This can be interpreted as the Λ preserving $-\frac{1}{3}$ of the Σ^0's original polarization. As discussed in section 1.3, a complication arises in this analysis due to the proton angular distribution being measured in the rest frame of the parent Σ^0. This results in ν having a value of $-\frac{1}{3.90}$. For the $K\Lambda$ analysis, ν has a value of $+1$. It is worth noting at this stage that the dilution of the Σ^0 polarization means that the uncertainties in its measurement will be almost four times as large as they are for the Λ.

By substituting equations 5.1 and 5.2 into 5.3 the following relation for the angular distribution of decay protons can be derived

$$N^{\parallel,\perp}(\theta_i, \Phi) = N_0(\theta_i, \Phi) \left\{1 \mp P_\gamma^{lin} \Sigma cos(2\Phi) \mp \alpha P_\gamma^{lin} O_i sin(2\Phi) cos\theta_i\right\}. \tag{5.4}$$

where $N^{\parallel,\perp}$ is the number of events detected for a parallel (perpendicular) polarized photon beam whilst N_0 represents the number of events for an unpolarized beam.

As the photon beam for g8b had two polarization settings, producing almost equal statistics, the simplest way to extract Σ, O_x and O_z is to construct the asymmetry, A, as a function of Φ and θ_i

$$A(\Phi, cos\theta_i) = \frac{N^{\parallel}(\theta_i, \Phi) - N^{\perp}(\theta_i, \Phi)}{N^{\parallel}(\theta_i, \Phi) + N^{\perp}(\theta_i, \Phi)} = -P_{\gamma}^{lin}\Sigma cos2\Phi - \alpha\nu P_{\gamma}^{lin} O_i sin2\Phi cos\theta_i \tag{5.5}$$

This measurement method has the advantage that the spectrometer's bin dependent acceptance is independent of the initial photon polarization orientation. Therefore, any correlated acceptance effects for the proton and kaon will cancel out. This removes the need to carry out any sophisticated acceptance calculations to extract these observables which could potentially result in the introduction of a large systematic uncertainty. As a caveat, the one instance in which the acceptance would not cancel out would be if there was any difference in the track reconstruction efficiency due to differences in the beam intensity between the two photon polarization states. For g8b this effect was minimized by changing the plane of polarization at constant intervals throughout the experimental run.

Now that the functional form of the asymmetry has been established the polarization observables can be extracted by fitting a function of the form shown in equation 5.5 to a two dimensional distribution of kaon azimuthal angle Φ versus $cos\theta_i$. An accurate extraction of the observables will, however, require knowledge of the degree of linear polarization, P_{γ}^{lin}. This measurement will be addressed before any attempt is made to extract the observables.

5.2 Measuring the Photon Polarization

To determine the degree of photon polarization it is necessary to know the position of the coherent edge and the relationship between photon energy and polarization for each edge position. The current position of the coherent edge is found by making an enhancement plot of the tagger scaler spectra. This is achieved by taking a random background subtraction of both the polarized and amorphous scaler distributions to remove random photons that did not cause a trigger. The tagger scalers for the polarized photons are then divided by the amorphous distribution giving the enhancement. The coherent edge, defined to be the part of the tailing slope of the peak with the highest negative gradient, is found by fitting a polynomial in the range of the coherent peak.

Once the enhancement is obtained, and the peak is found, it is compared to the ANB analytic bremsstrahlung calculation [95]. This calculation provides an approximate treatment of beam divergence and beam spot size. It can also allow for the adjustment of various parameters upon which the degree of polarization is

dependent, such as the beam energy, thickness of radiator, geometry of collimator e.t.c. A fuller description of these parameters is given in [75]. The calculation is run many times, and the parameters are adjusted until a good agreement with the enhancement is obtained, as shown in figure 5.1.

As the coherent peak is known to move around comparisons between the data and the calculation are made for a range of energy settings as displayed in figure 5.2. These values are then read into a look-up table of photon polarizations that can be read on an event by-event-basis. From this a table of the mean polarization as a function of photon energy for each run period can be generated.

5.2.1 Systematic Uncertainty

There are four main sources of systematic uncertainty in obtaining the photon polarization from the ANB calculation. These are the dependence of the polarization on the tagger E-plane, the theoretical and data comparison limits, the varying height of the coherent peak and the uncertainty from the TDC spectra normalization. In the first case the effect is due to the fact that up to as many as six E-bins can be associated with each T-bin for which the polarization is calculated. This can introduce an uncertainty in the true position of the coherent edge which can cause a change in the mean polarization. The second effect is caused by there being a range of parameters which will give equally good comparisons between the data and the calculation. The varying height of the coherent peak is due to instabilities in the position of the electron beam. This results in the height of the coherent peak varying, causing a change in the polarization of the photons under the peak. The final case results from the spikiness in the TDC spectra that can cause the normalization procedure to malfunction.

These effects were all considered in reference [75] which found the combined systematic uncertainty to be $\pm 4.3\%$. Further to this, it should be noted that there does appear to be some systematic effect when trying to calculate the photon polarization at energies right on the coherent edge. This is due to the comparison between the data and calculation not being reliable at these energies. To fully calculate the systematic contribution from this it will be necessary to study the photon polarization using a high statistics single pion analysis. Such a study is outwith the scope of this analysis but is currently being undertaken. Either the comparison will be improved with the higher statistics available or at least the size of the systematic uncertainty will become known and accounted

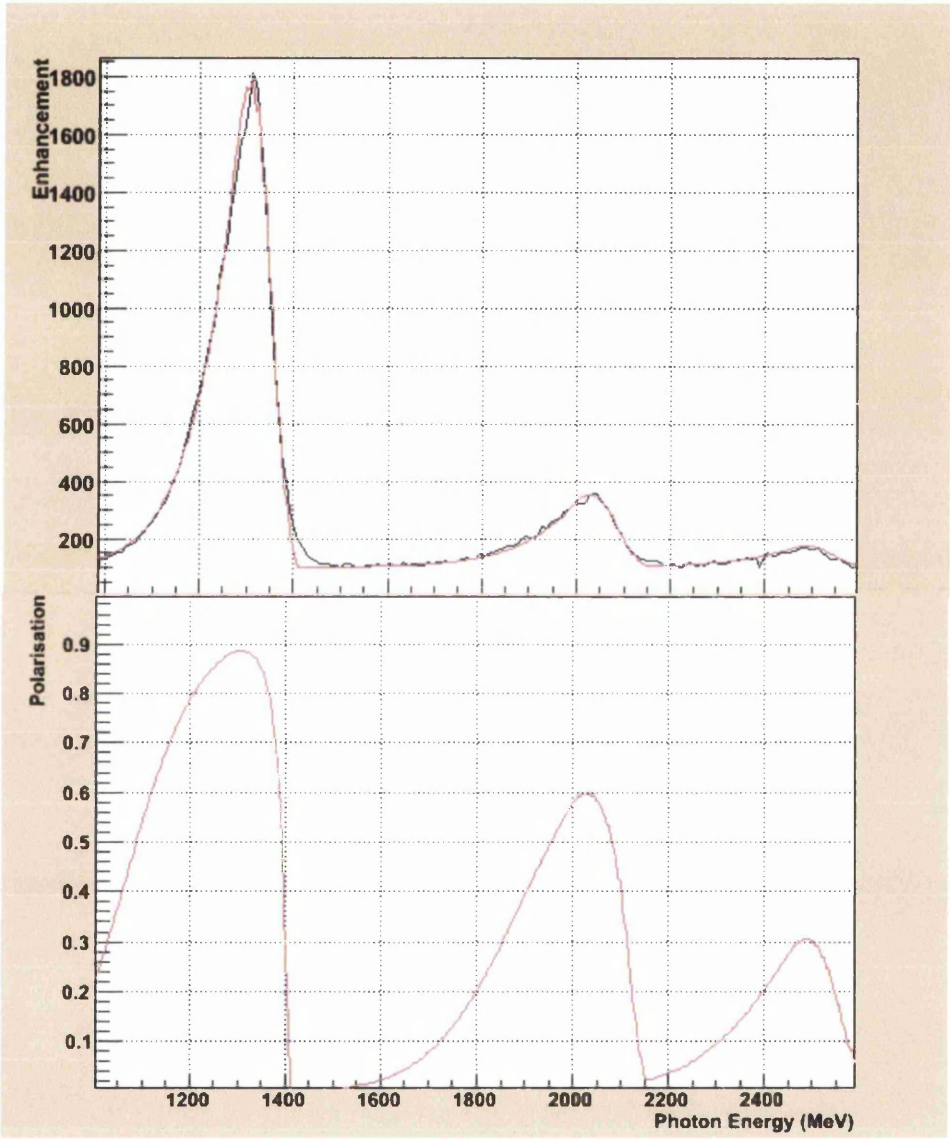

Figure 5.1: Collimated tagger scaler spectra compared with the ANB [95] calculation for the 1.3GeV coherent peak position (top). The calculated photon polarization versus energy (bottom).

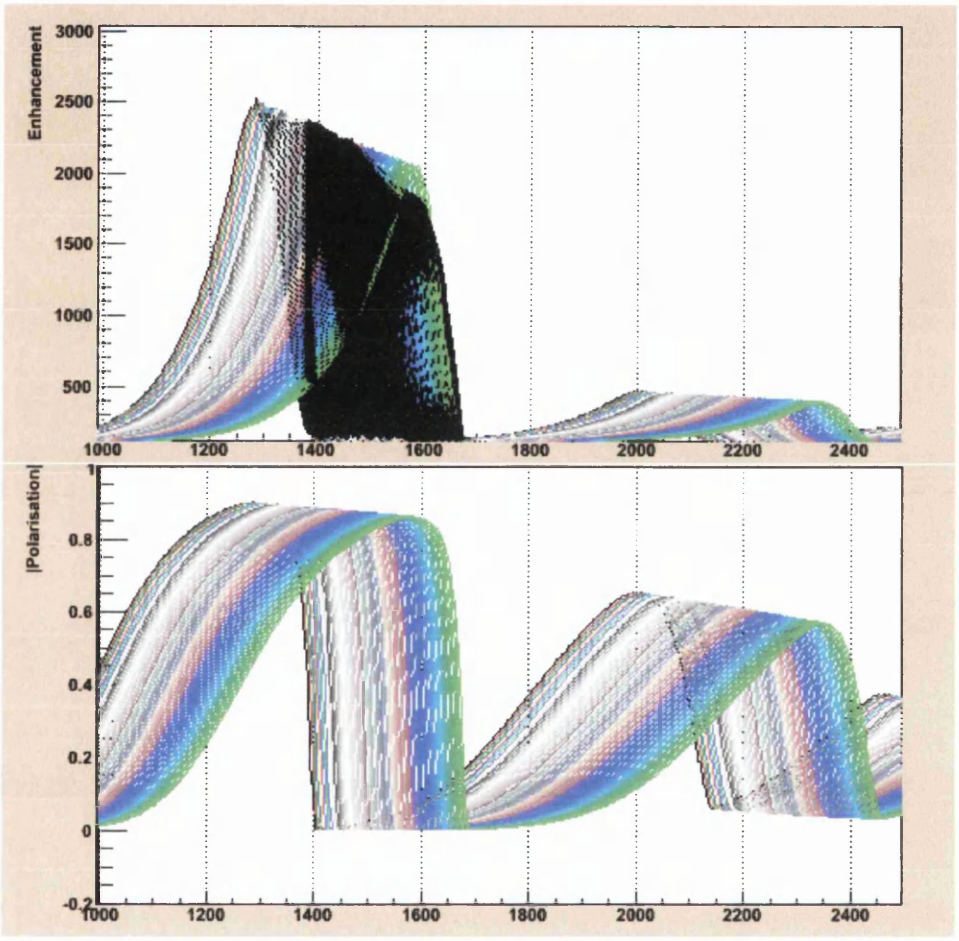

Figure 5.2: Collimated tagger scaler spectra compared with the ANB [95] calculation for the 1.5GeV coherent peak position over a range of photon energies (top). The calculated photon polarization versus energy (bottom).

for. It the meantime it should be recorded that for photon energies right on the coherent edge there may be some small but undetermined systematic uncertainty on top of the quoted 4.3%.

5.3 Photon Asymmetry

The photon asymmetry, Σ, can be measured by applying a two dimensional fit of the functional form of equation 5.5 to the asymmetry over Φ and θ_i. However, it should be noted that Σ is only dependent upon the meson azimuthal angle Φ. One can therefore integrate over all proton polar angles θ_i and derive a one dimensional asymmetry as a function of Φ only:

$$A(\Phi) = \frac{N^{\parallel}(\Phi) - N^{\perp}(\Phi)}{N^{\parallel}(\Phi) + N^{\perp}(\Phi)} = P_{\gamma}^{lin}\Sigma cos2\Phi \tag{5.6}$$

The asymmetry is measured for each kinematic bin in E_γ and $\theta_{cm}^{K^+}$. The photon asymmetry can then be extracted by performing a fit of the form of equation 5.6 over each distribution. A complication arises from the fact that for g8b the parallel and perpendicular polarized data sets do not in general have the same number of events or mean polarization. The two data sets were therefore scaled to account for the differences in yield and polarization. This results in the following modified relation for the asymmetry

$$A(\Phi) = \frac{N^{\parallel}(\Phi) - N^{\perp}(\Phi)}{N^{\parallel}(\Phi) + N^{\perp}(\Phi)} = \frac{P^{\parallel} - P^{\perp}}{P^{\parallel} + P^{\perp}} + \frac{2P^{\parallel}P^{\perp}}{P^{\parallel} + P^{\perp}}\Sigma cos2\Phi \tag{5.7}$$

where $P^{\parallel}$ and $P^{\perp}$ are the mean polarizations for the parallel and perpendicular photon polarization settings respectively.

5.3.1 Bin Selection

The choice of bin widths for each kinematic variable used in the measurement of Σ was made in an attempt to maximize the information extracted as a function of both E_γ and $\theta_{cm}^{K^+}$. A sensible choice would therefore be to have an approximately equal number of bins for each variable. A complication arises when binning in E_γ due to there being different discrete energy settings for the coherent peak. Both the luminosity and degree of photon polarization decrease rapidly when one moves away in energy from the coherent edge. Taking this into account it was

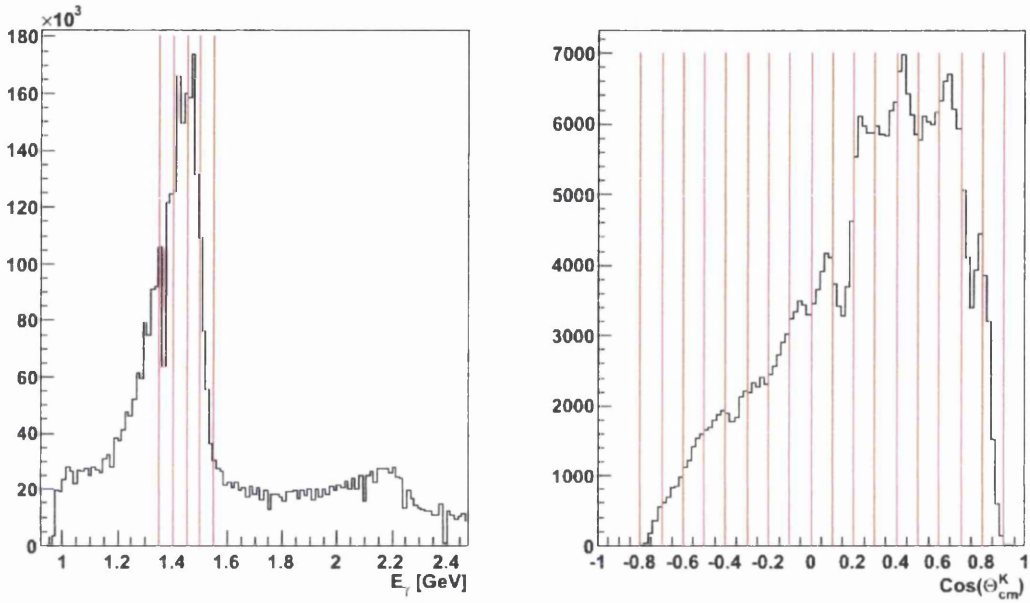

Figure 5.3: Left plot shows the 50 MeV photon energy bins superimposed on the 1.5 GeV coherent spectrum. These bins cover the regions in the energy spectrum with the highest photon polarization ranging from 1.35 to 1.55 GeV. The right plot shows the angular bins superimposed on the $cos(\theta^K_{cm})$ spectrum. The majority of the events detected in CLAS are forward angled which will result in lower statistics at the backward angles. These 17 bins range from $cos(\theta^K_{cm})$ = -0.8 to 0.9.

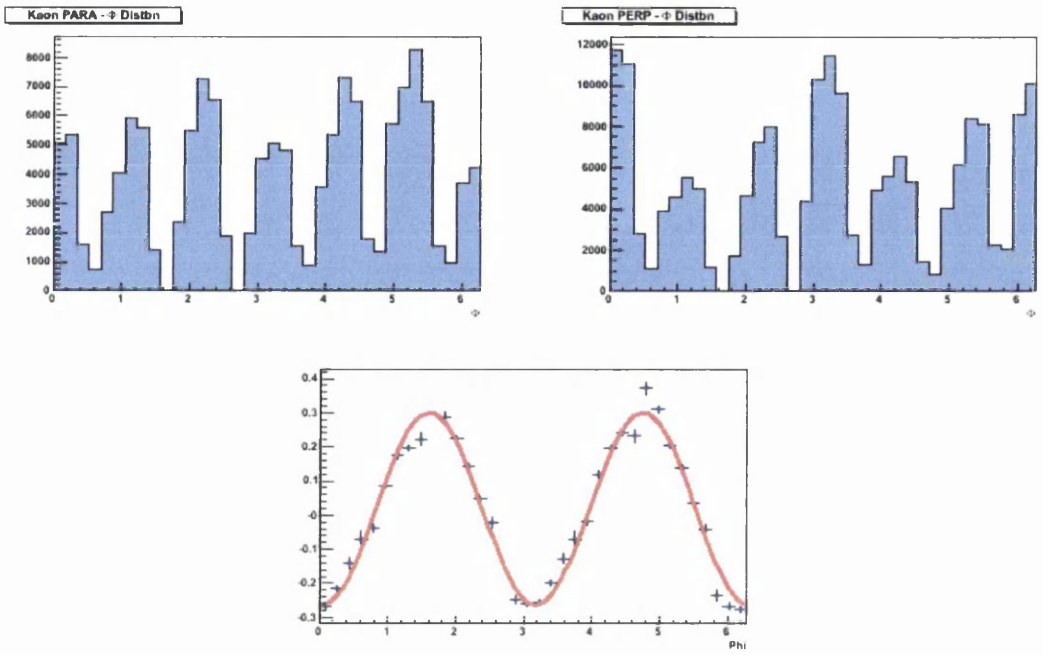

Figure 5.4: Φ-yield of kaons for the perpendicular polarized photon setting (top left) and the parallel setting (top right) for the 1.5 GeV coherent peak position integrated over the full angular range. The regions of low acceptance corresponding to presence of the torus magnetic coils can be clearly seen in the plots. The asymmetry of the two polarization settings is shown in the bottom plot along with a $cos2\Phi$ fit. This asymmetry technique removes any acceptance issues since the spectrometer acceptance is independent of the photon polarization state.

decided to use 4 E_γ bins, each of 50 MeV width per coherent peak setting. An illustration of this bin selection is shown for the 1.5 GeV coherent spectrum in figure 5.3 (left).

As there were 5 coherent peak settings for g8b, each separated by 200 MeV, this resulted in a total of 20 bins covering a continuous range in E_γ. It should be noted however that these bins will not contain equal numbers of events, with those closest to the coherent edge having a much higher number of counts as well as mean polarization. To complement this 17 bins were used for $cos\theta^{K^+}_{cm}$ as shown in figure 5.3 (right), ranging from $cos\theta^{K^+}_{cm}$ = -0.8 to 0.9. This size of bin width was chosen so that the statistical uncertainty of each extracted observable was approximately equal to the systematic uncertainty from the polarization calculation. In total there were 340 kinematic bins in which the photon asymmetry was measured.

5.3.2 Extraction of Σ

Having selected the size of kinematic bins to be used, the photon asymmetry, Σ, was extracted by fitting the function from equation 5.6 to each Φ-distribution on a bin-by-bin basis. Figure 5.4 (top left and right) shows the Φ distributions for the parallel and perpendicular data sets respectively, integrated over all $cos\theta_{cm}^{K^+}$ bins. The bottom plot shows the asymmetry of the two polarized data sets with error bars, demonstrating the power of the asymmetry technique to remove any acceptance effects, providing a very clean $cos2\Phi$ distribution.

The results of the fits to the kaon azimuthal distributions for one bin in E_γ and $cos\theta_{cm}^{K^+}$ are shown in figures 5.5 and 5.6. The resultant photon aymmetries are then plotted as a function of $cos\theta_{cm}^{K^+}$ in figures 5.7 and 5.8 for the $K^+\Lambda$ and $K^+\Sigma^0$ channels respectively. To inspect the performance of the fits, results are presented for the χ^2 per degree of freedom measured for each fit for both the $K^+\Lambda$ (left) and $K^+\Sigma^0$ (right) reactions in figure 5.9.

5.4 Extraction of O_x and O_z

The double polarization observables, O_x and O_z, are extracted from the 2-dimensional asymmetry over Φ and θ_i from equation 5.5. Some typical distributions are shown in figure 5.10 along with the Φ and θ_i projections. When integrating over the whole polar range, θ_i, the distribution reduces to the $cos2\Phi$ form as shown in the bottom left plot. The observables were extracted using two different methods. The first procedure used a slicing technique fit (STF), in which the distributions were sliced for each bin in θ_i before a 1-dimensional fit over Φ is performed. The second technique involves a direct 2-dimensional fit (D2F) of the asymmetry.

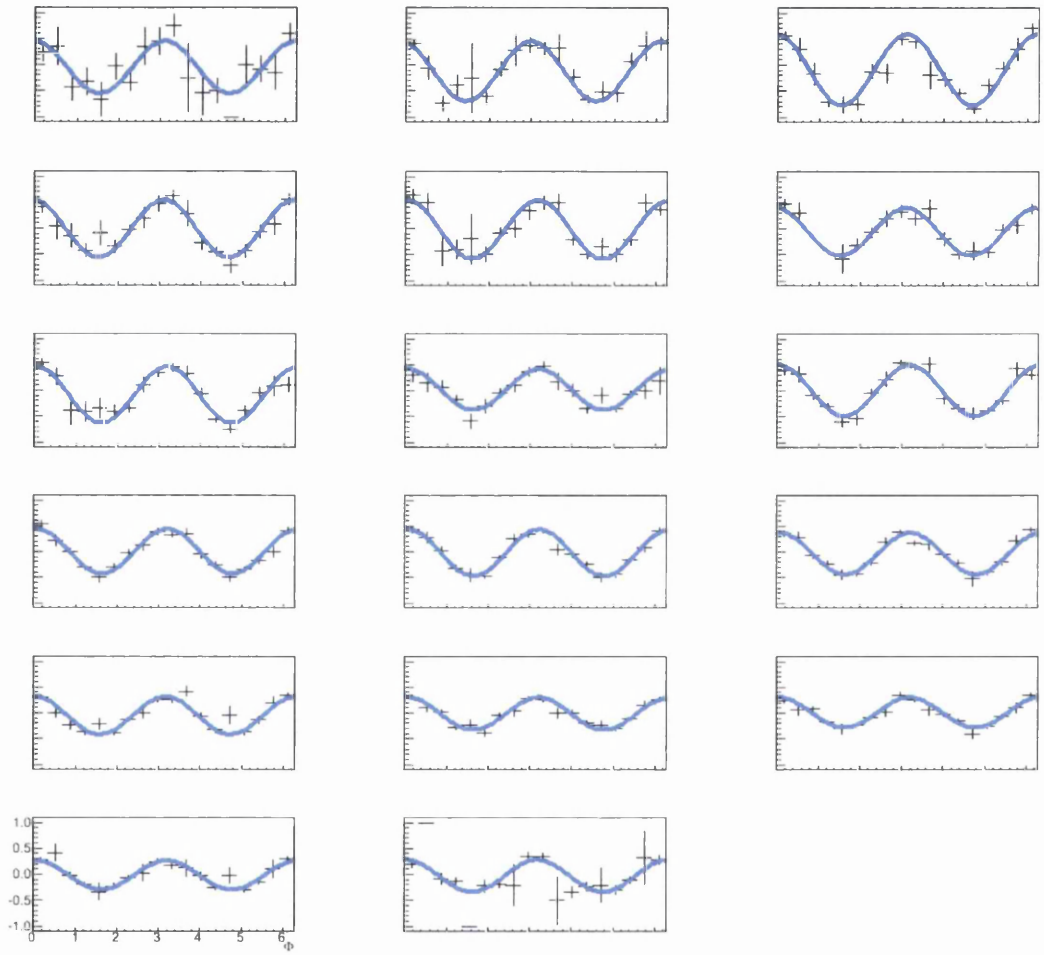

Figure 5.5: $cos2\Phi$ fits of the asymmetry over the kaon azimuthal angle Φ for E_γ = 1.675 GeV for the $K\Lambda$ channel. The histograms proceed from $cos\theta^{K^+}_{cm}$ = -0.75 in the upper left to $cos\theta^{K^+}_{cm}$ = 0.85 in the bottom right.

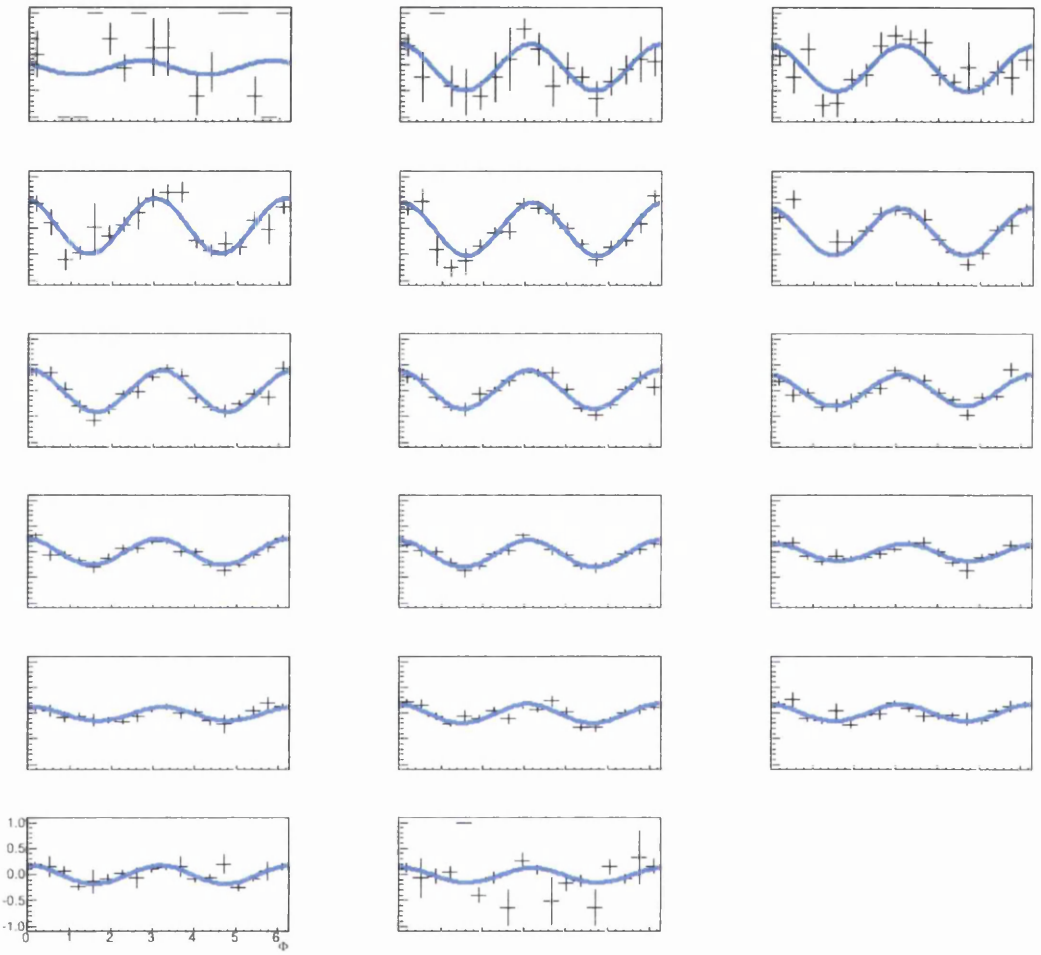

Figure 5.6: $cos2\Phi$ fits of the asymmetry over the kaon azimuthal angle Φ for E_γ = 1.675 GeV for the $K\Sigma^0$ channel. The histograms proceed from $cos\theta^{K^+}_{cm}$ = -0.75 in the upper left to $cos\theta^{K^+}_{cm}$ = 0.85 in the bottom right.

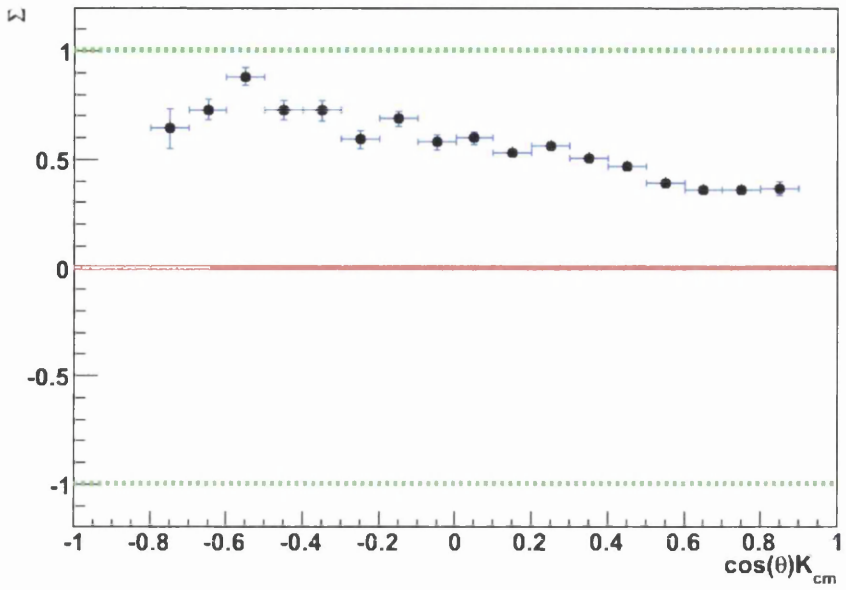

Figure 5.7: Graph displaying the resultant photon asymmetry at $E_\gamma = 1.675$ GeV, as a function of $cos\theta_{cm}^{K^+}$ for the $K^+\Lambda$ channel. All the error bars are purely statistical and no systematic errors have been considered at this stage.

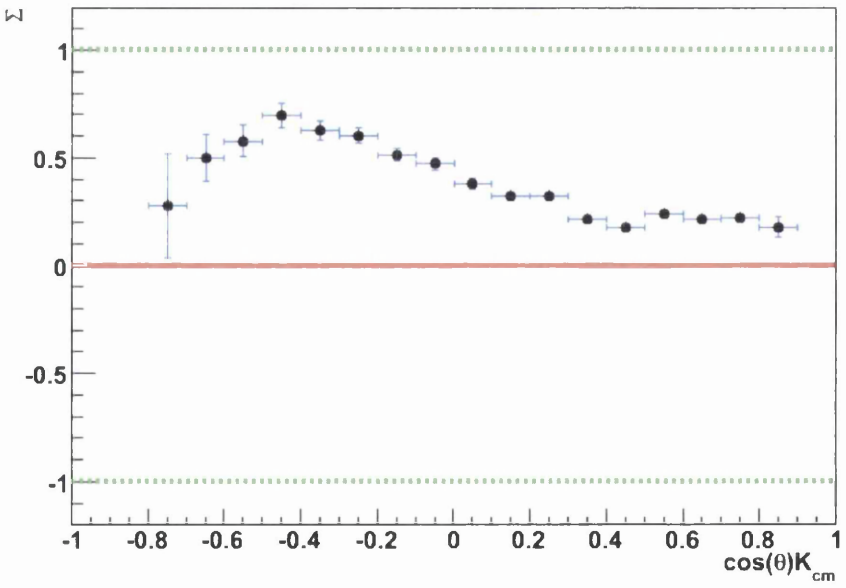

Figure 5.8: Graph displaying the resultant photon asymmetry at $E_\gamma = 1.675$ GeV, as a function of $cos\theta_{cm}^{K^+}$ for the $K^+\Sigma^0$ channel. All the error bars are purely statistical and no systematic errors have been considered at this stage.

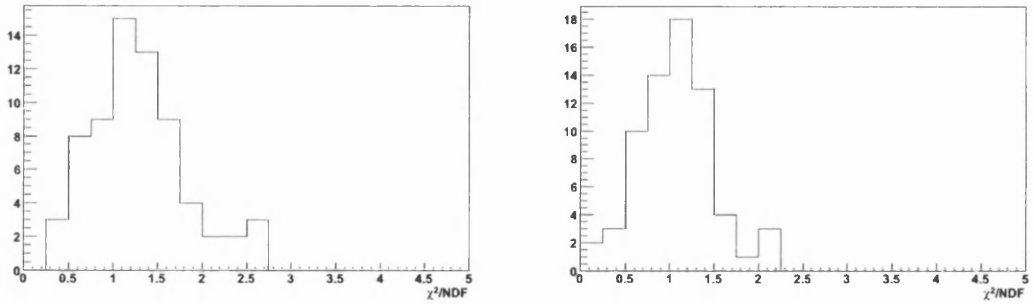

Figure 5.9: χ^2 values per degree of freedom for the $K^+\Lambda$ (left) and $K^+\Sigma^0$ (bottom) channels. These values are from fits for all photon asymmetry measurements over the full kinematic range.

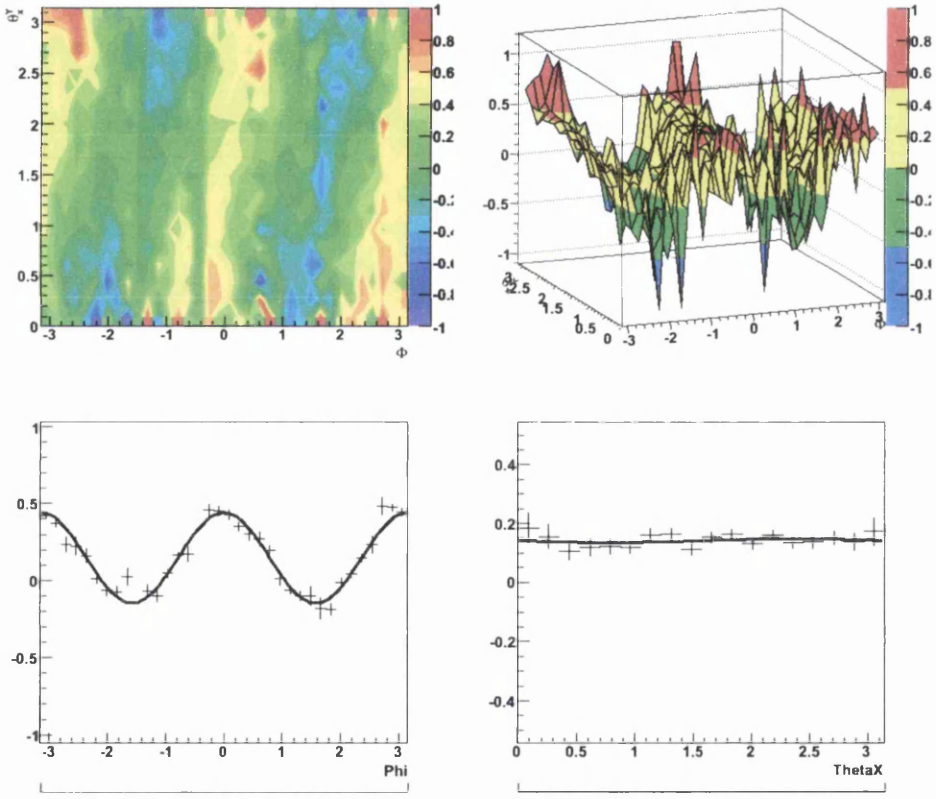

Figure 5.10: The 2-dimensional asymmetry over Φ and θ_i plotted on the top row for the x-component of the recoil polarization. Bottom row left displays the distribution integrated over the full θ_i range, showing the expected $cos2\Phi$ form. Bottom right plot displays the distribution integrated over the full Φ range with the fit of the expected $cos\theta_i$ form. These plots are for a photon energy of 1.65 GeV, integrated over the angular range $cos\theta^{K^+}_{cm} = 0.4$ to 1.0.

5.4.1 Slicing Technique

In the STF method the 2-dimensional asymmetry distribution is sliced for each bin in θ_i, a total of 18 bins covering the complete angular range. For each bin in θ_i the Φ distribution should reduce to functional form

$$-[Par1]cos(2\Phi) - [Par2]sin(2\Phi) \tag{5.8}$$

where:

$$[Par1] = P_\gamma^{lin}\Sigma \tag{5.9}$$

$$[Par2] = \alpha P_\gamma^{lin} O_i cos(\theta_i). \tag{5.10}$$

One can therefore extract $Par1$ and $Par2$ from a minimum chi-squared fit of the form of equation 5.8 to the Φ distribution for each θ_i bin. $Par1$ and $Par2$ are then plotted against the mean of each θ_i bin as shown in the top row of figure 5.11. The θ_i dependence of each variable is clear with $Par1$ showing a straight line distribution independent of θ_i, as expected by inspection of equation 5.9. $Par2$ however, displays the clear $cos(\theta_i)$ dependence expressed quantitatively in equation 5.10. By performing minimum chi-square fits of the functional form of equations 5.9 and 5.10 to each distribution, the values for the photon asymmetry Σ and the double polarization observable O_i can be extracted. The χ^2 values for each fit are plotted on the bottom row of figure 5.11 giving evidence for the fitting procedure working well. The Σ values extracted from this process were also found to agree well with results from the 1-dimensional fitting of the Φ distributions from section 5.3.2.

5.4.2 2-Dimensional fits

The second method used to extract O_i involved a direct 2-dimensional minimum chi-square fit (D2F) to the asymmetry distribution integrated over all Φ and θ_i angles. This fit was of the form of equation 5.5 and the result for one E_γ and one $cos\theta_{cm}^{K^+}$ bin is shown in figure 5.12 (top row). Results for O_i for the $K^+\Sigma^0$ were extracted using the same method but with a factor 4 less statistics due to the weak dilution of the Σ^0's polarization. This effect required that the binning used

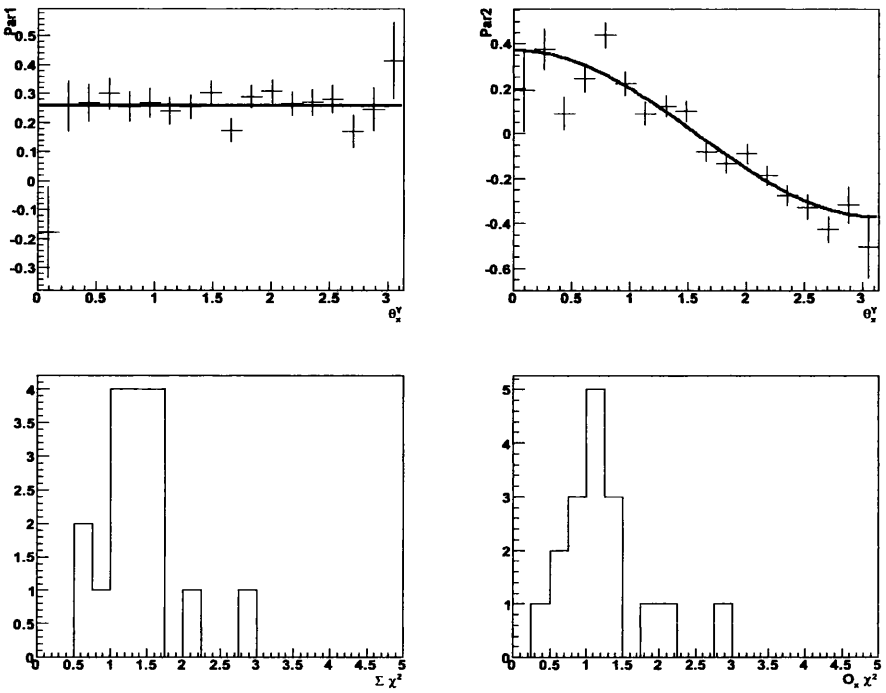

Figure 5.11: Top row displays the θ_i dependence of $Par1$ (left) and $Par2$ (right) extracted from the slicing technique fits. The χ^2 values for both sets of fits used to extract Σ and O_x are shown on the bottom row for one E_γ bin.

to present the $K^+\Sigma^0$ results be reduced to just just 4 angular bins ranging from $cos\theta^{K^+}_{cm}$ = -0.8 to 0.9. The E_γ bins were kept the same as for the $K^+\Lambda$ channel.

The extracted results from both the STF and D2F methods agreed to within 1% for both Σ and O_i. This gives confidence that the fitting procedures worked well and were well behaved. Further to this, the χ^2 values from the two dimensional fits for both O_x and O_z, for all kinematic bins, are displayed in figure 5.13. These represent good values, again giving confidence in the fitting procedure. As the two sets of results were in good agreement with each other the mean of the two values was taken as the final result.

5.5 Summary

The photon asymmetry and the O_x and O_z double polarization observables were measured by analyzing the x and z-components of the hyperon polarization. The photon asymmetry was extracted from a one dimensional fit to an asymmetry over the kaon azimuthal angle, while the double polarization observables required a

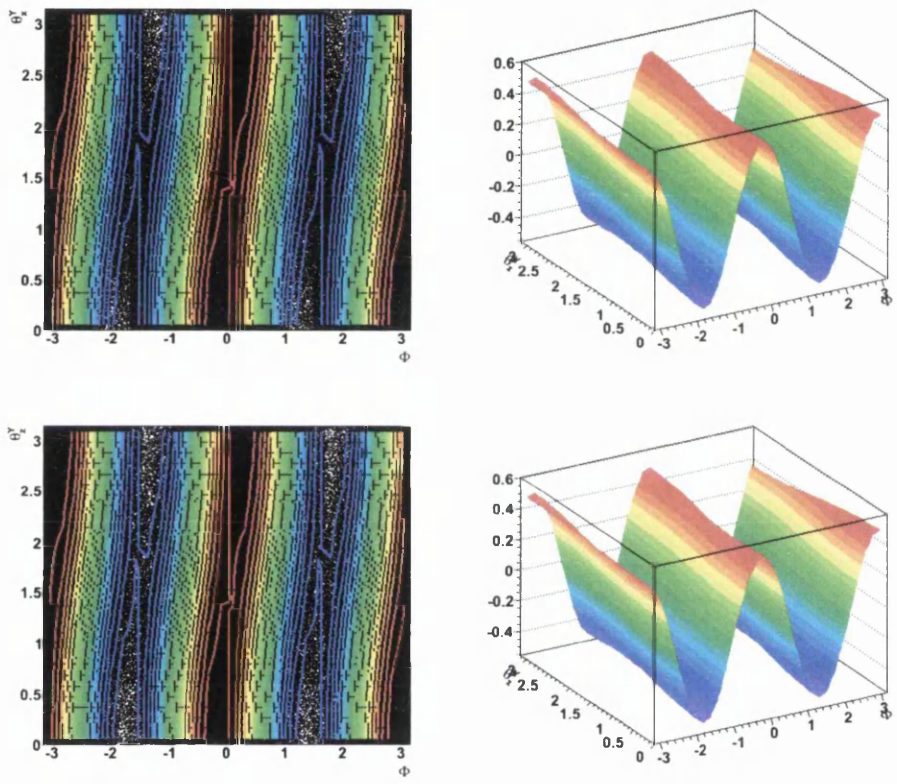

Figure 5.12: Two dimensional fits for one E_γ and one $cos\theta^{cm}_{K^+}$ bin for both the x-component (top row) and z-component (bottom row) of the hyperon polarization.

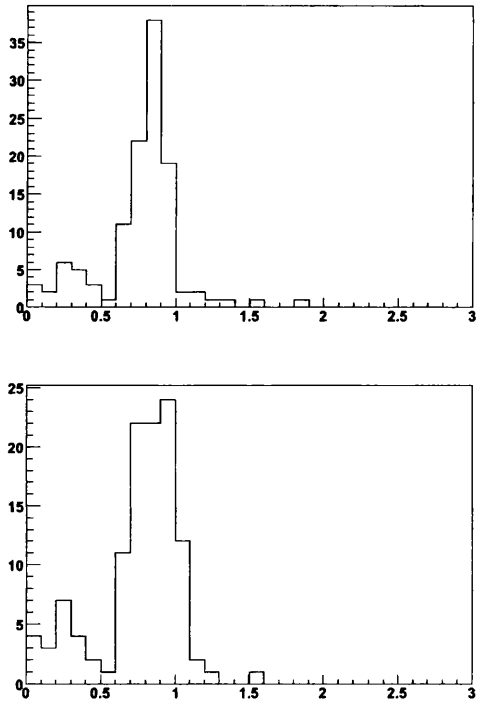

Figure 5.13: χ^2 per degree of freedom values from the two dimensional fits used to extract the O_x (left) and O_z (right) double polarization observables for the $K^+\Lambda$. These values are from all fits over the full kinematic range.

two dimensional fit to an asymmetry distribution over both the kaon azimuthal angle and the proton polar angle in the hyperon rest frame. The results for O_x and O_z were extracted using both a direct two dimensional fit and a slicing technique fit. Both procedures agreed well and the mean of two extracted values was taken as the final result. As these methods used asymmetries of the parallel and perpendicular polarized data sets in each kinematic bin, no acceptance correction was needed. It was, however, required to have an accurate measurement of the relative degree of photon polarization and this introduced a systematic uncertainty of 4.3% into the results. This, along with the uncertainty from the yield extraction, produced a final total systematic uncertainty of 4.74%. It should be noted, however, that there is evidence of some systematic effect when comparing the data to the polarization calculation at photon energies near the coherent edge. The magnitude of this effect is not known precisely and some futher study using the high statistics channel $\gamma p \rightarrow p\pi^0$ is required. This futher analysis is outwith the scope of the current work but should be completed in the near future to give a more accurate measurement of the photon polarization.

Chapter 6

Data Analysis: Extraction of Recoil Polarization and Target Asymmetry

Having completed the extraction of the photon asymmetry, Σ, along with the O_x and O_z double polarization observables, this chapter will describe the methods used to measure the target asymmetry, T, along with the hyperon recoil polarization P. As P is independent of the initial photon polarization state it cannot be extracted by means of an asymmetry measurement. This meant that it was necessary to acceptance correct the proton angular distribution, and this acceptance correction method will be described. The systematic error associated with this correction will also be discussed. Once P has been measured it will then be used to allow the extraction of T from a two dimensional asymmetry.

6.1 Measurement Method

The analysis technique used to extract the target asymmetry, T, and the hyperon recoil polarization, P, requires a measurement of the y-component of the hadron polarization

$$P_y = -\frac{P - P_\gamma^{lin} T cos(2\Phi)}{1 - P_\gamma^{lin} \Sigma cos(2\Phi)} \tag{6.1}$$

where the same conventions are used for the kinematics and coordinate system as Chapter 5. An identical procedure as was used for the x and z-components of the polarization can be applied to the relation above to give the following asymmetry:

$$A(\Phi, cos\theta_y) = \frac{N^{\parallel} - N^{\perp}}{N^{\parallel} + N^{\perp}} = \frac{-P_{\gamma}^{lin}\Sigma cos2\Phi - \alpha P_{\gamma}^{lin} T cos(2\Phi) cos(\theta_y)}{1 + \alpha P cos(\theta_y)} \quad (6.2)$$

where T is the target asymmetry, P is the hyperon recoil polarization and the other variables are as defined in chapter 5. In principle, it is therefore possible to extract P and T from a two dimensional asymmetry over Φ and θ_y. However, it was found that any two dimensional fit to this distribution was not stable when P was allowed to be a free parameter. It was therefore required that P be measured independently before being fixed in the two dimensional fit to allow the extraction of T. To measure P, which cannot be extracted from a one dimensional asymmetry, it will be necessary to carry out a full detector simulation to provide an acceptance correction of the decay proton's angular distribution.

6.2 Detector Simulation

In order to extract the hyperon recoil polarization it is necessary to have an estimation of the CLAS acceptance as a function of the kinematic variables. This requires the generation of simulated events that are reconstructed and analyzed using the same analysis methods as the real data. The first stage in this process requires the generation of physics events corresponding to the $K^+\Lambda$ and $K^+\Sigma^0$ channels that are being studied. These events are then passed through the CLAS detector simulation, where the timing distributions are smeared, before being reconstructed and analyzed. The actual simulation uses a GEANT [96] based simulation of CLAS (GSIM) [97] to reproduce the effects of charged particles moving through the detector subsystems. A flow chart representing the complete simulation process is shown in figure 6.1.

6.2.1 Event Generator

The simulation begins with the generation of 30 million $K^+\Lambda$ and $K^+\Sigma^0$ events, with 5 million for each coherent peak position. The genphoto package [98] was used to generate the events pseudo-randomly with a flat 3-body phase space. This generator allowed the production of unstable polarized particles as well as having the option to include either circularly or linearly polarized photon distributions. For this analysis the generator was modified to sample the photon

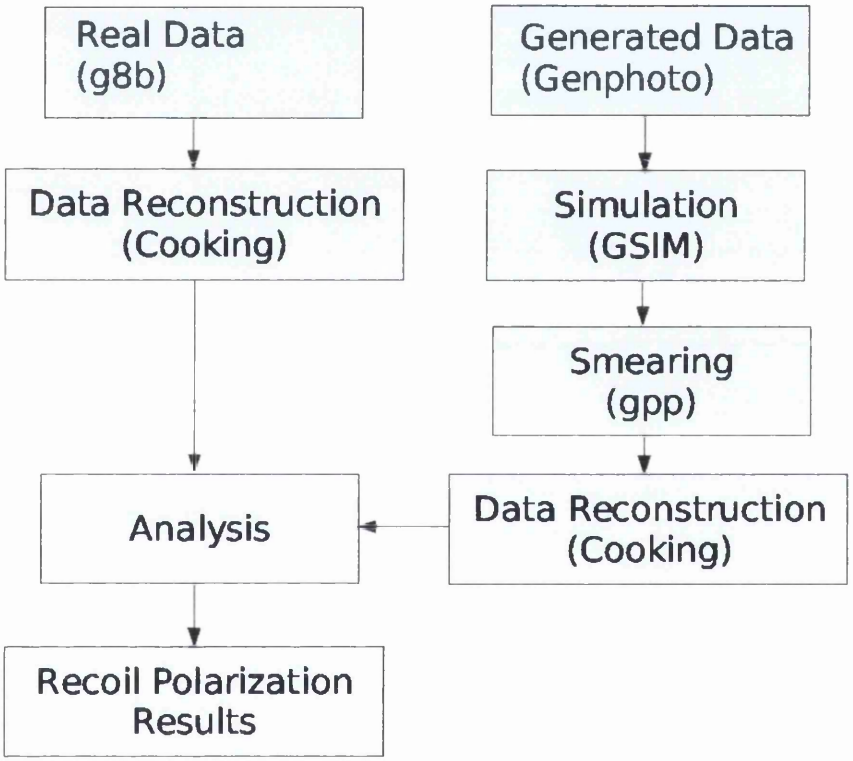

Figure 6.1: Flow chart representing the analysis and simulation processes that are required to extract the hyperon recoil polarization from the g8b dataset.

energy spectrum from the real data for the event generation. This meant that the generated Monte Carlo data had the same characteristic coherent peak structure for the photon energy spectrum as the real data.

6.2.2 GSIM and GPP

The GSIM software package is used to provide an accurate simulation of the CLAS detector. The particles from each generated event are propagated through the simulated detector creating a set of hits in the various subsystems. Figure 6.2 displays a cross section through CLAS showing tracks from a single generated $K^+\Lambda$ event. As the particles pass through the detector GSIM provides calculations for the effects of particle decays, multiple-scattering and secondary interactions. At the end of this process the simulated event information is output in the standard CLAS BOS format, which is then analyzed using the same methods as the real data.

GSIM produces simulated events with perfect timing resolution for each detector sub-system, which does not give an accurate representation of the spectrometer resolution. Therefore, after each event is simulated it is then passed through a program called GPP [99], which smears the timing output of the TOF scintillator paddles and drift chambers to give a more realistic representation of the true CLAS timing resolution. This smearing is achieved by adding a pseudo-random time from a Gaussian distribution to the timing resolution of each subsystem. Further to this, GPP also removes "dead" detector elements. This capability was utilized to remove dead drift chamber cells to allow for the rejection of charged particle tracks where the trajectory passes through a known hole in the drift chamber.

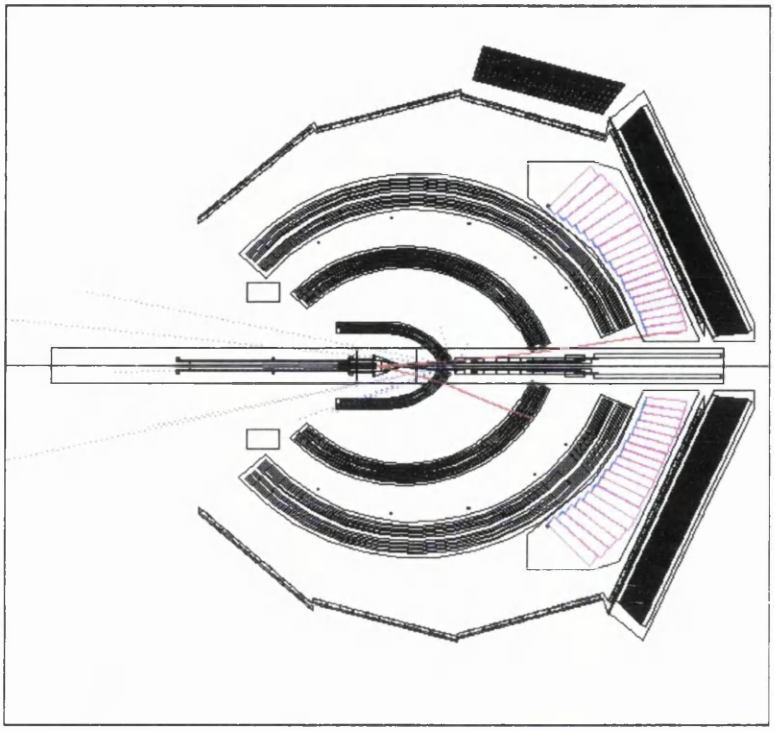

Figure 6.2: Cross section through CLAS, produced by the GSIM program [97], displaying a single generated $K^+\Lambda$ event.

6.2.3 Measuring the Acceptance

The spectrometer acceptance for the reactions $\gamma p \rightarrow K^+\Lambda$ and $\gamma p \rightarrow K^+\Sigma^0$, is calculated from the ratio of simulated accepted events to thrown (MC generated) events. In order to extract the hyperon recoil polarization, the acceptance of the proton angular distribution θ_y has to be corrected. This acceptance was studied as a function of the kaon polar angle $\theta_{cm}^{K^+}$. The acceptance was measured over the full photon energy range of g8b, and the same procedures and nominal cuts (as described in Chapter 4) were used in determining the accepted events.

To facilitate a study of possible systematic uncertainties, events were generated with different kinematic distributions. These events were modified by changing the $cos\theta$ distribution from flat phase space to various raised powers before studying the effect this had on the final acceptance. This modification of the theta distribution would cause a change in the four momentum transfer t-dependence of the proton, as shown in figure 6.3.

The acceptance was corrected for both $cos\theta_y$ and $cos\theta_{cm}^{K^+}$ simultaneously in a two dimensional histogram. The acceptance corrected yield as a function of

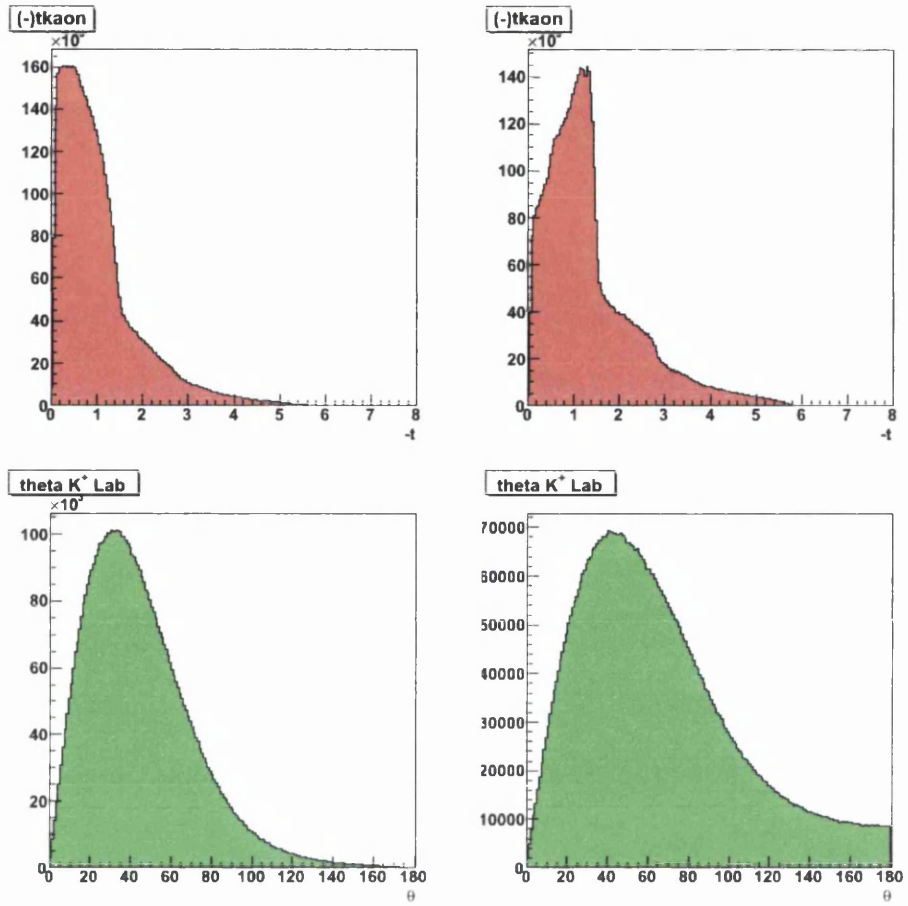

Figure 6.3: t-distributions on the top line for the original flat phase space (left) and modified (right) generated events. The corresponding θ distributions are shown on the bottom line for the original (left) and modified (right) events.

$cos\theta_y$, was then projected out of the histogram. The results for the two generated distributions are shown in figure 6.4. As can be seen in the plot, when the acceptance is corrected as a function of its dependent variables simultaneously, the final corrected yields are the same regardless of the kinematics of the generated events. This hypothesis was tested for several different generated data sets, each with a different kinematic distribution, and the final corrected yields were always the same. This gives confidence that, for the reactions and observables being studied in this analysis, the process of unfolding the detector acceptance is independent of the initial kinematic distributions. The acceptance corrected proton yields could now be used to extract the hyperon recoil polarization.

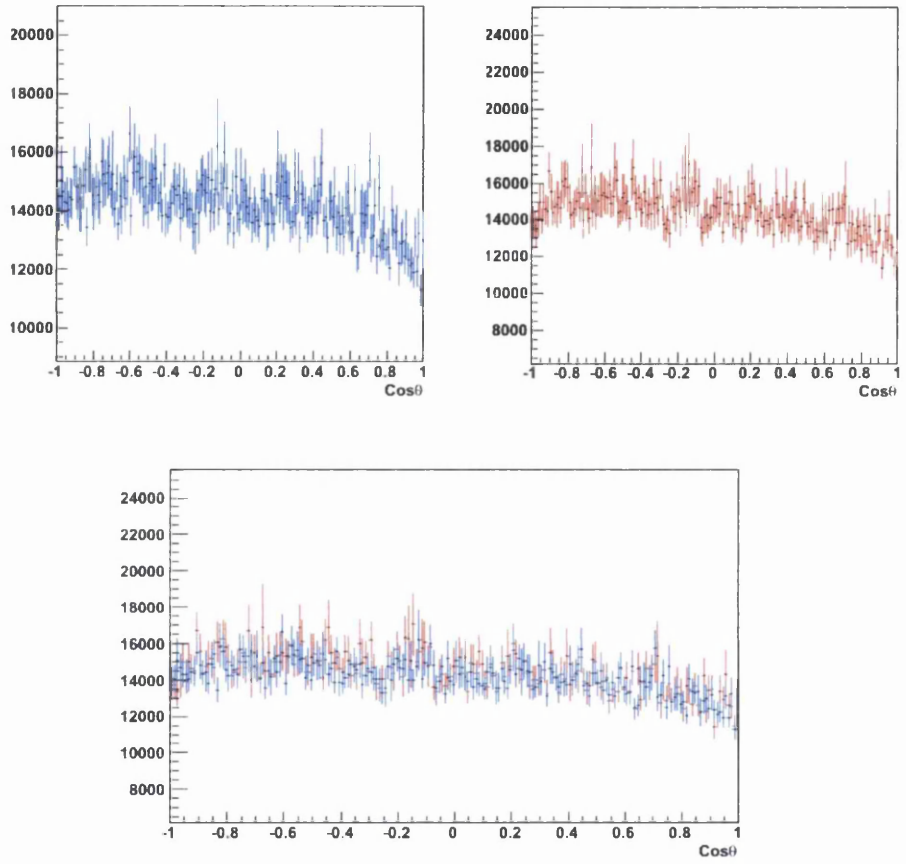

Figure 6.4: Plot showing the effect of correcting the acceptance as a function of both $cos\theta_y$ and $cos\theta^{K^+}_{cm}$ simultaneously on the final proton yield for the original flat phase space distribution (top left) and the modified distribution (top right). The bottom figure shows the two distributions (blue lines for flat phase space and red lines for the modified distribution) on the same plot. This illustrates that when the acceptance is corrected simultaneously as a function of both $cos\theta_y$ and $cos\theta^{K^+}_{cm}$, the final acceptance is the same regardless of the initial kinematic distributions of the generated events.

6.3 Extracting the Hyperon Recoil Polarization

As detailed in Chapter 1 the polarization of a recoiling Λ hyperon can be measured through its parity-violating weak decay to a proton and a pion. Indeed, in the hyperon rest frame, its decay is preferentially oriented in the direction of its polarization. One can therefore relate the decay angular distribution to the polarization with the relation:

$$I(\theta^P_{\Lambda_{RF}}) = 1 - \nu\alpha P cos(\theta^P_{\Lambda_{RF}}) \tag{6.3}$$

where $\theta^P_{\Lambda_{RF}}$ is the acceptance corrected proton yield, P is the Λ polarization, and α and ν are as defined in section 5.1.

A bin range in $cos\theta^{K^+}_{cm}$ similar to the photon asymmetry, but with a smaller photon energy bin size of 25 MeV, was used to present the final recoil polarization results. This finer binning is a direct result of the recoil polarizations independence from the initial photon polarization state. The result of this is that the data set is no longer split into two separate "sub-sets" of parallel and perpendicular polarization, giving an approximate factor of two increase in statistics. As in the case of the O_x and O_z observables, the final binning will have to be somewhat coarser for the Σ^0 to account for the dilution of its polarization. Figure 6.5 shows the linear fits of the proton angular distribution for one bin in E_γ and the full $cos\theta^{K^+}_{cm}$ range. Figure 6.6 displays the polarization as a function of $cos\theta^{K^+}_{cm}$ with the statistical error added for each point.

6.4 Extracting the Target Asymmetry

Having determined the hyperon recoil polarization, P, one can now aim to extract the target asymmetry, T, from the two dimensional asymmetry of equation 6.2. As the statistics for T will be comparable to those for the double polarization observables O_x and O_z, the same bin sizes for E_γ and $cos\theta^{K^+}_{cm}$ will be used to present the results.

Similar to O_x and O_z, the target asymmetry is extracted using both the STF slicing technique and the D2F two dimensional fit. Once again the results for both methods were found to be in good agreement to less than 1%, well within the expected statistical and systematic uncertainties for the final results. The two dimensional fit for the $K\Lambda$ channel is plotted in figure 6.7 for one E_γ and

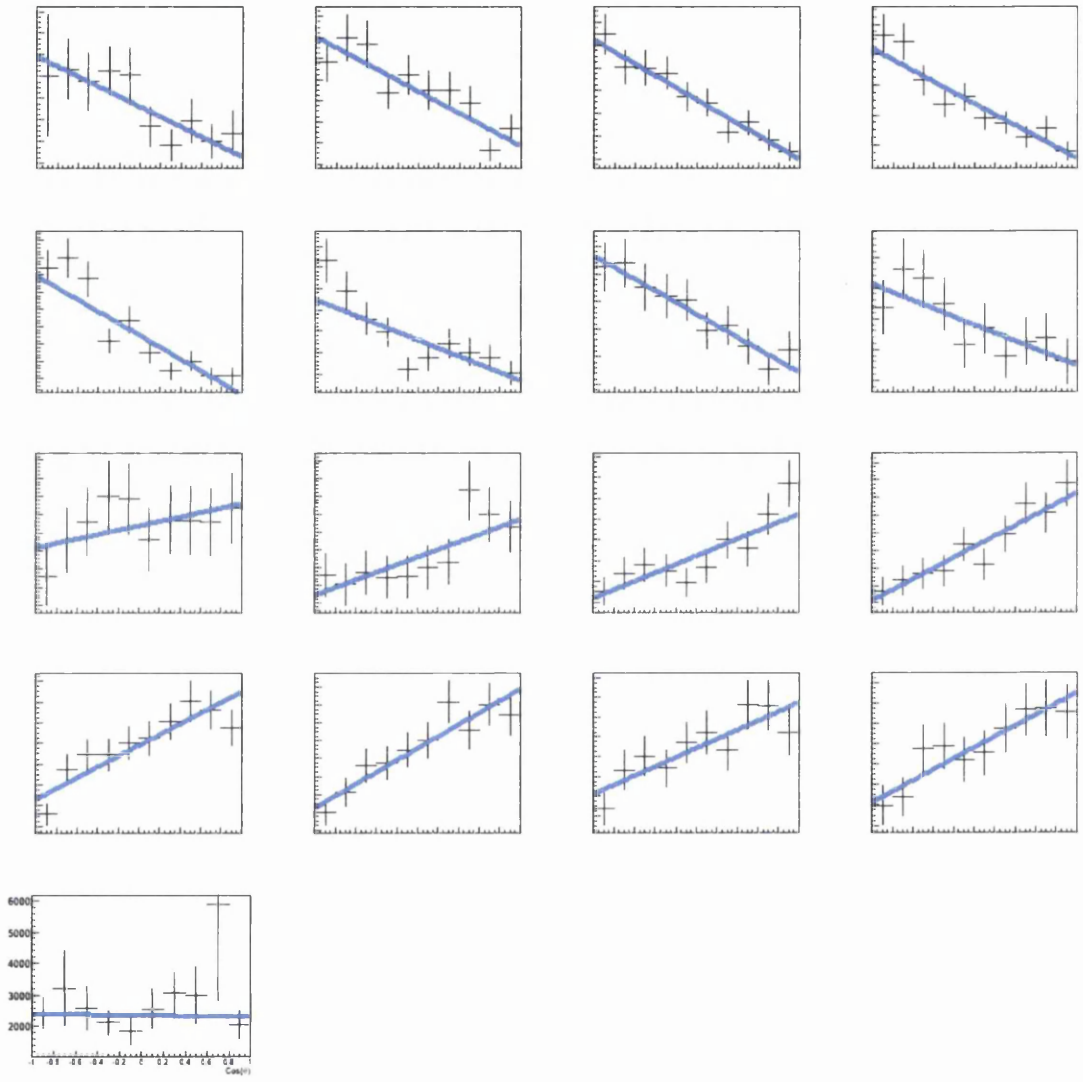

Figure 6.5: Linear fits of the acceptance corrected proton yield $\theta^{P}_{\Lambda_{RF}}$ for E_{γ} = 1.625 GeV. The histograms proceed from $cos\theta^{K^+}_{cm}$ = -0.75 in the upper left to $cos\theta^{K^+}_{cm}$ = 0.85 in the bottom plot.

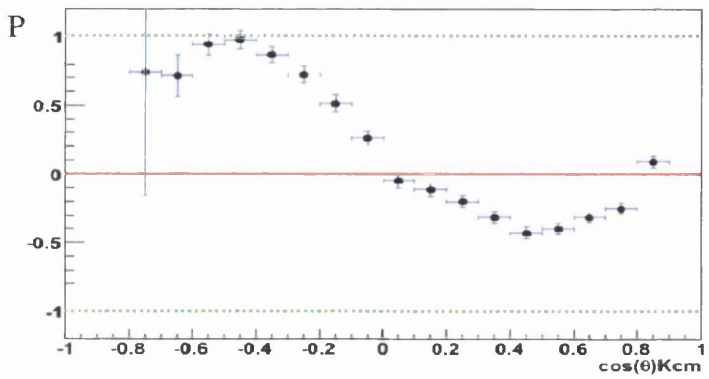

Figure 6.6: Resultant polarization at $E_\gamma = 1.625$ GeV, as a function of $cos\theta^{K^+}_{cm}$. All error bars are purely statistical and no systematic errors have been considered at this stage.

one $cos\theta^{K^+}_{cm}$ bin. The χ^2 values from the two dimensional fit, for the full range of kinematics, are displayed in figure 6.8. These good results, along with an inspection by eye of the slicing technique fits, gives confidence in the overall stability of the extraction methods.

6.5 Systematic Uncertainties

For both the hyperon recoil polarization and the target asymmetry, the main sources of systematic error will come from the methods used to extract the hyperon yields, the photon polarization calculation and an uncertainty associated with the acceptance correction. As discussed in section 5.2.1, the systematic uncertainty from the yield extraction process was measured to be $\sim 2\%$, with an uncertainty of 4.3% from the photon polarization calculation. An extra complication arises when considering the recoil polarization, from the fact that the proton angular distribution has to be acceptance corrected before P can be extracted. In most previous analyses where GSIM has been used for the purpose of acceptance correction, a systematic uncertainty on the order of 5-10% has been calculated. For this analysis the aim was to study any potential systematic effect by monitoring how the acceptance changes when different kinematic distributions are used for the generated events. As outlined in section 6.2.3, when the acceptance is corrected simultaneously as both a function of $cos\theta_y$ and $cos\theta^{K^+}_{cm}$, the final acceptance calculated is almost the same, regardless of the kinematics of the generated

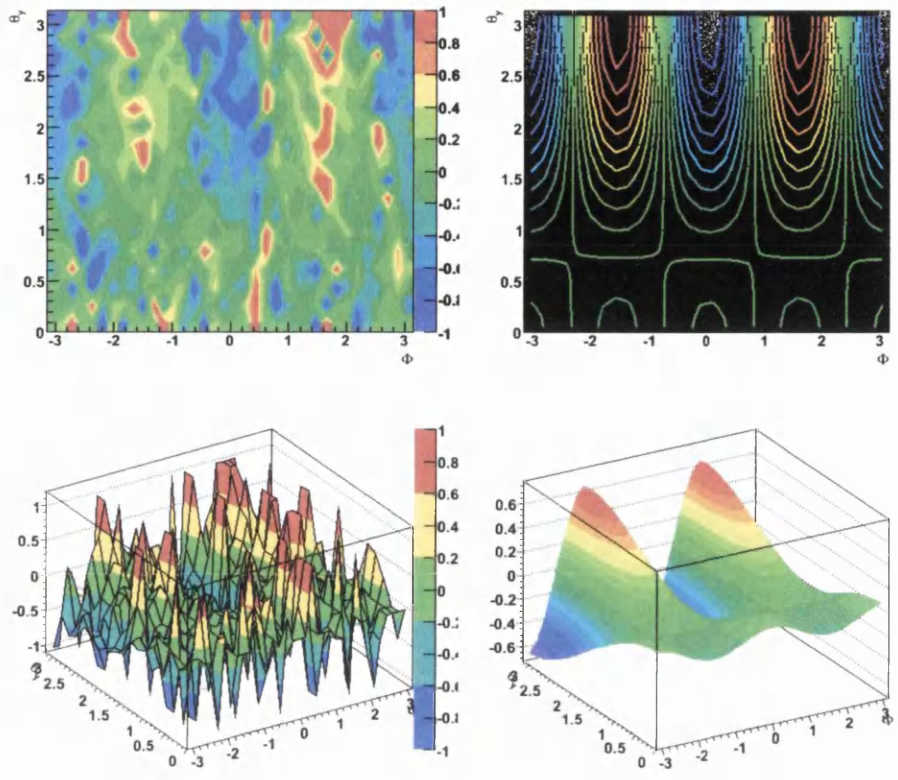

Figure 6.7: Two dimensional symmetry distribution over Φ and θ_y (top left) with the resultant two dimensional fit superimposed (top right). The two dimensional asymmetry distribution is then displayed as a surf plot (bottom left) with the resultant fit (bottom right). These plots are for a photon energy of 1.65GeV, integrated over the angular range $cos\theta^{K^+}_{cm} = 0.4$ to 1.0.

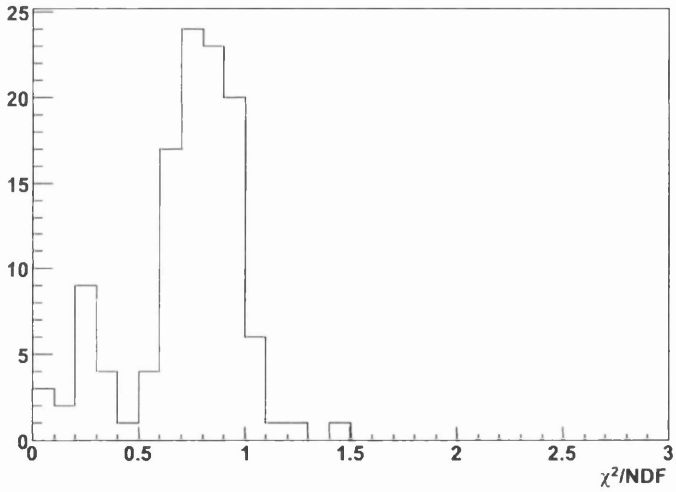

Figure 6.8: χ^2 values from the two dimensional fits used to extract the target asymmetry. These values are from all fits over the full kinematic range.

events. Further to this, it is worth noting that when the acceptance was only corrected as a function of $cos\theta_y$ the overall magnitude of the acceptance changed but the shape remained unchanged. This meant that the hyperon recoil polarization, which is given by the gradient of a linear fit to the acceptance corrected proton distribution, also remained unchanged. From this it can be concluded that, for the extracted hyperon recoil polarization, the systematic uncertainty from the acceptance correction is of the order of $\sim 1\%$. Taking this into account, along with the uncertainty from the photon polarization calculation measured in section 5.2.1, the final systematic uncertainty for both P and T is taken as 4.85%.

6.6 Summary

The recoil polarization was extracted from a fit to the decay proton's angular distribution in the hyperon rest frame. As the induced hyperon polarization is independent of the initial photon polarization state an asymmetry measurement could not be used and the angular distribution had to be acceptance corrected. This was achieved by using the GSIM simulation of CLAS to measure the detector's acceptance as a function of both the proton polar angle $cos\theta_y$ and the kaon production angle $cos\theta^{K^+}_{cm}$. Having determined the recoil polarization, the target asymmetry was then extracted from a two dimensional fit to an asymmetry over the kaon azimuthal angle Φ and the y-component of the proton polar angle θ_y. As in the case of the O_x/O_z double polarization observables two different fitting techniques were used and these gave good agreement for the extracted values. For the target asymmetry and the recoil polarization there was found to be a total sytematic uncertainty of 4.85%

Chapter 7

Results and Discussion

Having discussed the methods used to extract the final hyperon yields (Chapter 4) and measure the various polarization observables observables (Chapters 5 and 6), attention now turns to the presentation of the final results. All the systematic uncertainties associated with these results, along with the final choice of binning, have been discussed in the preceding three chapters. It should be noted that only error bars associated with the statistical uncertainties are shown in the plots. For the photon asymmetry and O_x and O_z results there is a systematic uncertainty of 4.74% with a corresponding uncertainty of 4.85% for the recoil polarization and target asymmetry.

The final measurements for the photon asymmetry, O_x and O_z double polarization observables, hyperon recoil polarization and the target asymmetry will be presented in this chapter. These results will be compared to previous measurements where they exist, and any discrepancies with existing results will be discussed. Further to this, the results will also be compared to model curves from the Kaon-MAID isobar prescription [38] and the Regge-plus-resonance approach of Corthals (RPR) [41, 64]. In addition to this some relations and inequalities between the observables, derived from positivity constraints of the transversity amplitudes, will also be investigated.

An interpretation of these results in light of the model comparisons will then be provided, and any potential physics results will be discussed.

7.1 Photon Asymmetry

The photon asymmetry results for the $K^+\Lambda$ channel are displayed in figure 7.1 as a function of the centre-of-mass kaon angle $cos\theta_{cm}^{K^+}$ and in figure 7.2 as a function of the photon energy E_γ. Comparisons to the GENT and MAID calculations

are shown in figures 7.3 and 7.4 respectively with comparisons to the previous asymmetry results from GRAAL [45] and LEPS [44] shown in figures 7.5 and 7.6. At photon energies above 1.775 GeV the statistical error bars are generally larger due to there being less events at these energies. In addition at lower energies some of the backward angle data are missing, again due to the limited data at these kinematics. Corresponding results are shown for the $K^+\Sigma^0$ channel in figures 7.7 through 7.11.

7.1.1 Discussion of photon asymmetry results for $K^+\Lambda$

The first obvious feature of the $K^+\Lambda$ results is that the photon asymmetry is positive for the full kinematic range of this analysis. The asymmetry remains largely flat for photon energies up to 1.375 GeV, where it then begins to display a slight peak at backward angles, approaching a maximum value of 1 at 1.575 GeV. At higher photon energies a second structure begins to appear at $cos\theta^{K^+}_{cm} = 0$, at a photon energy of around 1.675 GeV, before becoming a very strong signal at 1.725 GeV. Also, as one moves above 1.775 GeV, the peak at the backward angles appears to drop away.

Figure 7.3 shows a comparison of the $K^+\Lambda$ photon asymmetries to calculations from the Regge-plus-resonance model of Corthals *et al* [41] as described in chapter 2. This scheme utilized t-channel Regge-trajectory exchange to model the background, with the inclusion of the $S_{11}(1650)$, $P_{11}(1710)$ and $P_{13}(1720)$ "core" resonances to evolve the calculations into the resonance region. It also investigated the importance of two missing states, $P_{11}(1900)$ and $D_{13}(1900)$, by including them in the calculation. The dashed green lines in the plot correspond to calculations involving only the Regge background, the dot-dashed blue curves include the core set of resonances, the solid red lines are from calculations including the potential missing $D_{13}(1900)$ resonance and the black lines include the $P_{11}(1900)$. At photon energies up to 1.375 GeV the calculations including the $D_{13}(1900)$ describe the results well, with the other calculations generally giving asymmetry values that are too large. Above 1.375 GeV the $D_{13}(1900)$ calculations successfully describes the forward angle results but cannot reproduce the large asymmetries seen at the backward angles. This feature is better reproduced when the $P_{11}(1900)$ state is included. Overall, the calculations including the $D_{13}(1900)$ match the data well for the full angular range at lower energies and at forward angles for the higher energies. The calculations including the $P_{11}(1900)$ match the data well for the full angular range at energies above 1.575 GeV, including being able to reproduce the backward angle peak and the structure seen

at $cos\theta_{cm}^{K^+} \simeq 0$. The success of the model at higher energies and backward angles is perhaps expected from an approach based on a purely t-channel description of the background.

The photon asymmetry results are then compared to theory curves calculated using the Kaon-MAID program, shown in figure 7.4. Kaon-MAID uses an isobar approach that again includes the core $S_{11}(1650)$, $P_{11}(1710)$ and $P_{13}(1720)$ resonances along with the missing $D_{13}(1900)$. This scheme differs from the Regge-plus-resonance approach in the way it handles the background. In the plots the blue dashed curve represents calculations with only the core resonances while the red solid line includes the $D_{13}(1900)$. For photon energies from 1.175 to to 1.225 GeV the core calculation gives a good reproduction of the data with the inclusion of the $D_{13}(1900)$ generally pushing the calculations to higher values. From 1.275 to 1.575 GeV, both calculations give values that are too large. At energies above 1.575 GeV the inclusion of the $D_{13}(1900)$ gives a good comparison with the data, particularly at forward angles. As is the case with the Regge-plus-resonance approach the inclusion of the $D_{13}(1900)$ on its own is not enough to reproduce the structures seen at mid and backward angles.

Figures 7.5 and 7.6 display the $K^+\Lambda$ results compared to the previous measurements from GRAAL and LEPS respectively. The GRAAL data is all at photon energies below 1.5 GeV, covering almost the full angular range, and the agreement is extremely good. The results from this analysis have almost three times as many data points per energy bin than GRAAL, with smaller error bars, allowing for finer structure resolution. This is important at backward angles where a slight peak begins to appear at energies above 1.325 GeV that is not readily visible in the GRAAL results. For the LEPS results the data is all above 1.5 GeV and at forward angles. The data also comes in 100 MeV bins so to allow for a proper comparison the results from this analysis were changed to the coarser binning. However, all the final results for the photon asymmetry will be presented in the finer 50 MeV E_γ bins. Again the comparison is good, with LEPS results occasionally at slightly lower values. This disagreement is quite small and may be the result of some unknown systematic effect in one of the analyses. From the point of view of this work, no reason could be found why the results would be slightly systematically higher.

7.1.2 Discussion of photon asymmetry results for $K^+\Sigma^0$

For the $K^+\Sigma^0$ channel, the photon asymmetry is reasonably flat for for photon energies below 1.625 GeV with a backward angle peak starting to develop at 1.675

GeV and a forward angle peak forming at 1.825 GeV. Once again the values are positive for almost the full kinematic range, with just a few error bars moving into negative values at higher energies.

Figure 7.9 shows the results compared to calculations from the Regge-plus-resonance approach. These calculations are explained in detail in reference [64] for the $K^+\Sigma^0$ channel but essentially two different Regge schemes are used (RPR-3 and RPR-4) that differ in the sign used for the tensor couplings to the trajectories. Both schemes involve two sets of calculations, one for the Regge background and one for the core resonances - no missing resonances are considered. The dotted green line shows calculations for the RPR-3 background, the solid red line shows the RPR-3 core calculations, dashed black displays the RPR-4 background and the dot-dashed blue line shows the RPR-4 with core resonances included. At photon energies below 1.325 GeV the RPR-4 background model gives the best agreement with the data while at energies from 1.325 to 1.625 GeV the RPR-3 core and RPR-4 calculations give a good reproduction of the data, particularly at forward angles. For energies higher than this the two RPR-4 prescriptions give a reasonable comparison to the data at forward angles but none of the models are very successful at describing the rest of the data.

The photon asymmetry results are compared to Kaon-MAID calculations in figure 7.10 where an isobar prescription based on the inclusion of the $S_{11}(1650)$, $P_{11}(1710)$, $P_{13}(1720)$, $S_{31}(1900)$ and $P_{31}(1910)$ states is used. The calculations do not reproduce the general trend of the data well at photon energies below 1.675 GeV where they have the wrong sign for the full angular range. At higher energies the theory compares well with the backward angle peak then becomes negative at mid to forward angles. This disagrees with the positive forward angle peak seen in the data.

Comparisons are shown with the previously published data form GRAAL and LEPS in figures 7.11 and 7.12 respectively. The same binning and kinematic range is used as for the $K^+\Lambda$ channel. The comparison with GRAAL is again very good with a large increase in the number of angular bins, each with generally smaller error bars. The comparison with the LEPS data at forward angles is also very good with only the high energy results displaying slight inconsistencies.

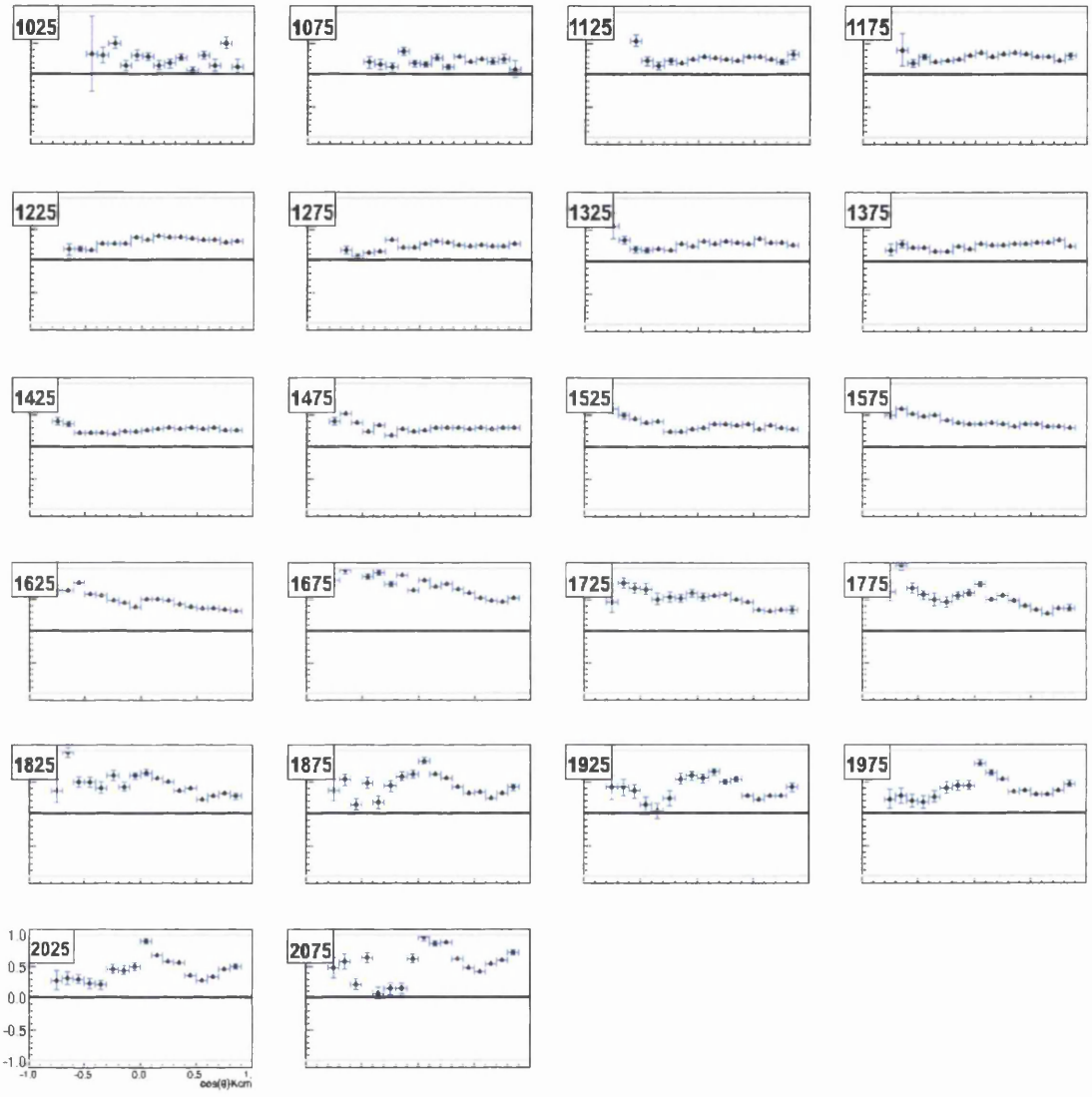

Figure 7.1: Photon asymmetries for the reaction $\gamma p \rightarrow K^+\Lambda$ as a function of $cos\theta^{K^+}_{cm}$ ranging from $E_\gamma = 1.025$ GeV (top left) to 2.075 GeV (bottom right). The photon energies are displayed in MeV in the top left boxes.

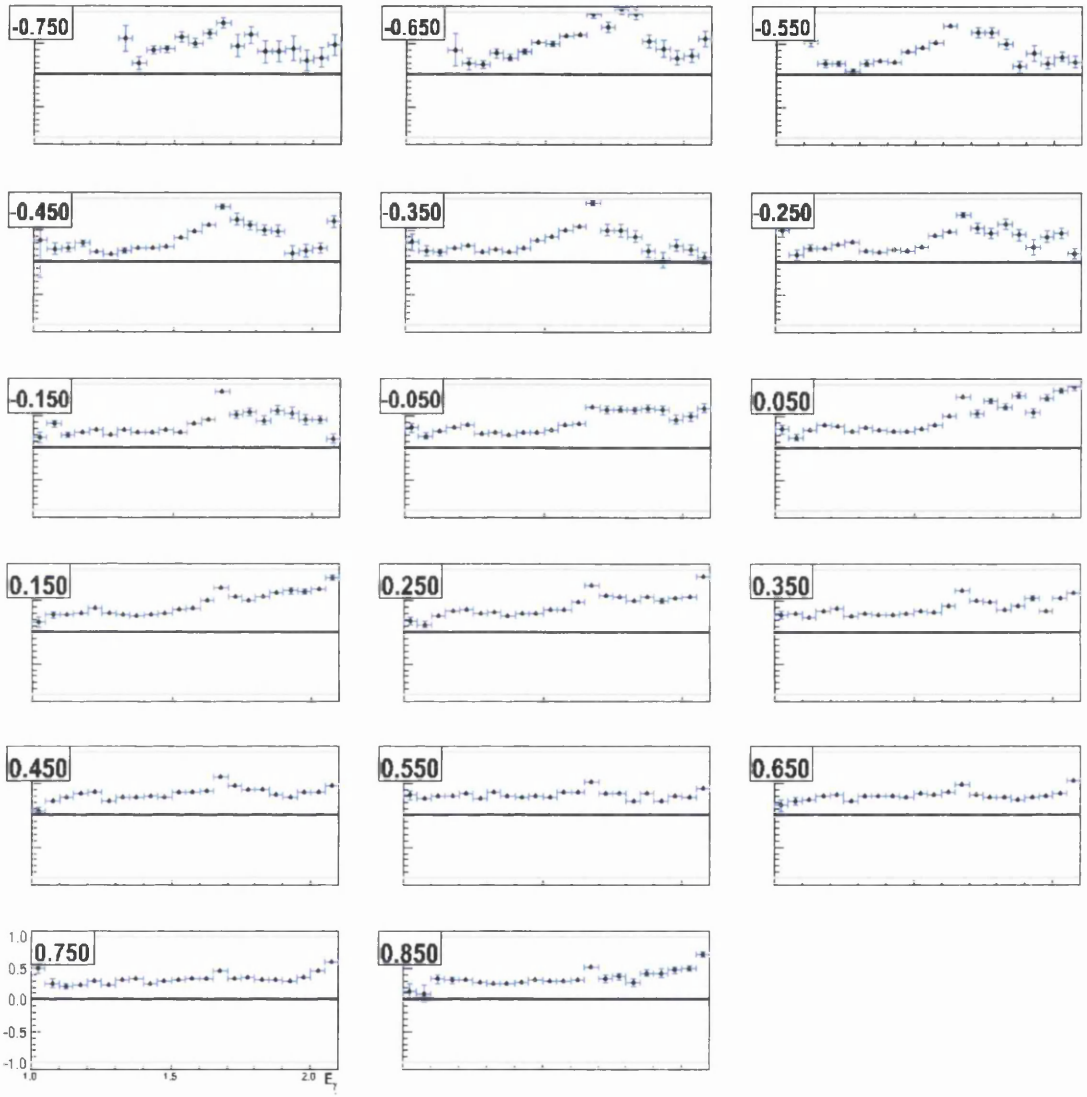

Figure 7.2: Photon asymmetries for the reaction $\gamma p \rightarrow K^+\Lambda$ as a function of E_γ ranging from $cos\theta^{K^+}_{cm}$ = -0.750 (top left) to 0.850 (bottom right) with the angles displayed in the top left box.

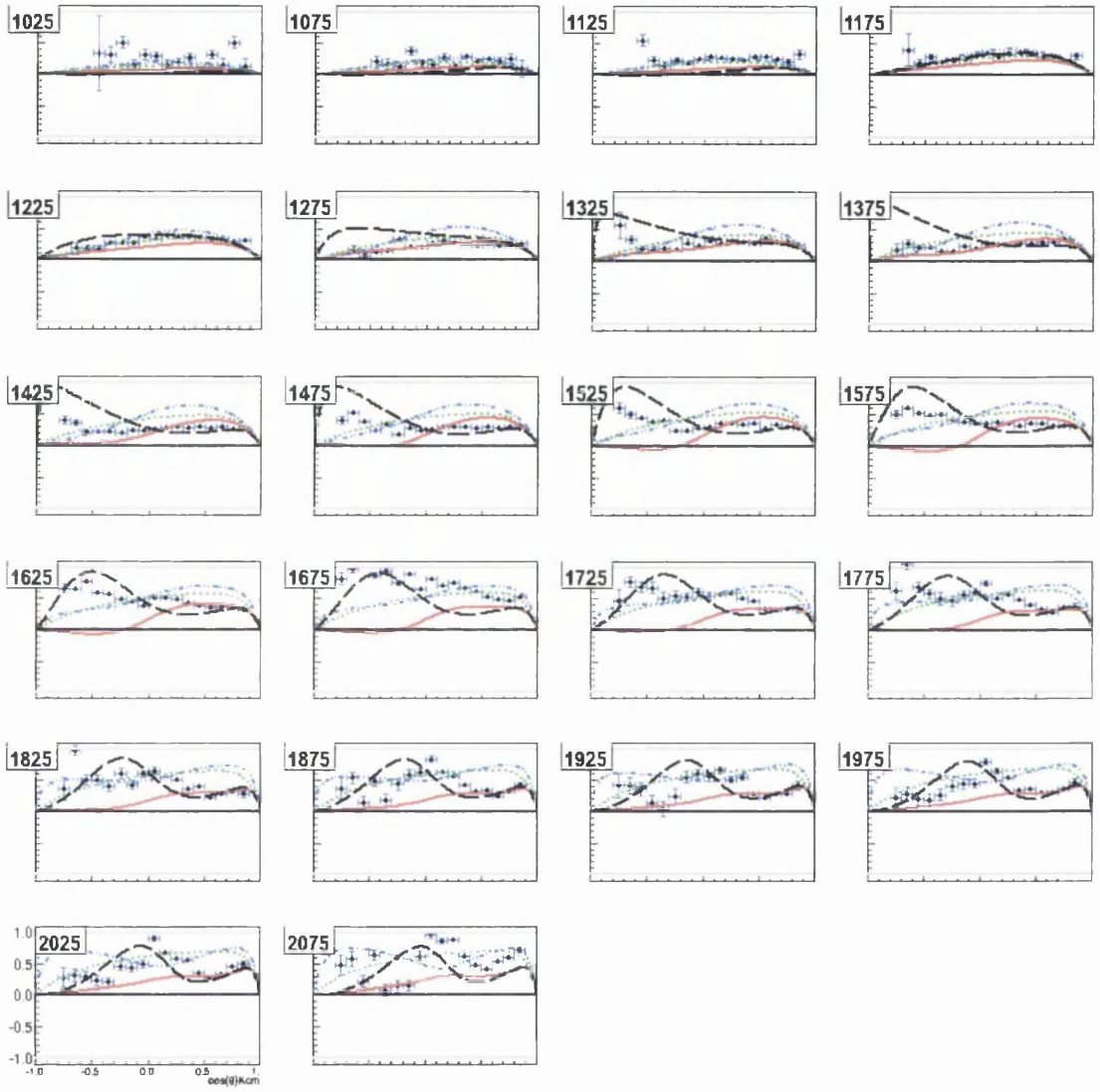

Figure 7.3: Photon asymmetries for the reaction $\gamma p \rightarrow K^+\Lambda$ as a function of $cos\theta^{K^+}_{cm}$ ranging from E_γ = 1.075 GeV (top left) to 2.075 GeV (bottom right). Data are compared with model curves from the Gent Regge-plus-resonance model: Regge background (dotted green line), core resonances (dot-dash blue line), $D_{13}(1900)$ (solid red line) and $P_{11}(1900)$ (dashed black line).

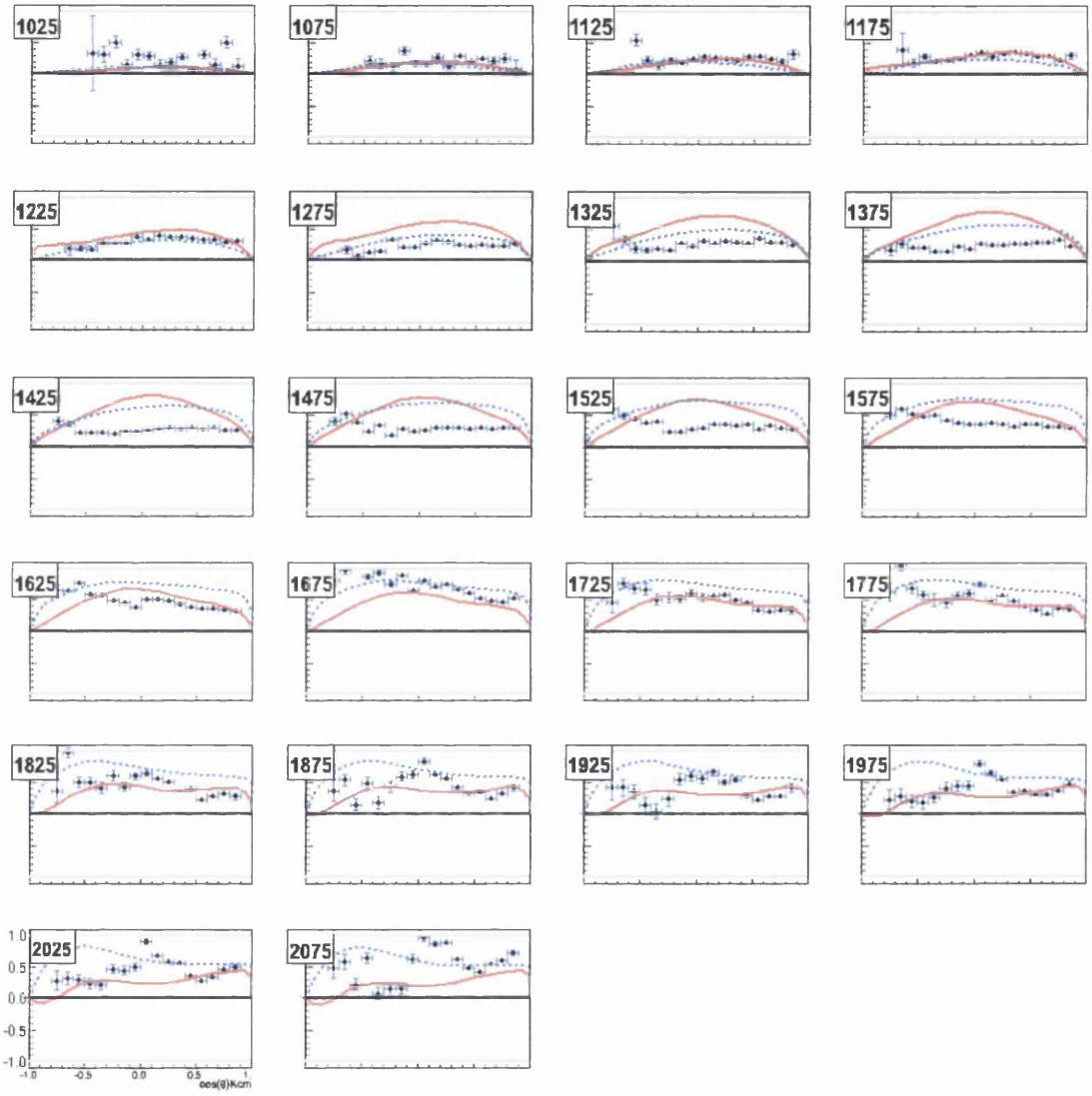

Figure 7.4: Photon asymmetries for the reaction $\gamma p \rightarrow K^+\Lambda$ as a function of $cos\theta_{cm}^{K^+}$ ranging from $E_\gamma = 1.025$ GeV (top left) to 2.075 GeV (bottom right). Data are compared with model curves from the Kaon-MAID isobar model: core resonances (dashed blue line) and $D_{13}(1900)$ (solid red line).

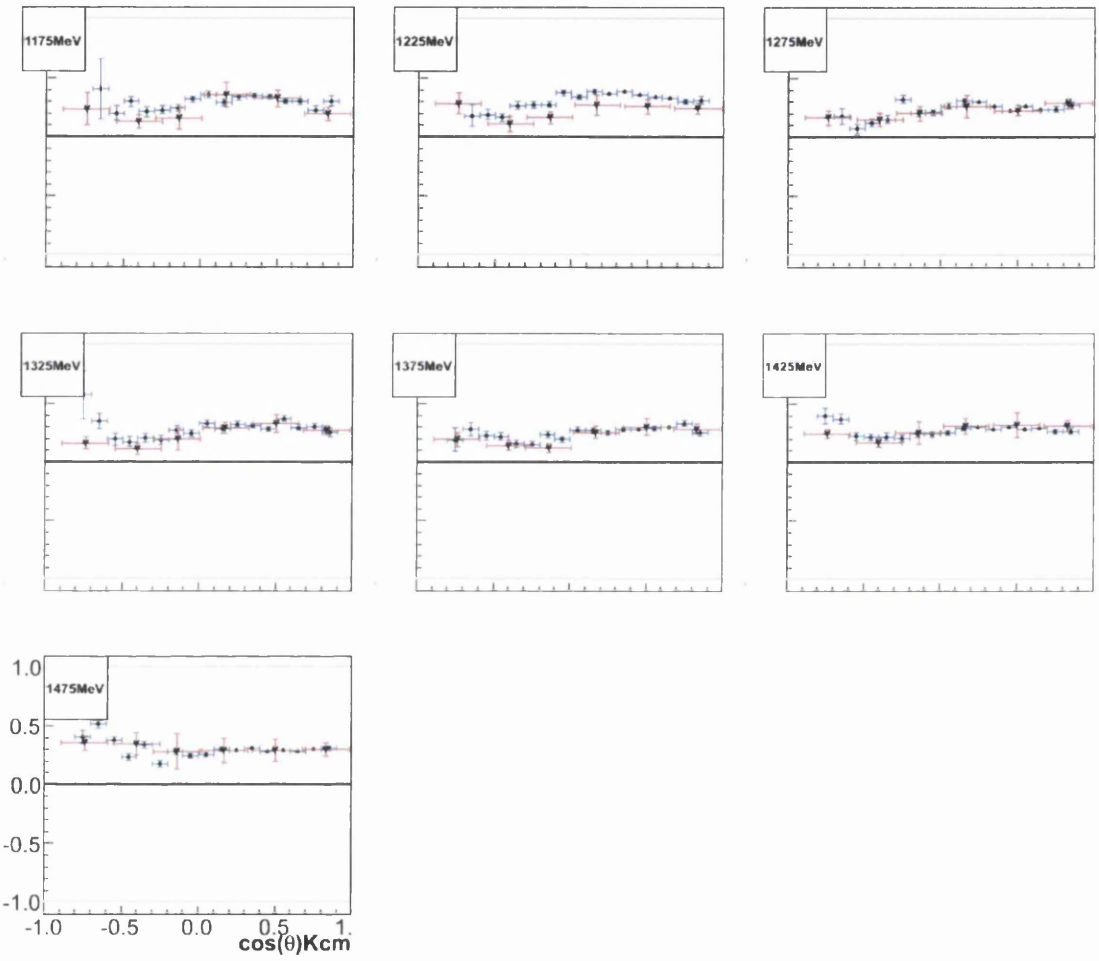

Figure 7.5: Photon asymmetries for the reaction $\gamma p \rightarrow K^+\Lambda$ as a function of $cos\theta^{K^+}_{cm}$ ranging from $E_\gamma = 1.175$ (top left) to 1.475 GeV (bottom right). Blue lines with circles are data points from this analysis and the triangles with red lines are from GRAAL.

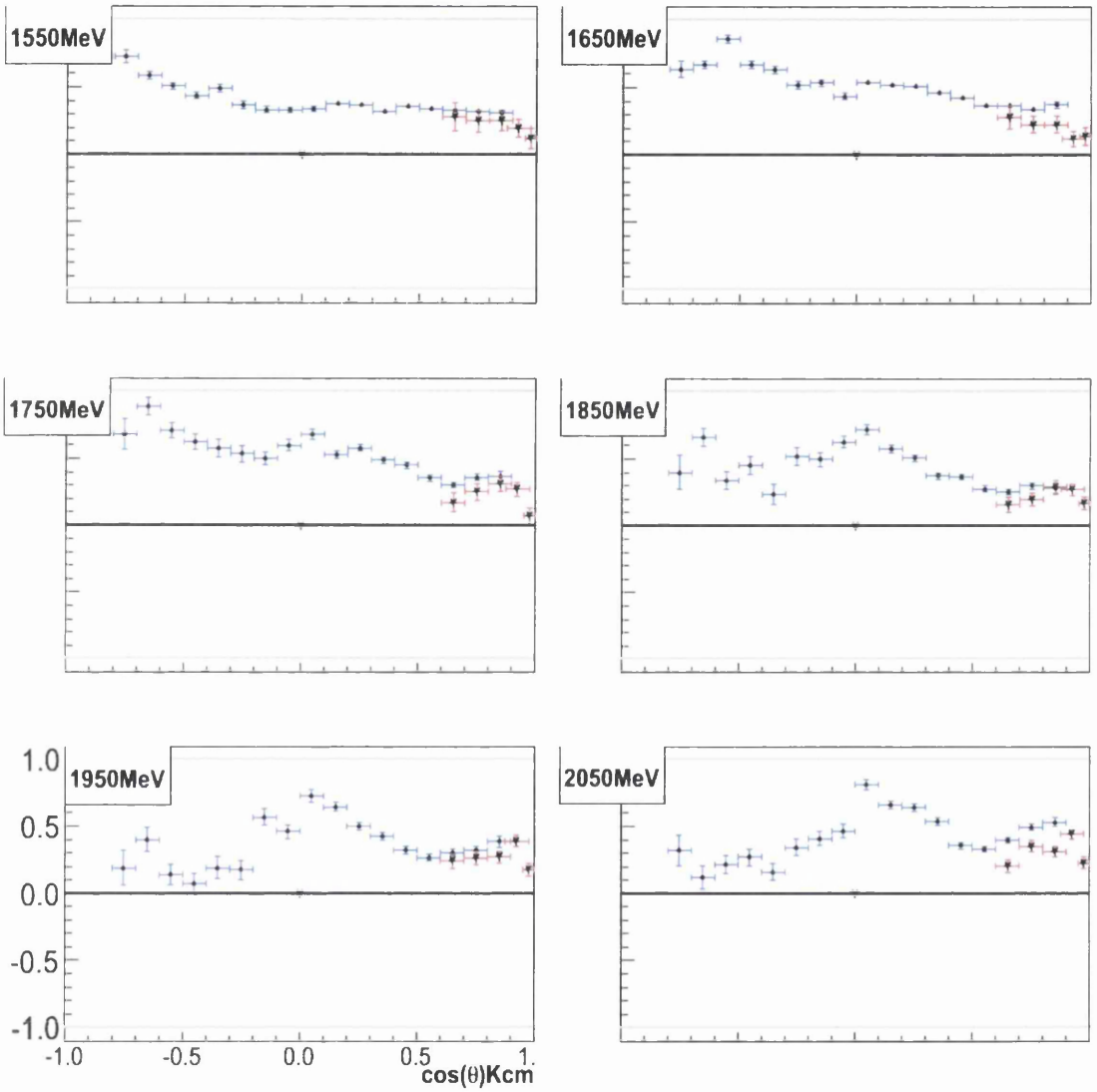

Figure 7.6: Photon asymmetries for the reaction $\gamma p \rightarrow K^+\Lambda$ as a function of $cos\theta^{K^+}_{cm}$ ranging from $E_\gamma = 1.55$ (top left) to 2.05 GeV (bottom right). Blue lines with circles are data points from this analysis and the triangles with red lines are from LEPS.

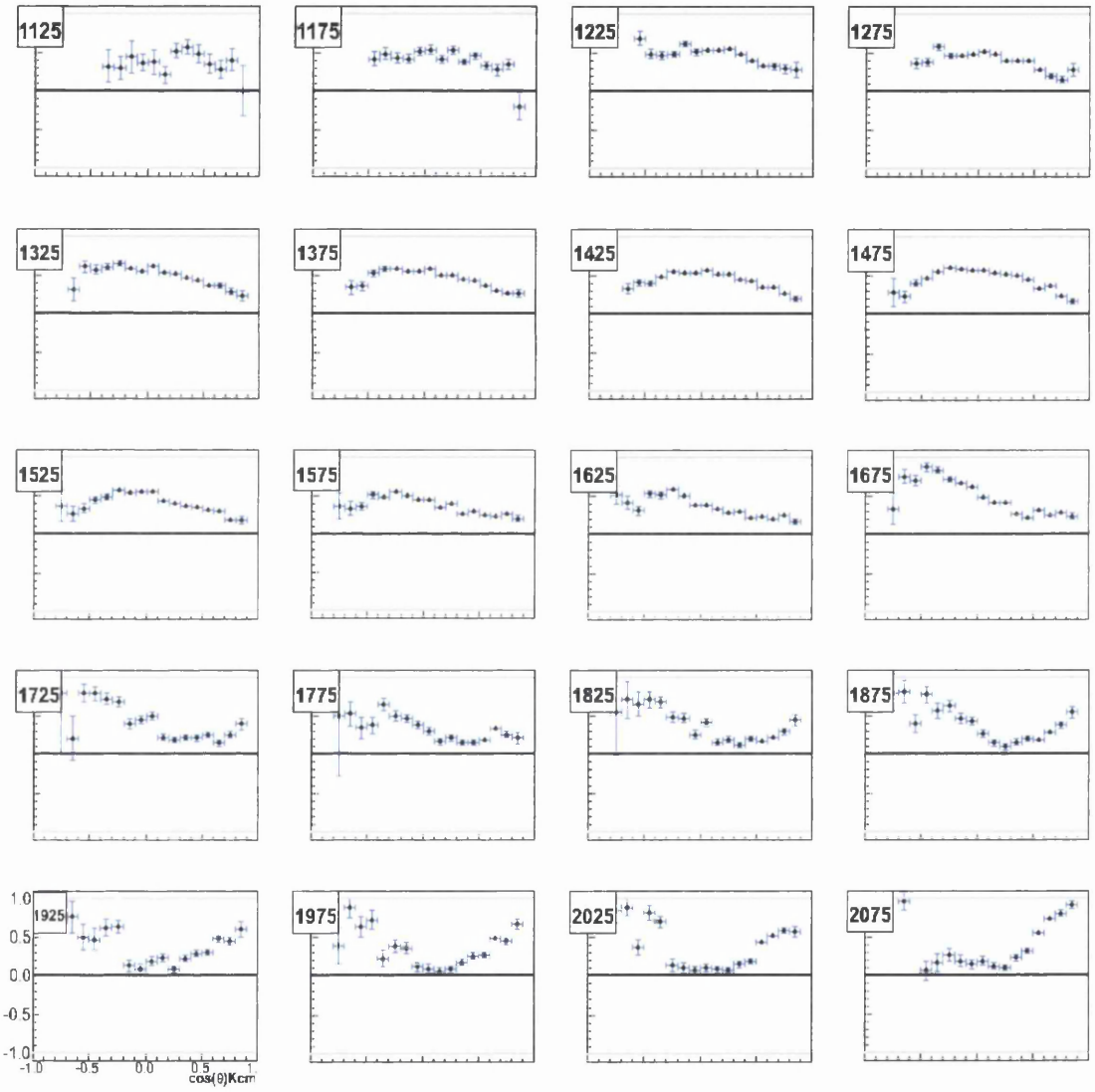

Figure 7.7: Photon asymmetries for the reaction $\gamma p \rightarrow K^+\Sigma^0$ as a function of $cos\theta^{K^+}_{cm}$ ranging from E_γ=1.125 GeV (top left) to 2.075 GeV (bottom right)

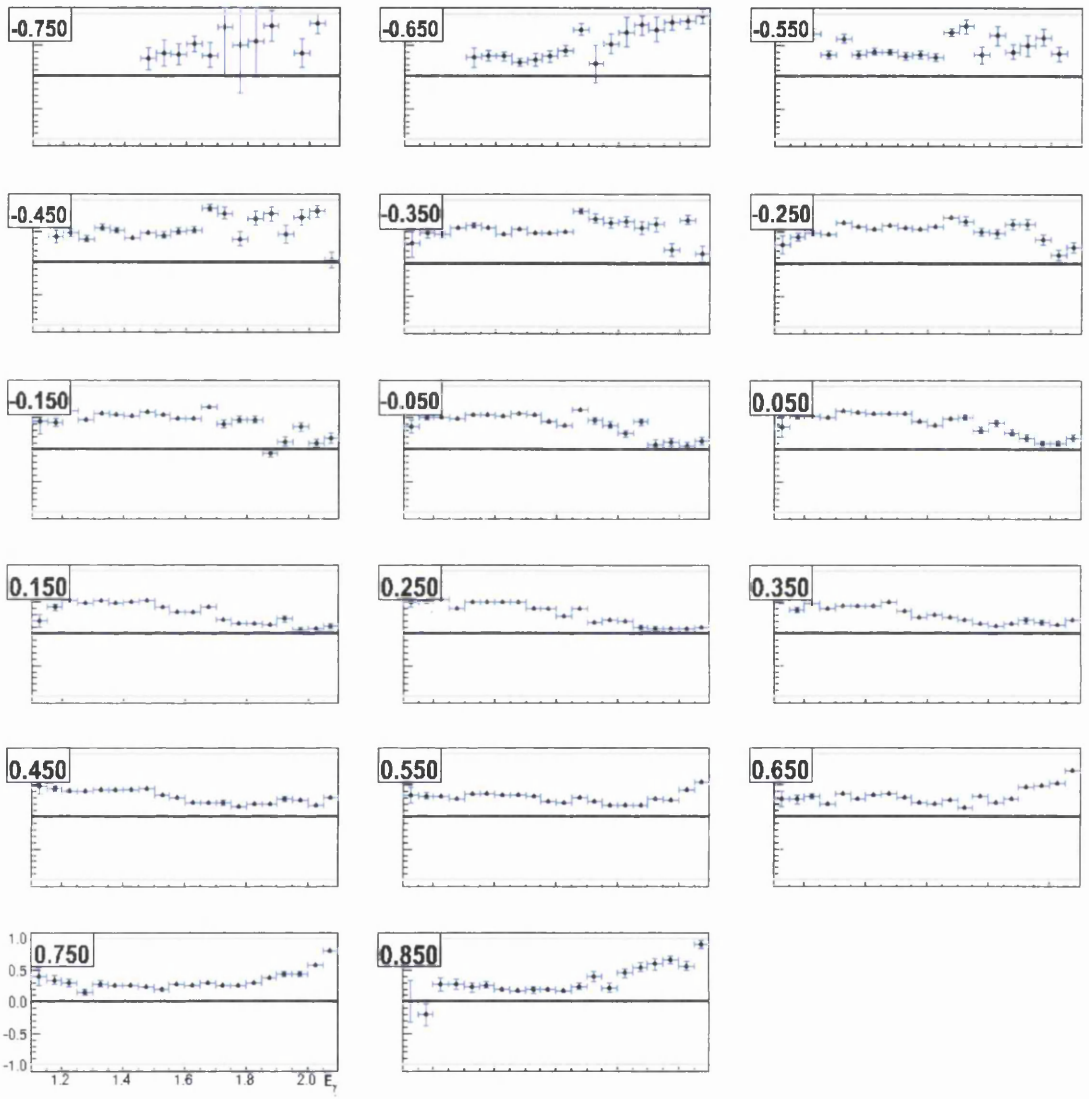

Figure 7.8: Photon asymmetries for the reaction $\gamma p \rightarrow K^+\Sigma^0$ as a function of E_γ ranging from $cos\theta^{K^+}_{cm}$ = -0.750 (top left) to 0.850 (bottom right)

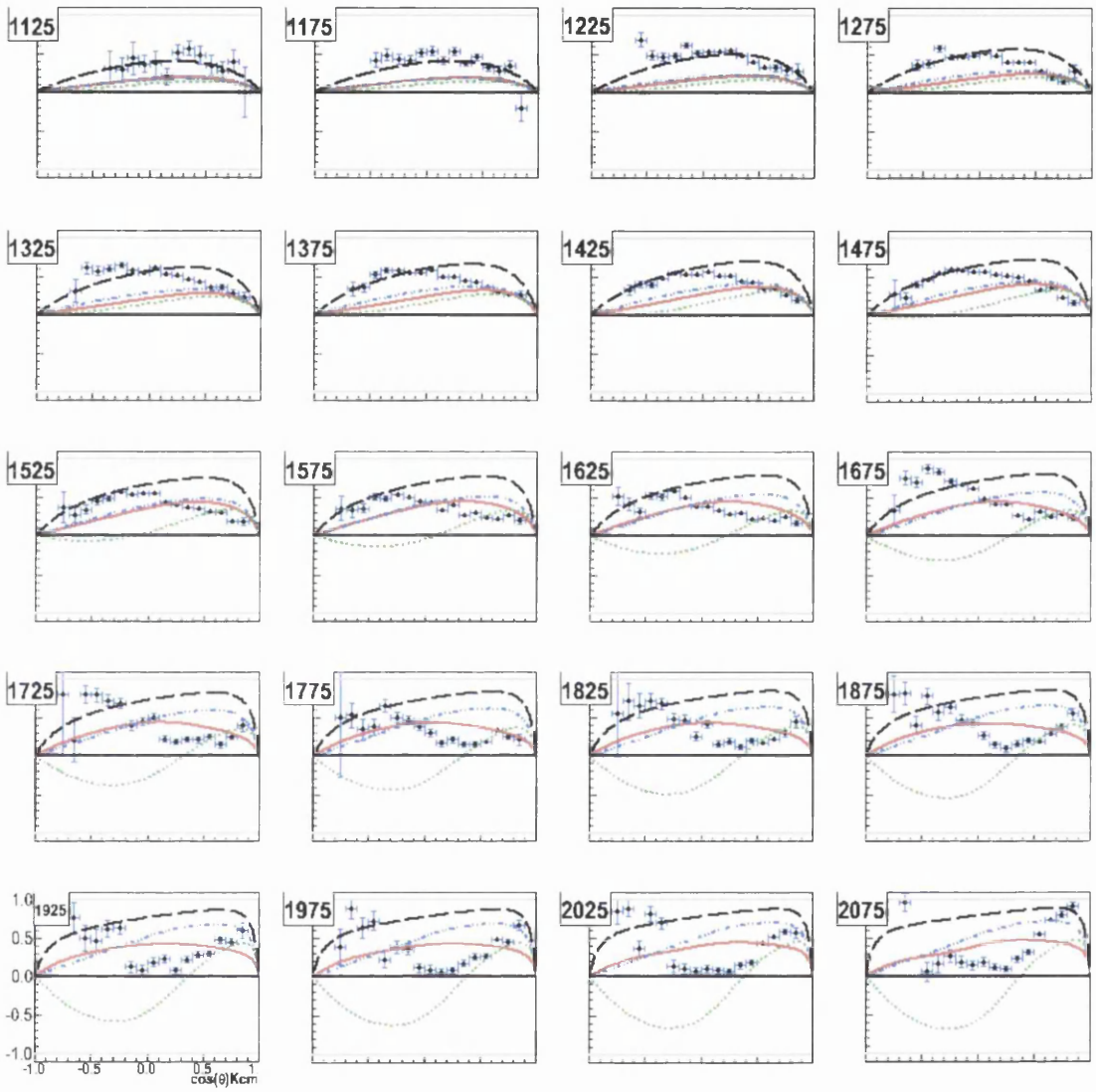

Figure 7.9: Photon asymmetries for the reaction $\gamma p \rightarrow K^+\Sigma^0$ as a function of $cos\theta^{K^+}_{cm}$ ranging from $E_\gamma = 1.125$ (top left) to 2.075 GeV (bottom right). Data are compared with model curves from the Gent Regge-plus-resonance model: RPR-3 background (dotted green line), RPR-3 core (solid red line), RPR-4 background (dashed black line) and RPR-4 core (dot-dashed blue line).

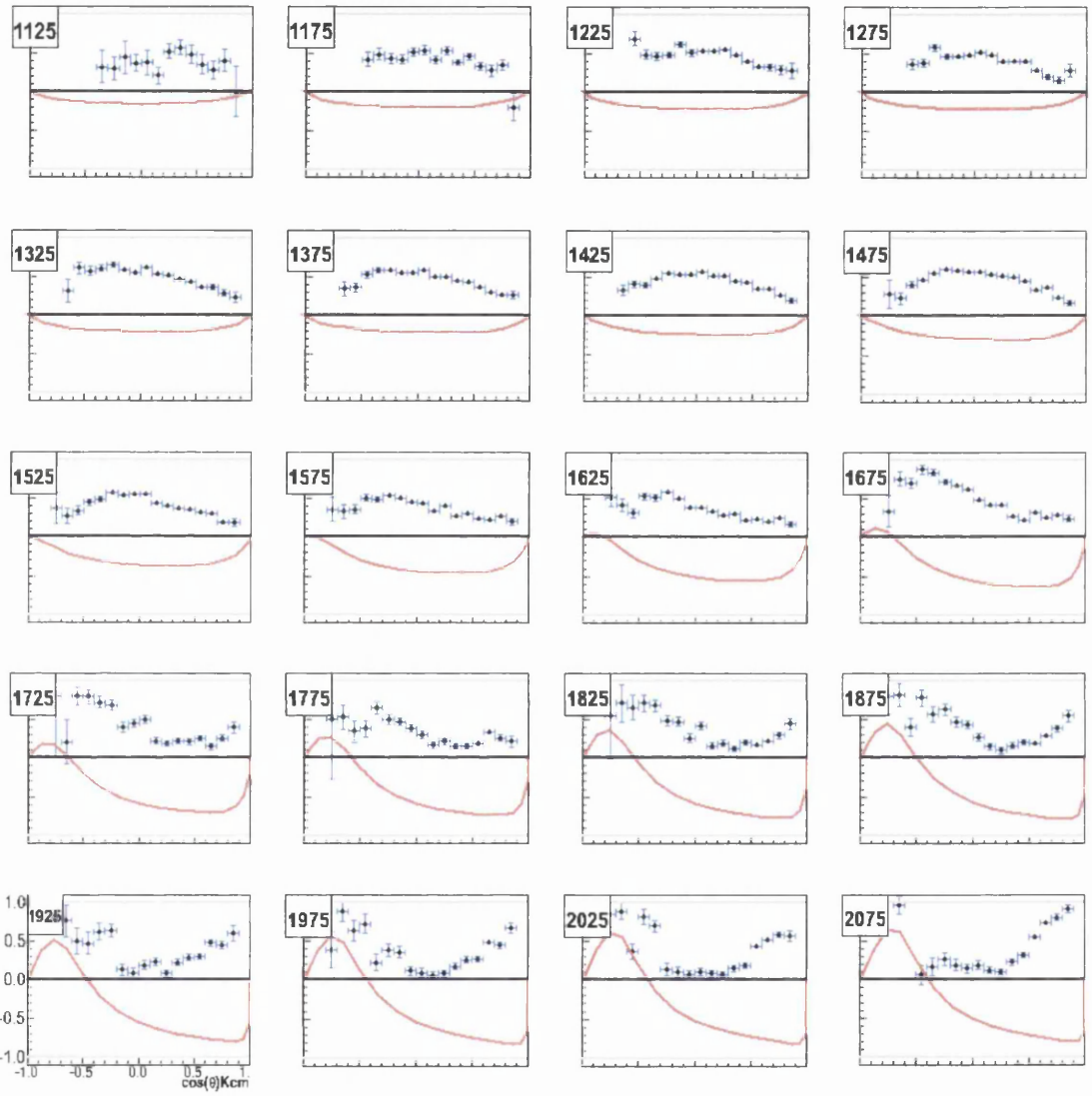

Figure 7.10: Photon asymmetries for the reaction $\gamma p \rightarrow K^+\Sigma^0$ as a function of $cos\theta^{K^+}_{cm}$ ranging from E_γ = 1.125 (top left) to 2.075 GeV (bottom right). Data are compared with model curves from the Kaon-MAID isobar model with a core set of resonances included (solid red line).

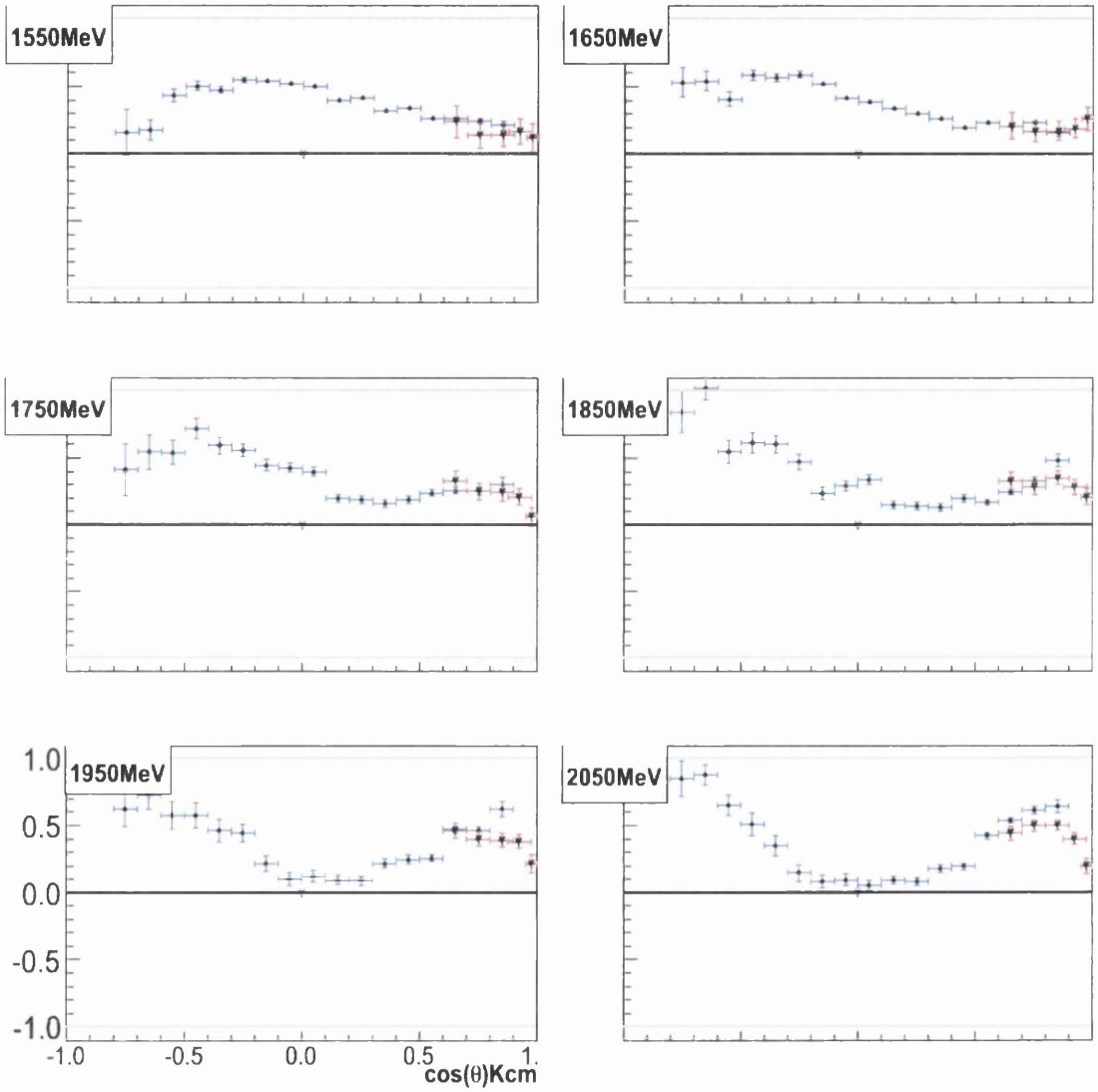

Figure 7.11: Photon asymmetries for the reaction $\gamma p \rightarrow K^+\Sigma^0$ as a function of $cos\theta^{K^+}_{cm}$ ranging from $E_\gamma = 1.55$ (top left) to 2.05 GeV (bottom right). Blue lines with circles are data points from this analysis and the triangles with red lines are from LEPS.

7.2 Double Polarization Observables, O_x and O_z

The double polarization observables, O_x and O_z, are compared to the Gent Regge-plus-resonance calculations for the $K^+\Lambda$ channel as a function of the centre-of-mass kaon angle $cos\theta^K_{cm}$ in figures 7.12 and 7.13. The results are compared to the Kaon-MAID solutions in figures 7.14 and 7.15, and then plotted as a function of E_γ in figures 7.16 and 7.17. Corresponding plots are shown for the $K^+\Sigma^0$ channel in figures 7.18 through 7.23.

7.2.1 Discussion of O_x/O_z results for $K^+\Lambda$

The most striking feature of the $K^+\Lambda$ results is the strong polarization signal for O_x at forward angles for all photon energies. This suggests that for mid to forward angles the reaction transfers almost 100% of the photon polarization to the Λ along the x-axis, as defined in the unprimed coordinate system. In contrast to this the O_z observables display only minimal polarization transfer for most of the kinematic range. When comparing with the RPR predictions for O_x in figure 7.12, it can be seen that the calculation including the $D_{13}(1900)$ state gives very good agreement with the data for energies above 1.35 GeV. It can also be readily seen that Regge background calculation is almost flat with zero polarization transfer for all kinematics, showing that the inclusion of s-channel resonances is essential to reproducing the experimental results. For the O_x results the $D_{13}(1900)$ calculation is again the most successful with some disagreement with the data evident at backward angles at energies above 1.55 GeV.

Figures 7.14 and 7.15 show comparisons with Kaon-MAID for both O_x and O_z respectively. As in the case of the RPR approach the $D_{13}(1900)$ resonance is required to reproduce the large polarizations at forward angles and high energies for O_x. However, the model calculations from Kaon-MAID, even with the inclusion of the $D_{13}(1900)$, fail to reproduce these strong polarizations at energies below 1.45 GeV. For the O_z results it is the calculation using just the core resonances that agrees best with the data, with the inclusion of the $D_{13}(1900)$ causing the polarization transfer to be too large at backward angles.

7.2.2 Discussion of O_x/O_z results for $K^+\Sigma^0$

The first obvious feature of the $K^+\Sigma^0$ results, shown in figures 7.18 and 7.19 compared to the RPR calculations, is the much coarser angular binning that has been used to cope with the dilution of the polarization. Despite reducing the number of bins by a factor of four the statistical uncertainty is still larger

than for the $K^+\Lambda$ results. The agreement between the RPR calculations and the data for O_x is somewhat poor except at forward angles where most of the model curves agree reasonably well. For O_z the agreement is much better, with the two RPR-3 prescriptions giving a good comparison. Overall, the large error bars for this channel, coupled with the similar predictions for all the model calculations, makes discrimination between the different curves very difficult on the basis of the $K^+\Sigma^0$ results only.

For the Kaon-MAID predictions, shown in figures 7.20 and 7.21, the general trend of the data for O_x is reproduced well. For O_z, the trend is again reproduced but the magnitude of the polarization transfer, particularly at the lower energies, doesn't compare so well.

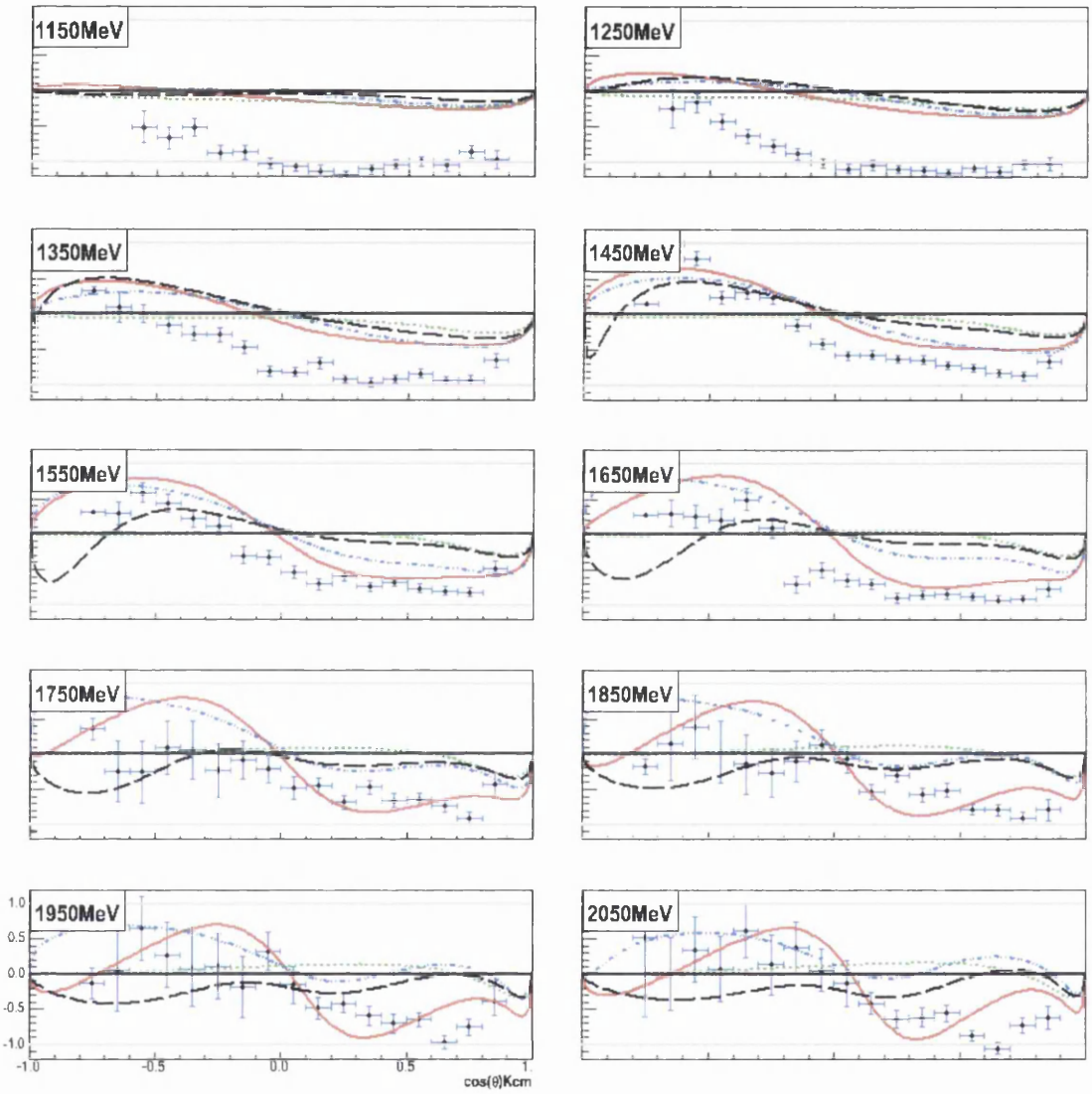

Figure 7.12: O_x double polarization observable for the reaction $\gamma p \rightarrow K^+\Lambda$ as a function of $cos\theta^{K^+}_{cm}$ ranging from $E_\gamma = 1.150$ (top left) to 2.050 GeV (bottom right). Data are compared with model curves from the Gent Regge-plus-resonance model: Regge background (dotted green line), core resonances (dot-dash blue line), $D_{13}(1900)$ (solid red line) and $P_{11}(1900)$ (dashed black line).

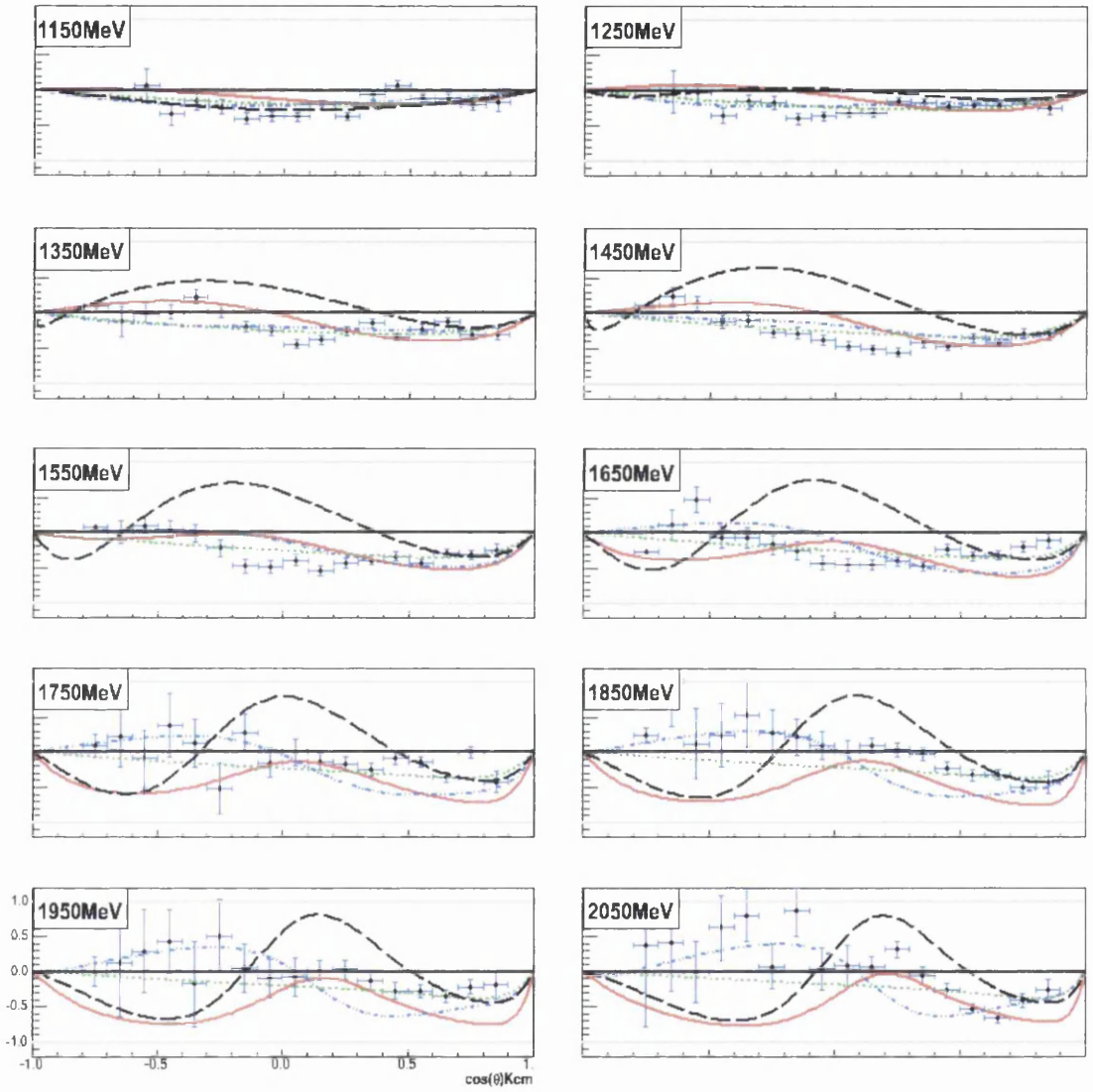

Figure 7.13: O_z double polarization observable for the reaction $\gamma p \rightarrow K^+\Lambda$ as a function of $cos\theta^{K^+}_{cm}$ ranging from $E_\gamma = 1.150$ (top left) to 2.050 GeV (bottom right). Data are compared with model curves from the Gent Regge-plus-resonance model: Regge background (dotted green line), core resonances (dot-dash blue line), $D_{13}(1900)$ (solid red line) and $P_{11}(1900)$ (dashed black line).

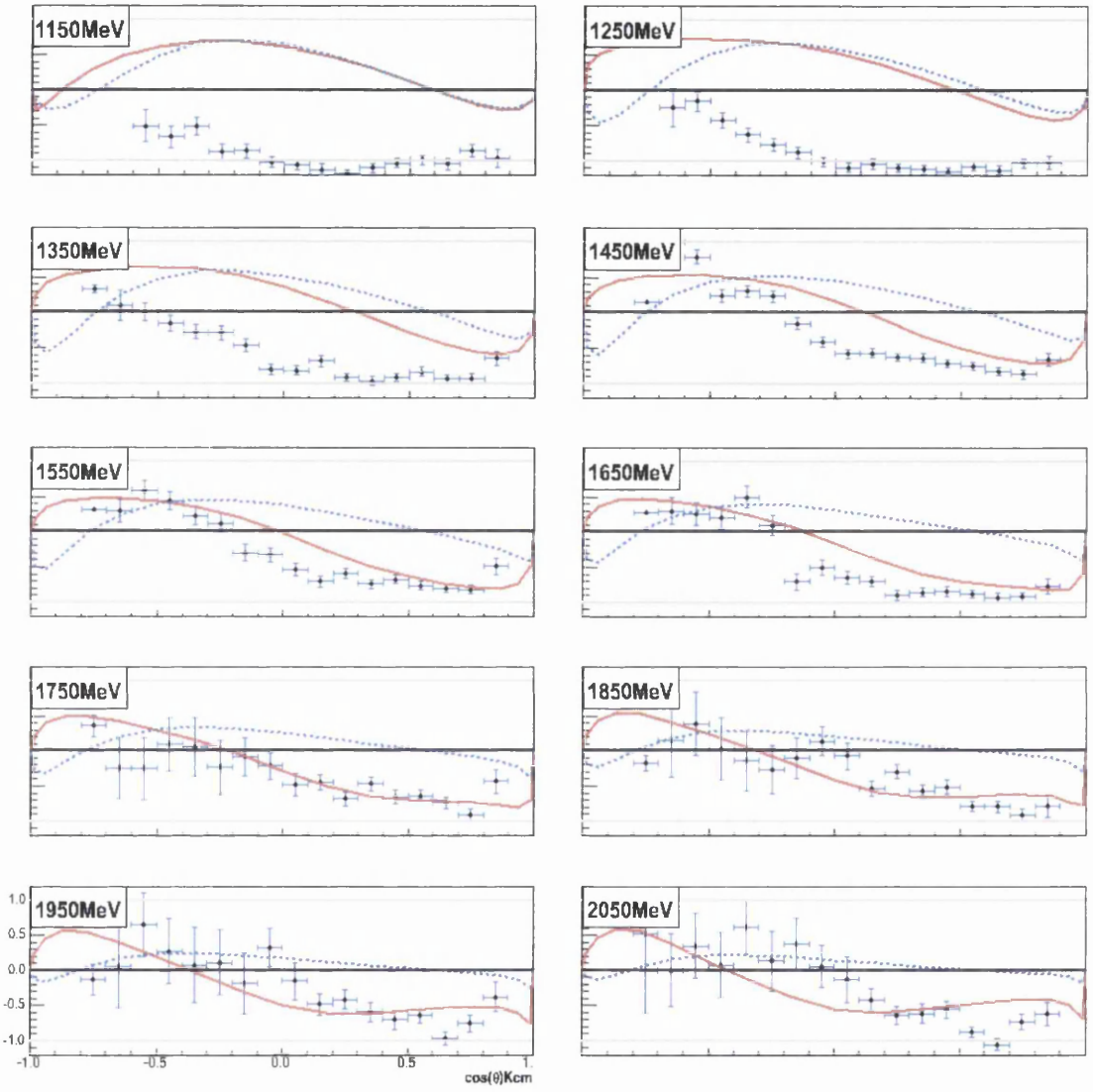

Figure 7.14: O_x double polarization observable for the reaction $\gamma p \rightarrow K^+\Lambda$ as a function of $cos\theta^{K^+}_{cm}$ ranging from $E_\gamma = 1.15$ (top left) to 2.05 GeV (bottom right). Data are compared with model curves from the Kaon-MAID isobar model: core resonances (dashed blue line) and $D_{13}(1900)$ (solid red line).

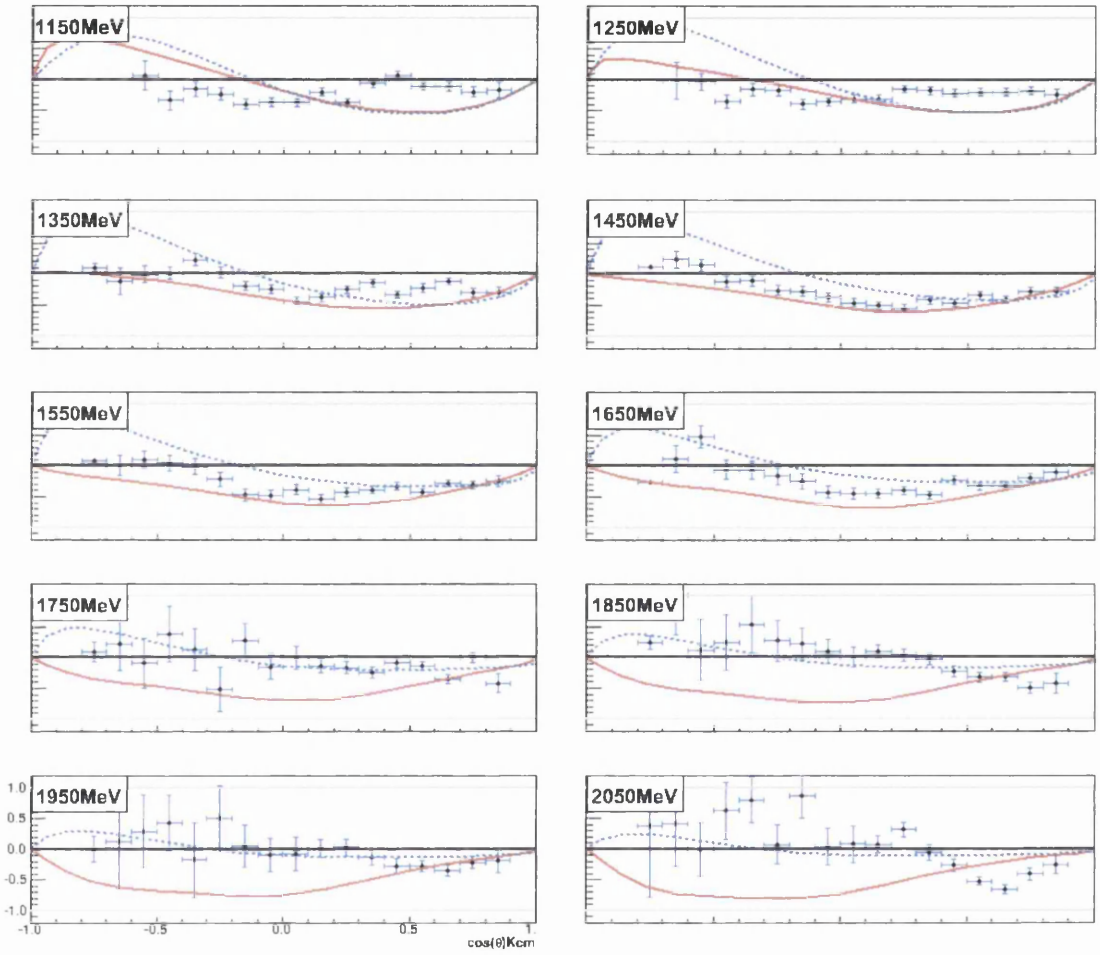

Figure 7.15: O_z double polarization observable for the reaction $\gamma p \rightarrow K^+\Lambda$ as a function of $cos\theta^{K^+}_{cm}$ ranging from $E_\gamma = 1.15$ (top left) to 2.05 GeV (bottom right). Data are compared with model curves from the Kaon-MAID isobar model: core resonances (dashed blue line) and $D_{13}(1900)$ (solid red line).

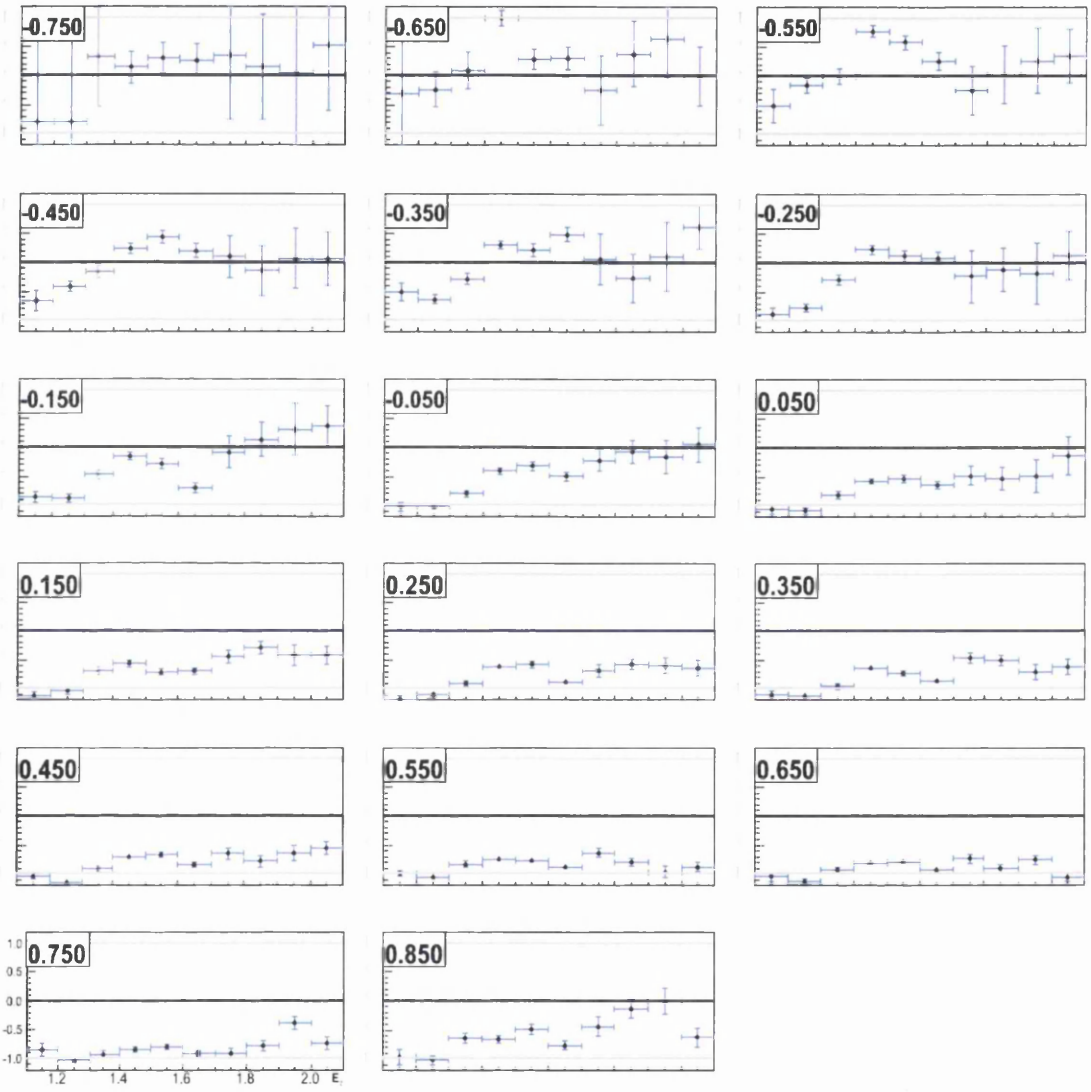

Figure 7.16: O_x double polarization observable for the reaction $\gamma p \rightarrow K^+\Lambda$ as a function of E_γ ranging from $cos\theta^{K^+}_{cm}$ = -0.750 (top left) to 0.850 (bottom right).

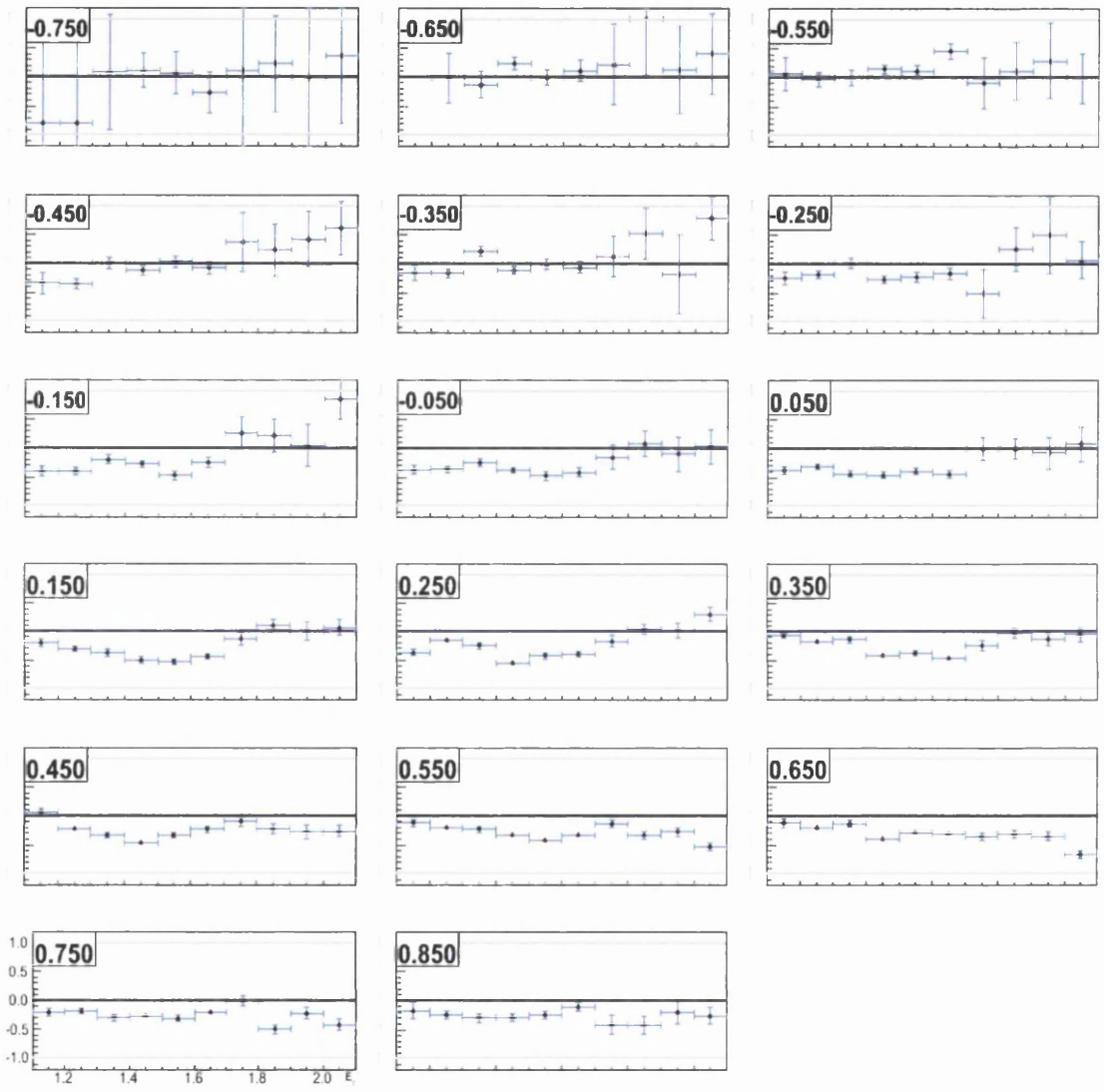

Figure 7.17: O_z double polarization observable for the reaction $\gamma p \rightarrow K^+\Lambda$ as a function of E_γ ranging from $cos\theta_{cm}^{K^+}$ = -0.750 (top left) to 0.850 (bottom right)

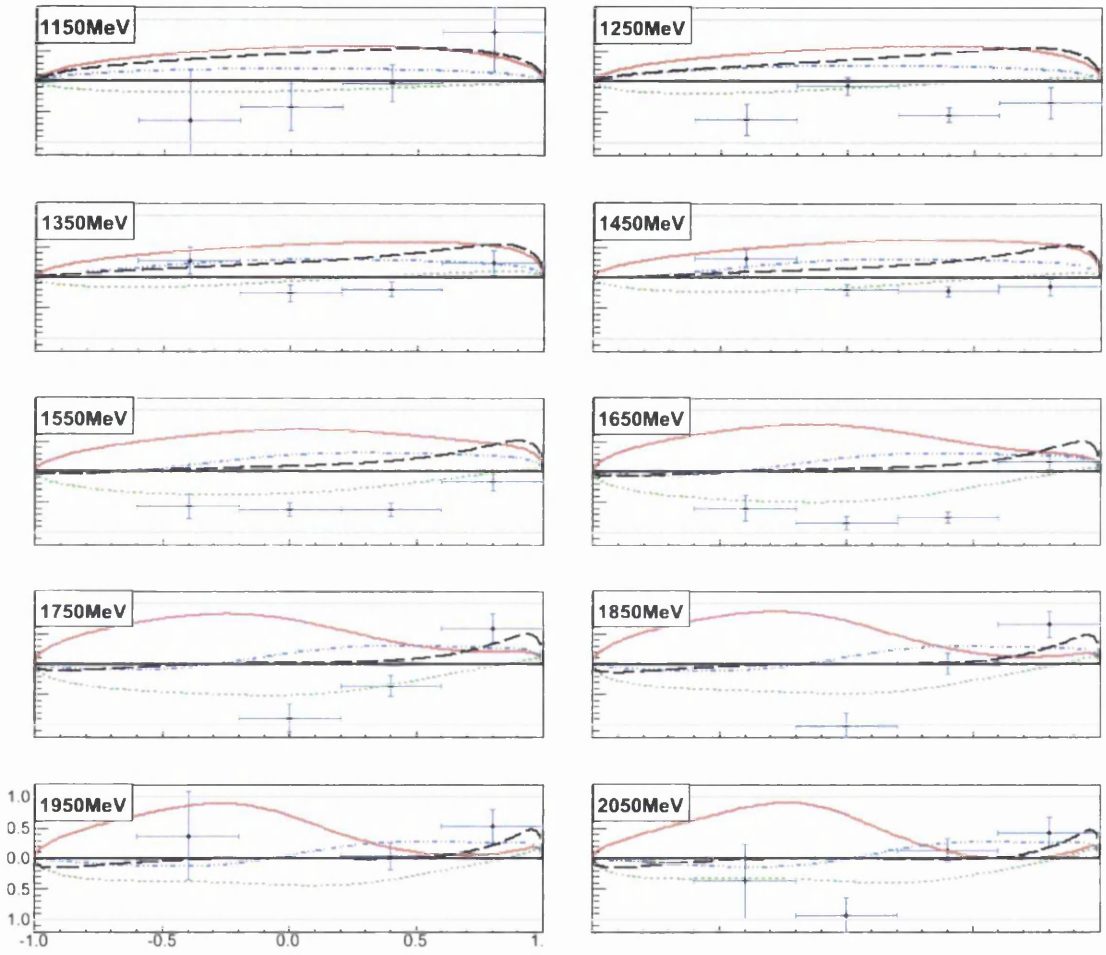

Figure 7.18: O_x double polarization asymmetry for the reaction $\gamma p \rightarrow K^+\Sigma^0$ as a function of $cos\theta_{cm}^{K^+}$ ranging from $E_\gamma = 1.15$ (top left) to 2.05 GeV (bottom right). Data are compared with model curves from the Gent Regge-plus-resonance model: RPR-3 background (dotted green line), RPR-3 core (solid red line), RPR-4 background (dashed black line) and RPR-4 core (dot-dashed blue line).

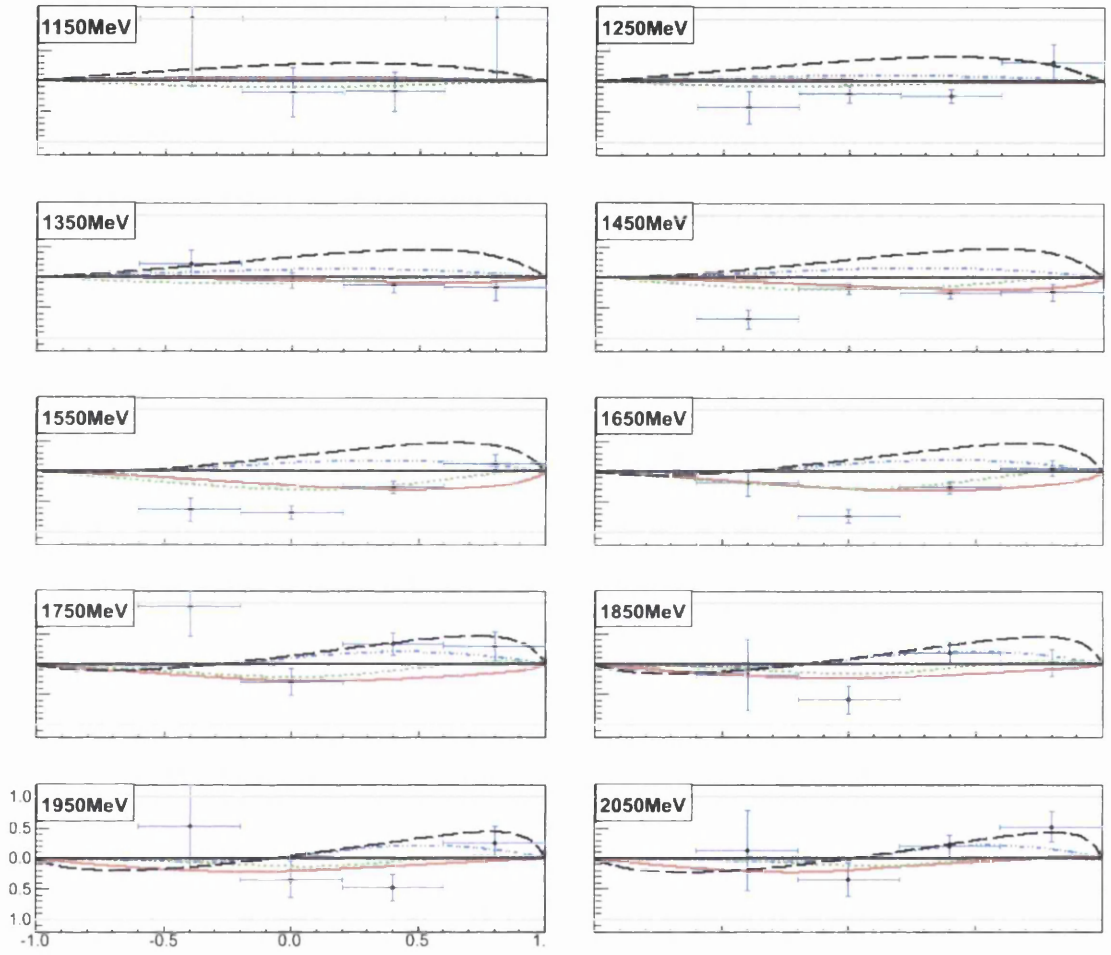

Figure 7.19: O_z double polarization asymmetry for the reaction $\gamma p \rightarrow K^+\Sigma^0$ as a function of $cos\theta_{cm}^{K^+}$ ranging from $E_\gamma = 1.15$ (top left) to 2.05 GeV (bottom right). Data are compared with model curves from the Gent Regge-plus-resonance model: RPR-3 background (dotted green line), RPR-3 core (solid red line), RPR-4 background (dashed black line) and RPR-4 core (dot-dashed blue line).

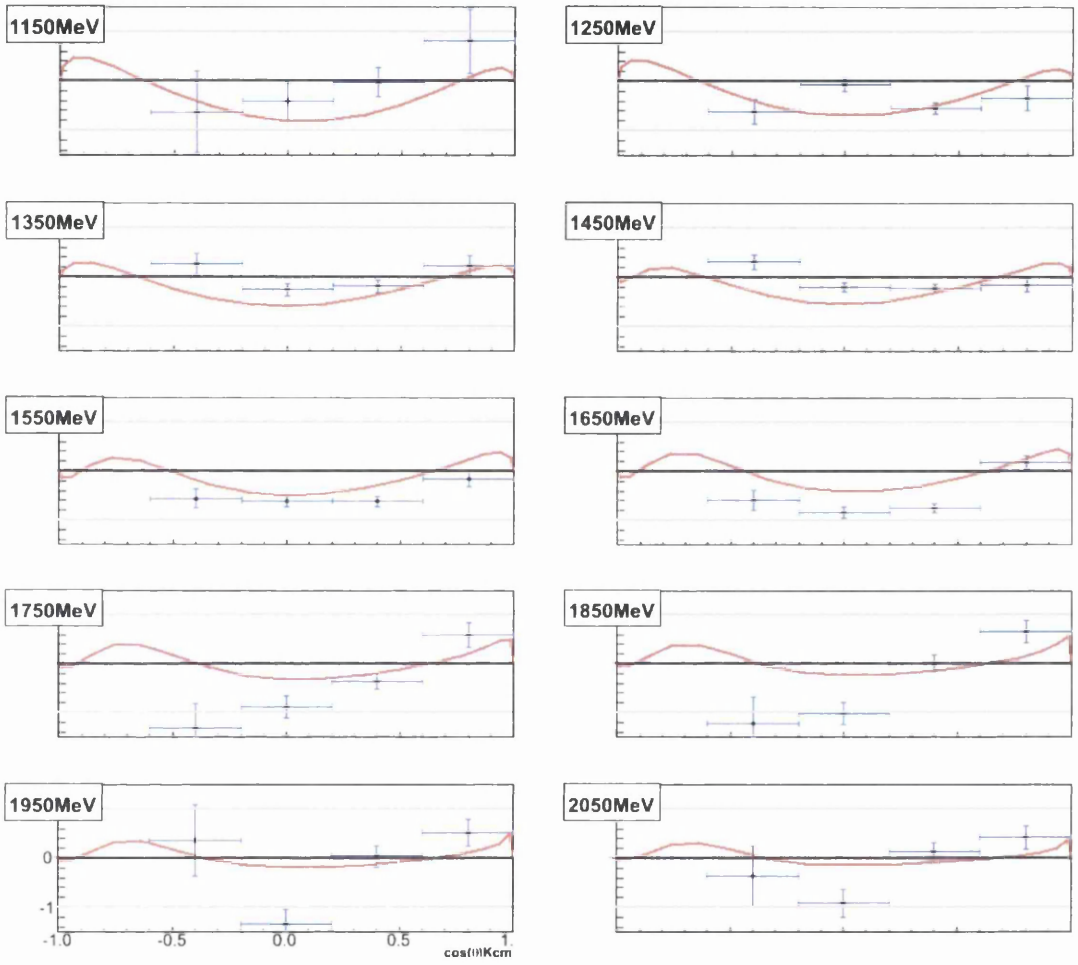

Figure 7.20: O_x double polarization observable for the reaction $\gamma p \rightarrow K^+\Sigma^0$ as a function of $cos\theta^{K^+}_{cm}$ ranging from $E_\gamma = 1.15$ (top left) to 2.05 GeV (bottom right). Data are compared with model curves from the Kaon-MAID isobar model with a core set of resonances included (solid red line).

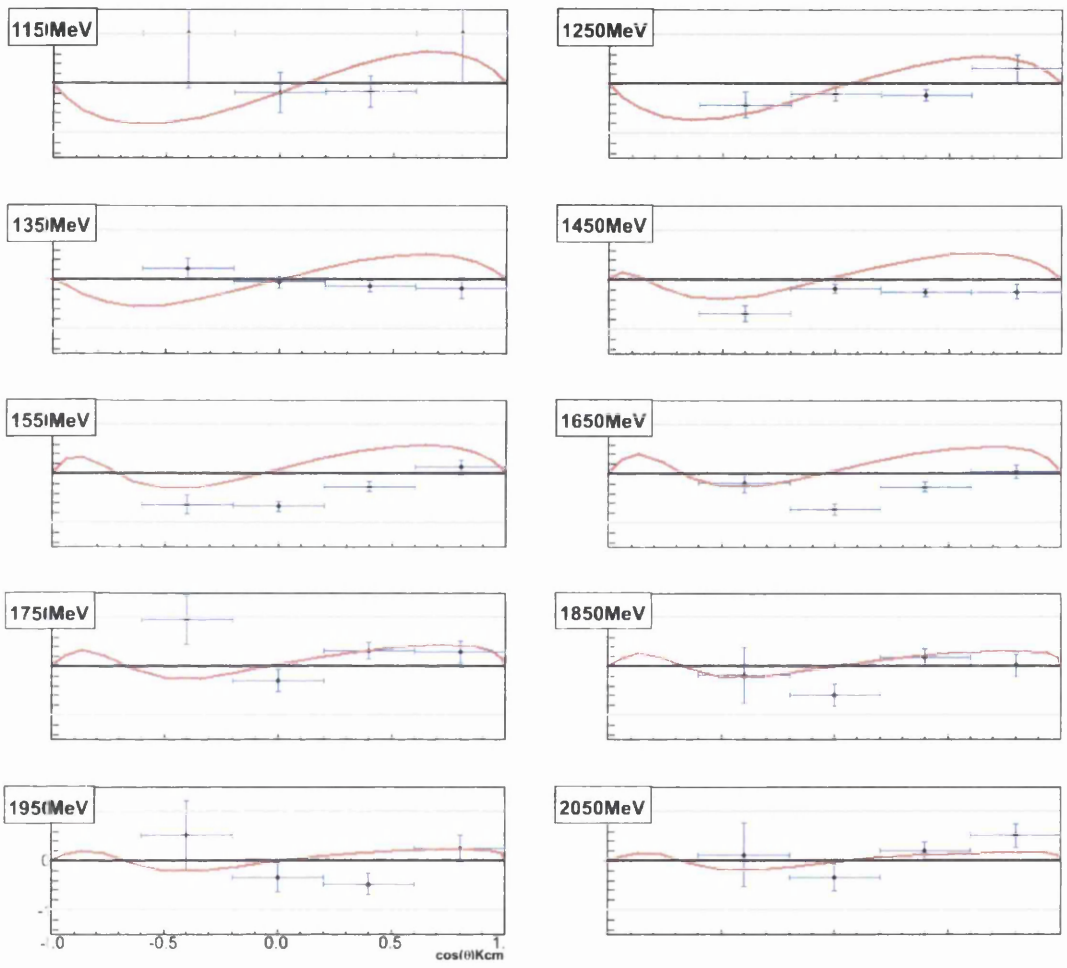

Figure 7.21: O_z double polarization observable for the reaction $\gamma p \rightarrow K^+\Sigma^0$ as a function of $cos\theta^{K^+}_{cm}$ ranging from $E_\gamma = 1.15$ (top left) to 2.05 GeV (bottom right). Data are compared with model curves from the Kaon-MAID isobar model with a core set of resonances included (solid red line).

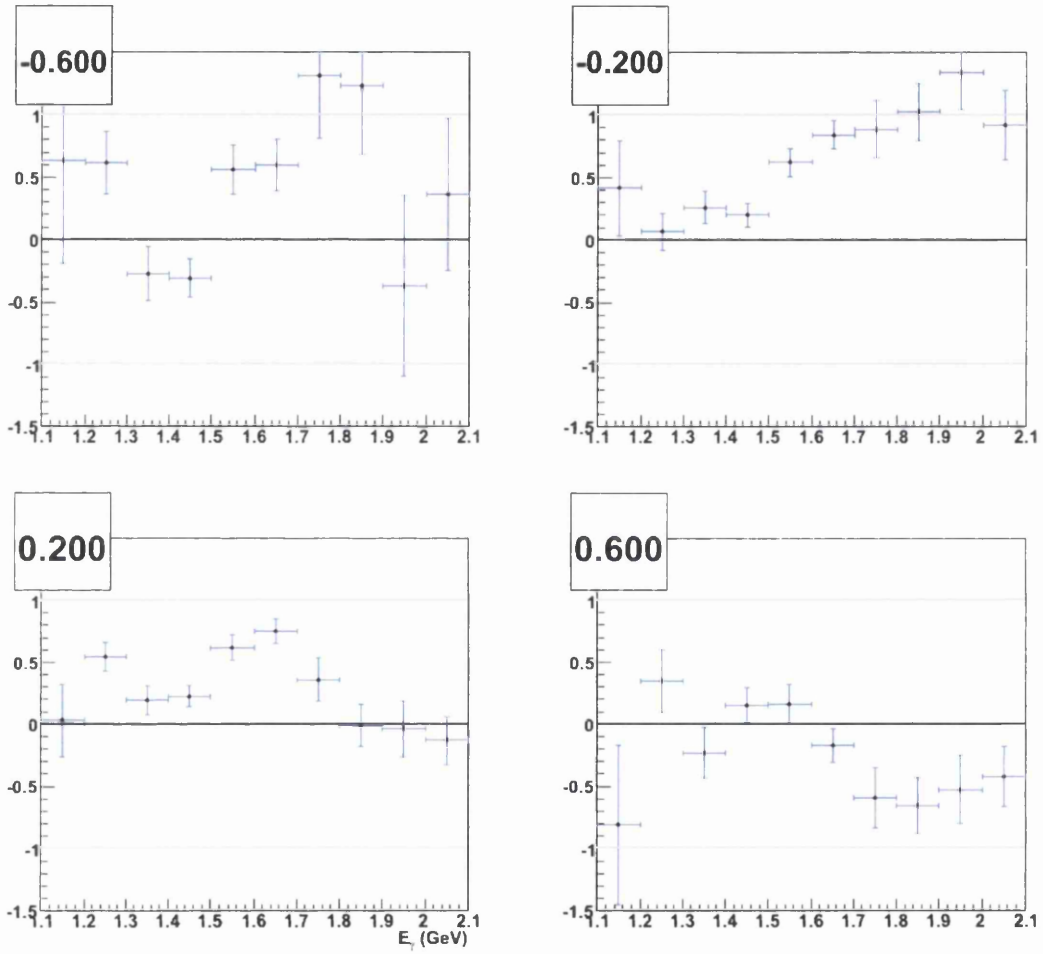

Figure 7.22: O_x for the reaction $\gamma p \rightarrow K^+\Lambda$ as a function of E_γ ranging from $cos\theta^{K^+}_{cm}$ = -0.6 (top left) to 0.6 (bottom right)

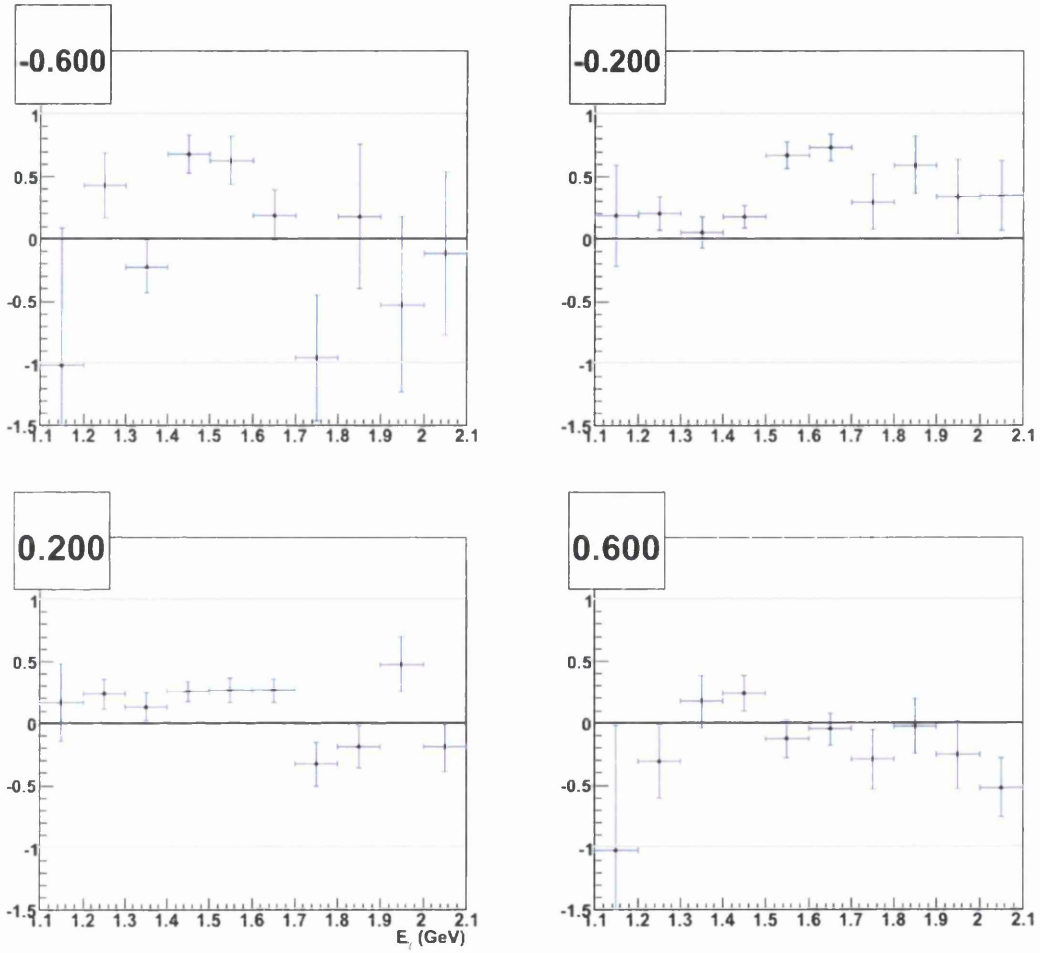

Figure 7.23: O_z for the reaction $\gamma p \rightarrow K^+\Lambda$ as a function of E_γ ranging from $cos\theta^{K^+}_{cm}$ = -0.6 (top left) to 0.6 (bottom right)

7.3 Recoil Polarization

The hyperon recoil polarization (P) is compared to the Gent Regge-plus-resonance calculations for the $K^+\Lambda$ channel as a function of the centre-of-mass kaon angle $cos\theta^K_{cm}$, in 25MeV E_γ bins, in figures 7.24 through 7.27. Figure 7.28 shows P as a function of E_γ, and figure 7.29 displays a comparison with previous measurements from GRAAL and CLAS. Results for the $K^+\Sigma^0$ channel are compared to the RPR calculations in figure 7.30 and are then displayed as a function of E_γ in figure 7.31.

7.3.1 Discussion of recoil polarization results for $K^+\Lambda$

Over a broad range of kinematics the recoil polarization results display a similar trend of having positive polarization at backward angles which becomes negative moving to forward kaon production angles. As shown in figures 7.24 through 7.27 at low energies there is very little discrimination between the different RPR prescriptions. However, at photon energies above 1.287 GeV the $P_{11}(1900)$ state is required to reproduce the large polarizations at backward angles, with all the calculations agreeing well at the very forward angles. At energies between 1.8 and 1.9 GeV the inclusion of the $P_{11}(1900)$ and the $D_{13}(1900)$ states give favourable agreement with the recoil polarization at mid to forward angles but neither can account for the large backward polarizations. As the photon energy increases beyond 1.9 GeV both of the calculations that include the missing states begin to give good agreement with the data over the full angular range. These comparisons suggest that s-channel contributions are required at photon energies above 1.1 GeV with the core resonances plus $P_{11}(1900)$ state giving good agreement for most of the kinematic range, and the core plus $D_{13}(1900)$ calculations agreeing favourably at energies above 1.8 GeV.

There is good agreement between the recoil polarization measurements from this work and those published by the CLAS and GRAAL collaborations as shown in figure 7.29. For almost the full kinematic range the results from this analysis are in good agreement with the previous published measurements, with smaller error bars and almost twice as many angular bins. These results were binned in 50MeV bins to allow for a comparison with the previous results, while the final measurements from this analysis will be binned in 25MeV E_γ bins.

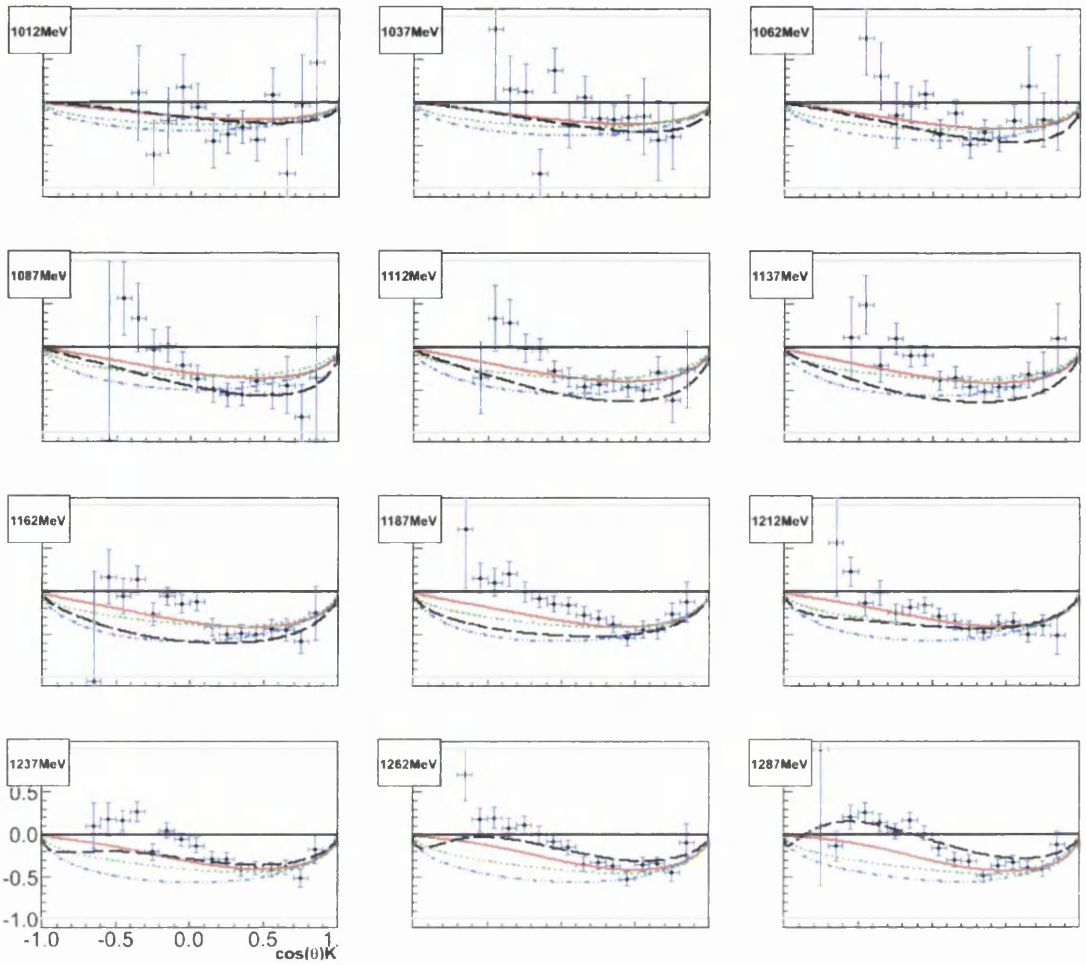

Figure 7.24: Recoil Polarization for the reaction $\gamma p \rightarrow K^+\Lambda$ as a function of $cos\theta^{K^+}_{cm}$ ranging from $E_\gamma = 1.012$ (top left) to 1.287 GeV (bottom right). Data are compared with model curves from the Gent Regge-plus-resonance model: Regge background (dotted green line), core resonances (dot-dash blue line), $D_{13}(1900)$ (solid red line) and $P_{11}(1900)$ (dashed black line).

7.3.2 Discussion of recoil polarization results for $K^+\Sigma^0$

Figure 7.30 displays the $K^+\Sigma^0$ recoil polarization results compared to the Gent RPR calculations. Again the binning has been significantly reduced due to the dilution of the hyperon polarization but a general trend appears where the recoil polarization is positive at lower energies before becoming negative at backward angles as the energy increases. In comparison with the GENT results, the RPR3 calculations both do reasonably well at mid to forward angles with the RPR4 approach working well at backward angles.

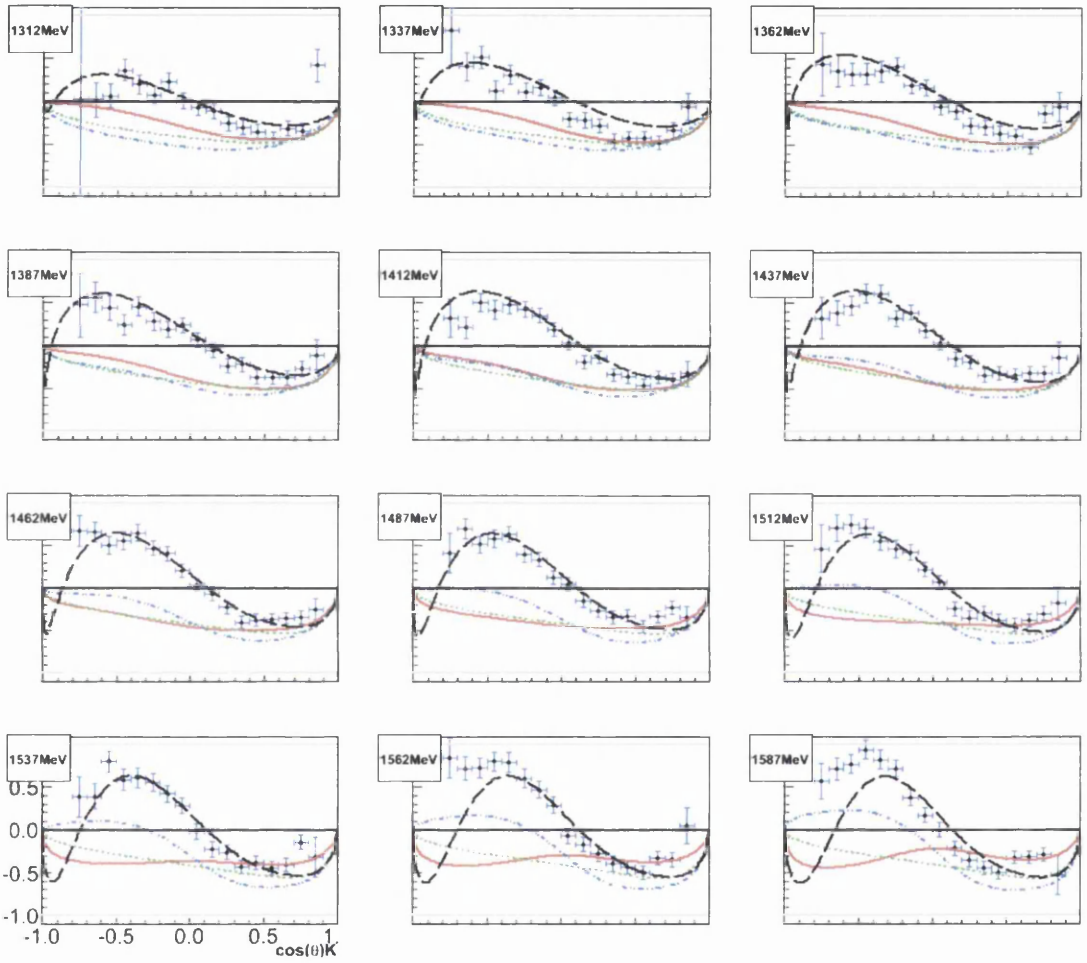

Figure 7.25: Recoil Polarization for the reaction $\gamma p \rightarrow K^+\Lambda$ as a function of $cos\theta^{K^+}_{cm}$ ranging from $E_\gamma = 1.313$ (top left) to 1.587 GeV (bottom right). Data are compared with model curves from the Gent Regge-plus-resonance model: Regge background (dotted green line), core resonances (dot-dash blue line), $D_{13}(1900)$ (solid red line) and $P_{11}(1900)$ (dashed black line).

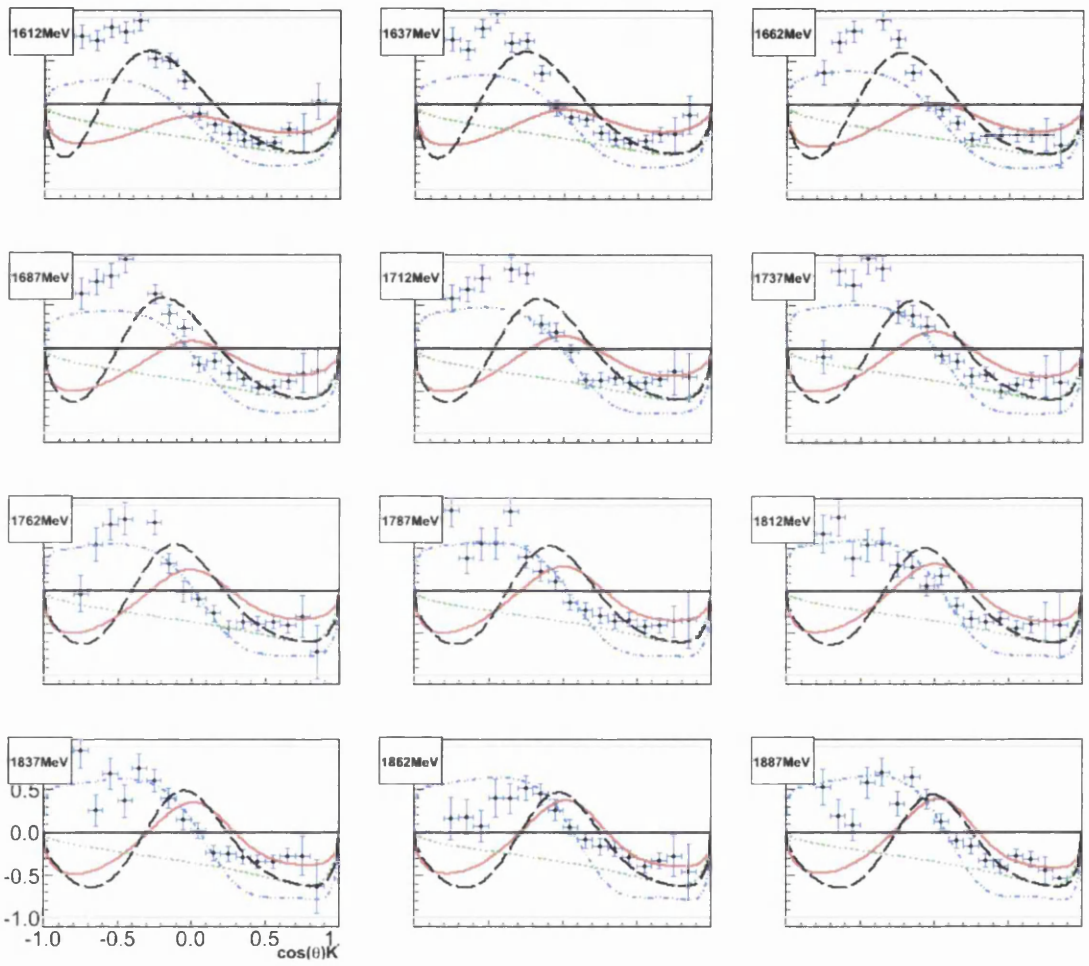

Figure 7.26: Recoil Polarization for the reaction $\gamma p \rightarrow K^+\Lambda$ as a function of $cos\theta^{K^+}_{cm}$ ranging from $E_\gamma = 1.612$ (top left) to 1.887 GeV (bottom right). Data are compared with model curves from the Gent Regge-plus-resonance model: Regge background (dotted green line), core resonances (dot-dash blue line), $D_{13}(1900)$ (solid red line) and $P_{11}(1900)$ (dashed black line).

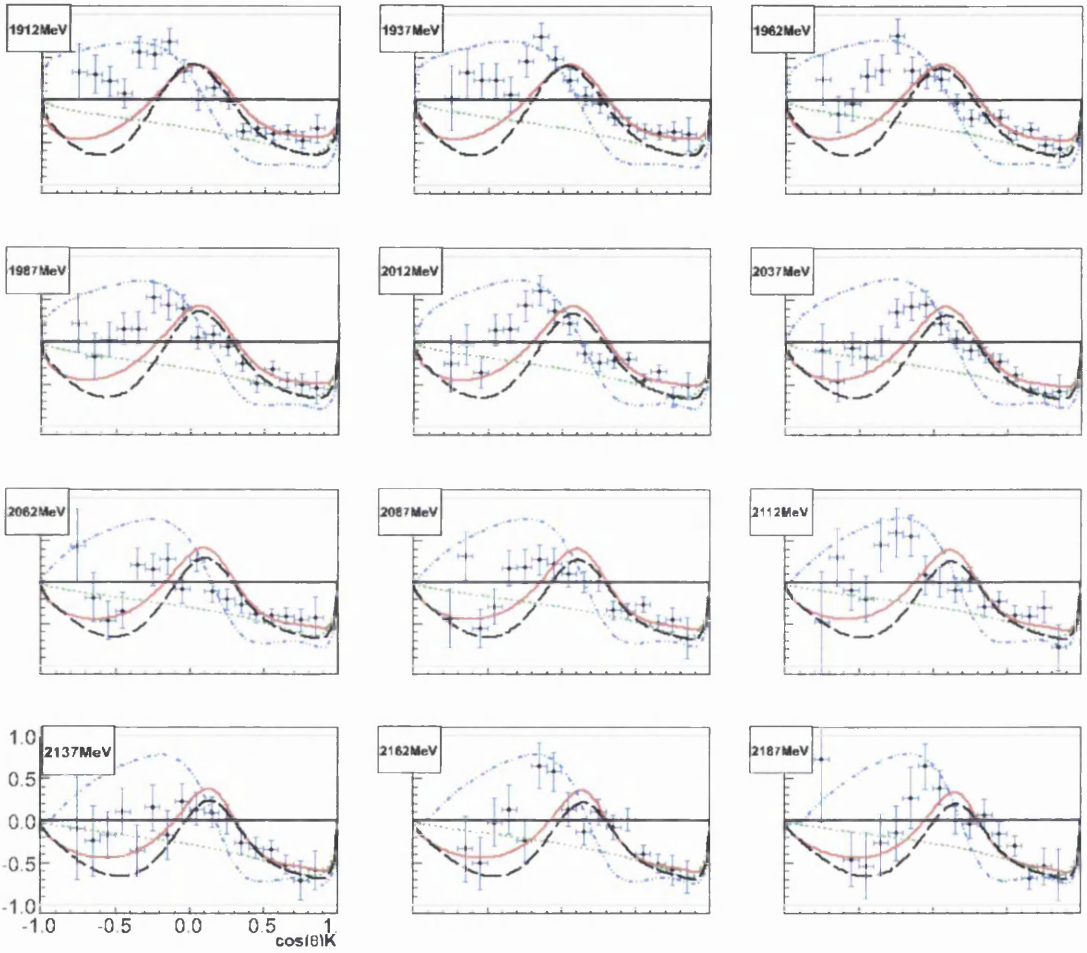

Figure 7.27: Recoil Polarization for the reaction $\gamma p \rightarrow K^+\Lambda$ as a function of $cos\theta^{K^+}_{cm}$ ranging from $E_\gamma = 1.912$ (top left) to 2.187 GeV (bottom right). Data are compared with model curves from the Gent Regge-plus-resonance model: Regge background (dotted green line), core resonances (dot-dash blue line), $D_{13}(1900)$ (solid red line) and $P_{11}(1900)$ (dashed black line).

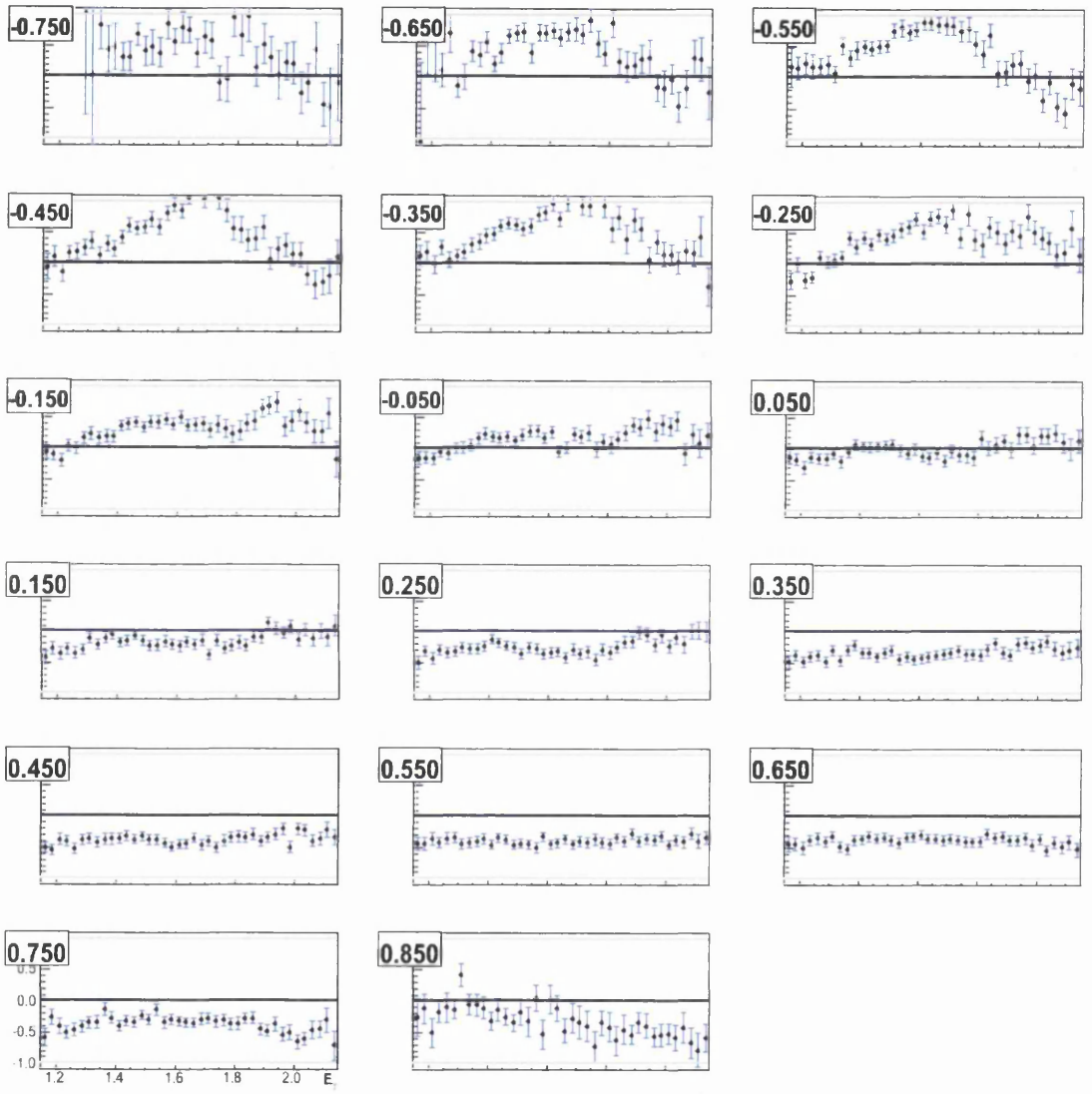

Figure 7.28: Hyperon recoil polarization for the reaction $\gamma p \rightarrow K^+\Lambda$ as a function of E_γ ranging from $cos\theta^{K^+}_{cm}$ = -0.750 (top left) to 0.850 (bottom right)

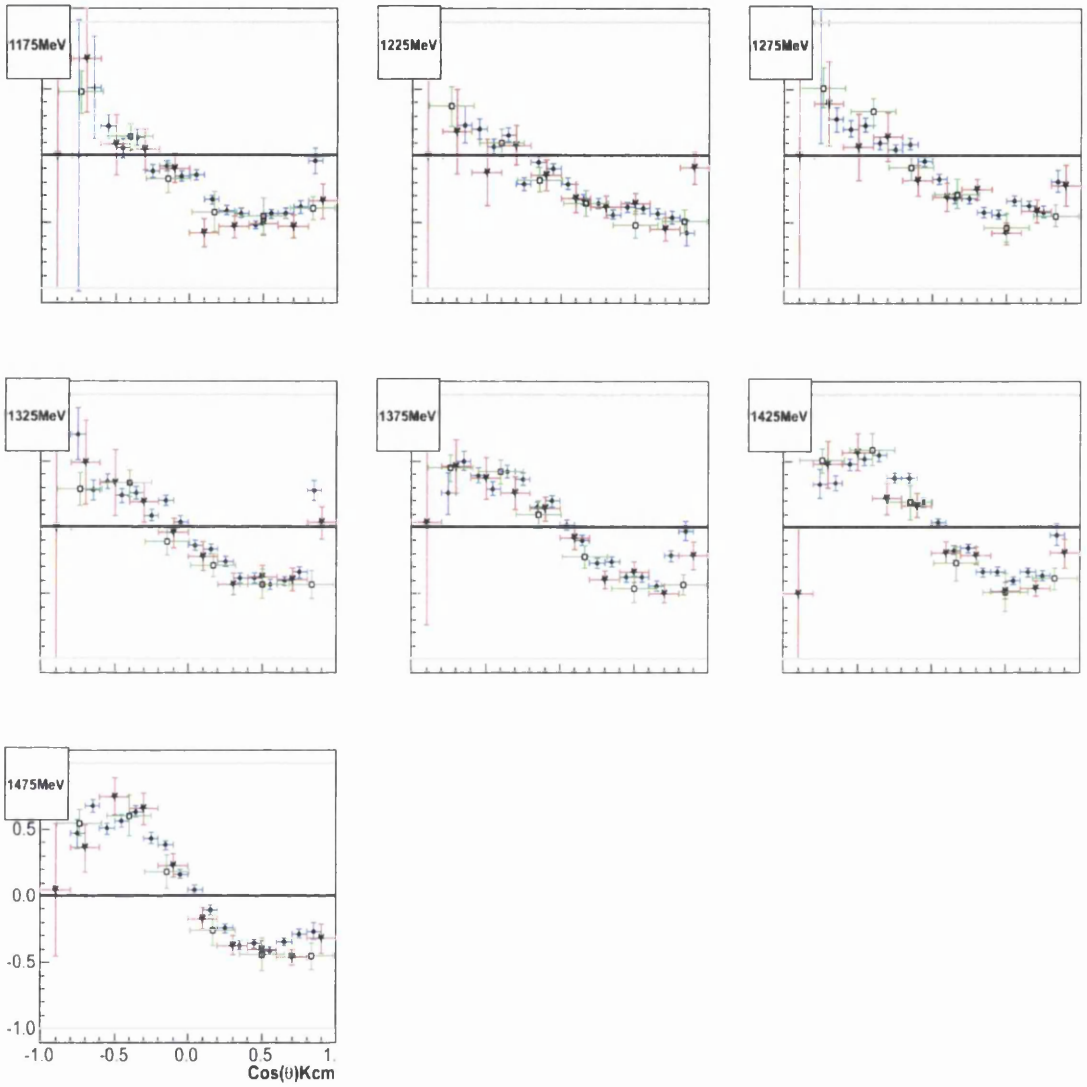

Figure 7.29: Hyperon recoil polarization for the reaction $\gamma p \rightarrow K^+\Lambda$ as a function of $cos\theta^{K^+}_{cm}$ ranging from E_γ = 1.175 (top left) to 1.475 GeV (bottom). Blue lines with circles are data points from this analysis, triangles with red lines are from CLAS and the squares with green lines are from GRAAL.

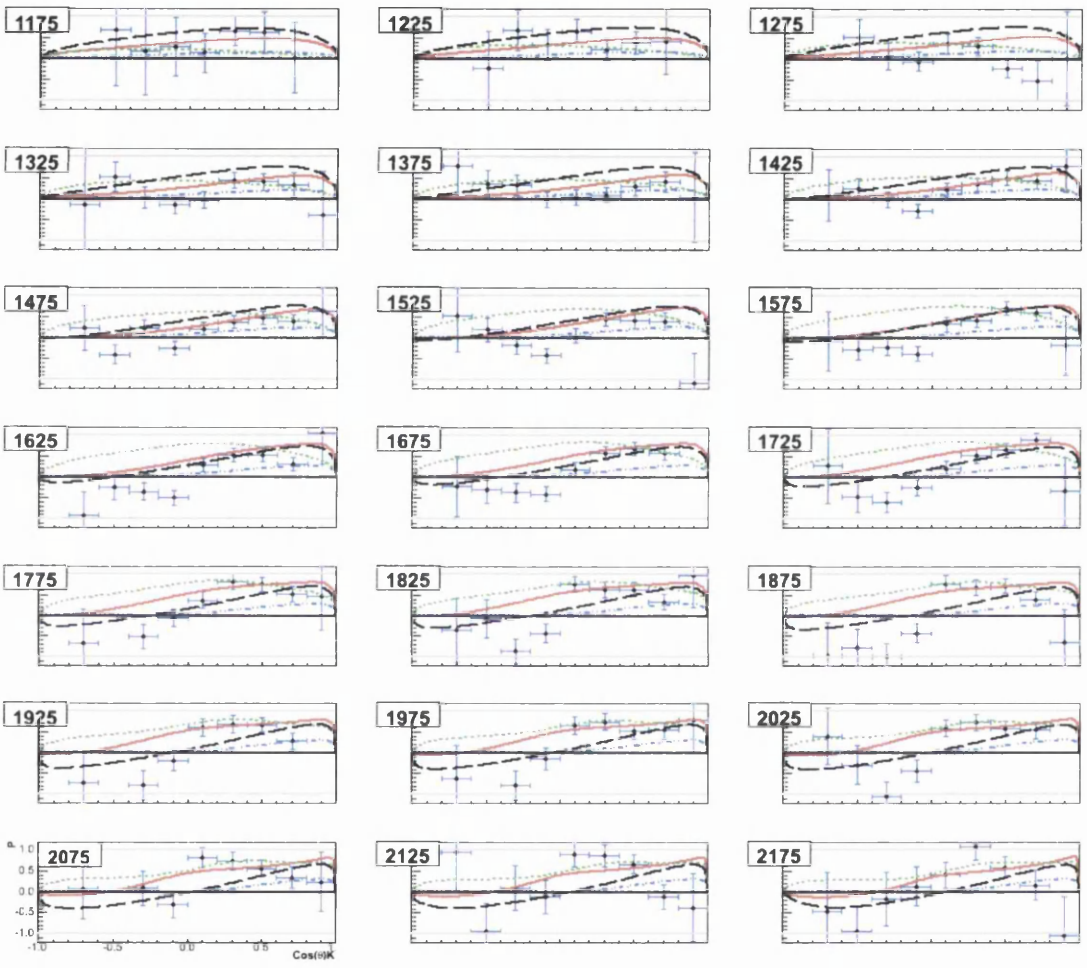

Figure 7.30: Recoil polarization for the reaction $\gamma p \rightarrow K^{+}\Sigma^{0}$ as a function of $cos\theta_{cm}^{K^{+}}$ ranging from $E_{\gamma} = 1.15$ (top left) to 2.05 GeV (bottom right). Data are compared with model curves from the Gent Regge-plus-resonance model: RPR-3 background (dotted green line), RPR-3 core (solid red line), RPR-4 background (dashed black line) and RPR-4 core (dot-dashed blue line).

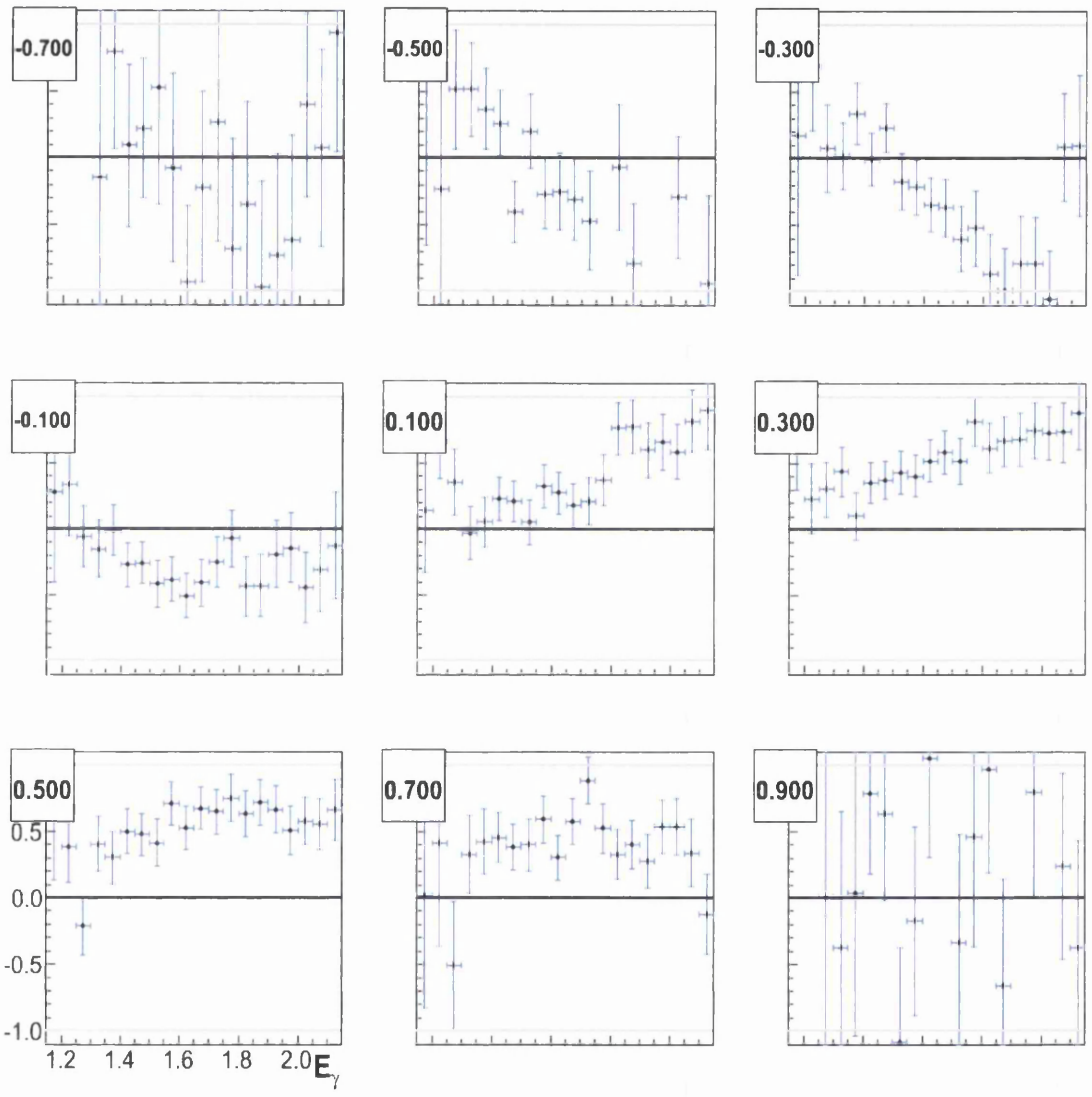

Figure 7.31: Hyperon recoil polarization for the reaction $\gamma p \rightarrow K^+\Sigma^0$ as a function of E_γ ranging from $cos\theta^{K^+}_{cm}$ = -0.7 (top left) to 0.9 (bottom right).

7.4 Target Asymmetry

The target asymmetry is compared to the RPR and Kaon-MAID calculations for the $K^+\Lambda$ channel, as a function of the centre-of-mass kaon angle $cos\theta^K_{cm}$, in figures 7.32 and 7.33 respectively. The results are also plotted as a function of E_γ in figure 7.34. Corresponding plots are shown for the $K^+\Sigma^0$ channel in figures 7.35 through 7.37.

7.4.1 Discussion of T results for $K^+\Lambda$

The most striking feature of the $K^+\Lambda$ target asymmetry results are the large negative asymmetries at mid to forward angles. This behaviour occurs over the full photon energy range with large backward angle asymmetries developing at energies between 1.45 and 1.75 GeV. For the RPR model, calculations involving only the core set of resonances along with calculations that include the $D_{13}(1900)$ resonance both give good agreement with the data. The calculations that include only the Regge background and those with a $P_{11}(1900)$ resonance fail to reproduce the large positive asymmetries evident at backward angles. For the Kaon-MAID calculations, the inclusion of the $D_{13}(1900)$ state is essential to reproducing the forward angle asymmetries at energies above 1.35 GeV.

7.4.2 Discussion of T results for $K^+\Sigma^0$

At backward angles the target asymmetry for the $K^+\Sigma^0$ channel is negative for energies close to threshold before increasing to positive values as the energy increases. At forward production angles the asymmetry displays the opposite behaviour, starting out positive and then decreasing to negative values. Regarding the RPR model, none of the calculations do particularly well at reproducing the data, particularly at low energy backward angles and high energy forward angles. The Kaon-MAID predictions also fail to reproduce the experimental results, with the exception of the high energy forward angle data where there is some agreement. Overall, it appears that some extra theoretical insight is required for $K^+\Sigma^0$ channel to produce model predictions that give good comparisons with the results of this analysis.

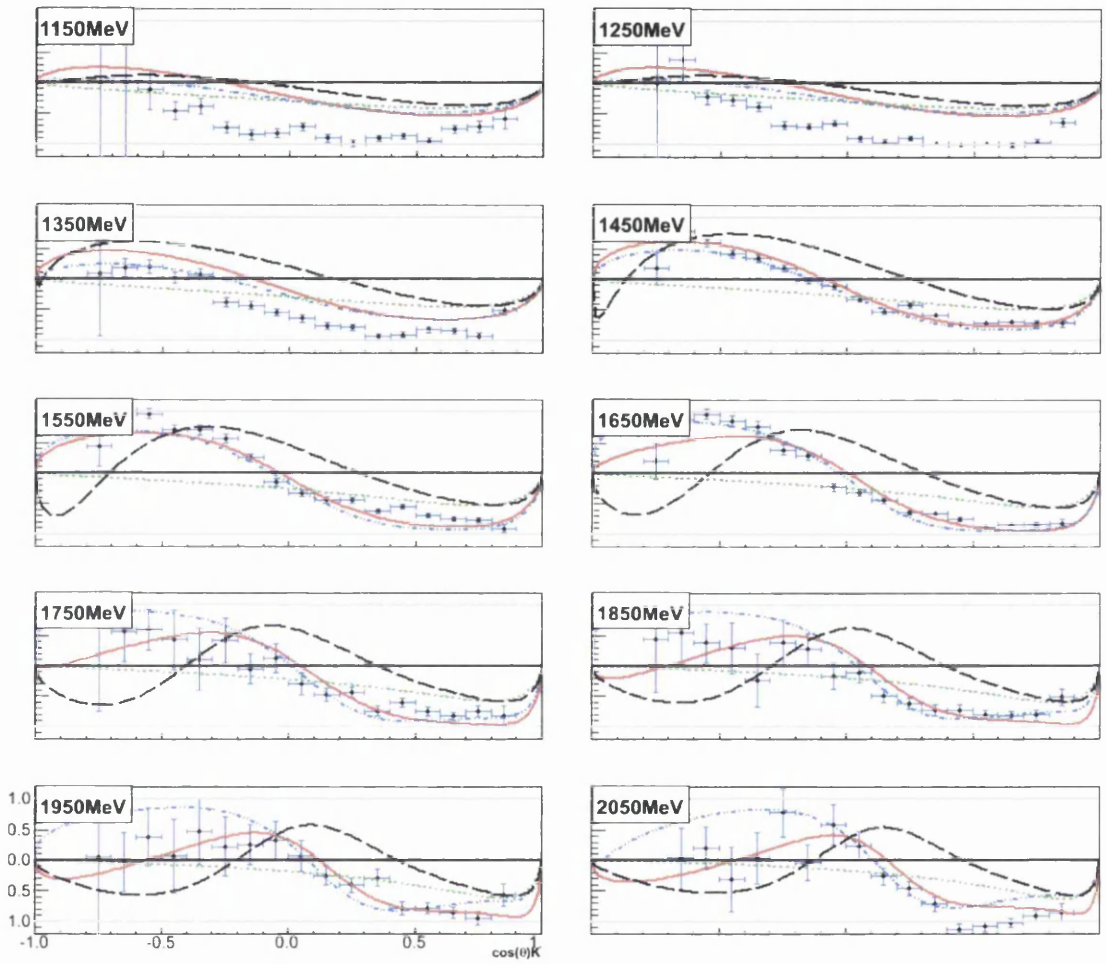

Figure 7.32: Target Asymmetry for the reaction $\gamma p \rightarrow K^+\Lambda$ as a function of $cos\theta^{K^+}_{cm}$ ranging from $E_\gamma = 1.150$ (top left) to 2.050 GeV (bottom right). Data are compared with model curves from the Gent Regge-plus-resonance model: Regge background (dotted green line), core resonances (dot-dash blue line), $D_{13}(1900)$ (solid red line) and $P_{11}(1900)$ (dashed black line).

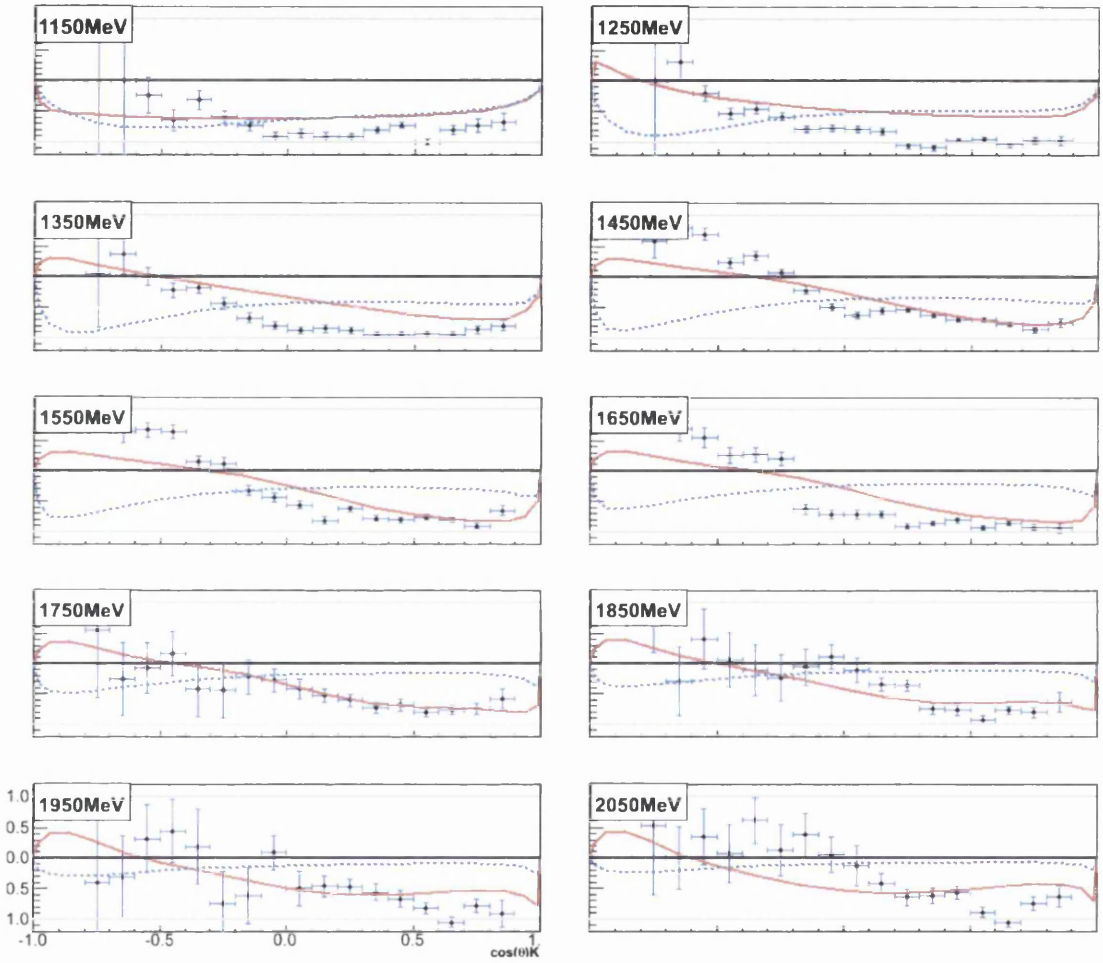

Figure 7.33: Target asymmetry for the reaction $\gamma p \rightarrow K^+\Lambda$ as a function of $cos\theta^{K^+}_{cm}$ ranging from $E_\gamma = 1.15$ (top left) to 2.05 GeV (bottom right). Data are compared with model curves from the Kaon-MAID isobar model: core resonances (dashed blue line) and $D_{13}(1900)$ (solid red line).

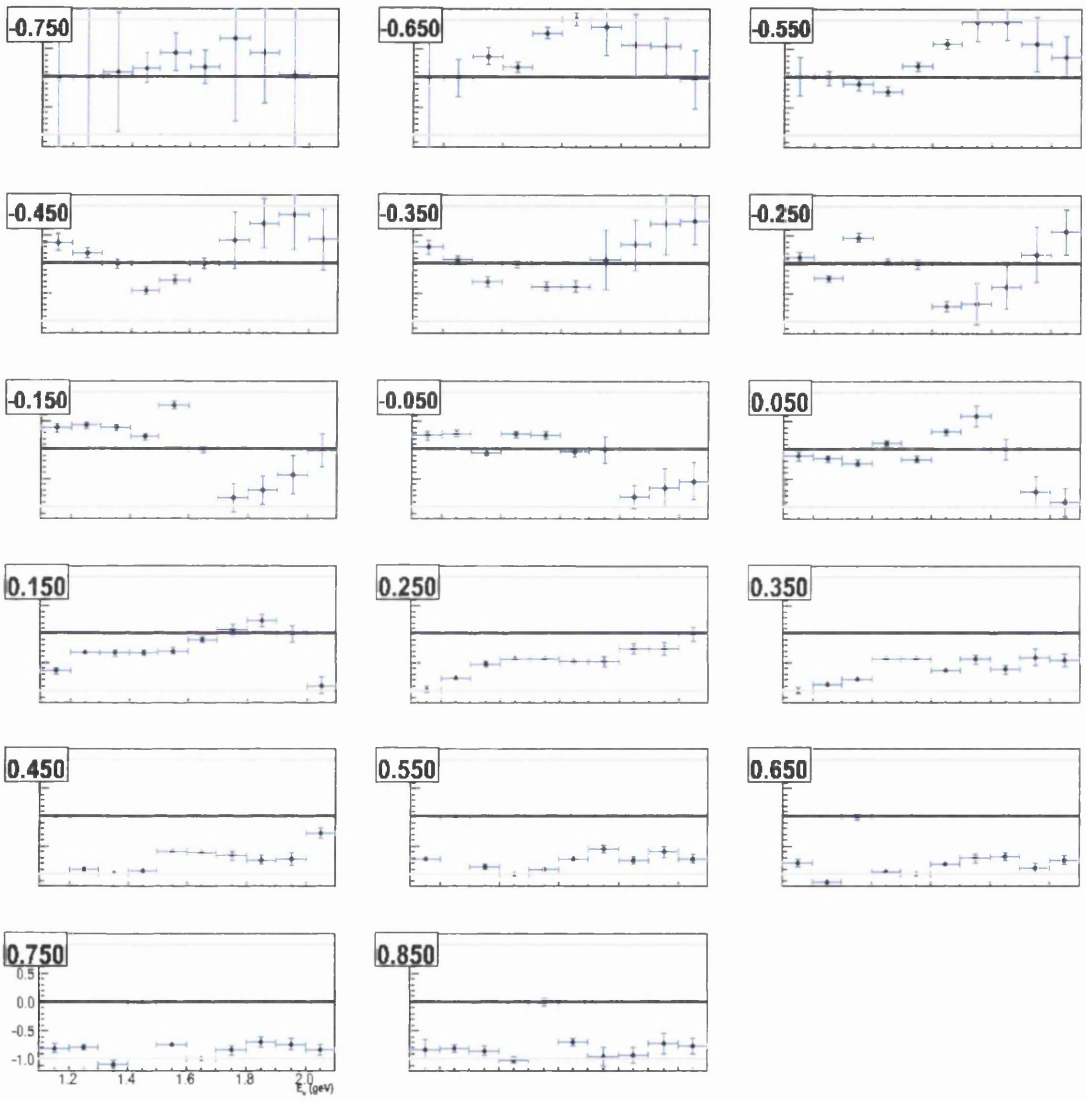

Figure 7.34: Target asymmetry for the reaction $\gamma p \rightarrow K^+\Lambda$ as a function of E_γ ranging from $cos\theta^{K^+}_{cm}$ = -0.750 (top left) to 0.850 (bottom right).

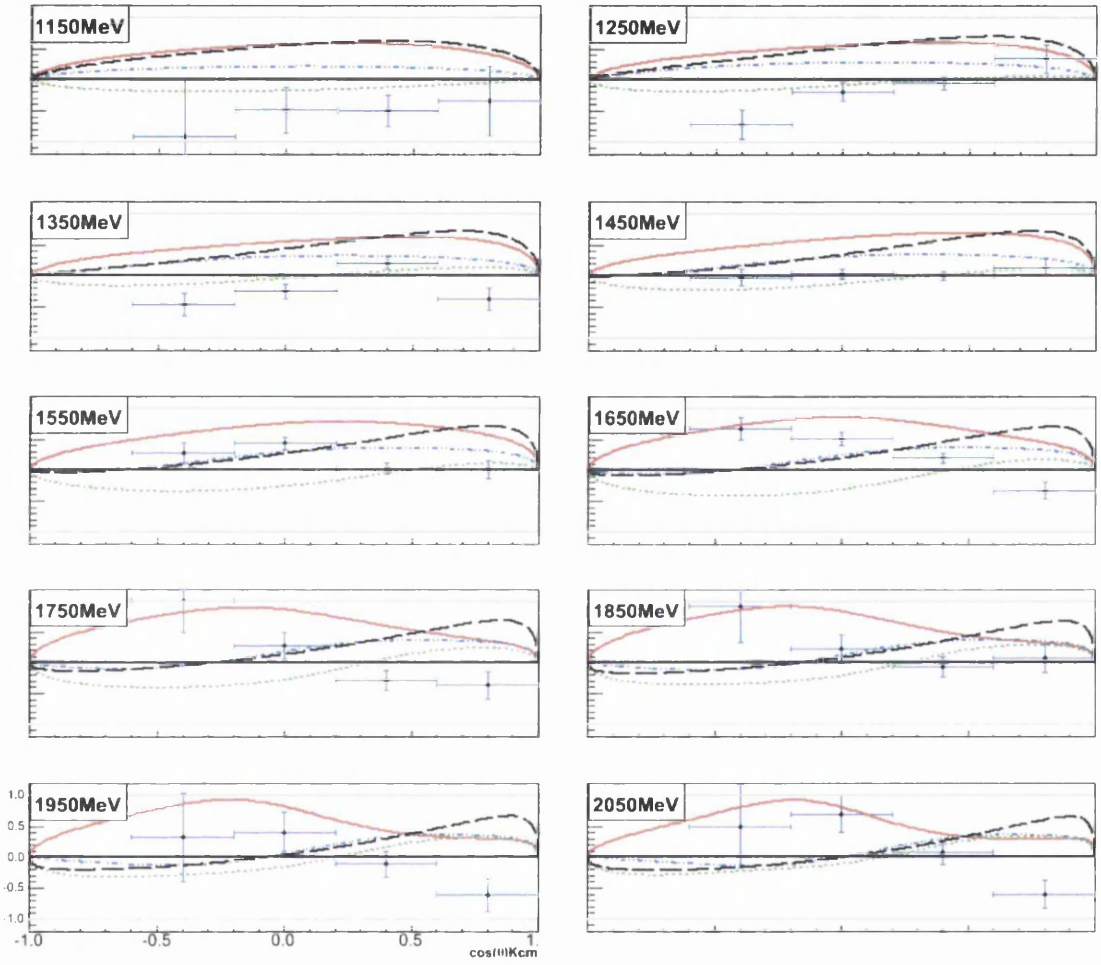

Figure 7.35: Target asymmetry for the reaction $\gamma p \rightarrow K^+\Sigma^0$ as a function of $cos\theta_{cm}^{K^+}$ ranging from $E_\gamma = 1.15$ (top left) to 2.05 GeV (bottom right). Data are compared with model curves from the Gent Regge-plus-resonance model: RPR-3 background (dotted green line), RPR-3 core (solid red line), RPR-4 background (dashed black line) and RPR-4 core (dot-dashed blue line).

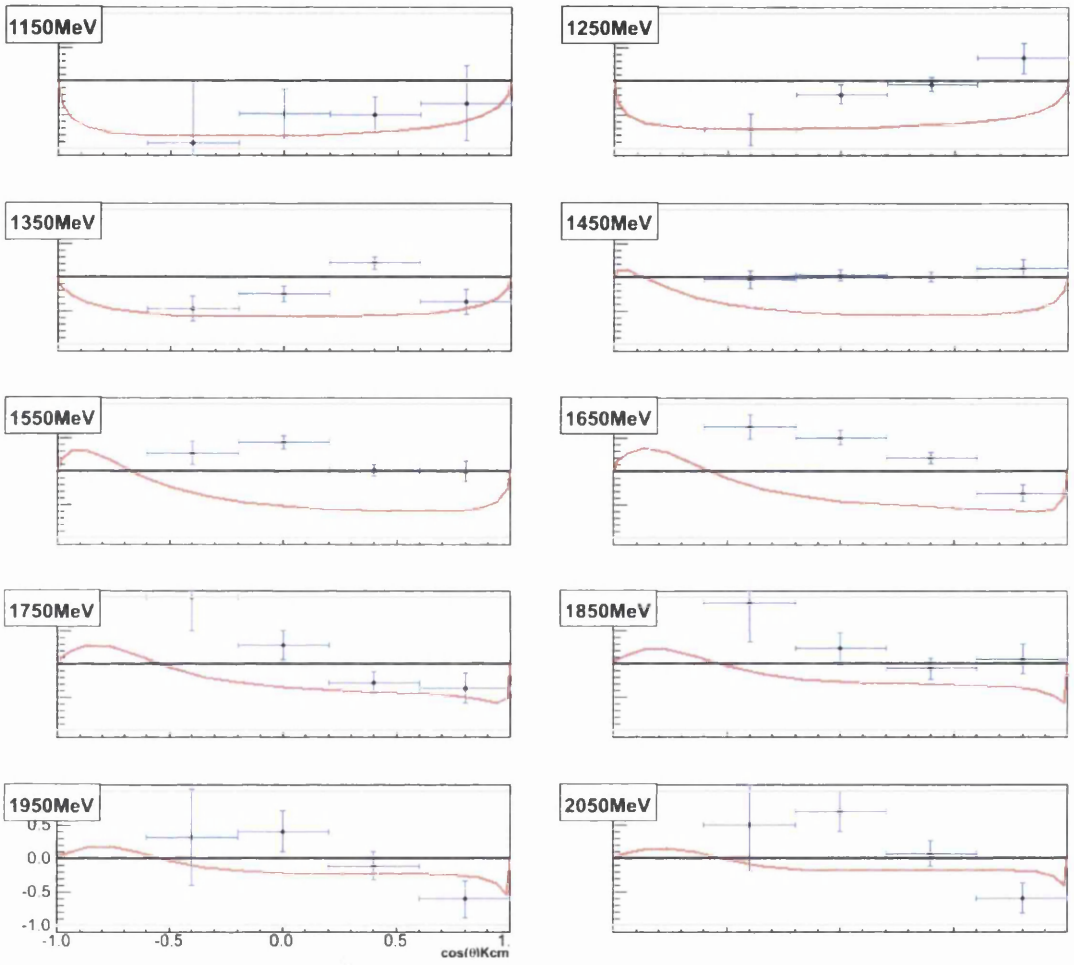

Figure 7.36: Target asymmetry for the reaction $\gamma p \rightarrow K^+\Sigma^0$ as a function of $cos\theta^{K^+}_{cm}$ ranging from $E_\gamma = 1.15$ (top left) to 2.05 GeV (bottom right). Data are compared with model curves from the Kaon-MAID isobar model with a core set of resonances included (solid red line).

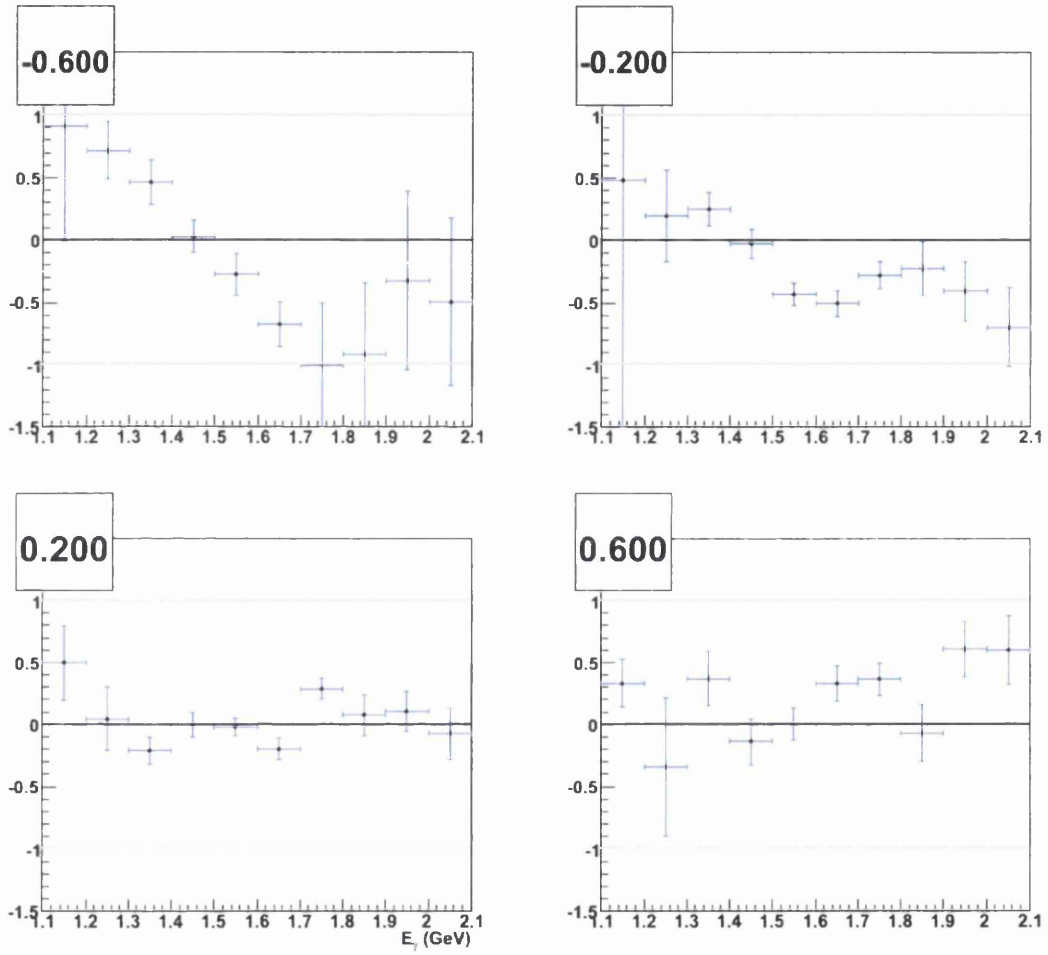

Figure 7.37: Target asymmetry for the reaction $\gamma p \rightarrow K^+\Sigma^0$ as a function of E_γ ranging from $cos\theta^{K^+}_{cm}$ = -0.6 (top left) to 0.6 (bottom right)

7.5 Positivity Constraints

An important property of polarization observables is that they are not independent, but are related by various identities and inequalities. These identities can be derived in a systematic manner by studying the positivity of the density matrix, as described in the work of Artu, Richard and Soffer [100]. Using the positivity constraints they derived a series of rigorous inequalities relating two or three spin observables, and in particular were able to demonstrate that for the observables measured in this work the following relations should hold:

$$R^2 \equiv P^2 + O_x^2 + O_z^2 \leq 1. \tag{7.1}$$

$$R^2 \equiv \Sigma^2 + O_x^2 + O_z^2 \leq 1 \tag{7.2}$$

These relations can provide an interesting test of the data by investigating to what extent each measurement is compatible with the others. Relation 7.1 is of particular interest as the three observables define the three orthogonal components of the hyperon polarization for a linearly polarized beam. This is analogous to the relation used in reference [42], and described in Chapter 3, to demonstrate that for a circularly polarized photon beam the Λ hyperon appears to be fully polarized. Figure 7.38 shows the equivalent quantity R for relation 7.1 plotted as a function of $cos\theta^K_{cm}$, with the E_γ dependence displayed in figure 7.39. A striking feature of these results is how close R is to unity, particularly at mid to forward angles. This compares to the analogous case with circularly polarized photons, although it is clear that R is not consistent with unity for the full range of kinematics. Figures 7.40 and 7.41 display R for the case when the photon asymmetry is included, and a similar trend is observed. One way of interpreting these results would be to develop a heuristic model, similar to that described in [42], which predicts full polarization transfer to the Λ at forward angles when a linearly polarized beam is used. Although the development of such a model is out with the scope of this current work, it does provide the opportunity for some future investigation.

Results are also presented for relation 7.1 for the $K^+\Sigma^0$ channel in figures 7.42 and 7.43. Although the limited statistics for this channel make drawing any real conclusions difficult it is clear that R is not consistent with unity for the full kinematic range.

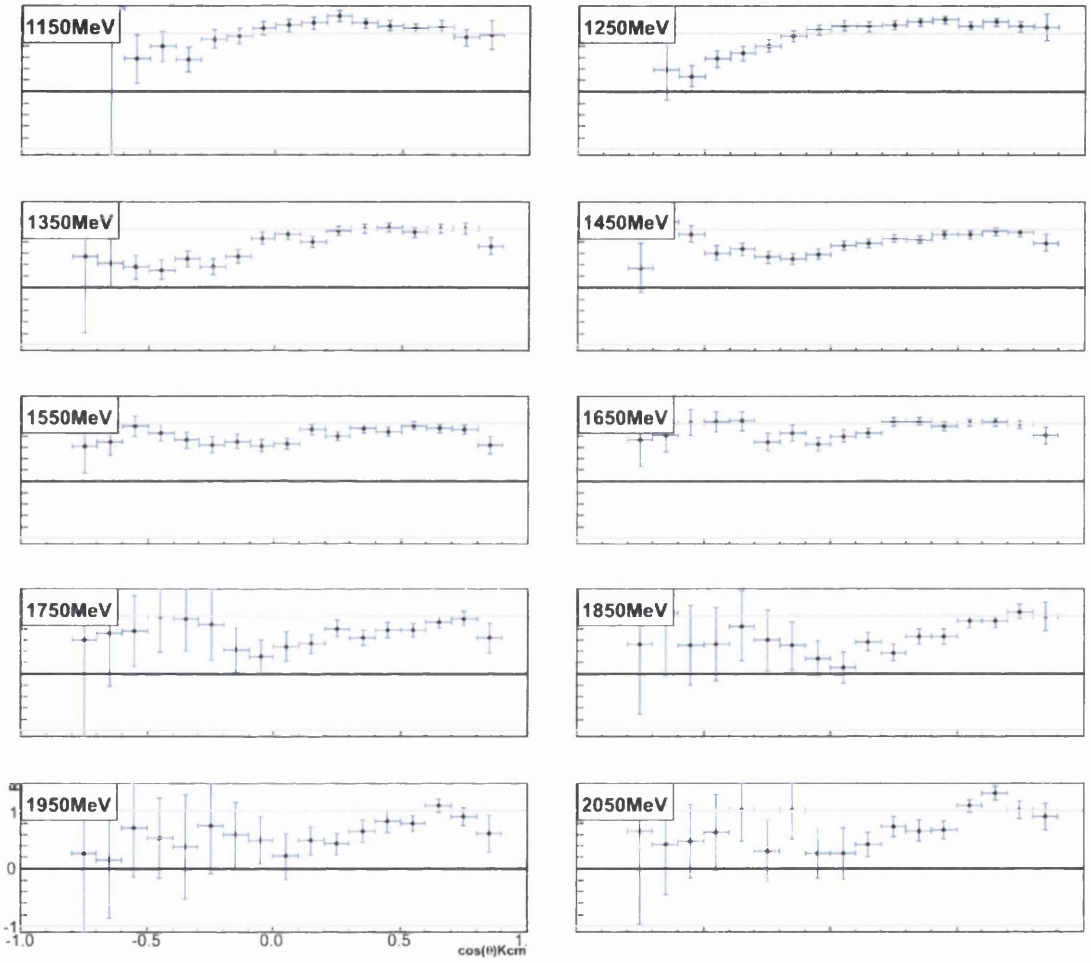

Figure 7.38: The magnitude of the quantity $R = \sqrt{P^2 + O_x^2 + O_z^2}$ for the $K^+\Lambda$ channel as a function of kaon angle.

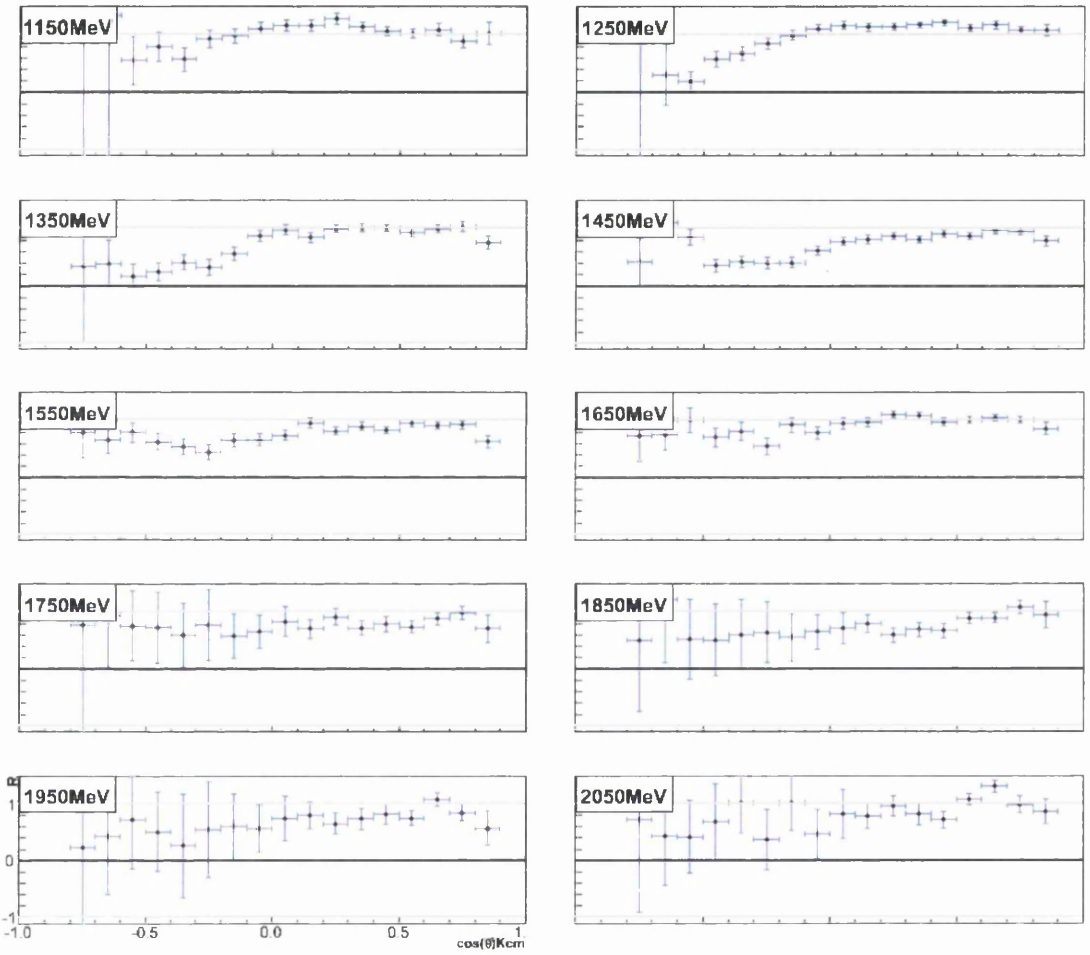

Figure 7.39: The magnitude of the quantity $R = \sqrt{P^2 + O_x^2 + O_z^2}$ for the $K^+\Lambda$ channel as a function of photon energy.

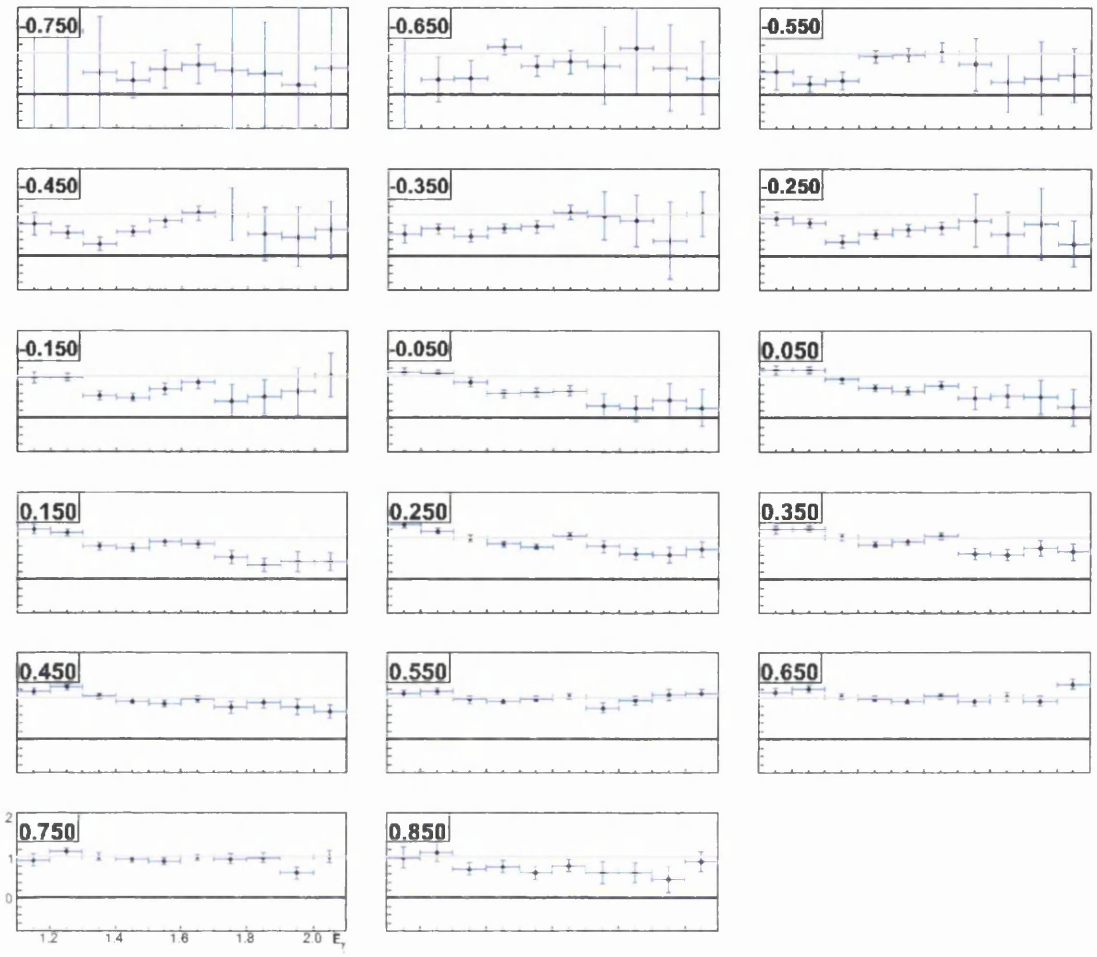

Figure 7.40: The magnitude of the quantity $R = \sqrt{\Sigma^2 + O_x^2 + O_z^2}$ for the $K^+\Lambda$ channel as a function of kaon angle.

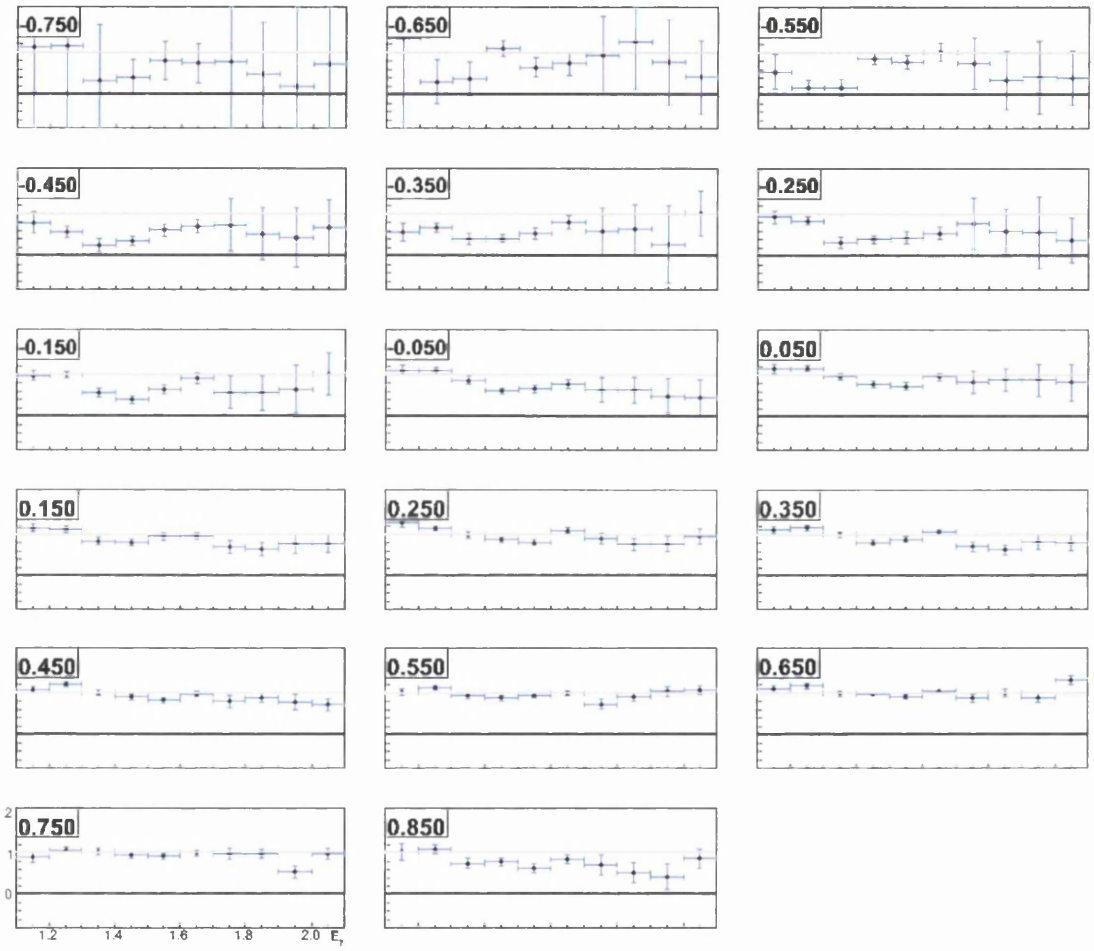

Figure 7.41: The magnitude of the quantity $R = \sqrt{\Sigma^2 + O_x^2 + O_z^2}$ for the $K^+\Lambda$ channel as a function of photon energy.

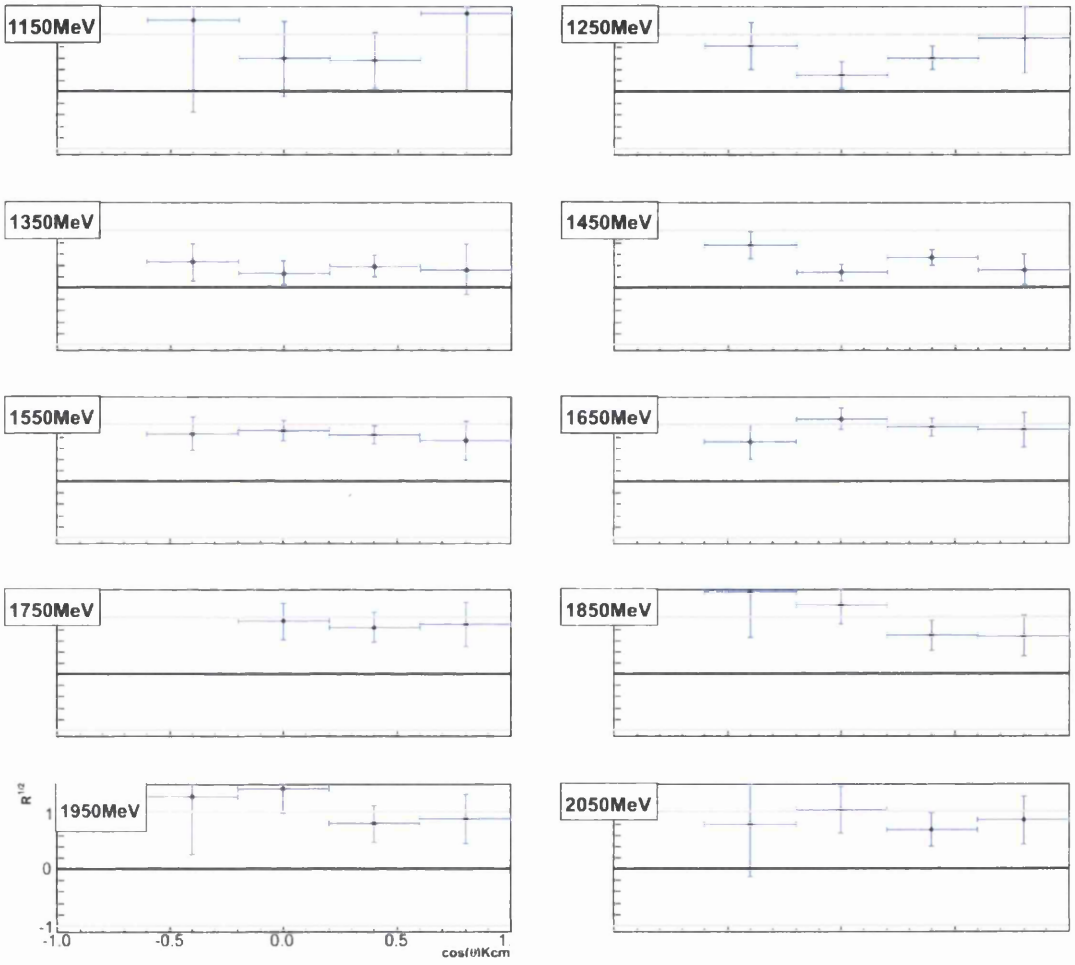

Figure 7.42: The magnitude of the quantity $R = \sqrt{P^2 + O_x^2 + O_z^2}$ for the $K^+\Sigma^0$ channel as a function of kaon angle.

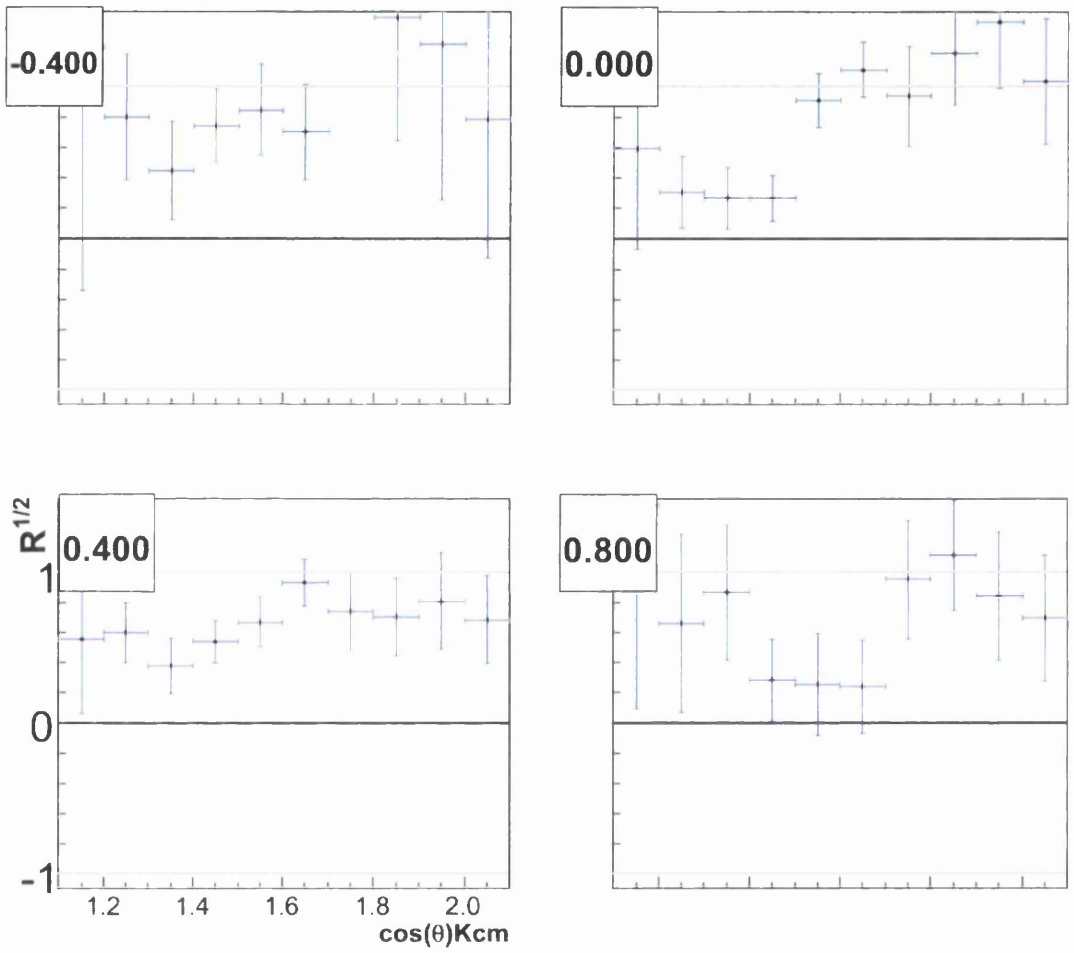

Figure 7.43: The magnitude of the quantity $R = \sqrt{P^2 + O_x^2 + O_z^2}$ for the $K^+\Sigma^0$ channel as a function of photon energy.

7.6 Conclusions

In summary, this work presents first ever results for the O_x and O_z double polarization observables for the reactions $\gamma p \rightarrow K^+\Lambda$ and $\gamma p \rightarrow K^+\Sigma^o$, along with new measurements of the target asymmetry which will significantly increase the current world database. Further to this, new measurements of the photon asymmetry have, for the first time, covered nearly the full angular range at the energies where resonance physics is expected to dominate the reaction. In addition the hyperon recoil polarization for both reactions has been measured to higher precision than ever before. The measurements of the photon asymmetry and recoil polarization have been compared to previous results from the CLAS, LEPS and GRAAL collaborations. Overall, the agreement between the data sets is excellent with the results from this analysis generally being more precise than the previous measurements, with finer binning and smaller statistical uncertainties.

The results for the O_x and O_z double polarization observables point to a reaction mechanism where the photon polarization is preferentially transferred along the x-axis, with $O_x \simeq 1$ for a broad range of kinematics. This contrasts with results from a previous experiment with a circularly polarized photon beam where the polarization is preferentially transferred along the z-axis, as defined by the photon momentum vector. Comparisons with several different calculations from the Regge-plus-resonance approach of Corthals *et al* indicate that the inclusion of a $D_{13}(1900)$ missing resonance to the core set of states is required to reproduce the experimental data. In particular the large polarizations seen at forward angles for the O_x observable can only be produced by the RPR approach when the $D_{13}(1900)$ is included. It should be noted however that none of the RPR calculations compare well with the data for O_x at photon energies below 1.35 GeV. The forward angle O_x data also looks similar to predictions made by the Kaon-MAID isobar model when the $D_{13}(1900)$ state is included. Once again, however, data below 1.35 GeV does not compare well with the calculations suggesting that some further theoretical insight is required at these energies. For the $K^+\Sigma^0$ channel, despite the reduced statistical precision due to the dilution of the hyperon polarization, the O_x results display a general trend of negative backward polarizations that increase to positive values at forward angles. For both O_x and O_z the large statistical error bars make discrimination between the different model calculations difficult.

For the photon asymmetry results the most striking feature for both channels is that the asymmetries are positive for all kinematics. In the RPR approach the $K^+\Lambda$ results agree well with the predictions that include the missing $P_{11}(1900)$

resonance, whilst the comparison for the $K^+\Sigma^0$ channel is poor for all the calculations. For the Kaon-MAID predictions, neither the core nor the $D_{13}(1900)$ calculations give good agreement with the results suggesting that a $P_{11}(1900)$ state is required to explain the $K^+\Lambda$ photon asymmetry results. For the $K^+\Sigma^0$ channel more theoretical work is clearly required to give calculations that accurately reproduce the experimental results.

Extensive previous measurements have already been published for the hyperon recoil polarization by the CLAS collaboration. The results of this analysis agree well with these measurements but with a higher overall precision. This agreement means that any theoretical results derived from the previous measurement will generally be consistent with these results. From the RPR calculations it would once again appear that the inclusion of $P_{11}(1900)$ state is required to give agreement with data, with a calculation that includes the $D_{13}(1900)$ resonance also providing a good comparison at energies above 1.8 GeV. For the $K^+\Sigma^0$ channel the RPR calculations based on the core set of nucleon resonances also give predictions that agree with the data. This may be expected as the model has been fitted to the previous CLAS recoil results to allow an extraction of the various coupling constants that are used to give these predictions.

The target asymmetry results for the $K^+\Lambda$ channel display a strong forward angle polarization that is reproduced with the inclusion of a $D_{13}(1900)$ resonance in both the RPR and Kaon-MAID models. Again the model calculations give the best comparisons at photon energies above 1.35 GeV. Regarding the $K^+\Sigma^0$ channel, neither the RPR or Kaon-MAID models do a good job of predicting the results.

Overall, the polarization observables measured for the $K^+\Lambda$ channel indicate that an important role is played by the $D_{13}(1900)$ resonance in the reaction dynamics, with some evidence that the $P_{11}(1900)$ also contributes. For the $K^+\Sigma^0$ channel, it appears that more theoretical work is required to reproduce the experimental data. This is perhaps to be expected as the channel is complicated by the presence of resonant Δ states. The two model approaches that are compared in this work have not been fitted to this data set. This makes the calculations for the double polarization observables purely predictive. The fact that there is such good agreement with the data when the $D_{13}(1900)$ state is included is encouraging, although this has to be tempered slightly with the general failure to predict the data at energies close to threshold. Taking this into account, both the Gent-RPR and Kaon-MAID models should be further refined by fitting to the new data. Clearly these are only two of many different model prescriptions and all

possible combinations of resonances, missing states and background terms have not been exhausted in this work. The interpretation of these results has only just begun with theorists likely to provide further insight as their models are refined and developed in light of the new data.

One obvious limitation with some of the results presented here is that occasionally the data points straddle the limits ± 1. Polarization observables, by construction, cannot have values with a magnitude larger than unity. Although statistically some level of disagreement may be expected, this constraint is enforced in the model calculations that the data are being compared to. In order to counteract this problem a future Bayesian analysis is being developed that will force the data points and their associated error bars to obey these limits.

In principle it should be possible to use this data set to make measurements of the cross sections for both channels. Although cross section measurements were not an aim of this research, the high quality yield extractions should make it feasible. Such an analysis would be of interest in light of the apparent discrepancies in the previous cross section results from CLAS and SAPHIR. These measurements were not attempted as part of this work as the process of photon normalization is likely to be non-trivial given the high rates of photons produced by the coherent bremsstrahlung process. It should however provide an opportunity for future analysis.

As well as constraining the current theoretical models, this dataset taken in conjunction with a current CLAS analysis with a polarized target will facilitate a complete measurement of the $\gamma p \rightarrow K^+\Lambda$ reaction. This will allow for a model independent identification of any missing resonances, free of phase ambiguities. Data from the polarized target experiment should be available from CLAS within the next two years.

To conclude, this work has produced measurements of five polarization observables with unrivaled precision for kaon photoproduction. These data should aid the refinement of current theoretical models, with the first measurements of the O_x and O_z double polarization observables likely to provide important new insights. Although comparisons with some model calculations hint at an important role for the $D_{13}(1900)$ and $P_{11}(1900)$ missing resonances, more theoretical work is required before their existence can be confirmed. Overall, there is much information to be gained from further study of this data set, which should provide a substantial basis for the continued development of a phenomenological understanding of associated strangeness production on the proton.

Bibliography

[1] S. Capstick and W. Roberts. *Phys. Rev. D, 58:074011*, 1998.

[2] T. Mart and C. Bennhold. Evidence for a missing nucleon resonance in kaon photoproduction. *Phys. Rev. C, 61:012201*, 1999.

[3] T. Mart and A. Sulaksono. *arXiv:nucl-th/0609077v1*, 2006.

[4] S. Janssen *et al. Phys. Rev. C 65 015201*, 2001.

[5] A.W. Thomas and W. Weise. *The Structure of the Nucleon.* Wiley, 2001.

[6] F. Close. *An Introduction to Quarks and Partons.* London: Academic Press, 1983.

[7] D.H. Perkins. *Introduction to High Energy Physics.* Cambridge, 1999.

[8] M. Gell-Mann and Y. Neeman. *The Eightfold Way.* Benjamin, 1984.

[9] F. X. Lee *et al. hep-lat/0208070*, 2002.

[10] T.D. Cohen and L.Y. Glozman. *Int. Journ. Mod. Phys. A17, 1327 (2002)*, 2002.

[11] G.F. de Teramond and S.J. Brodsky. *Phys. Rev. Lett. 94, 201601*, 2005.

[12] D. Faiman and A.W. Hendry. *Phys. Rev. 173 1720*, 1968.

[13] C.P. Forsyth and R.E Cutkosky. *Z. Phys. C. 18 219-227*, 1982.

[14] R. Koniuk and N. Isgur. *Phys. Rev. D, 21:1868*, 1980.

[15] W. M. Yao *et al* (Particle Data Group). *J. Phys. G: Nucl. Part. Phys 33, 1*, 2006.

[16] D.B. Lichtenberg *et al. Phys. Rev. 167, 1535*, 1968.

[17] R. Bradford *et al. Phys. Rev. C 75 035205*, 2007.

[18] F.J. Klein *et al.* Search for missing nucleon resonances in the photoproduction of hyperons using a polarized photon beam and a polarized target. *Jlab Internal Document.*

[19] R.A. Adelseck and B. Saghai. *Phys. Rev. C42 108*, 1992.

[20] G.F. Chew *et al. Phys. Rev. 106, 1345*, 1957.

[21] C.G. Fasano *et al. Phys. Rev. C. 46 2430-2455*, 1992.

[22] I.S. Barker *et al. Nuclear Physics, B95, 347-456*, 1975.

[23] W-T. Chiang and F. Tabakin. *Phys. Rev. C55 2054*, 1997.

[24] G. Keaton and R. Workman. *Phys. Rev. C53. 1434*, 1996.

[25] R. Bradford *et al. Phys. Rev. C 73 035202*, 2006.

[26] J. W. C. McNabb *et al. Phys. Rev. C 69 042201*, 2004.

[27] T. Mart *et al. Phys. Rev. C, 51 R1074*, 1995.

[28] D. Glazier. Private communication.

[29] R.L. Anderson *et al. Phys. Rev. Lett. 9 131*, 1962.

[30] D.E. Groom and J.H. Marshall. *Phys. Rev. 159 1213*, 1967.

[31] C.W. Peck *et al. Phys. Rev. 135 830*, 1964.

[32] M. Bockhorst *et al. Z. Phys. C 63, 37*, 1994.

[33] M. Q. Tran *et al. Phys. Lett. B445: 20-26*, 1998.

[34] K.-H. Glander *et al. Eur. Phys. .J A 25, 441*, 2004.

[35] R. Erbe *et al* (ABBHHM collaboration). *Phys. Rev. 188, 2060*, 1969.

[36] M. Guidal *et al. Nucl. Phys. A627, 645*, 1997.

[37] M. Guidal *et al. Phys. Rev. C 61 025204*, 2000.

[38] T. Mart *et al.* compute code kaonmaid 2000, available at www.kph.uni-mainz.de/maid/kaon/kaonmaid.html.

[39] B. Saghai. From unkown to undiscovered resonances. *Nucl-th/0105001*, 2001.

[40] A.V. Sarantsev *et al. Eur. Phys. J. A 25, 441-453*, 2005.

[41] T. Corthals *et al. Phys. Rev. C 73 045207*, 2006.

[42] R. Schumacher. Polarization of hyperons in elementary photoproduction. *arXiv:nucl-exp/0611035v1*, 2006.

[43] E. Merzbacher. *Quantum Mechanics, 2nd Edition.* Wiley, 1970.

[44] R.G.T. Zegers *et al. Phys. Rev. Lett 91 092001*, 2003.

[45] A. Lleres *et al. Eur. Phys. J. A 31, 79-93*, 2007.

[46] A.V. Anisovich *et al. Eur. Phys. J. A 25, 427*, 2005.

[47] A.V. Anisovich *et al. Eur. Phys. J. A 25, 441*, 2005.

[48] B. Julia-Diaz *et al. Phys. Rev. C 73, 055204*, 2006.

[49] R.A. Adelseck and C. Bennhold. *Phys. Rev. C 32 1681*, 1985.

[50] R.A. Williams *et al. Phys. Rev. C 46 1617*, 1992.

[51] H. Thom. *Phys. Rev. 151 1322*, 1966.

[52] T. Feuster and U. Mosel. *Phys. Rev. C 58 457*, 1998.

[53] H. Haberzettl. *Phys. Rev. C, 56 2041*, 1997.

[54] S. Janssen. *Strangeness Production on the Nucleon.* PhD thesis, Universiteit Gent, 2002.

[55] T. Feuster and U. Mosel. *Phys. Rev. C 58, 457*, 1998.

[56] N. Kaiser *et al. Nucl. Phys. A612, 297*, 1997.

[57] T. Sato and T.-S.H Lee. *Phys. Rev. C 54, 2660*, 1996.

[58] V. Shklyar *et al.* Coupled-channel analysis of $k\lambda$ production in the nucleon resonance region. *Phys. Rev. C 72, 052210*, 2005.

[59] J. Caro Ramon *et al. Nucl. Phys. A672, 249*, 2000.

[60] W.T Chiang *et al. arXiv:nucl-th/0104052v2*, 2001.

[61] A. Usov and O. Scholten. $k\lambda$ and $k\sigma$ photoproduction in a coupled-channels framework. *Phys. Rev. C 72, 025205*, 2005.

[62] K.H. Althoff *et al. Nucl. Phys. B 137, 269*, 1978.

[63] M. Q. Tran *et al. Phys. Lett. B 445 20*, 1998.

[64] T. Corthal *et al. arXiv:nucl-th/0612085v2*, 2008.

[65] T. Corthals. *Regge Plus Resonance Approach to Kaon Production from the Proton.* PhD thesis, Universiteit Gent, 2007.

[66] S. Goers *et al. Phys. Lett. B 464, 331*, 1999.

[67] J.D. Kellie *et al.* Photoproduction of vector mesons and hyperons with a beam of linearly-polarized photons. *Jlab Internal Document*, 2001.

[68] C.W. Leeman *et al.* The continuous electron beam accelerator facility: Cebal at the jefferson laboratory. Technical report, Jefferson Laboratory, 2001.

[69] B. Mecking. *Nucl. Instr. and Meth.A503/03, 513*, 2003.

[70] M. Crofford *et al.* The rf system for the cebaf polarized photoinjector. Technical report, Thomas Jefferson National Accelerator Facility, 1993.

[71] C. Sinclair. Polarized electrons at jefferson laboratory. Technical report, Thomas Jefferson National Accelerator Facility, 1997.

[72] C. Hovater *et al.* The cebaf rf system upgrade. In *Proceedings of LINAC 2004, Lubeck, Germany.*

[73] R.T Jones. Intense beams of polarized and nearly monochromatic photons from coherent bremsstrahlung. Technical report, Jlab internal Publication, 1999.

[74] U. Timm. Coherent bremsstrahlung of electrons in crystals. *Fortschritte der Physik*, 1969.

[75] C.I.O. Gordon. *Rho photoproduction using linearly polarized photons with the CLAS detector.* PhD thesis, Glasgow University, 2004.

[76] J. Melone. *Measurement of the photon asymmetry for the reaction* $\gamma p \rightarrow K^+\Lambda^0$ *at CLAS from 1.6 to 2.0GeV.* PhD thesis, Glasgow University, 2004.

[77] J. Kellie *et al. Nucl. Instr. and Meth. A545, 164-180*, 2005.

[78] The science of quark confinement and gluonic excitations, gluex/hall d design report, version 4. Technical report, Jefferson Laboratory, 2002.

[79] F. Rambo *et al. Phys. Rec. C 58 489*, 1998.

[80] L. Montanet *et al. Phys. Rev. D 50 1173*, 1994.

[81] W.J Briscoe *et al.* Nsf major research instrumentation, nsf award 9724489. Technical report.

[82] D.I. Sober *et al.* The nremsstrahlung tagged photon beam in hall b at jlab. *Nuclear Instruments and Methods in Physics Research A 440 (2000) 263-284*, 1999.

[83] F. Klein. The coherent-bremsstrahlung facility in hall b at jefferson lab. Private Communication.

[84] P. Cole. The ipn-orsy/utep instrumented collimator. *Jlab Internal Publication*, 1999.

[85] M. Amarian *et al. Nucl. Instr. and Meth.A460, 239*, 2001.

[86] G. Adams *et al.* The clas cerenkov detector. *Nucl Inst Meth A 465, 414*, 2001.

[87] M.D. Mestayer. *Nucl. Instr. and Meth.A449, 81*, 200.

[88] M. Anghinofli *et al.* Respone to cosmic rays of the large-angle eletromagnetic shower calorimeter of the clas detector. *Nucl Inst Meth A 447, 424*, 2000.

[89] E.S. Smith *et al. Nucl Inst Meth A 432, 265-298*, 1999.

[90] Jefferson lab online data acquisition. Technical report, http://coda.jlab.org.

[91] D. Cords *et al.* Clas event format with bos. *CLAS-NOTE 94-012*, 1994.

[92] V. Blobel. The bos system, dynamic memory management. 1994.

[93] K. Livingston. Rootbeer. Private Communication(2004).

[94] E. Pasyuk. Clas-note 2007-016. Technical report, 2007.

[95] A. Natter. Analytic bremsstrahlung code. http://www.pit.physik.uni.tuebingen.de/bremsanalytic.html.

[96] Application Software Group/ Geant. Detector description and simulation tool. Technical report, CERN, Geneva, Switzerland, 1993.

[97] M. Holtrop. Clas geant simulation website. www.physics.unh.edu/maurik/gsimintro.shtml.

[98] A. Tkabladze. http://clasweb.jlab.org/offline/genphoto/.

[99] K. Joo. Gpp clas software routine. Technical report, Jlab Internal Document.

[100] X. Artu *et al.* *arXiv:nucl-th/0606050v2*, 2007.